Design and Synthesis of Heteroleptic Cyclometalated Iridium(III) Complexes and Their Applications to Material and Biological Sciences

(ヘテロレプティックなシクロメタレート型イリジウム(Ⅲ)錯体の設計・合成と材料科学および生物科学への応用)

２０２２年９月

生物有機化学研究室（指導教授　青木　伸 教授）

東京理科大学大学院薬学研究科薬科学専攻

田村（たむら）　裕一（ゆういち）

Yuichi Tamura

Contents

List of abbreviation

acac	acetylacetone
AgOTf	silver triflate
aq.	aqueous
ATR	attenuated total reflection
A.u.	arbitary unit
Boc	*tert*-butoxycarbonyl
DIEA	*N*-ethyl-*N*-(1-methylethyl)propan-2-amine
DMF	*N*,*N*-dimethylformamide
DMSO	dimethyl sulfoxide
EDC	1-ethyl-3-(3-dimethylaminopropyl) carbodiimide
ESI-MS	electrospray ionization mass spectroscopy
F_2ppy	2-(4',6'-difluorophenyl)pyridine
FAB bardment	fast atom bom
FCS	fetal calf serum
Fmoc	9-fluorenylmethoxycarbonyl
HBTU	2-(1H-benzotriazole-1-yl)-1,1,3,3-tetramethyluronium hexafluorophosphate
HEPES	*N*-(2-hydroxyethyl)piperazine-*N'*-2ethanesulfonic acid
HFIP	1,1,1,3,3,3-hexafluoro-2-propanol
HOBt	1-hydroxybenzotriazol
HOMO	highest occupied molecular orbital
HR-MS	high resolution mass spectrometry
HPLC	high performance liquid chromatography
IR	infra-red
Ir	iridium
LUMO	lowest unoccupied molecular orbital
Me	methyl
mpiq	1-(4'-methylphenyl)isoquinoline
mppy	2-(4'-methoxyphenyl)pyridine
MS	mass spectrometry
MTT	3-(4,5-di-methylthiazol-2-yl)-2,5-diphenyltetrazolium bromide

NMR	nuclear magnetic resonance
PBS	phosphate buffered saline
ppy	2-phenylpyridine
PyBop	benzotriazol-1-yl-oxytripyrrolidinophosphonium hexafluorophosphate
R	an arbitrary organic substituent
RP-HPLC	reverse-phased high performance liquid chromatography
r.t.	room temperature
*t*Bu	*tert*-butyl
tfpiq	1-(4'-trifluoromethylphenyl)isoquinoline
TIPS	triisopropyl silane
TLC	thin-layer chromatography
TMSCl	trimethylsilyl chloride
tpy	2-(4'-tolyl)pyridine
tpy-Br	2-(5'-bromo-4'-tolyl)pyridine
tpy-NO_2	2-(5'-nitro-4'-tolyl)pyridine
TFA	trifluoroacetic acid
UV	ultra-violet
VIS	visible
8BSQ	8-benzenesulfonylamidoquinoline

Chapter 1

General Introduction

General Introduction

In the past decades, a significant research effort has been focused on the synthesis and photophysical characterization of octahedral $4d^6$ and $5d^6$ metal complexes.[1] The typical examples of d^6 complexes are ruthenium(II) (Ru(II)) and osmium(II) (Os(II)) complexes of 2,2'-bipyridine (bpy), which have been widely used in a variety of photonic applications, including photocatalysis and photoelectrochemistry,[2,3] because of their long excited-state lifetimes and high luminescence efficiencies. The photophysics of related tris-chelate iridium(III) (Ir(III)) complexes have also been investigated since the 1980s.[4-6] These d^6 Ir(III) complexes are prepared from cyclometalated ligand such as 2-phenylpyridine (ppy) and exhibit longer excited-state lifetimes, typically in the order of microseconds, and higher luminescence efficiencies [e.g., φ_{phos} (*fac*-Ir(ppy)$_3$) = 0.4][7] than those of the Ru(II) and Os(II) complexes, due to efficient intersystem crossing between the singlet and triplet excited states induced by the strong spin−orbit coupling of the Ir(III) complex core. Moreover, color diversity arises from the ligand-related excited states in Ir complexes. The energy of the lowest excited state can therefore be controlled by adjusting the energy levels of ligand orbitals through substituent effects or by the conversion of the cyclometalated ligand structures. In addition, most of cyclometalated Ir(III) complexes can be classified into IrL_3 and IrL_2A (where L is cyclometalating ligand and A is an ancillary ligand). The synthesis, structure, and photophysical properties of IrL_3 and IrL_2A of Ir complexes and their applications are yet to be studied.

Synthesis and structure of IrL_3 type complexes

In 1984, Watts et al. reported the first IrL_3-type Ir complex (L: ligand), *facial*-Ir(ppy)$_3$ (*fac*-**1**), which was prepared in 10% yield as a by product in the reaction of ppyH (2-phenylpyridine) with hydrated $IrCl_3 \cdot H_2O$.[5b] They subsequently attempted at the reaction of methyl-substituted ppy ligands, but only trace amount of the desired complex was obtained.[5h] In 1991, they developed a new procedure for the synthesis of *fac*-IrL_3 with ppy and its analogs by using Ir(acac)$_3$ (acac: acetylacetonate) instead of hydrated $IrCl_3$ (Chart 1-1). Although this method typically produced *fac*-IrL_3 in 40–75%, it was not appropriate for the synthesis of other cyclometalated ligands. To solve this problem, Güdel et al. reported the reaction of a μ-dichloro bridged dimer complex [{$IrL_2(\mu\text{-Cl})$}$_2$] with an excess amount of free cyclometalated ligands (HC^N) to obtain *fac*-Ir(C^N)$_3$ complexes containing different cyclometalated ligands in high chemical yields.[6b]

Chart 1-1

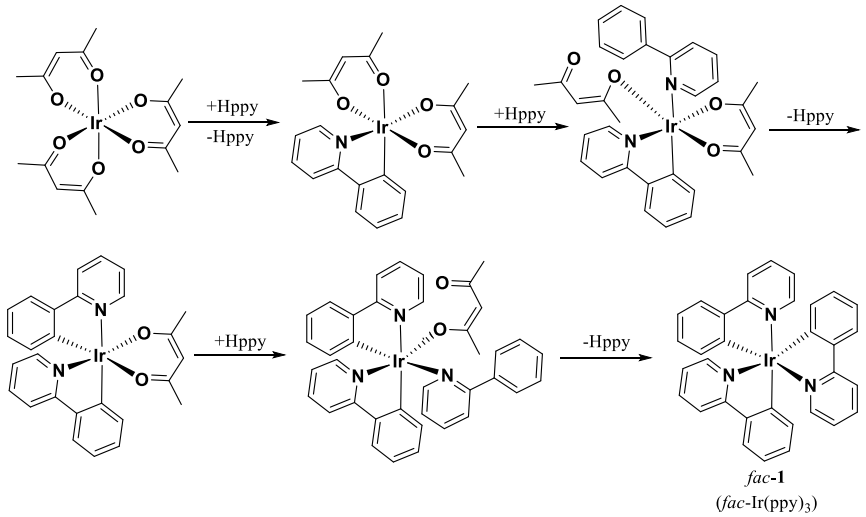

Meridional (abbreviated as *mer*) forms of IrL_3 complexes can also be prepared as stereoisomers of the *fac* forms (Chart 1-2). The results show that *fac*-IrL_3 complexes are obtained at higher temperature (e.g. 200°C), whereas *mer*-IrL_3 can be obtained at lower temperature at 150°C, suggesting that *fac* isomers are thermodynamically stable and that *mer*

isomers are kinetically favorable. Therefore, the *mer* isomer can be converted to the *fac* isomer by the reaction of *mer* isomers at high temperature.[8]

Chart 1-2

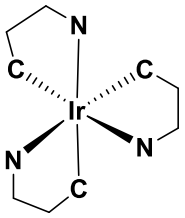

fac-Ir(C^N)$_3$

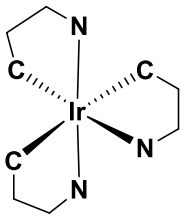

mer-Ir(C^N)$_3$

It should be mentioned that *mer* and *fac* isomers are different not only in their steric geometry configuration but also in Ir–N and Ir–C bond lengths. Typical bond lengths of *fac*-Ir(tpy)$_3$ (*fac*-**2**, tpy is 4-methylphenylpyridine) and *mer*-Ir(tpy)$_3$ (*mer*-**2**) are compared in Chart 1-3. In the *fac* isomer of **2**, all the Ir–C bonds are *trans* with respect to the Ir-N(pyridine) bonds, and the Ir–N bonds are *trans* with respect to the Ir-C(phenyl) bonds with almost same Ir–C and Ir–N bond lengths. Some bond lengths of *mer*-**2** are different from those of *fac*-**2**, possibly because Ir–C (or Ir–N) bonds in *mer*-**2** possess an different electronic environment from Ir–C (or Ir–N) bonds in *fac*-**2**.

Chart 1-3

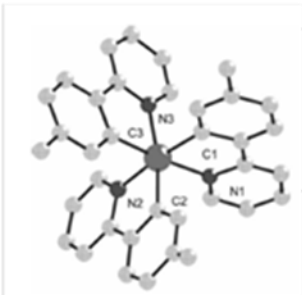

fac-**2**

	Bond Length (Å)	
Bond Type	*fac*-**2**	*mer*-**2**
Ir-N1		2.15
Ir-N2	2.13	2.04
Ir-N3		2.07
Ir-C1		2.08
Ir-C2	2.02	2.09
Ir-C3		2.02

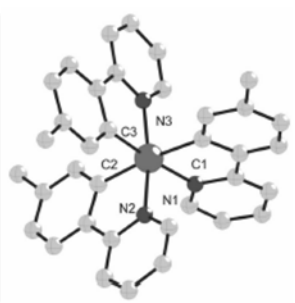

mer-**2**

Photophysical properties of IrL_3 type complexes

To date, the photophysical properties of different stereoisomers of IrL_3 have been examined by several research groups.[8,9] Two principal transitions include: (1) metal-to-ligand charge transfer (MLCT), in which an electron is promoted from a metal d orbital to a vacant π* orbital in one of the ligands and (2) ligand-centered (LC) transitions, in which an electron is promoted between π orbitals on one of the coordinated ligands. Phosphorescence in IrL_3-type complexes is induced by strong spin-orbit coupling mainly arising from a mixture of ^{3}LC and ^{3}MLCT excited states, whereas the emissive excited state has the lowest energy levels.

The lowest excited state of IrL_3-type complexes can be controlled by the introduction of electron-donating or electron-withdrawing groups on the cyclometalated ligands or by changing the cyclometalated ligand units. Table 1-1 summarizes the photophysical properties of complexes **1** , **2**, and $Ir(F_2ppy)_3$ **3** (Chart 1-4).[8] It is known that the energy levels of the highest occupied molecular orbital (HOMO) and the lowest unoccupied molecular orbital (LUMO) levels of these metal complexes are affected by the functionalization of ligand parts and hence photophysical properties of *mer*-IrL_3-type complexes are different from those of the corresponding *fac*-forms. Generally, meridional complexes exhibit a broad and red-shifted emission with low quantum yields, which can be attributed to strong *trans* effect from phenyl groups at the opposite side.[10]

Table 1-1 Photophysical properties of **1**, **2**, and **3** in 2-methyltetrahydrofuran at 298K

Compounds	λ_{em} (nm)	Quantum yield Φ	Emission liftime τ (μs)
***fac*-1**	510	0.40	1.9
***mer*-1**	512	0.036	0.15
***fac*-2**	510	0.50	2.0
***mer*-2**	550	0.051	0.26
***fac*-3**	468	0.43	1.6
***mer*-3**	482	0.053	0.21

Chart 1-4

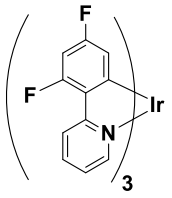

$Ir(F_2ppy)_3$
***fac*-3**
***mer*-3**

Synthesis and structure of IrL_2A type complexes

General synthetic method of IrL_2A-type complexes **5** (A: ancillary ligand) is shown in Chart 1-5, in which μ-dichloro bridged dimer complex $[\{IrL_2(\mu\text{-}Cl)\}_2]$ **4** is readily prepared from the reaction of the ligand precursor and $IrCl_3 \cdot nH_2O$[11] and its chloride ions can be subsequently replaced with an ancillary ligand (A) such as acac, picolinic acid, quinolinol, and so on.[12,13,14]

The X-ray crystal structure of **6** as one of typical examples of **5** is shown in Chart 1-6, where Ir-C bonds (1.98Å in average) are shorter than those of **2** and **3**, possibly due to weak *trans* effect of the acac ligand.

Chart 1-5

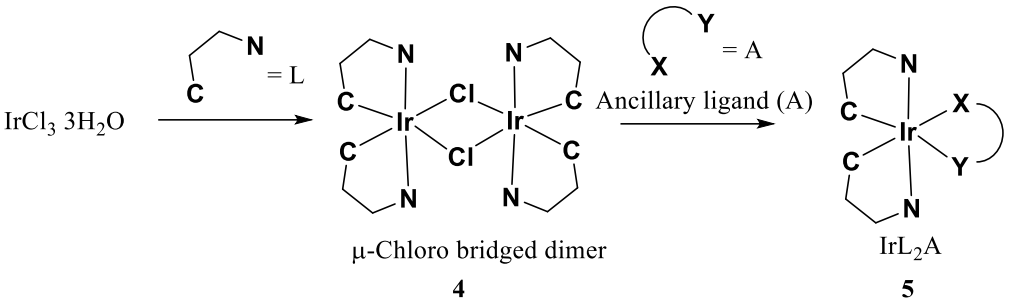

Chart 1-6

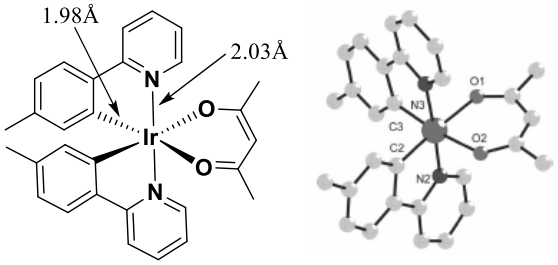

Photophysical properties of IrL_2A type complexes

It should be noted that the lowest triplet energy level of the ancillary ligand A is higher than that of LC and MLCT excited states in most of the IrL_2A-type complexes and hence the wavelength of emission maxima of IrL_2A is determined by ^{3}LC and ^{3}MLCT transitions. Similar phosphorescence emission is observed in the *fac*-IrL_3 containing the same cyclometalated ligand.[12,15] The results of density functional theory (DFT) calculations indicate that HOMOs are located mainly at the metal center and the LUMOs are localized on the heterocyclic rings of the cyclometalated ligand parts, not at the ancillary ligand unit.

Chart 1-7 shows the emission spectra of $Ir(tpy)_2(pz_2Bpz_2)$ (**7**), $Ir(tpy)_2(pz_2H)$ (**8**), $Ir(tpy)_2(pzH)Cl$ (**9**), and $Ir(tpy)_2(acac)$ (**6**), which have the tpy ligands, in solution at room temperature. It is likely that a blue-shift of the emission maximum of **7**-**9** is caused by the ancillary parts. Namely, the electron-withdrawing ligand lowers the HOMO level, resulting in

the blue-shift of the emission. On the other hand, the LUMO of $Ir(tpy)_2A$ complexes localized on the pyridyl rings raises in LUMO level.

Chart 1-7

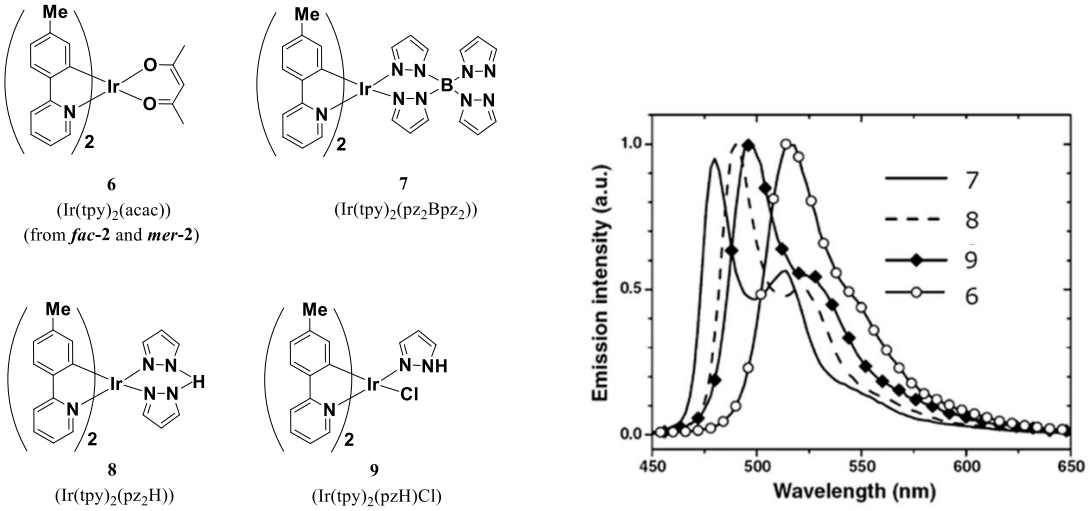

Purpose of this thesis

Homoleptic IrL_3 and bis-heteroleptic IrL_2A types of Ir(III) complexes have received considerable attention as phosphorescent emitters[16] and have been applied in a broad research areas related to organic light emitting diodes (OLEDs),[17] bioimaging probes,[18] oxygen sensors,[19] anticancer agents,[20] photoredox catalysts,[21] pH sensors,[22] and so on.[23] However, the selective synthesis and photophysical properties of *tris-heteroleptic* Ir complexes represented by IrLL'A or IrLL'L'' are yet to be studied.

We have discovered the selective degradation reactions of cyclometalated Ir(III) complexes promoted by ZnX_2 (X: halide such as Cl and Br) as presented in Chapter 2 (Chart 1-8).[24] Mechanistic studies suggest that the selective degradation reactions is controlled by the hardness and softness of the Brønsted and Lewis acid promoters. This degradation reaction is applied to the synthesis of *tris-heteroleptic tris-cyclometalated* Ir complexes in Chapter 3

(Chart 1-9).[25] The selective synthesis of specific isomers among eight possible stereoisomers of Ir complexes having the same combination of three cyclometalating ligands is reported.

Chart 1-8

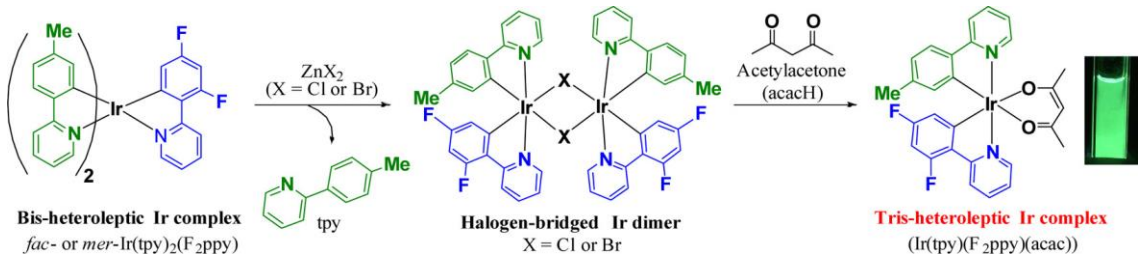

Chart 1-9

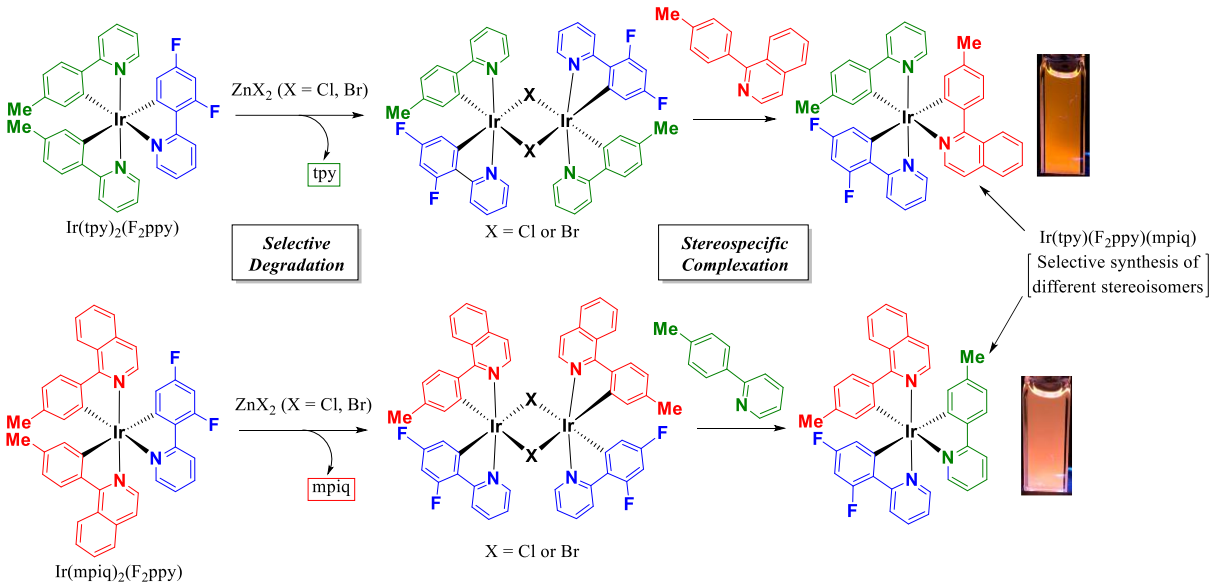

In this thesis, hybrid compounds of heteroleptic cyclometalated Ir(III) complexes with specific peptides were designed and synthesized for the induction of programmed cell death (PCD) in cancer cells. It is established that PCD is an essential mechanism for the control of intracellular homeostasis for cell survival, consists of apoptosis, necroptosis, paraptosis, and autophagy (Chart1-10).[26] Aoki et al. have reported the design and synthesis of tris-homoleptic Ir(III)-complex with cationic peptides such as GGKK and GGKKK (G: glycine and K: lysine) segments (IPHs: Ir(III)-complex peptide hybrids) that induce the paraptotic PCD in Jurkat cells

(T-lymphocyte leukemia).[27] These reports promoted us to study the effect of number of peptide units on anticancer activity. In Chapter 4, design and synthesis of bis- or mono-heteroleptic types of IPHs compared with tris-homoleptic types of IPHs and those of anticancer activity are reported (Chart 1-11).[28] The Ir(III) complex-bispeptide conjugate and the monopeptide conjugate exhibit potential anticancer activity against Jurkat cells and dead cells show a strong green emission. These peptide conjugates show more potent activity towards Jurkat cancer cells, indicative of a positive relationship between the number of the KKKGG peptide chains and hence net cationic charges and their anticancer activity (Chart 1-11). Mechanistic studies suggest that tris-homoleptic and bis-heteroleptic types of IPHs induce paraptotic cell death in Jurkat cells with the vacuolization of the cytoplasm, mitochondria, the ER, and lysosomes, as confirmed by TEM images of Jurkat cells.[27i,k,28]

Chart 1-10

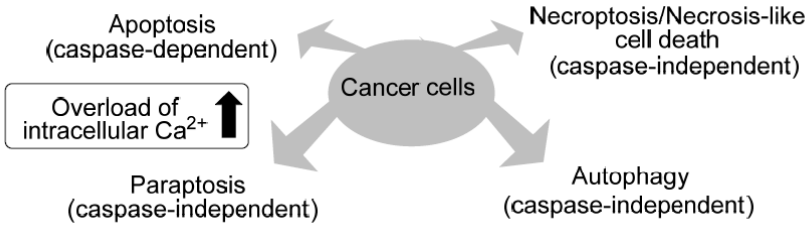

Chart 1-11

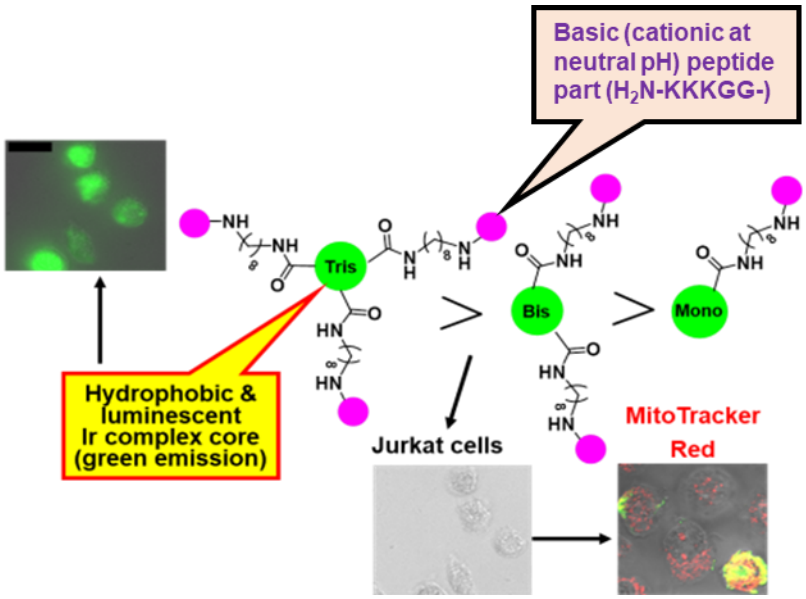
Basic (cationic at neutral pH) peptide part (H_2N-KKKGG-)
Tris
Bis
Mono
Hydrophobic & luminescent Ir complex core (green emission)
Jurkat cells
MitoTracker Red

Chapter 2

Efficient Synthesis of Tris-Heteroleptic Iridium(III) Complexes Based on the Zn^{2+}-Promoted Degradation of Tris-Cyclometalated Iridium(III) Complexes and Their Photophysical Properties

2-1 Introduction

Chart 2-1 shows the typical synthesis of tris-heteroleptic Ir complexes **11** (IrLL'A) by the reaction of a chloro-bridged dimers **10**, which are prepared from $IrCl_3$, and a mixture of two different cyclometalating ligands (L and L'), followed by the reaction with a corresponding ancillary ligand (A).[29] Because this method gives a mixture of IrLL'A with IrL_2A and IrL'_2A, their purification is usually difficult and results in low chemical yields. Baranoff and co-workers reported on the synthesis of the tris-heteroleptic Ir complex, Ir(ppy)(F_2ppy)(acac) (ppy: 2-phenylpyridine, F_2ppy: 2-(4',6'-difluorophenyl)pyridine and acac: acetylacetonate), by reacting an Ir(I) complex [{Ir(COD)(μ-Cl)}$_2$] complex (COD:1,5-cyclooctadiene) with ppy and F_2ppy ligands.[29e] Moreover, they reported that the degradation of Ir(ppy)(F_2ppy)(acac) induced by HCl (2M in Et_2O) provided a heteroleptic μ-complex [{Ir(ppy)(F_2ppy)(μ-Cl)}$_2$], which is a useful intermediate for the synthesis of other tris-heteroleptic Ir complexes containing ppy and F_2ppy ligands. Although this method is also accompanied by tedious purification and low product yields, it is the only reported method to date for preparing tris-heteroleptic Ir complexes.

Chart 2-1

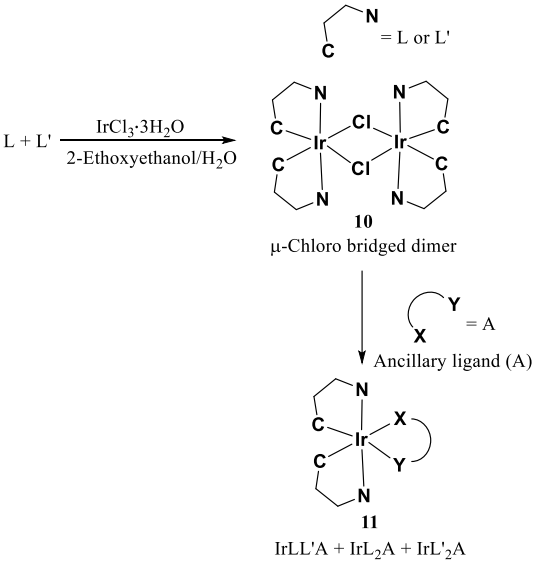

Aoki et al. previously reported on regioselective substitution reactions (*e.g.*; halogenations, nitration, and Vilsmeier-Haack formylation) of *fac*-tris-homoleptic cyclometalated Ir complexes, *fac*-Ir(ppy)$_3$ (***fac*-1**), *fac*-Ir(tpy)$_3$ (***fac*-2**) (tpy: 2-(4'-tolyl)pyridine), and *fac*-Ir(mppy)$_3$ (***fac*-12**) (mppy: 2-(4'-methoxyphenyl)pyridine), at the 5'-position (the *p*-position with respect to the C-Ir bond) on 2-phenylpyridine ligands and their subsequent conversions to produce **13** containing a variety of functional groups (Chart 2-2).[30,31] These findings allowed us to design and synthesize pH-responsive Ir complexes that contain basic groups,[30a,31a,c,d] blue-colored Ir complexes[30b] and amphiphilic Ir complexes containing cationic peptides (IPHs) that have cytotoxic activity against cancer cells.[31b]

Chart 2-2

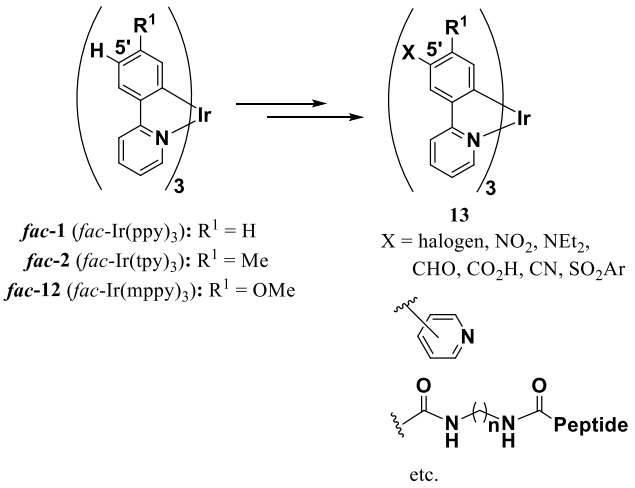

During these experiments, it was found that the reaction of ***fac*-2** with acetyl chloride in the presence of $AlCl_3$ (Friedel-Crafts acylation conditions) afforded the chloro-bridged Ir dimer **15a** in 68% yield, and not an acetyl derivative **14** (Chart 2-3).[30a] This finding prompted us to examine the degradation reactions of tris-cyclometalated Ir complexes with a variety of Lewis acids.

Chart 2-3

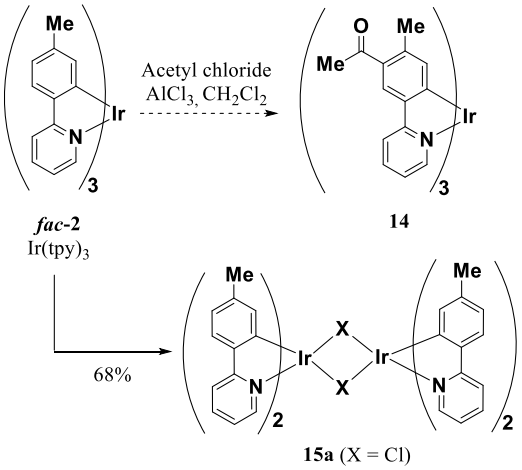

In Chapter 2 of this Ph.D thesis, we report that Lewis acids such as zinc halides (ZnX_2), $AlCl_3$ and TMSCl promote the degradation of tris-cyclometalated homoleptic Ir complexes including *fac*-Ir(ppy)$_3$ (***fac*-1**), *mer*-Ir(ppy)$_3$ (***mer*-1**), *fac*-Ir(tpy)$_3$ (***fac*-2**), *mer*-Ir(tpy)$_3$ (***mer*-2**), *fac*-Ir(mppy)$_3$ (***fac*-12**), *fac*-Ir(Br-tpy)$_3$ (***fac*-16**) (Br-tpy: 2-(5'-bromo-4'-tolyl)pyridine), *fac*-Ir(mpiq)$_3$ (***fac*-17**) (mpiq: 1-(4'-methylphenyl)isoquinoline) and *mer*-Ir(mpiq)$_3$ (***mer*-17**) to provide the corresponding halogen-bridged Ir dimers (μ-complexes) such as **15a** from ***fac*-** and ***mer*-2** (Charts 2-4 and 2-5). In contrast, tris-cyclometalated Ir complexes that contain cyclometalated ligands containing an electron-withdrawing group such as *fac*-Ir(F_2ppy)$_3$ (***fac*-3)**,*fac*-Ir(NO_2-tpy)$_3$ (***fac*-18**) (NO_2-tpy: 2-(5'-nitro-4'-tolyl)pyridine) and *fac*-Ir(tfpiq)$_3$ (***fac*-19**) (tfpiq: 1-(4'-trifluoromethylphenyl)isoquinoline) were less reactive. The μ-complex **15a** was reacted with acetylacetone (acacH) to afford Ir(tpy)$_2$(acac) **6** (Chart 2-5). Because these types of Ir complexes that contain two identical ligands are readily available (for example, **6** can be synthesized from tpy via **15a**), we examined the ligand-selective degradation reactions of tris-cyclometalated heteroleptic Ir complexes, ***fac*-20** and ***mer*-20-24** that contaion two different ligands such as tpy, mppy, mpiq, and F_2ppy (Chart 2-4) in the presence of Brønsted and Lewis acids. As a result, it was found that the reaction of ***fac*-20** with $ZnBr_2$ gives the heteroleptic μ-complex [{Ir(tpy)(F_2ppy)(μ-Br)}$_2$] as the major product due to the selective elimination of its

tpy ligand and the product, on reaction with acacH, afforded the tris-heteroleptic Ir complex Ir(tpy)(F_2ppy)(acac) **25** (Chart 2-5). Moreover, novel tris-heteroleptic Ir complexes containing an ancillary ligand (*e.g.*; 8-benzenesulfonylamidoquinoline (8BSQ)) were obtained.[24] Mechanistic studies of this degradation reaction and photochemical properties of these newly synthesized tris-heteroleptic Ir complexes are also described.[32] The chemical structures and numbers of Ir complexes presented in this chapter are also summarized in Chart 2-6.

Chart 2-4

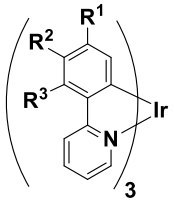

***mer*-1**: R^1, R^2, R^3 = H
***mer*-2**: R^1 = Me, R^2 = R^3 = H
***fac*-3:** R^1 = F, R^2 = H, R^3 = F
***mer*-3**: R^1 = F, R^2 = H, R^3 = F
***fac*-16**: R^1 = Me, R^2 = Br, R^3 = H
***fac*-18**: R^1 = Me, R^2 = NO_2, R^3 = H

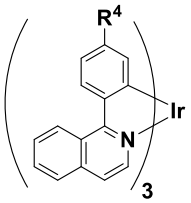

***fac*-17** (*fac*-Ir(mpiq)$_3$): R^4 = Me
***mer*-17** (*mer*-Ir(mpiq)$_3$): R^4 = Me
***fac*-19** (*fac*-Ir(tfpiq)$_3$): R^4 = CF_3

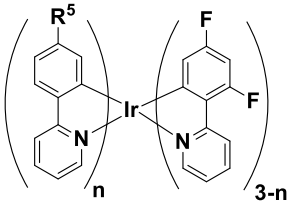

***fac*-20**: R^5 = Me, n = 2
***mer*-20**: R^5 = Me, n = 2
***mer*-21**: R^5 = Me, n = 1
***mer*-22**: R^5 = OMe, n = 2

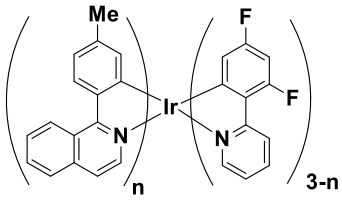

***mer*-23**: n = 2
***mer*-24**: n = 1

Chart 2-5

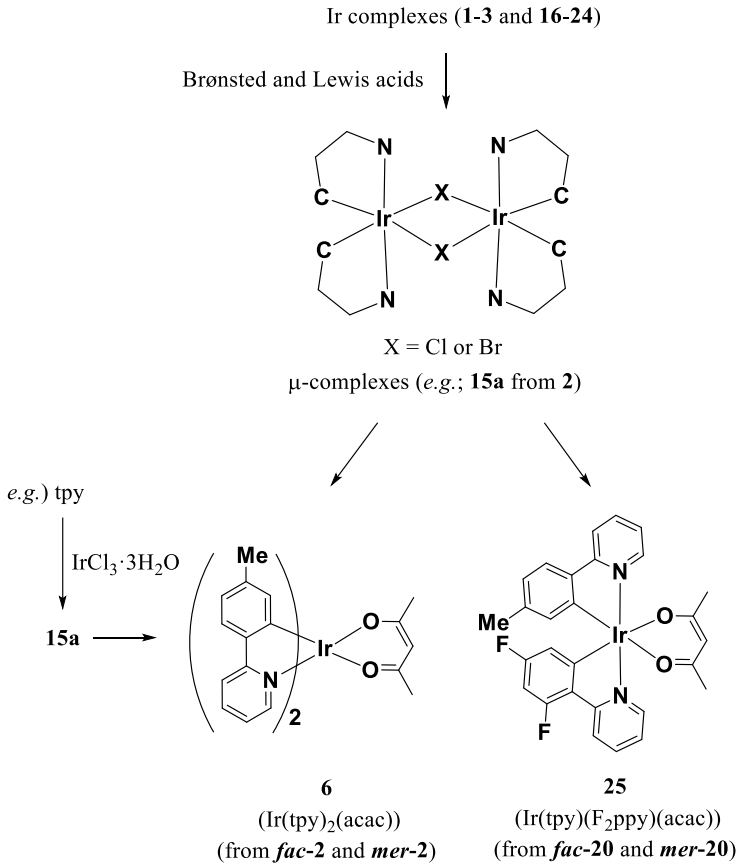
Ir complexes (1-3 and 16-24)
Brønsted and Lewis acids
X = Cl or Br
μ-complexes (e.g.; 15a from 2)
e.g.) tpy
IrCl3·3H2O
15a
6
(Ir(tpy)2(acac))
(from fac-2 and mer-2)
25
(Ir(tpy)(F2ppy)(acac))
(from fac-20 and mer-20)

Chart 2-6. A list of structures and numbers of Ir complexes presented in this manuscript.

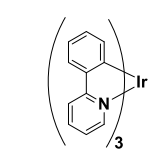

***fac*-1**: *fac*-Ir(ppy)$_3$
***mer*-1**: *mer*-Ir(ppy)$_3$

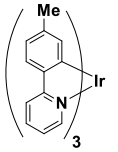

***fac*-2**: *fac*-Ir(tpy)$_3$
***mer*-2**: *mer*-Ir(tpy)$_3$

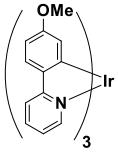

***fac*-12**: *fac*-Ir(mppy)$_3$

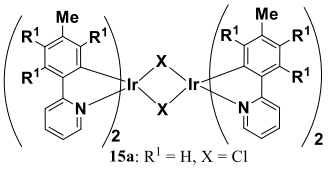

15a: R^1 = H, X = Cl
15b: R^1 = H, X = Br
d_{12}**-15a**: R^1 = D

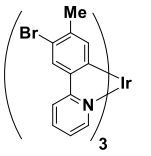

***fac*-16**: *fac*-Ir(Br-tpy)$_3$

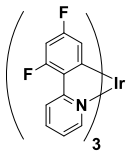

***fac*-3:** *fac*-Ir(F$_2$ppy)$_3$
***mer*-3:** *mer*-Ir(F$_2$ppy)$_3$

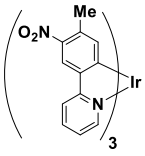

***fac*-18**: *fac*-Ir(NO$_2$-tpy)$_3$

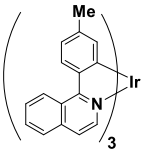

***fac*-17**: *fac*-Ir(mpiq)$_3$
***mer*-17**: *mer*-Ir(mpiq)$_3$

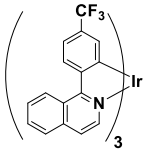

***fac*-19**: *fac*-Ir(tfpiq)$_3$

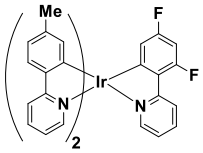

***fac*-20**: *fac*-Ir(tpy)$_2$(F$_2$ppy)
***mer*-20**: *mer*-Ir(tpy)$_2$(F$_2$ppy)

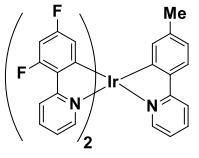

***mer*-21**: *mer*-Ir(F$_2$ppy)$_2$(tpy)
***fac*-21**: *mer*-Ir(F$_2$ppy)$_2$(tpy)

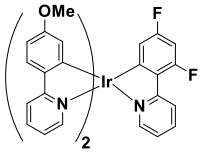

***mer*-22**: *mer*-Ir(mppy)$_2$(F$_2$ppy)

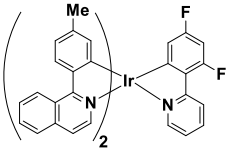

***mer*-23**: *mer*-Ir(mpiq)$_2$(F$_2$ppy)

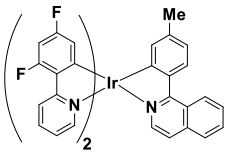

***mer*-24**: *mer*-Ir(F$_2$ppy)$_2$(mpiq)
***fac*-24**: *fac*-Ir(F$_2$ppy)$_2$(mpiq)

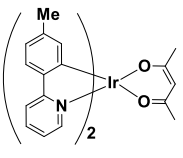

6: Ir(tpy)$_2$(acac)

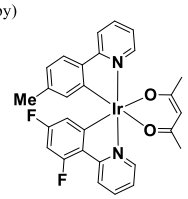

25: Ir(tpy)(F$_2$ppy)(acac)

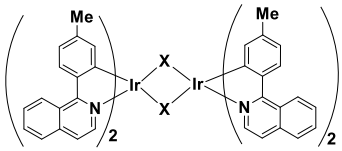

26a: X = Cl
26b: X = Br

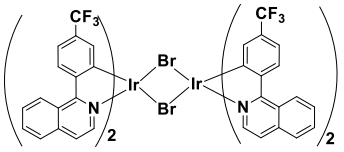

26c

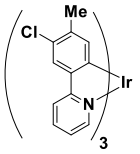

***fac*-27**: *fac*-Ir(Cl-tpy)$_3$

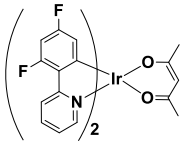

29b: Ir(F$_2$ppy)$_2$(acac)

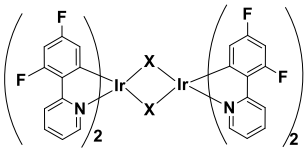

30a: X = Cl
30b: X = Br

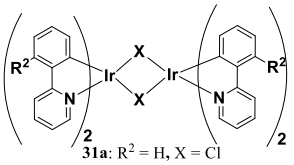

31a: R^2 = H, X = Cl
31b: R^2 = H, X = Br
d_4**-31a**: R^2 = D

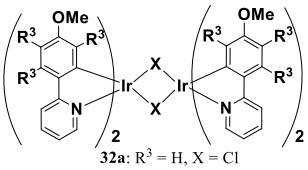

32a: R^3 = H, X = Cl
32b: R^3 = H, X = Br
d_{12}**-32a**: R^3 = D

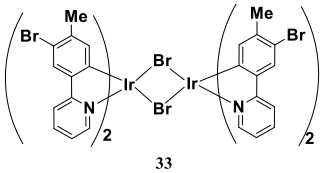

33

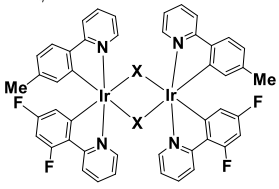

34a: X = Cl
34b: X = Br

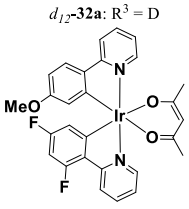

35: Ir(mppy)(F$_2$ppy)(acac)

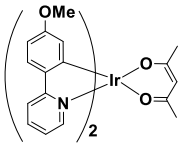

36: Ir(mppy)$_2$(acac)

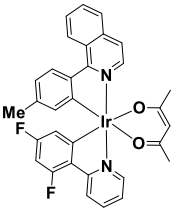

37: Ir(mpiq)(F$_2$ppy)(acac)

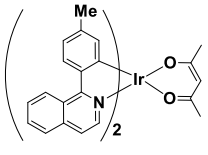

38: Ir(mpiq)$_2$(acac)

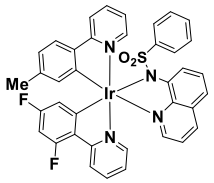

42a: Ir(tpy)(F$_2$ppy)(8BSQ$^-$)

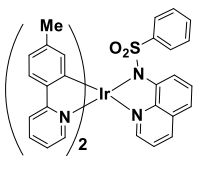

43: Ir(tpy)$_2$(8BSQ$^-$)

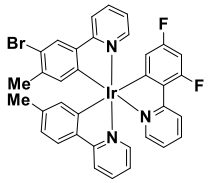

***mer*-50**: *mer*-Ir(tpy)(Br-tpy)(F$_2$ppy)

2-2 Results and Discussions

2-2-1 Synthesis of Cyclometalated Ir Complexes

The substrates for the decomposition reactions, bis- or tris-cyclometalated Ir complexes, were synthesized from $IrCl_3 \cdot 3H_2O$ and cyclometalating ligands. The facial (*fac*) isomers of the cyclometalated homoleptic Ir complexes, $Ir(ppy)_3$ (***fac*-1**), $Ir(tpy)_3$ (***fac*-2**), and $Ir(F_2ppy)_3$ (***fac*-3**) were synthesized at 200 ˚C and their meridional (*mer*) isomers were obtained at *ca.* 150 ˚C, as reported by Thompson and co-workers.[8] For example, the synthesis of ***fac*-2**, ***mer*-2**, ***fac*-20**, ***mer*-20**, ***fac*-17**, and ***mer*-23** is shown in Chart 2-7. Although negligible amounts of *fac*-$Ir(tpy)_2(F_2ppy)$ (***fac*-20**) were obtained by Thompson's method (a mixture of chloro-bridged Ir dimer $[\{Ir(tpy)_2(\mu\text{-}Cl)\}_2]$ **15a**, which was prepared from $IrCl_3 \cdot 3H_2O$ and tpy,[33] and F_2ppy in glycerol was refluxed at 200 ˚C) due to ligand sclambling,[34] it was successfully obtained from the same substrates by using AgOTf in 2-ethoxyethanol.[35] Meridional isomers of heteroleptic Ir complexes, ***mer*-20**, ***mer*-22**, and ***mer*-23**, were obtained in 74%, 17% and 81% yields, respectively, from the corresponding μ-complexes and ligands and ***mer*-21** and ***mer*-24** were synthesized according to a method reported in a patent,[36] in which the μ-complex $[Ir(F_2ppy)_2(\mu\text{-}Cl)]_2$ was reacted with tpy (for ***mer*-21**) or mpiq (for ***mer*-24**) in the presence of AgOTf and NEt_3. The synthesis of ***fac*-** and ***mer*-20** was carried out as shown in Chart 2-7.

Chart 2-7 The synthesis of ***fac*-2**, ***mer*-2**, ***fac*-20**, ***mer*-20**, ***mer*-17** and ***mer*-23**.

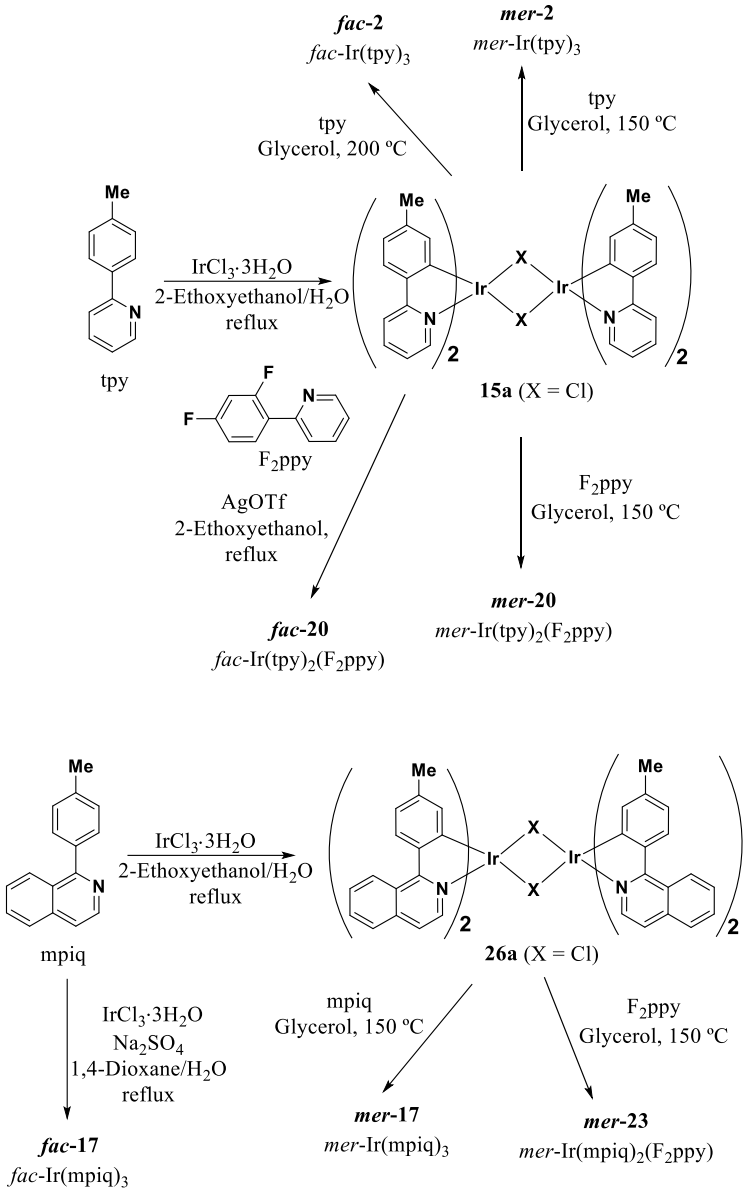

All the Ir complexes were structurally characterized by ^{1}H NMR, ESI-MS and related techniques, and X-ray structure analyses were carried out for ***fac*-20**, ***mer*-20**, and ***mer*-23** (ORTEP drawings[37] in Figure 2-1). As summarized in Table 2-1, selected bond lengths of ***fac*-20** are quite similar to those of *fac*-Ir(tpy)$_3$ (***fac*-2**) (Ir-C: 2.02 Å and Ir-N: 2.13 Å).[8] It should be noted that the Ir-C and Ir-N bond lengths of F$_2$ppy ligand in ***mer*-20** (Ir-C: 2.07 Å and Ir-N: 2.11 Å) and ***mer*-23** (Ir-C: 2.08 Å and Ir-N: 2.12 Å) are somewhat longer than those between Ir

and tpy ligands (Ir-C: 1.99, 2.04 Å and Ir-N: 2.02, 2.03 Å) and Ir and mpiq ligands (Ir-C: 1.97, 2.05 Å and Ir-N: 2.02, 2.03 Å). For these Ir complexes, the Ir-C and Ir-N bond lengths were estimated by DFT calculations and are listed in Table 2-1, because these calculated values are important in terms of the mechanism of the degradation reactions, as described below (the results of DFT calculations of other tris-cyclometalated homoleptic Ir complexes, ***fac*-2**, ***fac*-3,** ***fac*-12**, ***fac*-16**, and ***fac*-18**, are shown in Figure 2-2). The experimental Ir-C and Ir-N bond lengths of ***fac*-20**, ***mer*-20**, and ***mer*-23** are in good agreement with the calculated Ir-C and Ir-N bond lengths (DFT calculations in Table 2-1).

(a)

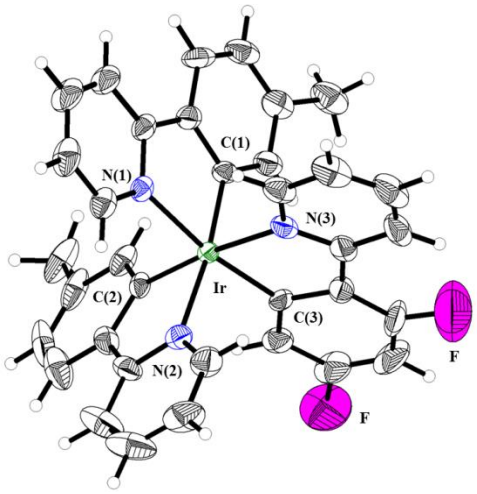

(b)

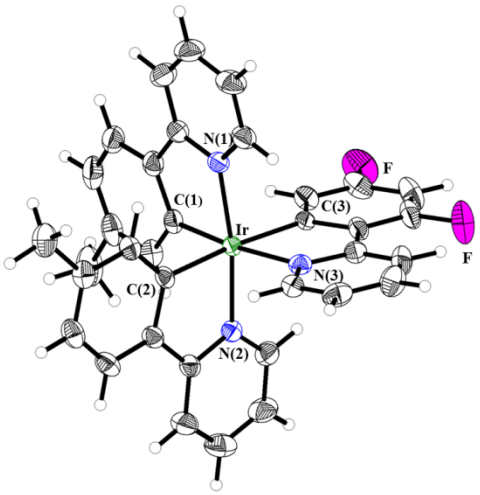

(c)

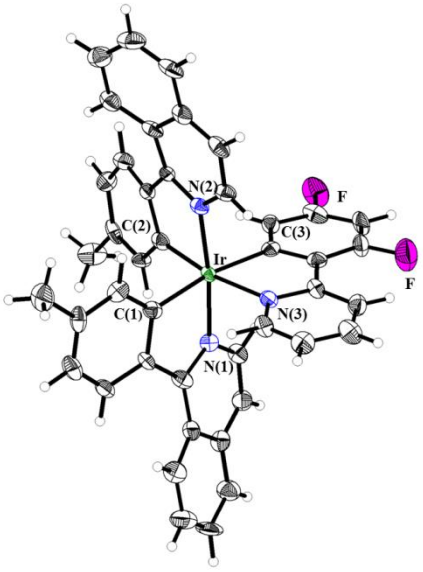

Figure 2-1. ORTEP drawings of single crystal structures of (a) ***fac*-20**, (b) ***mer*-20**, and (c) ***mer*-23** with 50% probability ellipsoids. For clarity, the CH_2Cl_2 in (b) and (c) is omitted.

Table 2-1. Selected bond lengths (Å) of (a) ***fac*-20**, (b) ***mer*-20**, and (c) ***mer*-23** in X-ray crystal structure (left) and those obtained by DFT calculations (right)

(a)	X-ray structure bond lengths (Å)	Calculated bond lengths (Å)
Ir-C(1) (tpy)	2.01	2.04
Ir-C(2) (tpy)	1.99	2.04
Ir-C(3) (F_2ppy)	1.99	2.03
Ir-N(1) (tpy)	2.12	2.17
Ir-N(2) (tpy)	2.12	2.16
Ir-N(3) (F_2ppy)	2.13	2.16

(b)	X-ray structure bond lengths (Å)	Calculated bond lengths (Å)
Ir-C(1) (tpy)	1.99	2.02
Ir-C(2) (tpy)	2.04	2.09
Ir-C(3) (F_2ppy)	2.07	2.11
Ir-N(1) (tpy)	2.02	2.07
Ir-N(2) (tpy)	2.03	2.08
Ir-N(3) (F_2ppy)	2.11	2.19

(c)	X-ray structure bond lengths (Å)	Calculated bond lengths (Å)
Ir-C(1) (mpiq)	1.97	2.02
Ir-C(2) (mpiq)	2.05	2.08
Ir-C(3) (F_2ppy)	2.08	2.10
Ir-N(1) (mpiq)	2.02	2.09
Ir-N(2) (mpiq)	2.03	2.08
Ir-N(3) (F_2ppy)	2.12	2.20

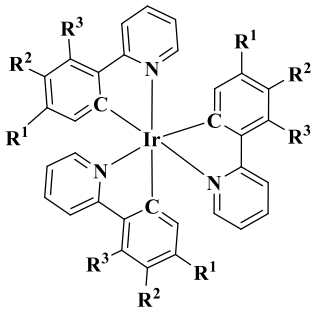

Bond distance (Å)

	fac-Ir(tpy)$_3$ ***fac*-2** R^1 = Me R^2 = H R^3 = H		*fac*-Ir(Br-tpy)$_3$ ***fac*-16** R^1 = Me R^2 = Br R^3 = H		*fac*-Ir(mppy)$_3$ ***fac*-12** R^1 = OMe R^2 = H R^3 = H	*fac*-Ir(F_2ppy)$_3$ ***fac*-3** R^1 = F R^2 = H R^3 = F	*fac*-Ir(NO_2-tpy)$_3$ ***fac*-18** R^1 = Me R^2 = NO_2 R^3 = H
Bond type	X-ray structure	Cal.	X-ray [a] structure	Cal.	Cal.	Cal.	Cal.
Ir-C	2.02	2.04	2.02	2.03	2.03	2.03	2.03
Ir-N	2.13	2.17	2.13	2.17	2.15	2.18	2.17

Figure 2-2. Optimized structures of tris-cyclometalated Ir complexes obtained by DFT calculations (B3LYP/LanL2DZ for Ir and Br atoms and 6-31G for H, C, N, O, and F atoms). a) From Ref. 30a in the text.

2-2-2 Degradation Reaction of *fac*-Ir(tpy)$_3$ by Brønsted or Lewis Acids

The results for the Brønsted or Lewis acid-promoted degradation reactions of *fac*-Ir(tpy)$_3$ (***fac*-2**) (43 μmol) in 1,2-dichloroethane (2.0 mL) are summarized in Table 2-2. The reaction of ***fac*-2** with $AlCl_3$ gave the corresponding chloro-bridged Ir dimer, **15a**, in 84% yield (Entry 1). It was found that $ZnCl_2$ and $ZnBr_2$ promoted the degradation of ***fac*-2** at reflux temperature to provide **15a** and the bromo-bridged Ir dimer **15b**, respectively, in reasonably good yields, while that reaction negligibly proceeds at room temperature (Entries 2-4). In Entry 3, the tpy ligand was recovered in *ca*. 30% yield, as determined by ^{1}H NMR (when 20-30 eq. of $ZnCl_2$ was used, tpy was recovered in 71-90%). Characterization of **15b** obtained in Entry 4 was carried out by ^{1}H NMR, ESI-MS, and X-ray structure analysis (See Figure 2-3). The representative parameters for the crystal structure of **15b** in Table 2-3 indicate that two Ir atoms of **15b** adopt a slightly distorted octahedral coordination geometry about the Ir(III) centers, at which two Ir-N bonds connected to the same Ir atom are in a *trans* configuration and the Ir-C

bonds have *cis* configuration.[38] The degradation reaction of ***fac*-2** was not promoted by ZnO in the absence or the presence of $(n\text{Bu})_4\text{NBr}$ as a bromide source (Entries 5 and 6). In Entries 7-9, the reaction of ***fac*-2** with $\text{Zn}(\text{ClO}_4)_2$ or ZnCl_2 in EtOH and CCl_4 gave **15a** in negligible or very low yields. Trimethylsilyl chloride (TMSCl) also promoted the degradation of ***fac*-2** to give **15a** in 71% (Entry 10) and FeCl_3 gave the chlorinated ***fac*-2** (*fac*-Ir(Cl-tpy) (***fac*-27**)) and the chlorinated tpy ligand in 9% and 4% yields and other organic compounds could not be isolated (Entry 11), suggesting a possibility that ***fac*-2** was decomposed after chlorination, while CuCl_2 and PdCl_2 afforded complex mixtures, the characterization of which was difficult (Entries 12 and 13).[39] A negligible amount of **15a** was obtained after the reaction of $\text{CdCl}_2\cdot 2.5\text{H}_2\text{O}$ and Zn^{2+}-1,4,7,10-tetraazacyclodecane (Zn^{2+}-cyclen) complex (**28a, b**)[40,41] and afforded byproducts, characterization of which was difficult (Entries 14-16). The reaction with TFA and $(n\text{Bu})_4\text{NCl}$ afforded **15a** in less than 42% yield, as determined by ^1H NMR (Entry 17). On the other hand, the treatment with TFA and ZnCl_2 resulted in negligible amounts of **15a** (Entry 18).

Table 2-2

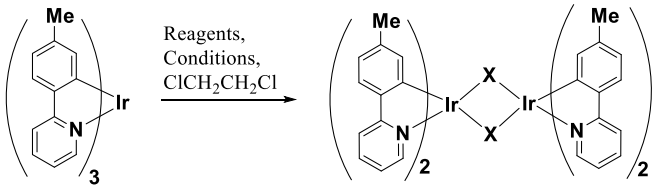

***fac*-2**
(*fac*-Ir(tpy)$_3$)

15a: X = Cl
15b: X = Br

Entry	Reagents	Reaction conditions	Recovery yield of ***fac*-2** (*fac*-Ir(tpy)$_3$) (%)	Yield of 15 (%)
1	$AlCl_3$ (5.0 equiv.)	r.t., 30 min	trace	84 (**15a**)
2	$ZnCl_2$ (50 equiv.)	r.t., 1.5 hr	88	trace
3	$ZnCl_2$ (80 equiv.)	reflux, 2 hr	trace	52 (**15a**)
4	$ZnBr_2$ (50 equiv.)	reflux, 3 hr	trace	93 (**15b**)
5	ZnO (50 equiv.)	reflux, 48 hr	66	trace
6	ZnO (25 equiv.), $(n\text{Bu})_4\text{NBr}$ (50 equiv.)	reflux, 96 hr	90	trace
7	$Zn(ClO_4)_2\cdot 6H_2O$ (10 equiv.)[a]	r.t., 48 hr	85	trace
8	$ZnCl_2$ (50 equiv.)[a]	reflux, 13 hr	15	trace
9	$ZnCl_2$ (50 equiv.)[b]	reflux, 10 hr	trace	14
10	Me_3SiCl (50 equiv.)	r.t., 2.5 hr	trace	71 (**15a**)
11	$FeCl_3$ (50 equiv.)	r.t., 2 hr	trace	trace[c]
12	$CuCl_2$ (5 equiv.)	reflux, 44 hr	trace	trace[d]
13	$PdCl_2$ (5 equiv.)	reflux, 28 hr	trace	trace
14	$CdCl_2\cdot 2.5H_2O$ (5 equiv.)	reflux, 48 hr	58	trace
15	Zn^{2+}-cyclen(H_2O) (**26a**) (10 equiv.)	reflux, 12 hr	100	trace
16	Cyclen·$ZnCl_2$ (**26b**) (10 equiv.)	reflux, 16 hr	23	trace
17	TFA (60 equiv.), $(n\text{Bu})_4\text{NCl}$ (10 equiv.)	r.t. 20 min	trace	<42[e] (**15a**)
18	TFA (60 equiv.), $ZnCl_2$ (60 equiv.)	r.t. 10 min	trace	trace
19	HCl (4M in 1,4-dioxane) (50 equiv.)	r.t., 1 hr	trace	68 (**15a**)
20	$BF_3\cdot Et_2O$ (5 equiv.), $(n\text{Bu})_4\text{NCl}$ (10 equiv.)	r.t., 6 hr	trace	trace[f]

[a] EtOH was used as the solvent. [b] CCl_4 was used as the solvent. [c] ***fac*-27** was obtained in 9%. [d] See Ref. 37.
[e] A mixture contaning **15a** was obtained. [f] See Ref. 39.

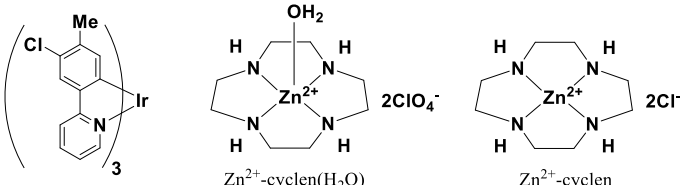

fac-Ir(Cl-tpy)$_3$
***fac*-27**

Zn^{2+}-cyclen(H_2O)
28a
(isolated)

Zn^{2+}-cyclen
28b
(prepared *in situ*)

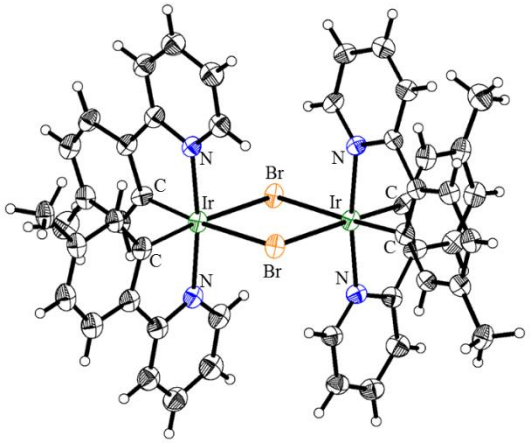

Figure 2-3. ORTEP drawing of single crystal structure of **15b** with 50% probability ellipsoids.

Table 2-3 Selected bond lengths (Å) and selected bond angles (º) of **15b**.

(a)

	Bond Length (Å)
Ir-C (tpy)	2.01, 2.01, 2.02, 2.02
Ir-N (tpy)	2.04, 2.04, 2.05, 2.06
Ir-Br	2.62, 2.62, 2.65, 2.65

(b)

	Bond Angles (º)
N (tpy)-Ir-Br	91.2, 91.3, 93.4, 93.7
Br-Ir-Br	84.1, 84.3
Ir-Br-Ir	95.7, 95.8

Baranoff and co-workers reported that HCl (2M in Et_2O) and $BF_3{\cdot}Et_2O$ promote the degradation of heteroleptic Ir complexes that contain an ancillary ligand, such as $Ir(F_2ppy)_2(pic)$ (pic: picolinate) **29a** or $Ir(F_2ppy)_2(acac)$ **29b** to give the corresponding Ir dimer $[Ir(F_2ppy)_2(\mu\text{-}Cl)]_2$ **30a** (Chart 2-8).[29c] For comparison, the degradation of ***fac*-2** by hydrochloric acid (4M HCl in 1,4-dioxane) gave **15a** in 68% yield (Entry 19 of Table 2-2), while the treatment of ***fac*-2** with *2M HCl aq. in THF/H_2O (2/1)* was negligible, suggesting that H_3O^+ (pK_a = -1.74) generated by levelling effect is not a sufficiently strong acid to decompose ***fac*-2**. Only trace amount of **15a** was obtained in the case of $BF_3{\cdot}Et_2O$ and $(n\text{Bu})_4NCl$ (added as a Cl^- source)

(Entry 20).[42] In this work, it was found that **29b** undergoes decomposition in the presence of $ZnCl_2$ (60 equiv.) in 1,2-dichroloethane at room temperature to give **30a** in 93% yield (Chart 2-8). These results indicate that $AlCl_3$, $ZnCl_2$, $ZnBr_2$, TMSCl and HCl/1,4-dioxane promote the degradation of ***fac*-2** to give **15a** or **15b** in moderate good yields and that the reactivity of tris-cyclometalated Ir complexes such as ***fac*-2** is different from bis-cyclometalated Ir complexes such as **29**.

Chart 2-8

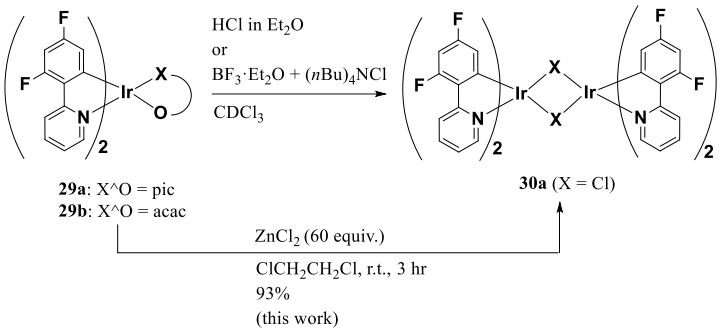

2-2-3 Degradation Reaction of Tris-Cyclometalated Homoleptic Ir Complexes by $ZnBr_2$

The reactivity of other tris-cyclometalated Ir complexes with $ZnBr_2$ or HCl (4M in 1,4-dioxane) was examined and the results are summarized in Tables 2-4 and 2-5. The decomposition of ***fac*-1**, ***mer*-1**, ***fac*-2**, ***mer*-2** and ***fac*-12** by $ZnBr_2$ provided the corresponding bromo-bridged Ir dimers **31b**, **15b** and **32b** as major products (Entries 1-6 in Table 2-4). The μ-complex **33** was obtained from ***fac*-16** and $ZnBr_2$ in 25% yield after 5 h and in 83% yield after 25 h (Entries 7 and 8 in Table 2-4). It was found that ***fac*-3** and ***fac*-18** required longer reaction times than those of ***fac*-1** and ***fac*-2** (Entries 5-8 vs. Entries 1 and 3 in Table 2-4). A comparison of the reactivity between *fac*- and *mer*-forms were inconclusive (Entry 1 vs. Entry 2, Entry 3 vs. Entry 4 in Table 2-4 and Entry 1 vs. Entry 2 in Table 2-5). Interestingly, the degradation of ***fac*-3** and ***fac*-18** containing electron-withdrawing groups (two F and NO_2) on the phenyl rings of the ppy ligands negligibly proceeded (Entries 9 and 12 in Table 2-4), while the *mer*-form of **3** underwent decomposition to give **30b** in 55% (Entry 11). Similarly, ***fac*-19**

having CF_3 groups on the phenyl rings had a lower reactivity than that of ***fac*-17** and ***mer*-17** (Entry 3 vs. Entries 1 and 2 in Table 2-5). As shown in Table 2-2, HCl (4M in 1,4-dioxane) is a stronger promoter of the degradation reaction than $ZnBr_2$, because the reaction of ***fac*-2** in the presence of HCl proceeds at room temperature, while $ZnBr_2$ requires a refluxing temperature (Entry 4 vs. Entry 19 in Table 2-2). It should be noted that ***fac*-3** and ***fac*-18** have a low reactivity in the presence of HCl/1,4-dioxane under refluxing conditions (Entries 10 and 13 in Table 2-4) and ***mer*-3** is more reactive than ***fac*-3** (Entry 11 vs. Entry 9 in Table 2-4).

These results indicate that electron-withdrawing groups on the phenyl ring of cyclometalating ligands stabilize the corresponding Ir complexes. From the results shown in Tables 2-4 and 2-5, the order of susceptibility to degradation for the ligands against $ZnBr_2$ is assumed to be: mpiq, tpy and ppy > mppy > Br-tpy > tfpiq > F_2ppy > NO_2-tpy.

Table 2-4

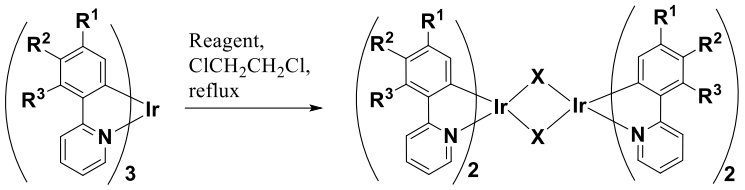

15b: R^1 = Me, R^2 = R^3 = H, X = Br
30b: R^1 = R^3 = F, R^2 = H, X = Br
31b: R^1 = R^2 = R^3 = H, X = Br
32b: R^1 = OMe, R^2 = R^3 = H, X = Br
33b: R^1 = Me, R^2 = Br, R^3 = H, X = Br

Entry	Tris-cyclometalated Ir complex	R^1	R^2	R^3	Reagents	Reaction time	Yield of halogen-bridged Ir dimer (%)	Recovery of S.M. (%)
1	***fac*-1**	H	H	H	$ZnBr_2$ (50 equiv.)	4.5 hr	50 (**31b**)	trace
2	***mer*-1**	H	H	H	$ZnBr_2$ (50 equiv.)	1 hr	47 (**31b**)	trace
3	***fac*-2**	Me	H	H	$ZnBr_2$ (50 equiv.)	3 hr	93 (**15b**)	trace
4	***mer*-2**	Me	H	H	$ZnBr_2$ (50 equiv.)	2 hr	33 (**15b**)	trace
5	***fac*-12**	OMe	H	H	$ZnBr_2$ (50 equiv.)	5 hr	70 (**32b**)	13
6	***fac*-12**	OMe	H	H	$ZnBr_2$ (50 equiv.)	20 hr	80 (**32b**)	trace
7	***fac*-16**	Me	Br	H	$ZnBr_2$ (50 equiv.)	5 hr	25 (**33b**)	60
8	***fac*-16**	Me	Br	H	$ZnBr_2$ (50 equiv.)	25 hr	83 (**33b**)	trace
9	***fac*-3**	F	H	F	$ZnBr_2$ (60 equiv.)	24 hr	trace	74
10	***fac*-3**	F	H	F	HCl (60 equiv.)[a]	19 hr	trace	78
11	***mer*-3**	F	H	F	$ZnBr_2$ (60 equiv.)	25 hr	55 (**30b**)	23
12	***fac*-18**	Me	NO_2	H	$ZnBr_2$ (60 equiv.)	28 hr	trace	100
13	***fac*-18**	Me	NO_2	H	HCl (60 equiv.)[a]	19 hr	trace	95

[a] 4M HCl in 1,4-dioxane was used.

Table 2-5

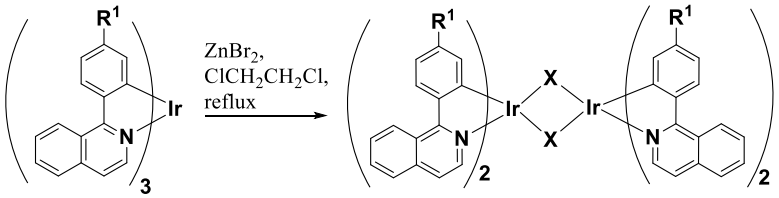

26a: R^1 = Me, X = Cl
26b: R^1 = Me, X = Br
26c: R^1 = CF_3, X = Br

Entry	Tris-cyclometalated Ir complex	R^1	$ZnBr_2$	Reaction time	Yield of halogen-bridged Ir dimer **21** (%)	Recovery of S.M. (%)
1	***fac*-17**	Me	60 equiv.	3 hr	98 (**26b**)	trace
2	***mer*-17**	Me	60 equiv.	1 hr	67 (**26b**)	trace
3	***fac*-19**	CF_3	60 equiv.	24 hr	<49[a] (**26c**)	51

[a] A mixture contaning **26c** was obtained.

2-2-4 Degradation of Tris-Cyclometalated Heteroleptic Ir Complexes in the Presence of Brønsted or Lewis Acids

The aforementioned findings prompted us to examine the ligand-selective degradation of heteroleptic Ir complexes such as *fac*- and *mer*-Ir(tpy)$_2$(F$_2$ppy) (***fac***-**20** and ***mer***-**20**) by $ZnBr_2$, $ZnCl_2$, TMSCl, $AlCl_3$, and HCl/1,4-dioxane) (Chart 2-9 and Table 2-6). Because it was assumed that the degradation of ***fac***-**20** and ***mer***-**20** with $ZnBr_2$ would likely provide a mixture of **15b** and **34b**, the non-selective degradation products were reacted with acacH to convert to **6** (from **15b**) and **25** (from **34b**), respectively, in order to characterize the products more accurately (Chart 2-9). As shown in Entries 1 and 2 of Table 2-6, Ir(tpy)$_2$(acac) **6** and Ir(tpy)(F$_2$ppy)(acac) **25** were obtained in 20% and 40% yields, respectively, from ***fac***-**20**, and the chemical yields of **6** and **25** from ***mer***-**20** were 13% and 63%, respectively. ^{1}H NMR spectra in Figures 2-4a and 2-4b support the conclusion that the main products of the reaction of ***mer***-**20** with $ZnCl_2$ or $ZnBr_2$ are the corresponding heteroleptic μ-complexes [{Ir(tpy)(F$_2$ppy)(μ-X)}$_2$] **34a** (X = Cl) or **34b** (X = Br), respectively.[43] In Entry 3 of Table 2-6, the crude products containing **15a** and **34a** were reacted with acacH to afford **6** in 6% and **25** in 63% yields. Importantly, **6**, but not **25**, was obtained as a major product of the degradation of ***mer***-**20** with TMSCl, $AlCl_3$, or HCl (4M in 1,4-dioxane) (Entries 4-6 in Table 2-6). These results indicate that only ZnX_2 (X = Cl or Br) promotes the selective elimination of a tpy ligand on ***mer***-**20**, while TMSCl, $AlCl_3$, and HCl selectively remove the F$_2$ppy ligand from the same complex.[44]

Chart 2-9

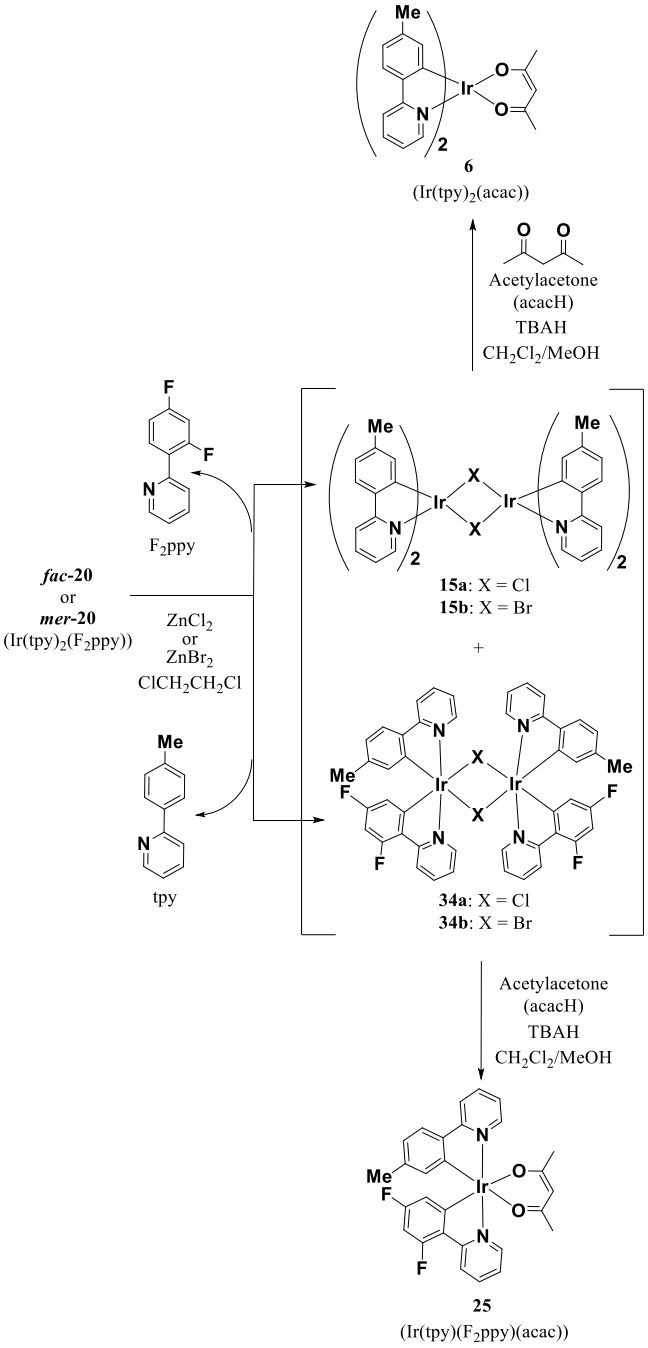
Me
Ir
O
O
N
2
6
(Ir(tpy)2(acac))
Acetylacetone
(acacH)
TBAH
CH2Cl2/MeOH
F
F
N
F2ppy
fac-20
or
mer-20
(Ir(tpy)2(F2ppy))
ZnCl2
or
ZnBr2
ClCH2CH2Cl
Me
N
tpy
X
Ir
15a: X = Cl
15b: X = Br
+
Me
F
34a: X = Cl
34b: X = Br
Acetylacetone
(acacH)
TBAH
CH2Cl2/MeOH
25
(Ir(tpy)(F2ppy)(acac))

Table 2-6

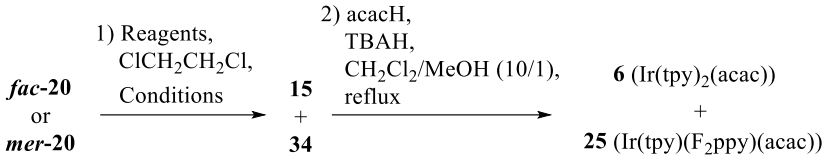

Entry	substrates	1) Reagents	1) Conditions	Yield of **6** (%)	Yield of **25** (%)	Recovery of **20** (%)
1	***fac*-20**	$ZnBr_2$ (50 equiv.)	reflux, 20 hr	20	40	trace
2	***mer*-20**	$ZnBr_2$ (50 equiv.)	reflux, 3 hr	13	63	trace
3	***mer*-20**	$ZnCl_2$ (50 equiv.)	reflux, 3 hr	6	63	trace
4	***mer*-20**	TMSCl (50 equiv.)	r.t., 10 min	49	trace	21
5	***mer*-20**	$AlCl_3$ (5.0 equiv.)	r.t., 30 min	44	6	29
6	***mer*-20**	HCl (3.0 equiv.)[a]	r.t., 1 hr	66	trace	15

[a] 4M HCl in 1,4-dioxane was used.

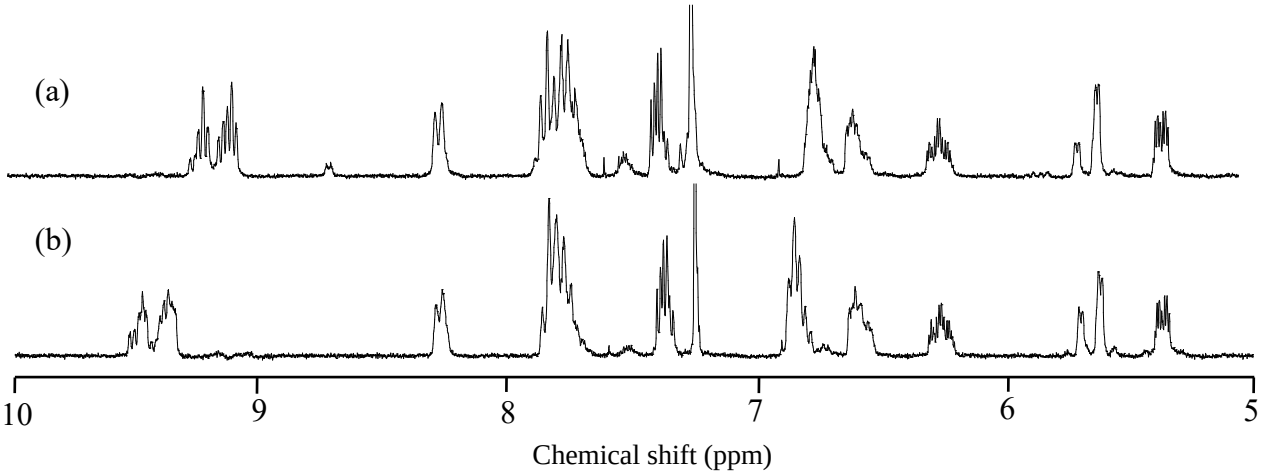

Figure 2-4. Aromatic regions of the ^1H NMR spectra (300 MHz, $CDCl_3$) of μ-complexes obtained by the reaction of ***mer*-20** with $ZnCl_2$ and $ZnBr_2$ (a) **34a** (X = Cl) and (b) **34b** (X = Br).

Table 2-7. Orbital and total energies for *fac*/*mer*-Ir(C^N)$_3$ using Density Functional Theory (DFT)

Complex	HOMO (eV) [a]	HOMO (eV) [b]	LUMO (eV) [a]	LUMO (eV) [b]	Total Energies (a.u.) [a,c]	Total Energies (a.u.) [b,c]
Ir(ppy)$_3$ (**1**)						
***fac*-1**	-4.80	-4.85	-1.22	-1.22	-1540.62282	-1541.04708
***mer*-1**	-4.67	-4.73	-1.28	-1.26	-1540.68201	-1541.03600
Ir(tpy)$_3$ (**2**)						
***fac*-2**	-4.71	-4.77	-1.13	-1.12	-1658.61848	-1569.00703
***mer*-2**	-4.60	-4.66	-1.19	-1.18	-1658.60796	-1568.99514
Ir(F$_2$ppy)$_3$ (**3**)						
***fac*-3**	-5.60	-5.42	-1.75	-1.51	-2135.98582	-2136.44555
***mer*-3**	-5.52	-5.32	-1.80	-1.56	-2135.97666	-2136.43469
Ir(mpiq)$_3$ (**17**)						
***fac*-17**	-		-		-2119.41655	
***mer*-17**	-4.60		-1.69		-2119.40682	
Ir(tpy)$_2$(F$_2$ppy) (**20**)						
***fac*-20**	-4.98		-1.36		-1817.74168 ←	0.01 a.u. ≅ 26 kJ/mol
***mer*-20**	-4.84		-1.42		-1817.73163 ←	

[a] Calculated in this work. [b] Values were reported by Thompson and co-workers (Ref. 8). [c] 1 a.u. = 627.5 kcal/mol

The ligand-selective degradation reactions by $ZnBr_2$ were further examined using various *mer*-tris-cyclometalated heteroleptic Ir complexes, *mer*-Ir(F$_2$ppy)$_2$(tpy) (***mer*-21**), *mer*-Ir(mppy)$_2$(F$_2$ppy) (***mer*-22**), *mer*-Ir(mpiq)$_2$(F$_2$ppy) (***mer*-23**), and *mer*-Ir(F$_2$ppy)$_2$(mpiq) (***mer*-24**) (Chart 2-10). The reaction of ***mer*-21**, which is composed of two F$_2$ppy ligands and one tpy ligand, with $ZnBr_2$ afforded Ir(F$_2$ppy)$_2$(acac) **29b** in 43% yield and a trace amount of **25**, implying that the tpy ligand is selectively released from ***mer*-21** under these reaction conditions. The reaction of ***mer*-22** consisting of two mppy and one F$_2$ppy ligands provided Ir(mppy)(F$_2$ppy)(acac) **35** in 54% yield and Ir(mppy)$_2$(acac) **36** in 13% yield, as predicted by the higher reactivity of tpy and mppy compared to that of F$_2$ppy. Similar results were obtained for the reactions of ***mer*-23** and ***mer*-24** with $ZnBr_2$. Namely, Ir(mpiq)(F$_2$ppy)(acac) **37** and Ir(mpiq)$_2$(acac) **38** were obtained in 67% yield and trace amounts from ***mer*-23**, due to the elimination of the mpiq ligand and **30b** was the major product produced from ***mer*-24**. Aromatic

regions of the ^{1}H NMR spectra of **35** and **37** (obtained from ***mer*-22** and ***mer*-23** as a mixture of enantiomers (Δ and Λ forms)) are shown in Figures 2-5b and 2-5c in comparison with that of **25** (Figure 2-5a).

Chart 2-10

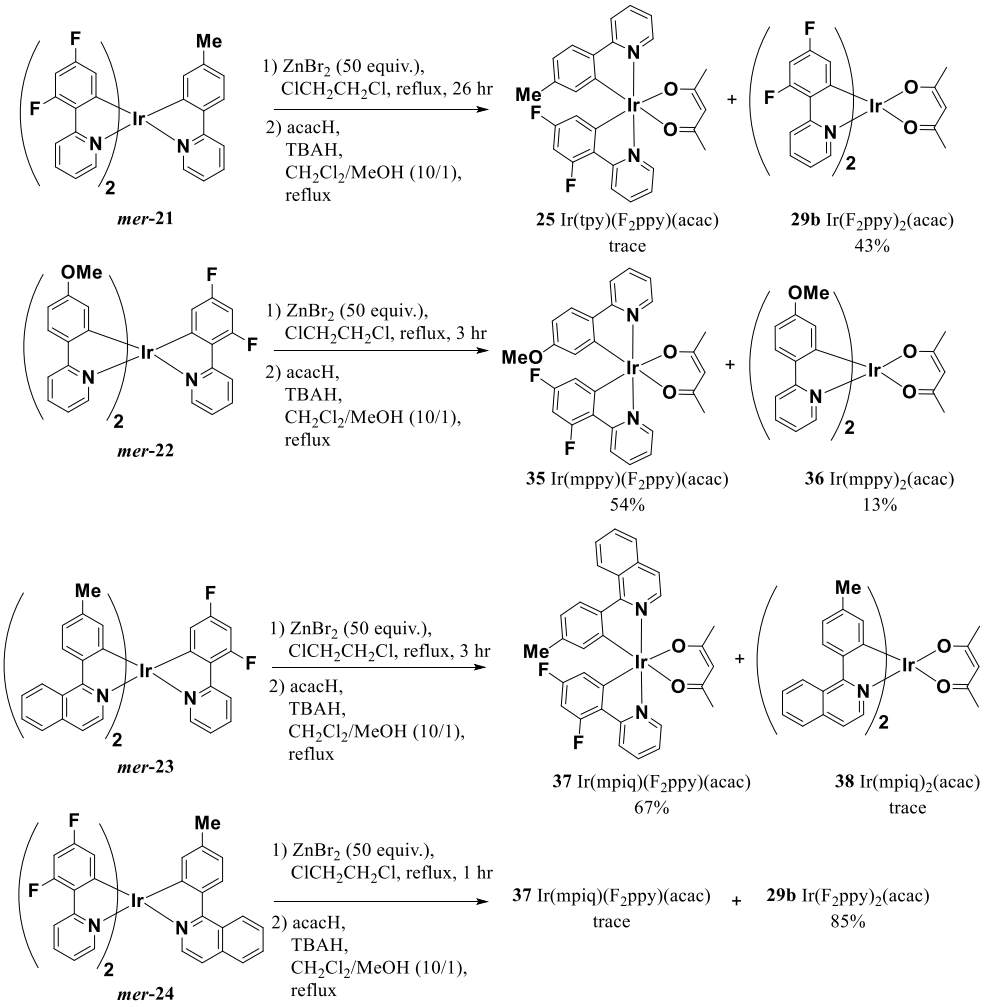

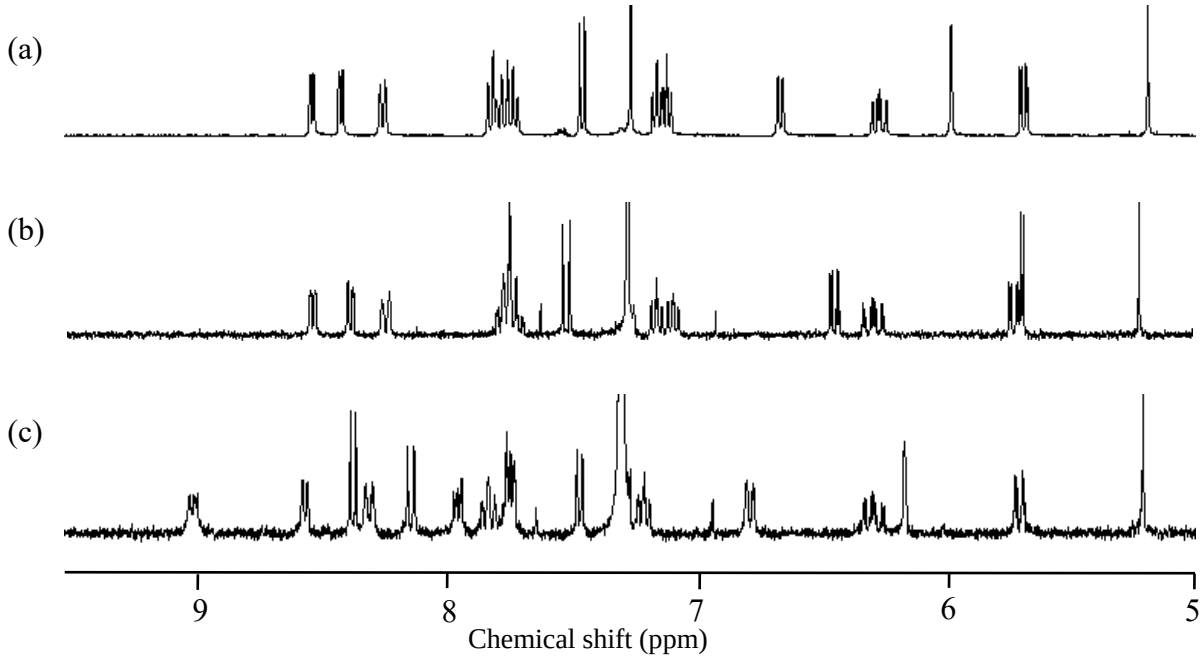

Figure 2-5. Aromatic regions of the ^{1}H NMR spectra (300 MHz, $CDCl_3$) of (a) **25**, (b) **35**, and (c) **37**.

We recently reported on the preparation of dual-emissive cyclometalated Ir complexes such as **39** and **40** containing 8BSQ ligand **41** as an ancillary ligand (Chart 2-11).[13,45] These Ir complexes exhibit two different emission peaks (dual emission) at *ca.* 475-500 nm (blue to green-color emission) and *ca*. 600 nm (red-color emission). It was concluded that the F_2ppy unit and the deprotonated 8BSQ group in **39** and **40** contribute to the blue-color emission and red-color emission, respectively, to produce a near-to-white emission.

Chart 2-11

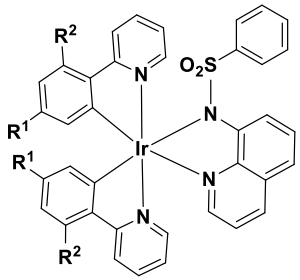

39: $R^1 = R^2 = H$
40: $R^1 = R^2 = F$

With the aforementioned method in hand, we synthesized the tris-heteroleptic Ir complexes **42a** and **42b** containing F_2ppy as a blue emitting ligand, tpy as a green emitting ligand, and a 8BSQ ligand **41** as a red-emitting ligand. After reacting ***mer*-20** with $ZnBr_2$ or $ZnCl_2$, the resulting μ-complexes were treated with **41** to afford **42** (a mixture of diastereomers **42a** and **42b**) in 36% or 24% yields, respectively, as summarized in Table 2-8, with a trace amount of **43**. In contrast, **43** was obtained as the major product when TMSCl, $AlCl_3$, $FeCl_3$, or HCl was used (Entries 3-6). In Entry 5, treatment with $FeCl_3$ afforded trace amounts of **42** or **43**.

As shown in Figure 2-6a, the ^{1}H NMR spectrum of **42** shows two sets of signals, indicating that it is composed of a mixture of two diastereomers (**42a** and **42b**) in a 1:0.4 ratio, among 8 possible diastereomers (the enantiomers of all the diastereomers are not considered). Careful separation of these diastereomers by silica gel column chromatography (hexanes/$CHCl_3$/THF) afforded **42a** as the major product (Figure 2-6b). Its structure was determined by X-ray single crystal analysis, as shown in Figure 2-7 and Table 2-9, in which two N atoms in tpy and F_2ppy units connected to Ir atom exhibit *trans* configuration, N(1) of quinolone (N(3) in Figure 2-7) and C(2) of tpy (C(1) in Figure 2-7) are *trans*, and NSO_2Ph (N(4) in Figure 2-3) and C(2) of F_2ppy are also *trans*.[46] To the best of our knowledge, **42a** is the first example of tris-heteroleptic Ir complexes containing a non-symmetric ancillary ligand isolated as a single stereoisomer (a mixture of Δ and Λ enantiomers).[14]

Table 2-8

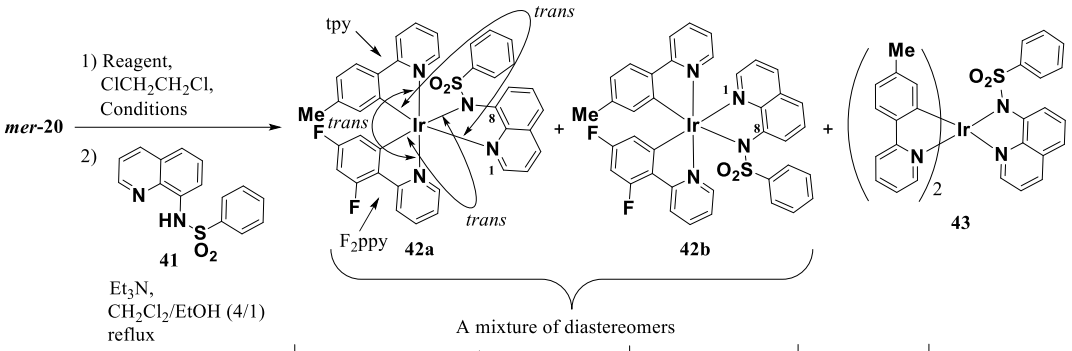

Entry	Reagents	Conditions	Yield of **42** (%) (**42a**:**42b**)[a]	Yield of **43** (%)
1	$ZnBr_2$ (50 equiv.)	reflux, 4 hr	36 (1:0.4)	<5
2	$ZnCl_2$ (60 equiv.)	reflux, 22 hr	24 (1:0.4)	<5
3	TMSCl (60 equiv.)	r.t., 10 min	trace	61[c]
4	$AlCl_3$ (5 equiv.)	r.t., 10 min	trace	71[c]
5	$FeCl_3$ (5 equiv.)	r.t., 10 min	trace	trace
6	HCl (3 equiv.)[b]	r.t., 10 min	trace	35[c]

[a] Ratios were determined by ^{1}H NMR. [b] 4M HCl in1,4-dioxane was used. [c] The products were identical to **43** that was prepared according to Ref. 13.

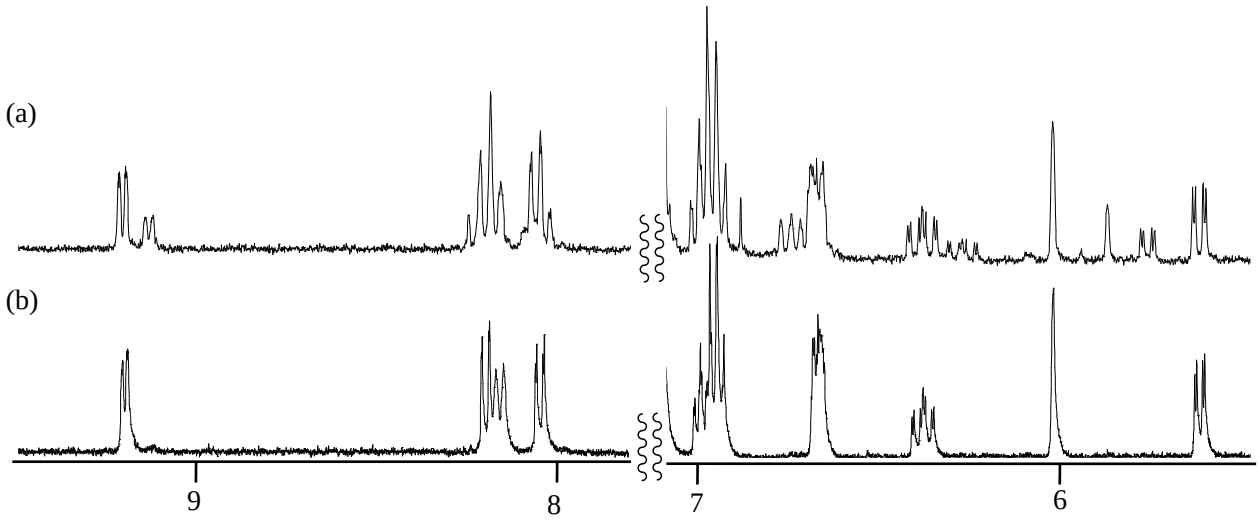

Figure 2-6. Aromatic regions of ^{1}H NMR spectra (300 MHz in $CDCl_3$) of (a) a mixture of **42a** and **42b** (b) **42a** alone after purification.

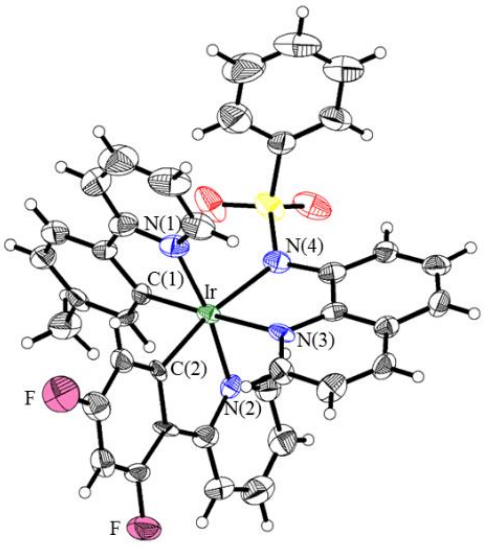

Figure 2-7. ORTEP drawing of single crystal structure of **42a** with 50% probability ellipsoids.

Table 2-9. Selected bond lengths (Å) of **42a**.

	Bond lengths (Å)
Ir-C(1)	1.99
Ir-C(2)	1.99
Ir-N(1)	2.05
Ir-N(2)	2.04
Ir-N(3)	2.13
Ir-N(4)	2.16

2-2-5 Mechanistic Study of the Degradation of Ir Complexes Promoted by Brønsted and Lewis Acids

As described above, Baranoff and co-workers reported on the degradation of heteroleptic Ir complexes containing ancillary ligands such as $Ir(F_2ppy)_2(pic)$ **29a** and $Ir(F_2ppy)_2(acac)$ **20b** with HCl (2M in Et_2O) and $BF_3 \cdot Et_2O$ to give the corresponding Ir dimer $[Ir(F_2ppy)_2(\mu\text{-}Cl)]_2$ **30a** (Chart 2-8).[29c]

In contrast, our findings reported herein are that: 1) $AlCl_3$, $ZnCl_2$, $ZnBr_2$, TMSCl and HCl/1,4-dioxane promote the degradation of *tris-cyclometalated Ir complexes* such as ***fac*-2** to afford the corresponding halogen-bridged Ir dimers (Table 2-2), 2) ***fac*-3**, ***fac*-18** and ***fac*-19** having electron-withdrawing groups confer a lower reactivity than that of ***fac*-1** and ***fac*-2** (Tables 2-4 and 2-5), 3) ZnX_2 (X = Cl or Br) promotes the selective elimination of tpy, mppy or mpiq ligands from ***fac*-** or ***mer*-20**, ***mer*-22**, and ***mer*-23**, respectively, and the successive reaction with acacH affords heteroleptic Ir complexes that contain three different ligands, such as **25** (Chart 2-9), **35**, and **37** (Chart 2-10), while $AlCl_3$, TMSCl and HCl/1,4-dioxane cause the F_2ppy ligand to be removed from ***mer*-20** (Table 2-6), 4) the order of reactivity of the *fac*- and *mer*-forms is not conclusive, 5) the order of reactivity of acid promoters is assumed to be: HCl/1,4-dioxane, TMSCl, $AlCl_3 >> ZnX_2$ (Tables 2-2 and 2-4), and 6) the optimized structures of ***mer*-21** ***mer*-22**, and ***mer*-24** were obtained by DFT calculations (Figure 2-8), because sufficient crystals of these Ir complexes were not obtained for X-ray crystal structure analysis. The Ir-C and Ir-N bond lengths of ***fac*-20**, ***mer*-20**, and ***mer*-23** observed by these crystal structures and those obtained by DFT calculation are nearly identical (Table 2-1), suggesting that the calculated structures of ***mer*-21**, ***mer*-22**, and ***mer*-24** in Figure 2-8 are sufficiently close to those for the intristic structures (crystal structures, if obtained).

(a)

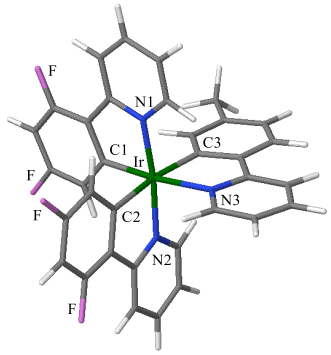

Bond type	Bond distance (Å)
Ir-C1 (F_2ppy)	2.02
Ir-C2 (F_2ppy)	2.09
Ir-C3 (tpy)	2.11
Ir-N1 (F_2ppy)	2.06
Ir-N2 (F_2ppy)	2.08
Ir-N3 (tpy)	2.19

(b)

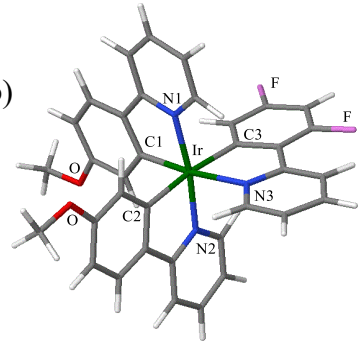

Bond type	Bond distance (Å)
Ir-N1 (mppy)	2.02
Ir-N2 (mppy)	2.09
Ir-N3 (F_2ppy)	2.11
Ir-C1 (mppy)	2.07
Ir-C2 (mppy)	2.08
Ir-C3 (F_2ppy)	2.18

(c)

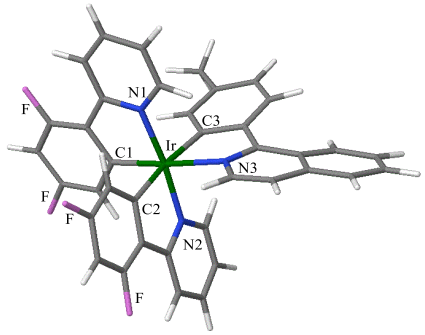

Bond type	Bond distance (Å)
Ir-C1 (F_2ppy)	2.02
Ir-C2 (F_2ppy)	2.09
Ir-C3 (mpiq)	2.10
Ir-N1 (F_2ppy)	2.06
Ir-N2 (F_2ppy)	2.08
Ir-N3 (mpiq)	2.20

Figure 2-8. Optimized structures of (a) *mer*-Ir(F_2ppy)$_2$(tpy) (***mer*-21**), (b) *mer*-Ir(mppy)$_2$(F_2ppy) (***mer*-22**), and (c) *mer*-Ir(F_2ppy)$_2$ (F_2ppy) (***mer*-24**) obtained by DFT calculation (B3LYP/LanL2DZ for Ir atom and 6-31G for H, C, N, O, and F atoms).

Based on the aforementioned data, we assume two mechanisms for the degradation of tris-cyclometalated Ir complexes (typically, ***mer*-20**) according to the used acids, as shown in Chart 2-12. In hard and soft acids and bases (HSAB) theory, H^+, Al^{3+}, and Si^{4+} are categorized as hard Lewis acids and Zn^{2+} is categorized as borderline acids.[47] When H^+, $AlCl_3$ or TMSCl are used for the degradation, the nitrogen atom on the F_2ppy ligand in the ***mer*-20** reacts with H^+,

Al^{3+} (of $AlCl_3$), or Si^{4+} (of TMSCl), which are hard acids (**44**), resulting in the formation of the intermediate **46** via **45** (Chart 2-12a). This can be attributed to the fact that the Ir-N bond of F_2ppy is longer (namely weaker) than the other Ir-N bonds between Ir and the tpy ligand (Table 2-1b). Cleavage of the Ir-C bond of **45** affords **46**, which may easily dimerize to give **15a**.

Chart 2-12

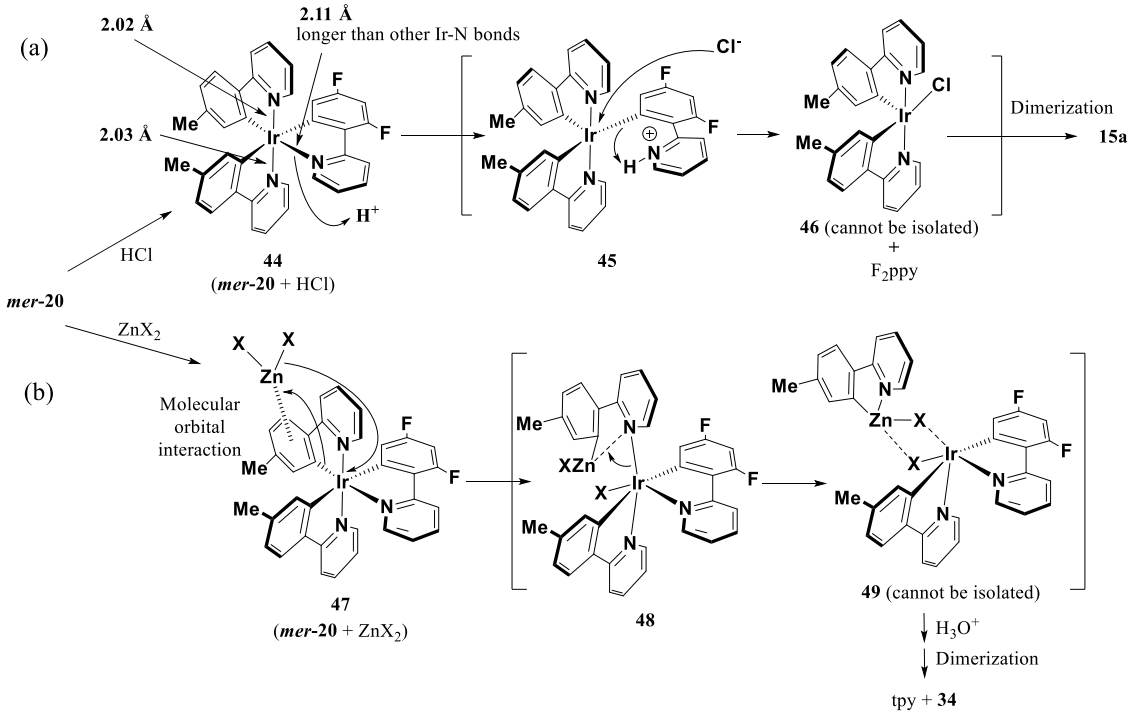

In the case of Zn^{2+}-promoted degradation reactions, on the other hand, we hypothesize an interaction between the molecular orbital of the phenyl ring of ***mer*-20** and that of Zn^{2+} (**47** in Chart 2-12b), because Zn^{2+} is one of the borderline acids. This reaction is considered to initiate the metal exchange reaction from Ir-C to Zn-C to give the intermediate **49** via **48**, resulting in the production of **34** and tpy (30-70%) (Entries 3 and 4 in Table 2-2 and Entries 2 and 3 in Table 2-6).

The decomposition reaction of ***fac*-2** with ZnX_2 (X = Cl or Br) was carried out in the presence of aldehyde to trap the Zn^{2+}-coordinated species such as **49**. It was hypothesized that

Reformatsky reagent-like species in **49** (Chart 2-12) may undergo C-C bond formation reaction with benzaldehyde, considering an analogy to the nucleophilic C(sp^2)-H addition of manganase reagents to aldehyde, as reported by Wang and co-workers.[48] In a typical experiment, a solution of benzaldehyde in THF was added to a degradation reaction mixture of ***fac*-2** and $ZnBr_2$ after cooling to room temperature. It should be noted that THF was used as a co-solvent to dissociate **49** and activate organozinc species in it. In this reaction, however, **15b** was obtained in 53% and benzaldehyde was recovered in 73%.

Next, we carried out the quenching experiments of the Zn^{2+}-promoted degradation reaction with D_2O/DCl or MeOD to check the formation of the deuterated tpy ligand. The reaction mixture of ***fac*-2** and $ZnCl_2$ was refluxed for 2 hours, to which D_2O/DCl was added at room temperature for 30 min. However, **15a** and not deuterated tpy were obtained in 82% yield and 13% yield. After the decomposition of ***fac*-2** and $ZnCl_2$, D_2O/DCl or MeOD was added and refluxed again for 30 min. In these experiments, tpy was recovered in 30-70% without substitution with deuterium (D), though deuterated **15a** (*d_{12}*-**15a**) was obtained only quenched by D_2O/DCl. The quenching of MeOD gave **15a** and tpy in 77% and 43% yield. It should be noted that a mixture of **15a** and D_2O/DCl was refluxed in 1,2-dichloroethane for 16 hours to afford *d_{12}*-**15a**. Subsequently, *d_{12}*-**15a** was reacted with acac or ppy to obtain the corresponding deuterated **6** (*d_6*-**6**) or *mer*-Ir(*d_3*-tpy)$_2$(ppy). For a comparison, the ^{1}H NMR spectra of **15a** and *d_{12}*-**15a** are given in Figure 2-9. The treatment of **31a** and **32a** with D_2O/DCl in 1,2-dichloroethane at reflux for *ca*. 2-6 hours also gave the corresponding deuterated **30a** and **31a** (*d_4*-**31a** and *d_{12}*-**32a**) in good yields, respectively. This deuteration mechanism is now in progress. Futhermore, the degradation of ***fac*-2** with $ZnCl_2$ in 1,2-dichloroethane-*d_4* ($ClCD_2CD_2Cl$) gave tpy in 28% without deuteriumation, denying that 1,2-dichloroethane functions as a proton donor to **49**. These experimental results suggest that a very small amount

of H_2O contained in ZnX_2 may function as a proton donor to the organozinc species in **49**. Further study is now in progress.

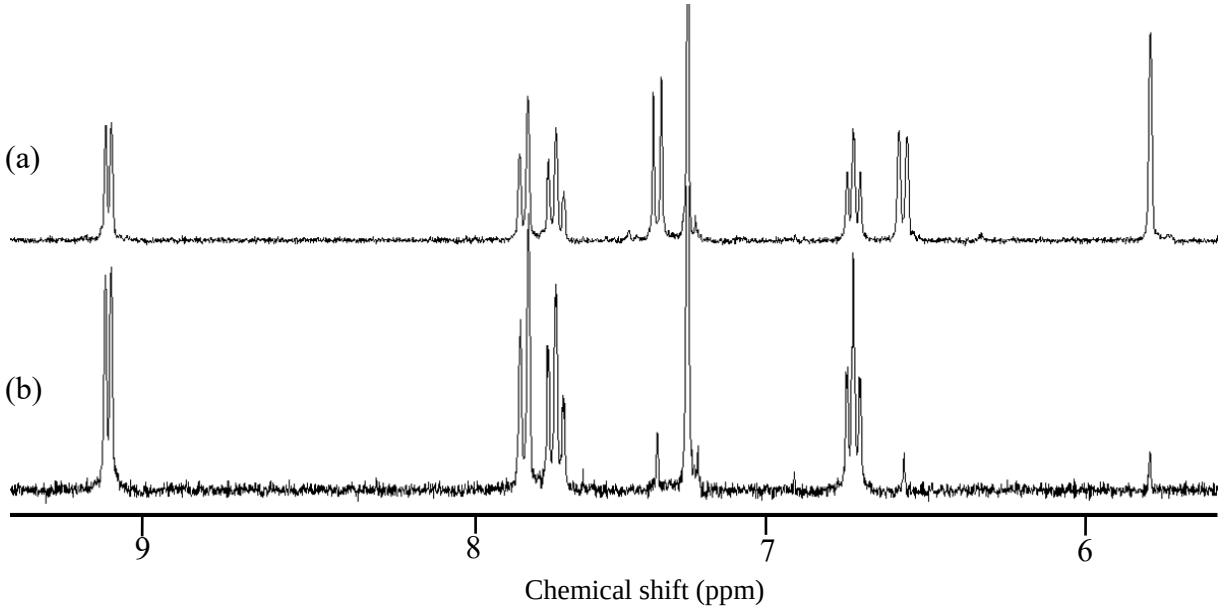

Figure 2-9. Aromatic regions of ^{1}H NMR spectra (300 MHz in $CDCl_3$) of (a) **15a** and (b) *d_{12}*-**15a**.

The energy levels and shapes of HOMO of ***fac*-20**, ***mer*-20**, and ***mer*-21** are presented in Figure 2-10. The same parameters of ***mer*-22**, and ***mer*-23**, and ***mer*-24** are shown in Figure 2-11. The successive cleavage of Ir-N may afford **49**, which could exist as a hetero μ-complex between them (**48**) and are then decomposed to tpy and **34b** after quenching.

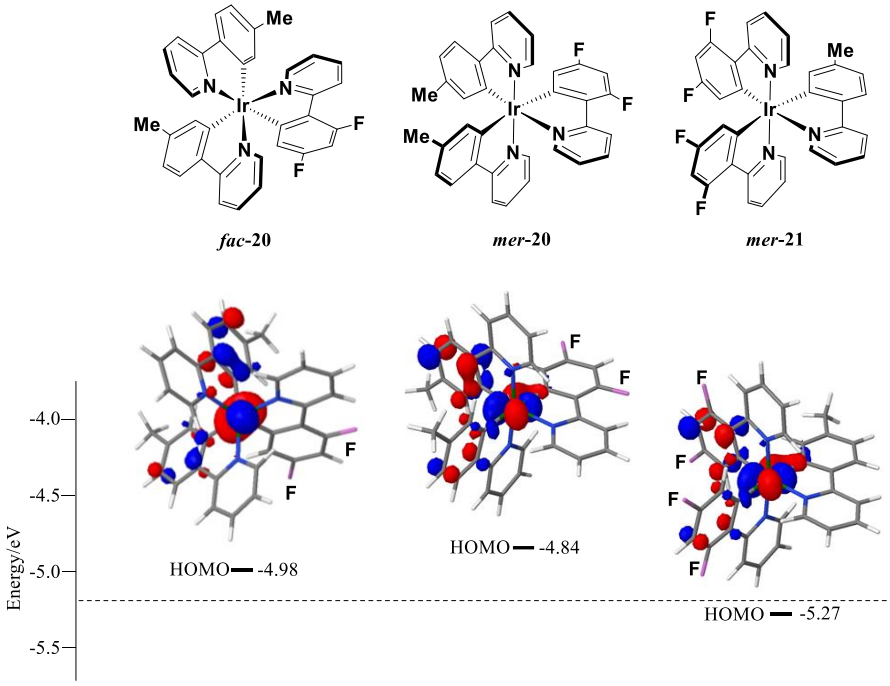

Figure 2-10. HOMOs of tris-cyclometalated Ir complexes ***fac*-20**, ***mer*-20**, and ***mer*-21** calculated by the Gaussian09 program using the B3LYP hybrid functional together with the LanL2DZ basis for the Ir atom and the 6-31G basis sets for the H, C, N, and F atoms.

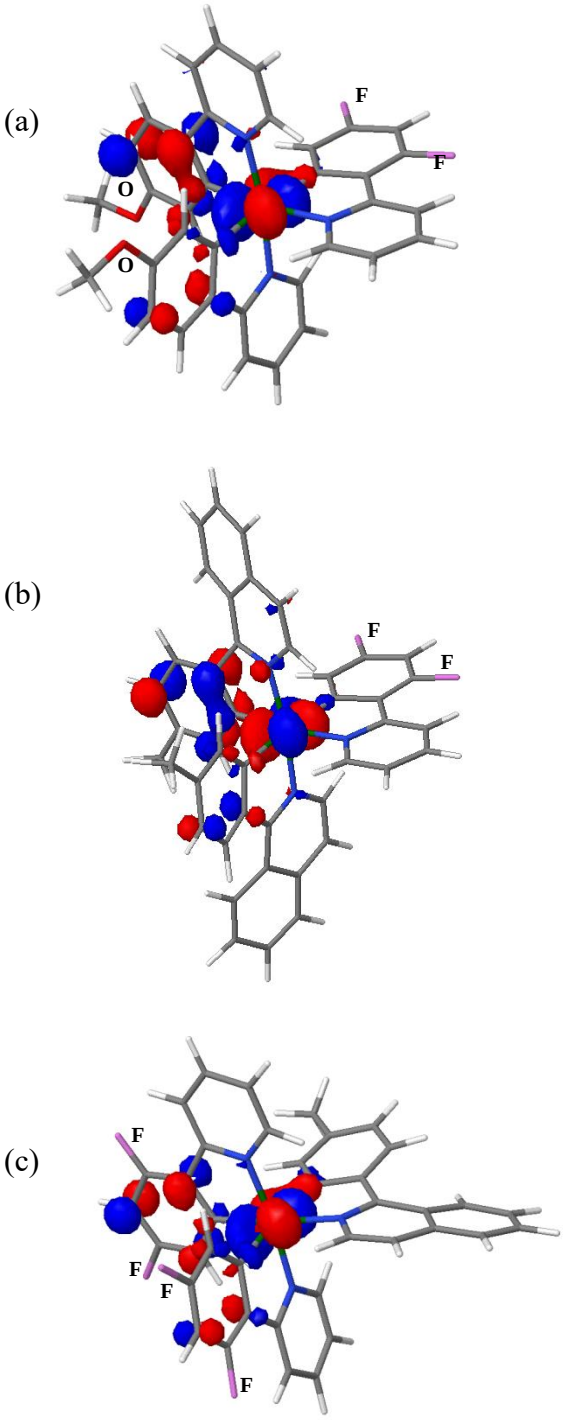

Figure 2-11. HOMO of (a) ***mer*-22**, (b) ***mer*-23**, and (c) ***mer*-24** calculated by the Gaussian09 program using the B3LYP hybrid functional together with the LanL2DZ basis for the Ir atom and the 6-31G basis sets for the H, C, N, O, and F atoms.

In support of the reactivity of their phenyl groups, the treatment of ***mer*-20** with NBS afforded ***mer*-50**, whose 5'-position is brominated (Chart 2-13),[30,31] as confirmed by X-ray structure (Figure 2-12). Note that ***mer*-50** is, to the best of our knowledge, the first example of tris-heteroleptic tris-cyclometalated Ir complex that is synthesized without the formation of other diastereomers. As shown in Figure 2-3, two Ir atoms in **15a** have *N,N-trans* configuration and the same product **15a** is obtained from ***fac*-20** and ***mer*-20**, in which Ir has *N,N-cis* configuration and *N,N-trans* configuration, although this mechanism is yet to be studied.

Chart 2-13

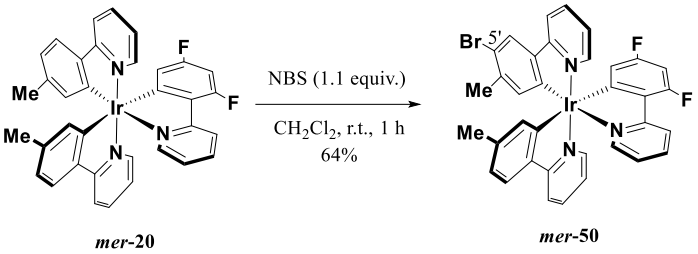

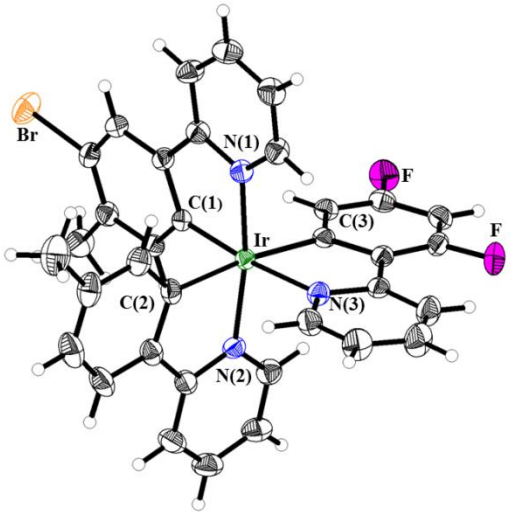

Bond type	Bond distance (Å)
Ir-C1 (Br-tpy)	1.99
Ir-C2 (tpy)	2.07
Ir-C3 (F_2ppy)	2.07
Ir-N1 (Br-tpy)	2.03
Ir-N2 (tpy)	2.05
Ir-N3 (F_2ppy)	2.13

Figure 2-12. ORTEP drawing of single crystal structure of ***mer*-50** with 50% probability ellipsoids. For clarity, the H_2O was omitted. Selected bond lengths (Å) of ***mer*-50** are shown in the right part.

The data in Table 2-4 indicate, that ***fac*-3** and ***fac*-18**, which include the electron-withdrawing groups, have lower reactivity in the presence of ZnX_2 and HCl. For reference, it has been reported that the bonds between M and the oxygen atom of the M(8-hydroxyquinolyl)$_3$ complex (M = Al(III) or In (III)) are stabilized by the introduction of Br and NO_2 groups on the 8-hydroxyquinolyl ligand.[49] We then asked ourselves why Ir complexes having electron-withdrawing groups such as ***fac*-3**, ***fac*-18**, and ***fac*-19** are less reactive than ***fac*-1** and ***fac*-2**.

It is well described that Ir complexes are one of most kinetically inert class of metal complexes[50] and the significant stability of cyclometalated Ir complexes in comparison with organometallic reagents such as organolithium and organomagnesium reagents can be explained by the difference of electronegativity of the carbon (χ_c) and the corresponding metals (χ_{Ir}, χ_{Li}, and χ_{Mg}).[51] The electronegativity values for carbon and iridium are 2.55 (χ_c) and 2.20 (χ_{Ir}), respectively, from which the $\Delta\chi$ value between C and Ir is calculated to be 0.35, as displayed in Figure 2-13. This value is smaller than the corresponding values for reactive organometalic reagents like organolithium, organomagnesium, and organozinc reagents, which explains the higher stability of C-Ir bonds in Ir complexes in comparison with C-Li, C-Mg, and C-Zn bonds. It is possible that electron-withdrawing groups (R in Figure 2-13) on the phenyl rings of ***fac*-3**, ***mer*-3**, ***fac*-18**, and ***fac*-19** (Tables 2-4 and 2-5) would decrease the electronegativity of carbon atoms in Ir-C bonds indicated in Figure 2-13, resulting in a decrease in the $\Delta\chi$ value and the higher stability of these complexes compared to ***fac*-1** and ***fac*-2**.

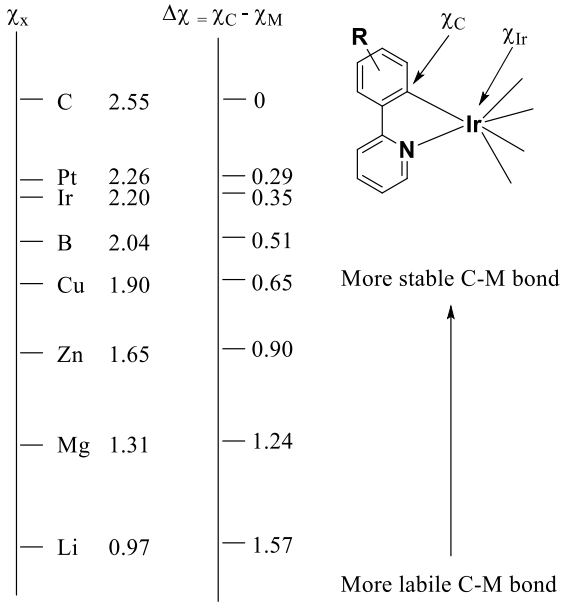

Figure 2-13. Electronegativity values for carbon and several metals.

The HOMO and LUMO energy levels of the Ir complexes were also considered. Figure 2-14 provides information on the HOMO and LUMO levels of the Ir complexes used in the decomposition reaction tested. In the left half of Figure 2-14, the HOMO and LUMO levels of the more reactive Ir complexes are shown and the less reactive complexes are listed in the right half.[52] We next focused on the relationship between HOMO levels of Ir complexes and LUMO levels of $ZnBr_2$. Among the reactive Ir complexes, ***mer*-21** (*mer*-Ir(F_2ppy)$_2$(tpy)) has the most negative HOMO level (-5.27 eV) and the less reactive Ir complexes (*e.g.*; **3** and **18**) possess more negative HOMO levels (< -5.4 eV).

The LUMO level of the optimized structure of $ZnBr_2$ is estimated to be *ca*. -1 eV by DFT calculation (B3LYP/LanL2DZ). Thus, we assume that orbital interactions between the LUMO of $ZnBr_2$ (*ca.* -1 eV) and the HOMOs (more positive than *ca.* -5.2 eV) of the Ir complexes are important for these degradation reactions. LUMO energy level of $ZnBr_2$ (-0.99 eV) is lower than that of $ZnCl_2$ (-0.85 eV) and we assume that this is the reason why higher yield was obtained in the decomposition of ***fac*-2** with $ZnBr_2$ than that with $ZnCl_2$. At the same time, ZnX_2 functions as a halide source to afford μ-complex.

Regarding the mechanism of the selective-degradation reaction of *mer*-tris-cyclometalated heteroleptic Ir complexes such as ***fac*-20**, ***mer*-20**, and ***mer*-21** promoted by $ZnBr_2$ (Charts 2-9 and 2-10), the HOMOs of these complexes are located on the major ligand in each complex (Figure 2-10). Namely, ***mer*-20** and ***fac*-20** contain two tpy and one F_2ppy ligands and its HOMO is located on tpy as well as the Ir metal core. ***Mer*-21** includes two F_2ppy and one tpy groups and its HOMO is located on the F_2ppy unit and the Ir core. Therefore, we assume that the HOMO on tpy ligands in **21** and that on the F_2ppy of **21** interact with the LUMO of $ZnBr_2$, as speculated in **46** of Chart 2-12a, thus initiating the selective decomposition of the corresponding ligand (similarly, the HOMOs of ***mer*-22**, ***mer*-23**, and ***mer*-24** are shown in Figure 2-11, in which similar behavior is observed). It should be noted that ***mer*-21** and ***mer*-24** are exceptions, from which the minor ligand (tpy or mpiq) is ejected faster than the major ligand (F_2ppy).

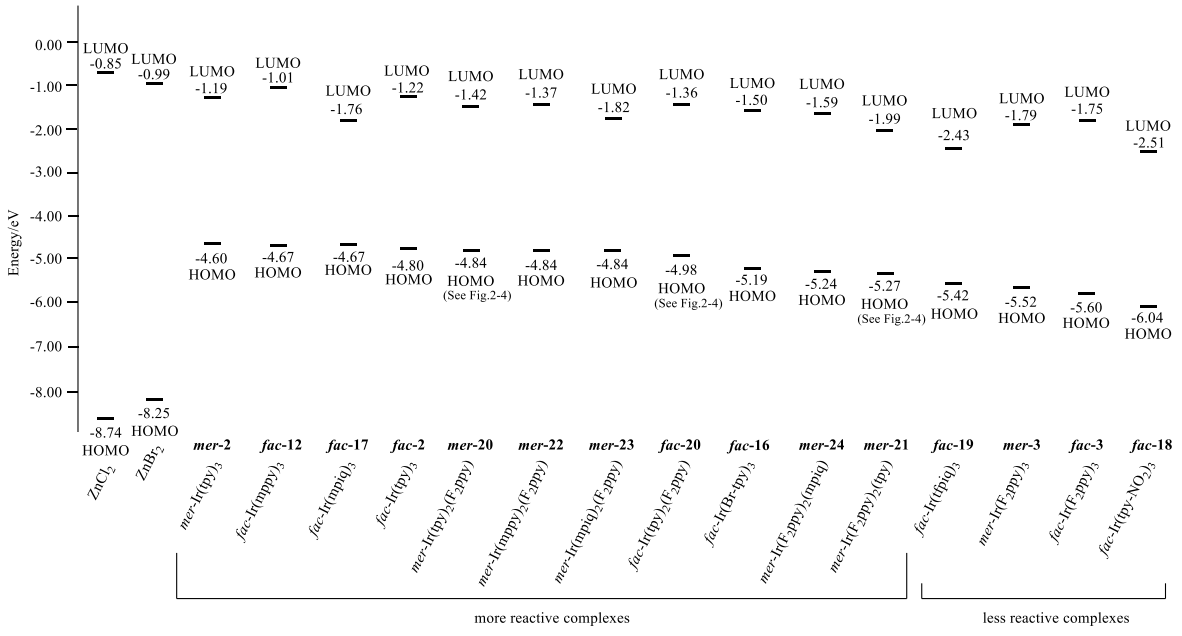

Figure 2-14. Energy diagram for the HOMO and LUMO of tris-cyclomatalated Ir complexes (***fac*-2**, ***mer*-2**, ***fac*-3**, ***mer*-3**, ***fac*-12**, ***fac*-16**, ***fac*-17**, ***fac*-18**, ***fac*-19**, ***fac*-20**, and ***mer*-20-24**) $ZnCl_2$, and, $ZnBr_2$ calculated by the Gaussioan09 program using the B3LYP hybrid functional together with the LanL2DZ basis for the Ir, Zn, Cl, and Br atoms and the 6-31G basis sets for the H, C, N, O, and F atoms.

2-2-6 Photophysical Properties of the Ir Complexes

UV/vis absorption spectra of ***mer*-17**, ***mer*-20-24**, ***fac*-20**, **6**, **25**, **29b**, and **35-38** (10 μM) in DMSO at 298 K are shown in Figure 2-15 and their photochemical properties are summarized in Table 2-10. These complexes exhibit a weak absorption in the region of *ca*. 350-500 nm, which are due to spin-allowed and spin-forbidden metal-ligand change transfer (MLCT) transitions and spin-forbidden π—π* transitions.

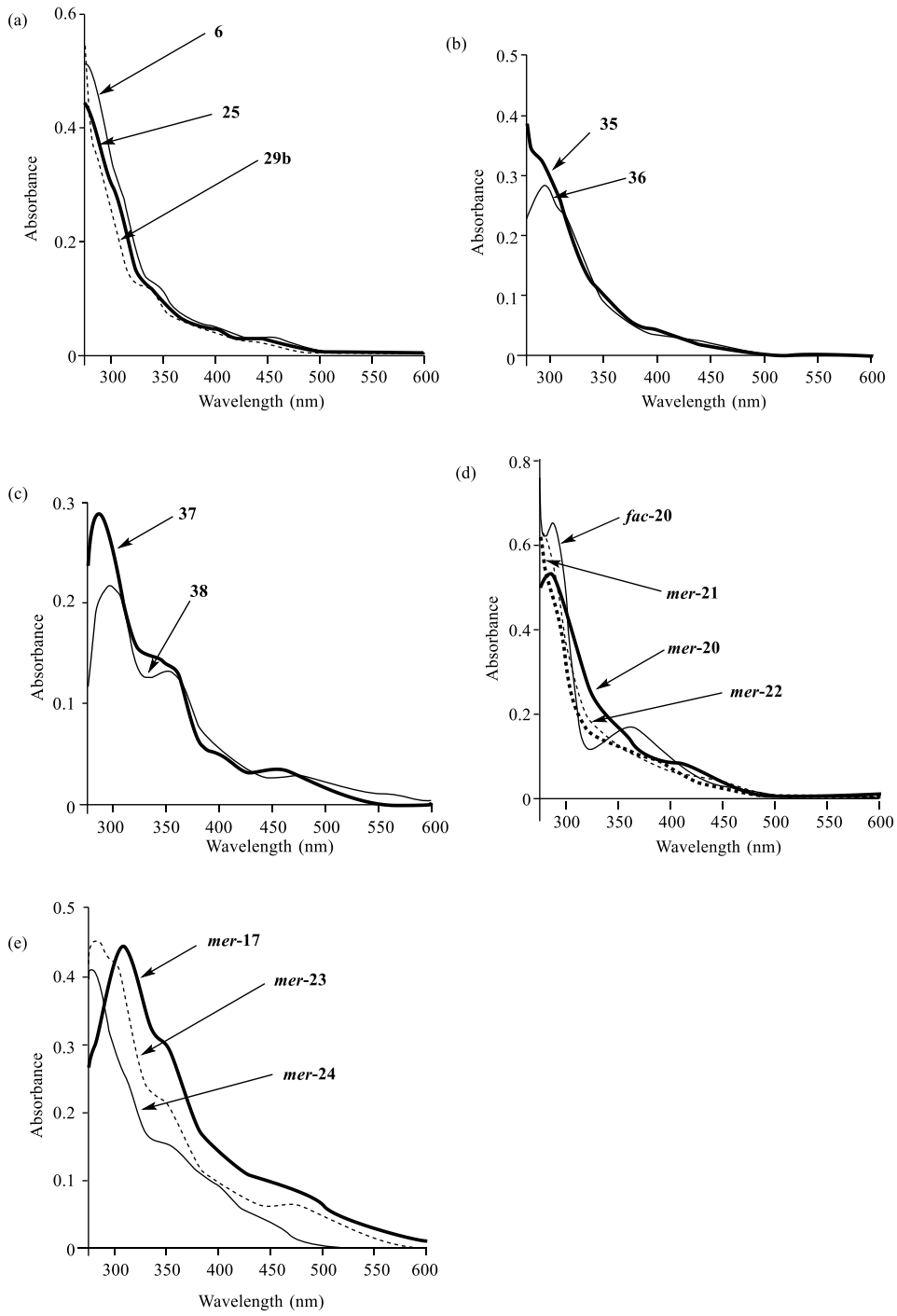

Figure 2-15. UV/vis spectra of Ir complexes in DMSO at 298 K ([Ir complex] = 10 μM). (a) **6** (plain curve), **25** (bold curve), and **29b** (dashed curve). (b) **35** (bold curve) and **36** (plain curve). (c) **37** (bold curve) and **38** (plain curve). (d) ***mer*-20** (bold curve), ***fac*-20** (plain curve), ***mer*-21** (dashed bold curve), and ***mer*-22** (dashed curve). (e) ***mer*-17** (bold curve), ***mer*-23** (dashed curve) and ***mer*-24** (plain curve).

Emission spectra of the substrates of degradation, ***mer*-17**, ***mer*-20-24**, ***fac*-20**, and products obtained in this work, **6**, **25**, **29b**, and **35-38** (10 μM in degassed DMSO), were measured at 298 K (excitation at 366 nm), as shown in Figure 2-16, respectively, and their quantum yields were determined based on the Φ value of quinine sulfate in 0.1 M H_2SO_4 (Φ = 0.55) or *fac*-Ir(mpiq)$_3$ in toluene (Φ = 0.26) used as a standard reference (see Table 2-10).[53] The emission maxima of **6**, **25** and **29b** are 518, 508, and 489 nm, respectively, indicating that the emission maxima of tris-heteroleptic Ir complex **25** are located between those of **6** and **29b**. As expected, it was found that **37** exhibits a dual emission at *ca*. 493 nm and *ca*. 602 nm, respectively, because the F_2ppy and mpiq ligands emit a blue and a red color, respectively. It should be noted that **37** was recrystallized twice in order to minimize contamination by **29b** and **38** and the exactly the same spectra were observed after recrystallization.

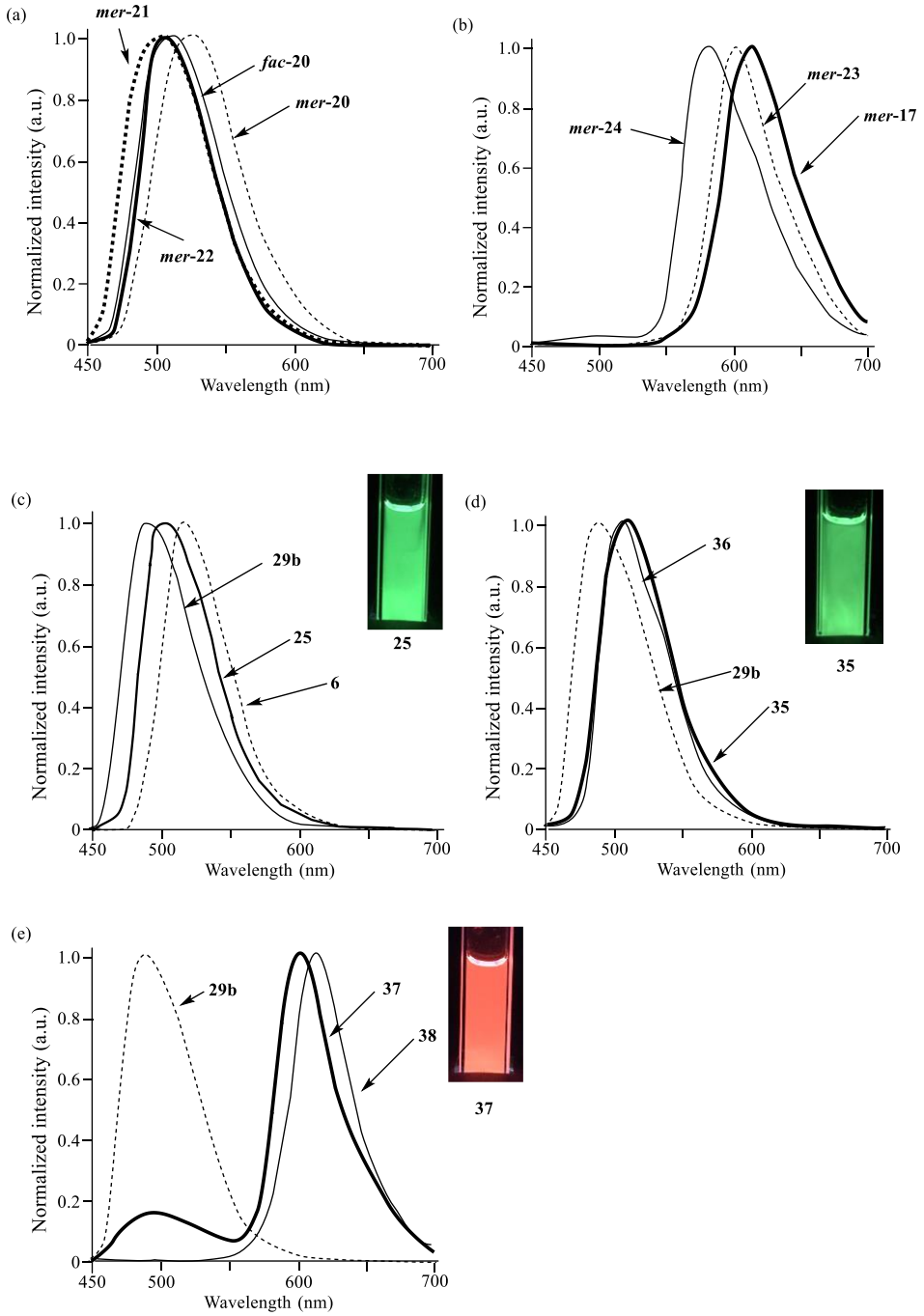

Figure 2-16. Normalized emission spectra of (a) ***fac*-20** (plain curve), ***mer*-20** (dashed curve), ***mer*-21** (dashed bold curve) and ***mer*-22** (bold curve). (b) ***mer*-17** (bold curve), ***mer*-23** (dashed curve) and ***mer*-24** (plain curve). (c) **6** (dashed curve), **25** (bold curve), and **29b** (plain curve) in degassed DMSO at 298 K ([Ir complex] = 10 μM and excitation at 366 nm). Inset: Photograph showing DMSO solution of **25** (10 μM) excited by UV light at 365 nm. (d) **29b** (dashed curve), **35** (bold curve) and **36** (plain curve). Inset: Photograph showing DMSO solution of **35** (10 μM) excited by UV light at 365 nm. (e) **29b** (dashed curve), **37** (bold curve) and **38** (plain curve). Inset: Photograph showing DMSO solution of **37** (10 μM) excited by UV light at 365 nm. in degassed DMSO at 298 K ([Ir complex] = 10 μM and excitation at 366 nm)

Table 2-10. Photophysical properties of ***mer*-17**, ***mer*-20-24**, ***fac*-20**, **6**, **25**, **29b**, and **35-38** in degassed DMSO solutions at 298 K (excitation at 366 nm) ([Ir complex] = 10 μM).

Compounds	λ_{abs} (nm)	λ_{em} (nm)	Quantum yield Φ	Emission liftime τ (μs)
***mer*-17** (*mer*-Ir(mpiq)$_3$)	303, 350, 486	614	2.0 x 10^{-2} [a]	0.17[c]
***fac*-20** (*fac*-Ir(tpy)$_2$(F$_2$ppy))	281, 362	516	0.57[b]	1.9[d]
***mer*-20** (*mer*-Ir(tpy)$_2$(F$_2$ppy))	336,366, 400	528	4.7 x 10^{-2} [b]	0.30[e]
***mer*-21** (*mer*-Ir(F$_2$ppy)$_2$(tpy))	278, 389	504	0.31[b]	1.0[d]
***mer*-22** (*mer*-Ir(mppy)$_2$(F$_2$ppy))	278, 409	512	8.3 x 10^{-2} [b]	0.25[d]
***mer*-23** (*mer*-Ir(mpiq)$_2$(F$_2$ppy))	281, 343, 470	603	0.22[a]	1.1[c]
***mer*-24** (*mer*-Ir(F$_2$ppy)$_2$(mpiq))	272, 354, 395	581	0.31[a]	4.7[f]
6 (Ir(tpy)$_2$(acac))	408, 462	518	0.42[b]	1.4[d]
25 (Ir(tpy)(F$_2$ppy)(acac))	400, 450	508	0.51[b]	1.3[d]
29b (Ir(F$_2$ppy)$_2$(acac))	330, 389, 437	489	0.53[b]	1.0[d]
35 (Ir(mppy)(F$_2$ppy)(acac))	283, 395, 472	507	0.52[b]	1.3[d]
36 (Ir(mppy)$_2$(acac))	286, 401	505	0.46[b]	1.2[d]
37 (Ir(mpiq)(F$_2$ppy)(acac))	280, 340, 455	493, 602	0.38[a]	1.9,[d] 2.0[c]
38 (Ir(mpiq)$_2$(acac))	289, 345, 474	616	0.25[a]	1.3[c]

[a] Quantum yields were determined using *fac*-Ir(mpiq)$_3$ as a standard reference (Φ = 0.26 in toluene). [b] Quantum yields were determined using quinine sulfate as a standard reference (Φ = 0.55 in 0.1 M H_2SO_4 *aq*.). [c] A 590 nm long wave pass filter was used. [d] A 475 nm long wave pass filter was used. [e] A 515 nm long wave pass filter was used. [f] A 550 nm long wave pass filter was used.

The UV/Vis absorption spectra and emission spectra of **40**, **42a**, and **43** (10 μM in degassed DMSO solutions at 298 K) are shown in Figure 2-17 and their photochemical properties are summarized in Table 2-11. These complexes also exhibited a weak absorption in the region of *ca*. 350-530 nm, which are due to spin-allowed and spin-forbidden metal-ligand charge transfer (MLCT) transitions and spin-forbidden π—π* transitions.

Since these Ir complexes contain 8BSQ ligand as an ancillary ligand, they exhibit dual emissions at *ca*. 475-525 nm (HE (high energy) emission band) and *ca*. 610 nm (LE (low energy) emission band) ($\Phi = 2.5 \times 10^{-2}$ for **42a**, 9.8×10^{-2} for **40**, and 1.5×10^{-2} for **43**) (Figure 2-17b and Table 2-11).[13] The maximam of HEB of **42a** was found to be observed between those of **43** and **40**. As shown in the inset of Figure 2-17b, **42a** exhibits a pale-pink emission

color. The CIE of representative Ir complexes synthesized in this work is presented in Figure 2-18.

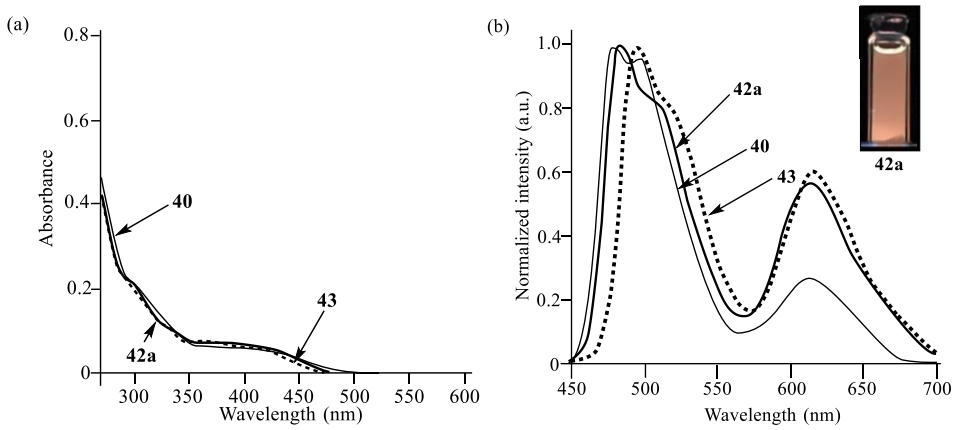

Figure 2-17. (a) UV/vis spectra of Ir complexes **40** (plain curve), **42a** (bold curve), and **43** (dashed bold curve) in DMSO at 298 K. (b) Normalized emission spectra of **40** (plain curve), **42a** (bold curve), **43** (dashed bold curve) in degassed DMSO at 298 K ([Ir complex] = 10 μM and excitation at 366 nm). Inset: Photograph showing DMSO solution of **42a** (10 μM) excited by UV light at 365 nm.

Table 2-11. Photophysical properties of **40**, **42a**, and **43** in degassed DMSO solutions at 298 K (excitation at 366 nm) ([Ir complex] = 10 μM).

Compounds	λ_{abs} (nm)	λ_{em} (nm) HEB[a]	LEB[a]	Quantum yield (Φ)	Emission lifetime τ (μs)
40	331, 366, 417	474, 493	613	9.8×10^{-2}	1.4, 9.3[b]
42a	299, 381, 424	485, 515	613	2.5×10^{-2}	1.9, 13[c]
43	304, 335, 386, 446	497, 525	617	1.5×10^{-2}	1.6, 10[c]

[a] HEB = Higher energy emission band, and LEB = Lower energy emission band.
[b] A 435 nm long wave pass filter was used. [c] A 475 nm long wave pass filter was used.

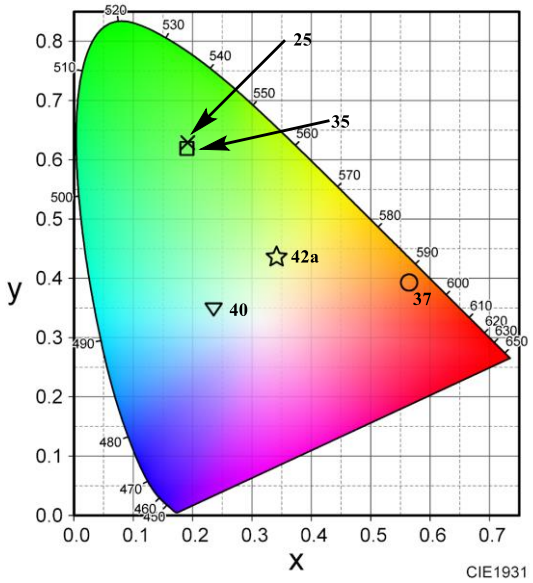

Figure 2-18. Chromaticity diagram showing the xy color coordinates of **25**, **35**, **37**, **40**, and **42a** (CIE 1931). The xy color coordinates of these complexes were calculated from their emission spectra in degassed DMSO.

2-2-7 Mechanistic Studies of Dual Emission of Ir complexes (37 and 42a)

TD-DFT calculations were performed for **37** and **42a** using the Gaussian09 program.[54] For **37**, the calculated triplet energies T_1 and T_3 are close to the experimentally determined values (T_1: 2.06 eV (602 nm) and T_3: 2.52 eV (493 nm) (Table 2-12). The HOMO and HOMO-2 of **37** are mainly localized on the Ir center and mpiq ligands and HOMO-1 is mainly localized on the Ir centers and acac ligands, as shown in Figure 2-19a. The LUMO and LUMO+1 are localized on the mpiq and F_2ppy ligands, respectively. TD-DFT calculations show that $^3ML_{mpiq}CT$ (d(π)(Ir)→π*(mpiq)), $^3L_{mpiq}C$ (π(mpiq)→π*(mpiq)), and $^3L_{acac}L_{mpiq}CT$ transitions (π(acac)→π*(mpiq)) (Table 2-12) are included in the lowest-energy triplet excited state T_1. The third lowest-energy state T_3 of **37** is identical to its experimentally determined HEB, indicating that T_3 is a mixture of $^3ML_{F2ppy}CT$ (d(π)(Ir)→π*(F_2ppy)), $^3L_{mpiq}L_{F2ppy}CT$ (π(mpiq)→π*(F_2ppy)), and $^3L_{acac}L_{F2ppy}CT$ transitions (π(acac)→π*(F_2ppy)).

As shown in Table 2-12, The calculated triplet energies T_1 and T_2 of **42a** were 1.94 eV and 2.59 eV, respectively, which are in fairly good agreement with the experimentally determined

values (T_1: 2.02 eV (613 nm) and T_2: 2.56 eV (485 nm). As shown in Figure 2-19b, the HOMO of **42a** is mainly localized on the Ir center, the quinoline ring (quin), and the nitrogen atom (n) of the sulfonamide group of quinoline, and the HOMO-1 and HOMO-2 are mainly localized on the Ir centers and tpy ligands. On the other hand, its LUMO is localized on the quinoline ring, and LUMO+1 and LUMO+2 are mainly localized on the F_2ppy and tpy ligands, respectively. The results of TD-DFT calculations suggest that the lowest-energy triplet excited state T_1 is a mixture of $^3ML_{quin}CT$ (d(π)(Ir)→π*(quin)), $^3L_{quin}C$ (π(quin)→π*(quin)), $^3IL_{quin}CT$ (n(sulfonamide)→π*(quin)), and $^3L_{tpy}L_{quin}CT$ transitions (π(tpy)→π*(quin)) (Table 2-12). Furthermore, the second lowest-energy state T_2 of **42a** is a mixture of $^3ML_{tpy}CT$ (d(π)(Ir)→π*(tpy)), $^3ML_{F2ppy}CT$ (d(π)(Ir)→π*(F_2ppy)), $^3L_{tpy}C$ (π(tpy)→π*(tpy)), $^3L_{tpy}L_{F2ppy}CT$ (π(tpy)→π*(F_2ppy)), $^3L_{quin}L_{tpy}CT$ (π(quin)→π*(tpy)), and $^3L_{quin}L_{F2ppy}CT$ transitions (π(quin)→π*(F^2ppy)). These results indicate the contribution of each of the three different ligands (F_2ppy, tpy, and 8BSQ) to the triplet emission states of **42a**.

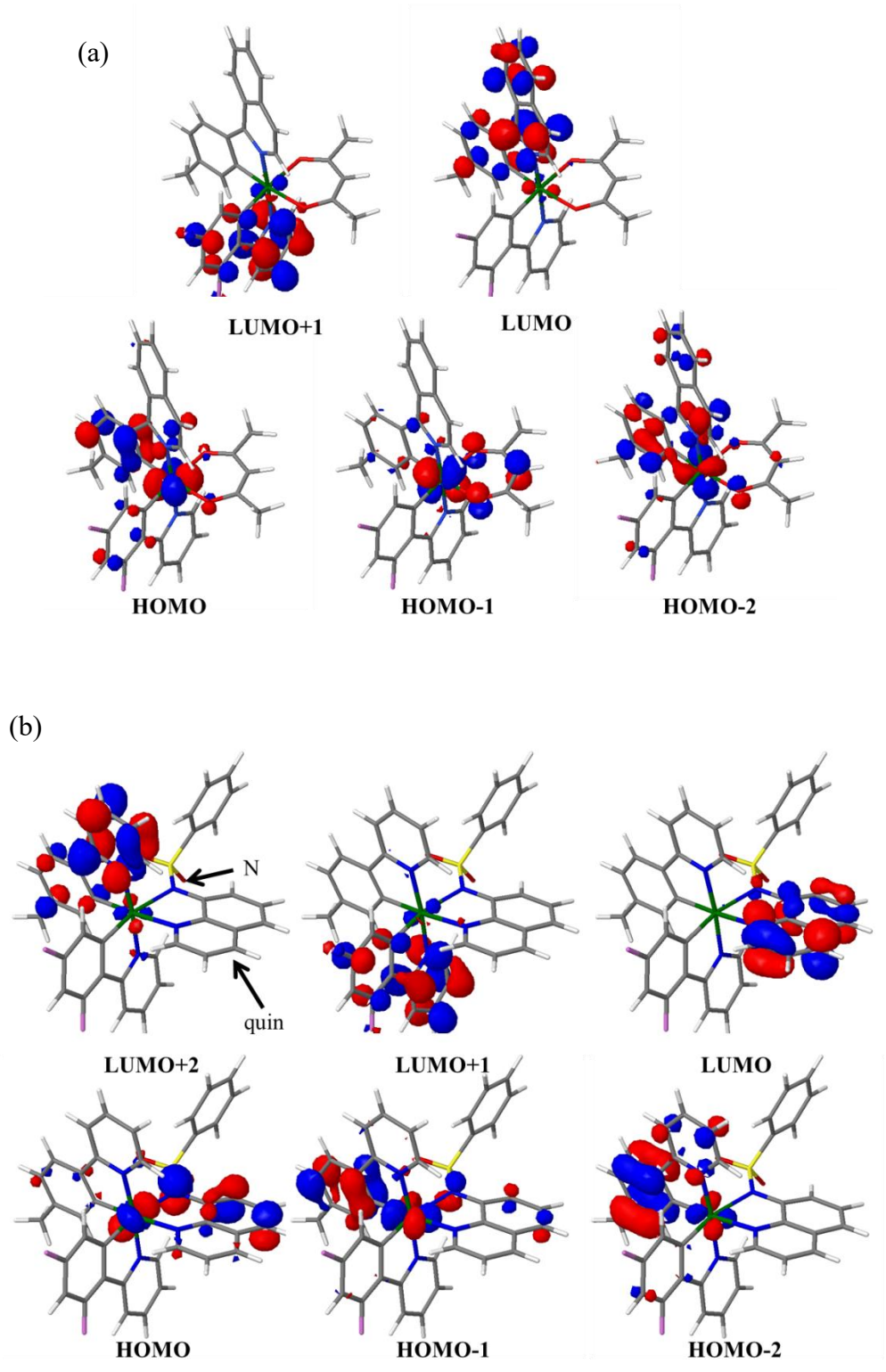

Figure 2-19. Selected molecular orbitals of (a) **37** and (b) **42a** obtained from DFT calculations at B3LYP (the LANL2DZ/6-31G level).

Table 2-12. Calculated triplet transition states and characteristics of the transitions of **37** and **42a** using TD-DFT calculation at B3LYP (the LANL2DZ/6-31G level).

Compound	λ_{em} (nm) Exp.	E (eV) Exp.	E (eV) TD-DFT	State	Assignment	Main transition character[a]
37	602	2.06	1.91	T_1	HOMO-2→LUMO (17%) HOMO-1→LUMO (8%) HOMO→LUMO (69%)	$^3ML_{mpiq}CT+^3L_{mpiq}C$ $+^3L_{acac}L_{mpiq}CT$
			2.40	T_2	HOMO-2→LUMO (23%) HOMO-1→LUMO (42%) HOMO→LUMO (25%)	$^3ML_{mpiq}CT+^3L_{mpiq}C$ $+^3L_{acac}L_{mpiq}CT$
	493	2.52	2.57	T_3	HOMO-1→LUMO+1 (6%) HOMO→LUMO+1 (79%)	$^3ML_{F2ppy}CT+^3L_{mpiq}L_{F2ppy}CT$ $+^3L_{acac}L_{F2ppy}CT$
42a	613	2.02	1.94	T_1	HOMO-1→LUMO (13%) HOMO→LUMO (79%)	$^3ML_{quin}CT+^3L_{quin}C+^3IL_{quin}CT$ $+^3L_{tpy}L_{quin}CT$
	485	2.56	2.59	T_2	HOMO-2→LUMO+2 (11%) HOMO-1→LUMO+1 (4%) HOMO-1→LUMO+2 (33%) HOMO→LUMO+1 (6%) HOMO→LUMO+2 (34%)	$^3ML_{tpy}CT+^3ML_{F2ppy}CT+^3L_{tpy}C$ $+^3L_{tpy}L_{F2ppy}CT+^3L_{quin}L_{tpy}CT+$ $^3L_{quin}L_{F2ppy}CT$

[a] The metal-to-ligand charge transfer, interligand charge transfer, intraligand charge transfer, and ligand centered are represented by ML_xCT, L_xL_yCT, IL_xCT, and LC_x, respectively. quin: quinoline ligand

2-3 Conclusions

In this manuscript, we report on the degradation of tris-cyclometalated Ir complexes (IrL_3, L: cyclometalating ligand) promoted by Brønsted acids such as HCl/1,4-dioxane and Lewis acids such as ZnX_2 (X = Br or Cl), TMSCl, and $AlCl_3$. Among the various Lewis acids, $ZnBr_2$ exhibited a good reactivity for $Ir(ppy)_3$ **1**, $Ir(tpy)_3$ **2**, and $Ir(mppy)_3$ **12** to provide the corresponding halogen-bridged Ir dimers (μ-complexes). It was also found that the reactivity of tris-cyclometalated Ir complexes containing electron-withdrawing groups such as fluorine atoms, nitro or CF_3 groups on the ligands is quite low. This reaction was applied to the selective degradation of *mer*-tris-cyclometalated Ir complexes such as *mer*-$Ir(tpy)_2(F_2ppy)$ (***mer*-20**). The reaction of ***mer*-20** with $ZnBr_2$ gave a mixture of a halogen-bridged Ir dimer **15b** and **34b**, and the tris-heteroleptic Ir complex **25** (IrLL'A, A: ancillary ligand) was then obtained by treatment with acetylacetone. Furthermore, we successfully isolated a novel tris-heteroleptic Ir complex **42a** having a non-symmetric ancillary ligand after careful separation of its diastereomers. Mechanistic studies suggest that the formation of different products from some Ir complexes by H^+, TMSCl, and $AlCl_3$ and ZnX_2 is due to the hardness and softness of these Brønsted and Lewis acids used. The reactivity and selectivity in the ZnX_2-promoted degradation can be explained by the interaction of the HOMO of Ir complexes with the LUMO of ZnX_2 and by the difference of electronegativity of iridium and carbon in the ligand part. Further mechanistic study is now underway. Such selective degradation reactions of tris-cyclometalated Ir complexes represents a potentially useful synthetic method for preparing a variety of metal complexes.

Chapter 3

Stereospecific Synthesis of *Tris-Heteroleptic Tris-Cyclometalated* Iridium(III) Complexes via Different Heteroleptic Halogen-Bridged Iridium(III) Dimers

3-1 Introduction

To date, numerous examples of Ir complexes have been prepared and most of them can be categorized as IrL_3, IrL_2L', IrLL'L'', IrL_2A, IL_2A', IrLL'A, and IrLL'A', as shown in Chart 3-1, where L, L', and L'' are different cyclometalating ligands that chelate to the Ir ion via carbon and hetero atoms, A depicts a symmetric ancillary ligand that binds to Ir via two hetero atoms and A' is a nonsymmetric ancillary ligand (Chart 3-1).

Chart 3-1

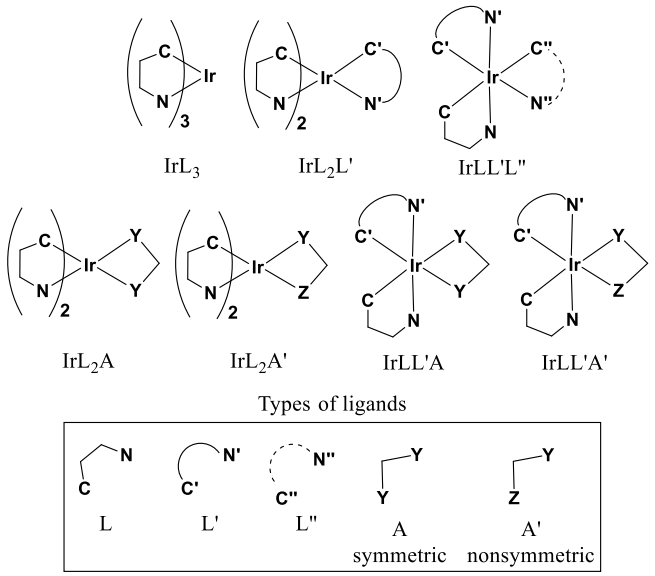

Tris-heteroleptic Ir complexes comprising an Ir ion with three different cyclometalating ligands, IrLL'L'', or a combination of two different cyclometalating ligands and one ancillary ligand, IrLL'A or IrLL'A', represent new classes of highly-functionalized Ir complexes, which may open new avenues for the fine-tuning of their photochemical and electrochemical properties and fill a function gap between a series of the homoleptic and bis-heteroleptic Ir complexes.

Representative synthetic methods of IrLL'A and IrLL'A' are shown in Chart 3-2, in which A is a symmetric ancillary ligand such as acacH, bipyridine (bpy), and 1,10-phenanthroline (phen) ligands, and A' presents nonsymmetric ancillary ligands such as picolinate (pic). The

synthesis depicted in the left part of Chart 3-2 (Method 1) involves a reaction of a mixture of two different cyclometalating ligands (1:1) with Ir sources such as $[Ir(COD)(\mu\text{-}Cl)]_2$ or $IrCl_3 \cdot nH_2O$, resulting in the production of the inseparable chloro-bridged Ir dimers **51**, which are converted to a mixture of the corresponding tris-heteroleptic Ir complexes **52** having an ancillary ligand for its purification.[29,55] As an example of this method, Baranof and co-workers synthesized Ir(ppy)(F_2ppy)(acac) **60** (corresponds to **55** in Chart 3-2) from a mixture of 2-(4',6'-difluorophenyl)pyridine **58** (F_2ppyH) and 2-phenylpyridine **59** (ppyH) (Chart 3-3).[29c] Furthermore, they carried out the conversion of **60** to Ir(ppy)(F_2ppy)(pic) **61a** and **61b** (corresponds to the conversion of **52** to **56** via **53** in Chart 3-2),[56] while **61a** and **61b** exhibit insufficient stability for device applications.[57]

Chart 3-2

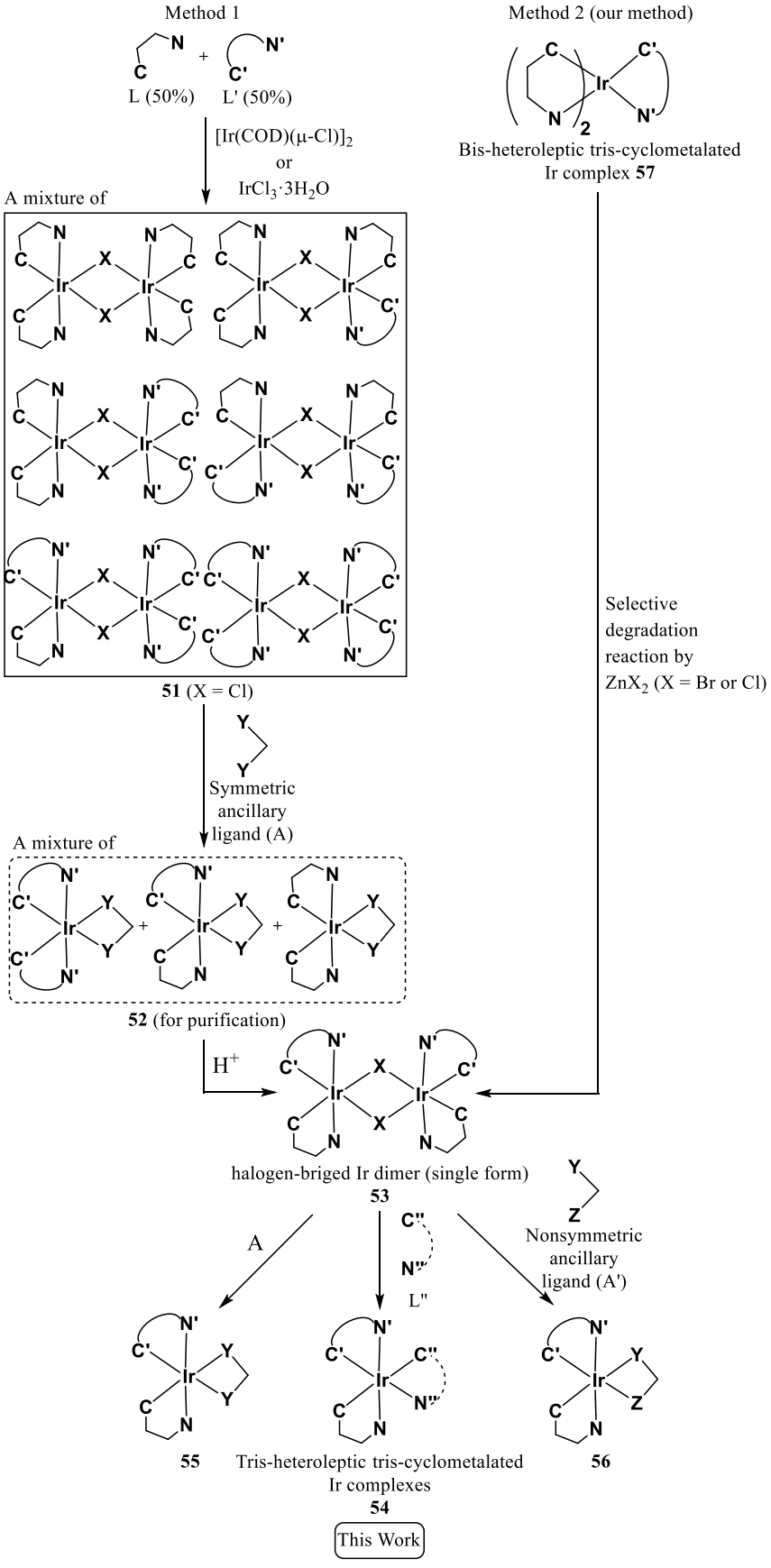
Method 1
L (50%)
L' (50%)
[Ir(COD)(μ-Cl)]2
or
IrCl3·3H2O
A mixture of
51 (X = Cl)
Symmetric ancillary ligand (A)
A mixture of
52 (for purification)
H+
Method 2 (our method)
Bis-heteroleptic tris-cyclometalated Ir complex 57
Selective degradation reaction by ZnX2 (X = Br or Cl)
halogen-briged Ir dimer (single form)
53
Nonsymmetric ancillary ligand (A')
A
L"
55
Tris-heteroleptic tris-cyclometalated Ir complexes
54
56
This Work

Chart 3-3

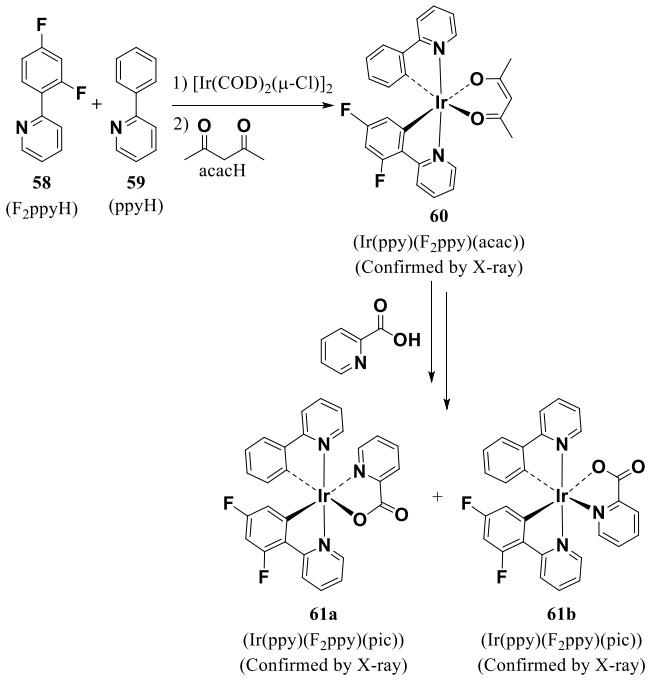

The reports on the synthesis of tris-heteroleptic *tris-cyclometalated* Ir complexes represented by IrLL'L'' (**54** in Chart 3-2) are still so limited.[58] Park and co-workers reacted $Ir(acac)_3$ with a mixture of **58**, **59**, and 1-(4'-fluorophenyl)isoquinoline **62** (F-piqH) in glycerol to afford a diastereomer mixture of $Ir(F_2ppy)(ppy)$(F-piq) **63** as shown in Method A of Chart 3-4.[58a] Lepeltier and Dumur *et al*. reported on the synthesis of $Ir(tpy)(F_2ppy)(ppy)$ **64** (Method B in Chart 3-4).[58b] In this case, $Ir(tpy)(F_2ppy)(acac)$ **25** was prepared by a reaction of a mixture of **58** and 2-(4'-tolyl) pyridine **63** (tpyH) with $IrCl_3$ and the successive reaction with acacH and then **25** was converted to heteroleptic chloro-bridged Ir dimer $[Ir(tpy)(F_2ppy)(\mu\text{-}Cl)]_2$ **34a** (corresponds to **53** in Chart 3-2) by the partial decomposition (the release of acac part) by HCl in Et_2O. The reaction of **34a** and **59** afforded a diastereomer mixture of **64** (corresponds to **54** in Chart 3-2). To the best of our knowledge, there is no report on the selective synthesis of one or several stereoisomers of tris-heteroleptic tris-cyclometalated Ir complexes, to date. Therefore, the comparison of chemical and photophysical properties of diastereomers of the Ir complexes that have the same combination of three ligands has been yet to be studied.

Chart 3-4

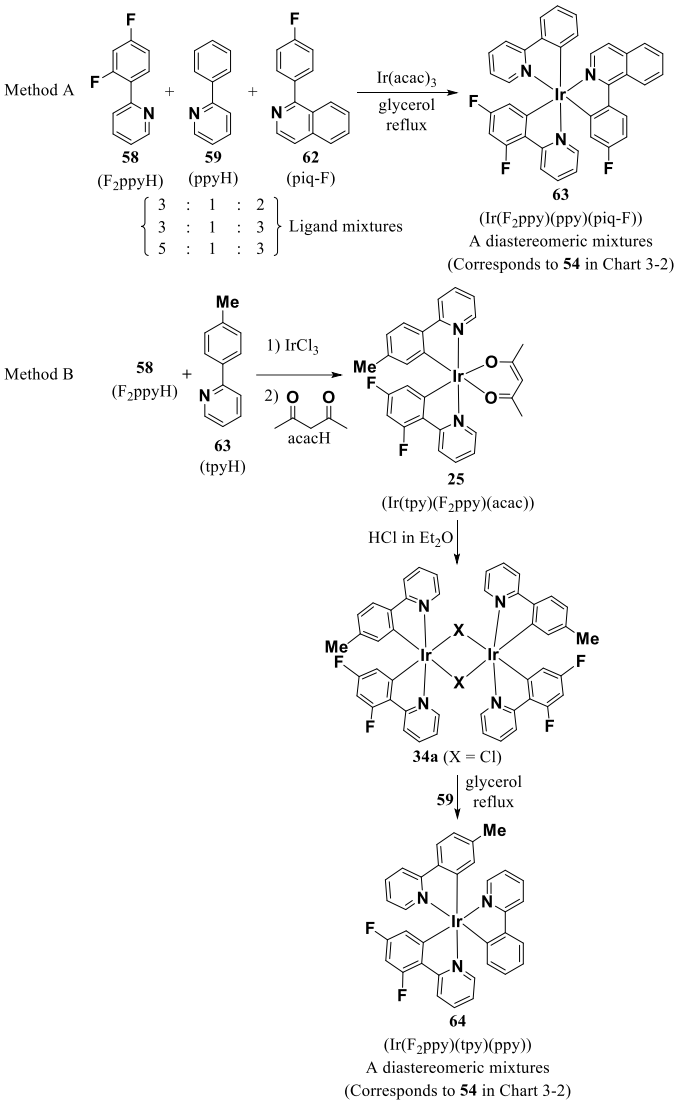
Method A
Ir(acac)3
glycerol
reflux
58
(F2ppyH)
59
(ppyH)
62
(piq-F)
3 : 1 : 2
3 : 1 : 3
5 : 1 : 3
Ligand mixtures
63
(Ir(F2ppy)(ppy)(piq-F))
A diastereomeric mixtures
(Corresponds to 54 in Chart 3-2)
Method B
58
(F2ppyH)
1) IrCl3
2)
acacH
63
(tpyH)
25
(Ir(tpy)(F2ppy)(acac))
HCl in Et2O
34a (X = Cl)
59
glycerol
reflux
64
(Ir(F2ppy)(tpy)(ppy))
A diastereomeric mixtures
(Corresponds to 54 in Chart 3-2)

Quite recently, we have reported on the decomposition reactions of Ir complexes, as shown in Chart 3-5.[24] Typically, the reaction of tris-homoleptic Ir complex $Ir(tpy)_3$ **2** in the presence of Brønsted and Lewis acids such as HCl (in 1,4-dioxane) and ZnX_2 (X = Cl or Br) afforded the corresponding halogen-bridged Ir dimers (μ-complexes) **15a,b**.[24] It was also found that tris-cyclometalated Ir complexes containing electron-withdrawing groups such as fluorine, nitro, and CF_3 moieties on the ligand parts are less reactive than **2**. This different reactivity of Ir complexes was applied to the selective degradation of bis-heteroleptic tris-cyclometalated Ir complexes such as $Ir(tpy)_2(F_2ppy)$ **20** to afford the corresponding heteroleptic μ-complexes **34a,b** (corresponds to the conversion of **57** to **53** in Method 2 of Chart 3-2). The treatment of **34a,b** with acacH and 8-benzenesulfonylamidoquinoline **41** (8BSQ) gave **25** (corresponds to **55** in Chart 3-2) and $Ir(tpy)(F_2ppy)(8BSQ^-)$ **42a** (corresponds to **56** in Chart 3-2), respectively. The selective elimination of 1-(4'-methylphenyl)isoquinoline unit **65** (mpiqH) from $Ir(mpiq)_2(F_2ppy)$ **23** gave **67a,b**, which were reacted with acacH to give $Ir(mpiq)(F_2ppy)(acac)$ **37**. Interestingly, it was discovered that **25** exhibits single broad emission, while **37** and **42a** have dual emission.

Chart 3-5

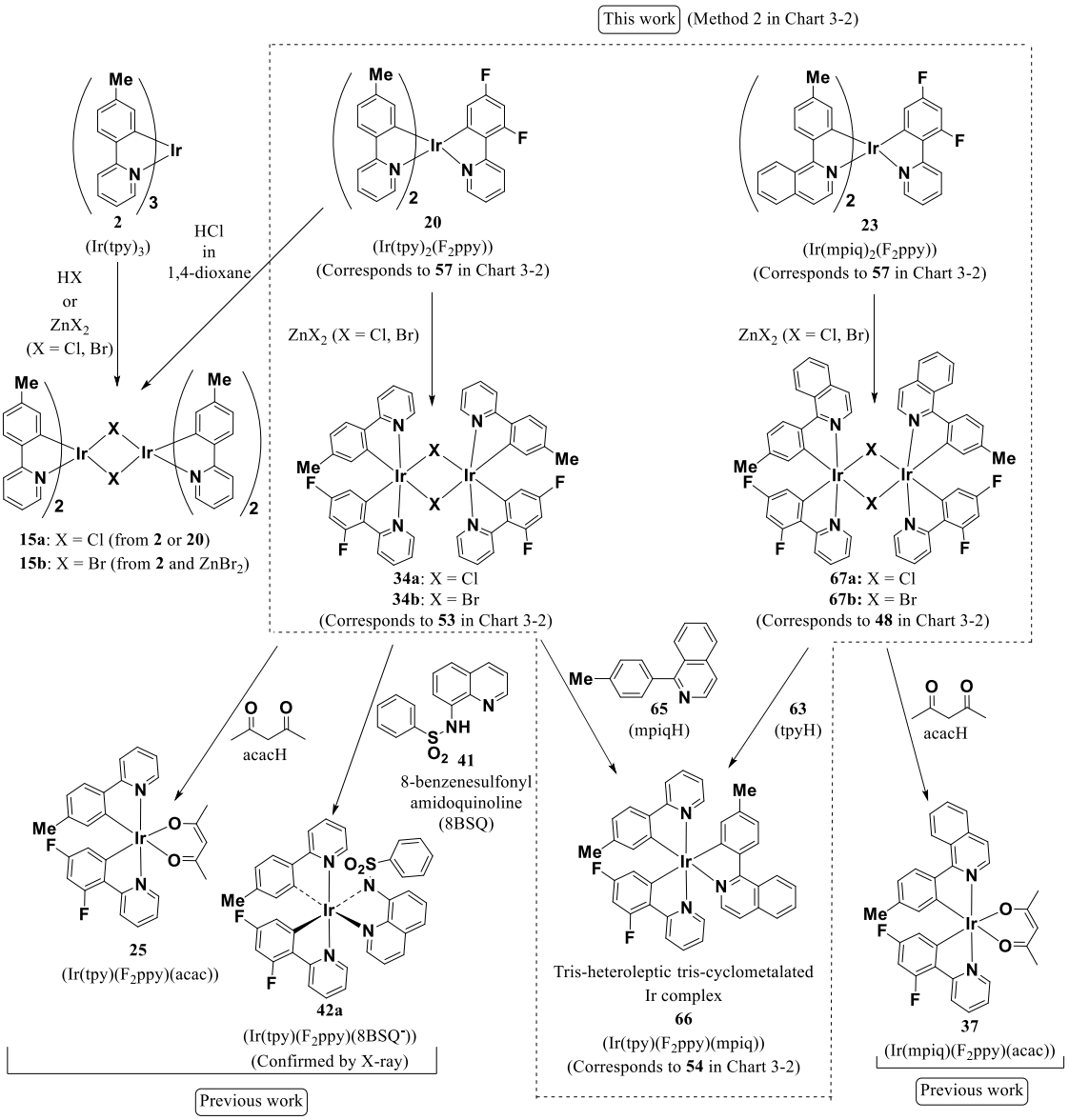
This work (Method 2 in Chart 3-2)
2
(Ir(tpy)3)
HCl
in
1,4-dioxane
HX
or
ZnX2
(X = Cl, Br)
20
(Ir(tpy)2(F2ppy))
(Corresponds to 57 in Chart 3-2)
23
(Ir(mpiq)2(F2ppy))
(Corresponds to 57 in Chart 3-2)
ZnX2 (X = Cl, Br)
ZnX2 (X = Cl, Br)
15a: X = Cl (from 2 or 20)
15b: X = Br (from 2 and ZnBr2)
34a: X = Cl
34b: X = Br
(Corresponds to 53 in Chart 3-2)
67a: X = Cl
67b: X = Br
(Corresponds to 48 in Chart 3-2)
65
(mpiqH)
63
(tpyH)
acacH
acacH
41
8-benzenesulfonyl
amidoquinoline
(8BSQ)
25
(Ir(tpy)(F2ppy)(acac))
42a
(Ir(tpy)(F2ppy)(8BSQ-))
(Confirmed by X-ray)
Tris-heteroleptic tris-cyclometalated
Ir complex
66
(Ir(tpy)(F2ppy)(mpiq))
(Corresponds to 54 in Chart 3-2)
37
(Ir(mpiq)(F2ppy)(acac))
Previous work
Previous work

Herein, we report on the stereospecific synthesis and isolation of a *tris-heteroleptic tris-cyclometalated* Ir complex via different heteroleptic halogen-bridged Ir dimers based on the aforementioned Zn^{2+}-promoted selective degradation reactions of Ir complexes (in a dashed area of Chart 3-5).[25] Namely, **20** and **23** were degraded by ZnX_2 to obtain the corresponding halogen-bridged Ir dimers **34** and **67**, respectively. It was expected that the reaction of **34** with **65** and the reaction of **67** with **63** would afford the same product, Ir(tpy)(F_2ppy)(mpiq) **66**. Interesting and important findings of this manuscript are that: i) different synthetic routes afford different diastereomer pairs of **66** (**66a-d** were obtained, as described below). ii) different diastereomers of **66** have different stability. iii) different diastereomers of **66** exhibits different photophysical properties. In addition, finding of strong emission from μ-complex **67a** is also reported.

3-2 Results and Discussions

3-2-1 Synthesis of Tris-Heteroleptic Tris-Cyclometalated Ir Complexes.

As shown in Chart 3-5, halogen-bridged Ir dimers **34b** and **67a,b** were prepared as substrates for the synthesis of **66** (by Method 2 in Chart 3-2). A mixture of **20** or **23** with ZnX_2 in 1,2-dichloroethane was refluxed to furnish heteroleptic μ-complexes **34b** or **67a,b**. It should be noted that **67a,b** was obtained only by Method 2 in Chart 3-2, though **34** can be obtained by both methods in Chart 3-2 (Chart 3-6 and Chart 3-7).[58b] The structure of **34b** was confirmed by ^{1}H NMR, ESI-MS, and X-ray structure analysis. The ORTEP drawing[37] of **34b** is presented in Figure 3-1a and the representative parameters for its crystal structure are summarized in Table 3-1. The stereochemistry of **34b** is important to discuss the stereochemistry of the reaction of **34b** with the third ligand (mpiq in that case). The comparison of the structure of **34b** with that of **15b** ($[Ir(tpy)_2(\mu\text{-}Br)]_2$)[24] (Figure 3-1b and Table 3-1) indicates that two Ir atoms of both μ-complexes have pseudo-octahedral 6-coordinated structure and two Ir-N bonds connected to the same Ir atom are in a *trans* configuration and the two Ir-C bonds have *cis* configuration.[24] The two Ir centers have the same absolute stereochemistry, Δ and Δ or Λ and Λ, as previously described by Watts and Garces.[5i]

Chart 3-6

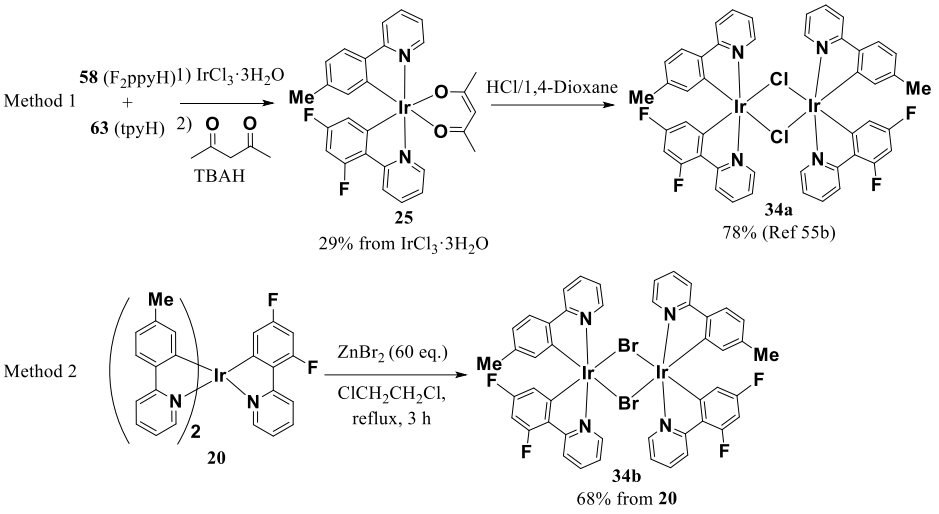

Chart 3-7

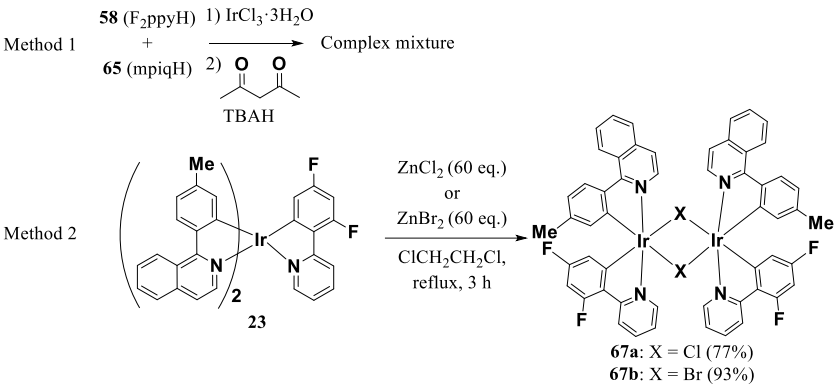

(a)

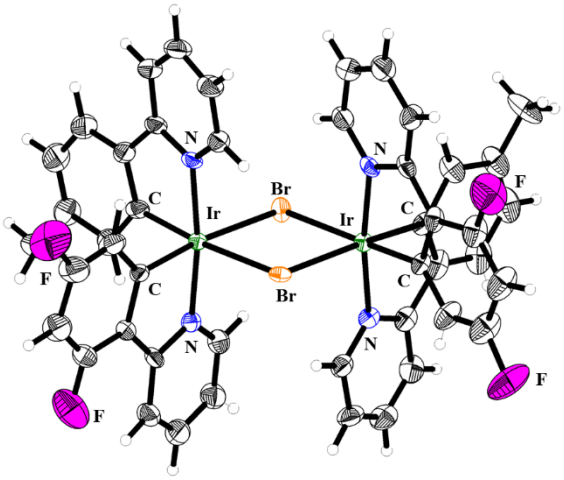

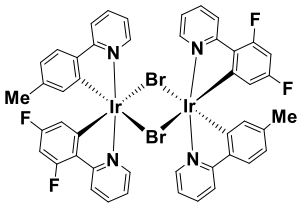

(b)

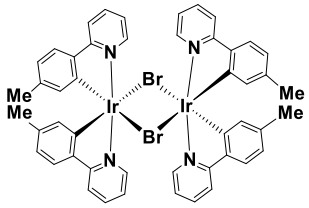

Figure 3-1. (a) ORTEP drawing with 50% probability ellipsoids and the stereochemical presentation of **34b**. For clarity, CH_2Cl_2 and H_2O were omitted. (b) stereochemical presentation of **15b**.

Table 3-1 (a) Selected bond lengths (Å) and (b) selected bond angles (º) of **34b** and **15b**.

(a)

	Bond Length of **34b** (Å)	Bond Length of **15b** (Å)
Ir-C (tpy)	2.00	2.01, 2.01, 2.02, 2.02
Ir-N (tpy)	2.04	2.04, 2.04, 2.05, 2.06
Ir-C (F_2ppy)	1.99	-
Ir-N (F_2ppy)	2.04	-
Ir-Br	2.63, 2.64	2.62, 2.62, 2.65, 2.65

(b)

	Bond Angles of **34b** (º)	Bond Angles of **15b** (º)
N (tpy)-Ir-Br	90.4	91.2, 91.3, 93.4, 93.7
N (F_2ppy)-Ir-Br	95.7	-
Br-Ir-Br	84.1	84.1, 84.3
Ir-Br-Ir	95.5, 96.2	95.7, 95.8

As shown in left part of Chart 3-8, a reaction of **34b** with **65** in 1,2-dichloroethane in the presence of AgOTf and Et_3N at 80 °C afforded a 1:0.4 mixture of two diastereomers of Ir(tpy)(F_2ppy)(mpiq) **66** (Figure 3-2a) among its eight possible diastereomers, **66a-h** listed in Chart 3-8 (the enantiomers of all the diastereomers are not considered). Careful separation of **66a,b** by silica gel column chromatography (hexanes/$CHCl_3$) afforded **66a** as a major product (Figure 3-2b). It was not possible to isolate **66b**, possibly due to its instability under the condition silica gel column chromatography. Other four diastereomers shown in the bottom of Chart 3-8 (in a dashed area) have not been obtained yet.

Chart 3-8

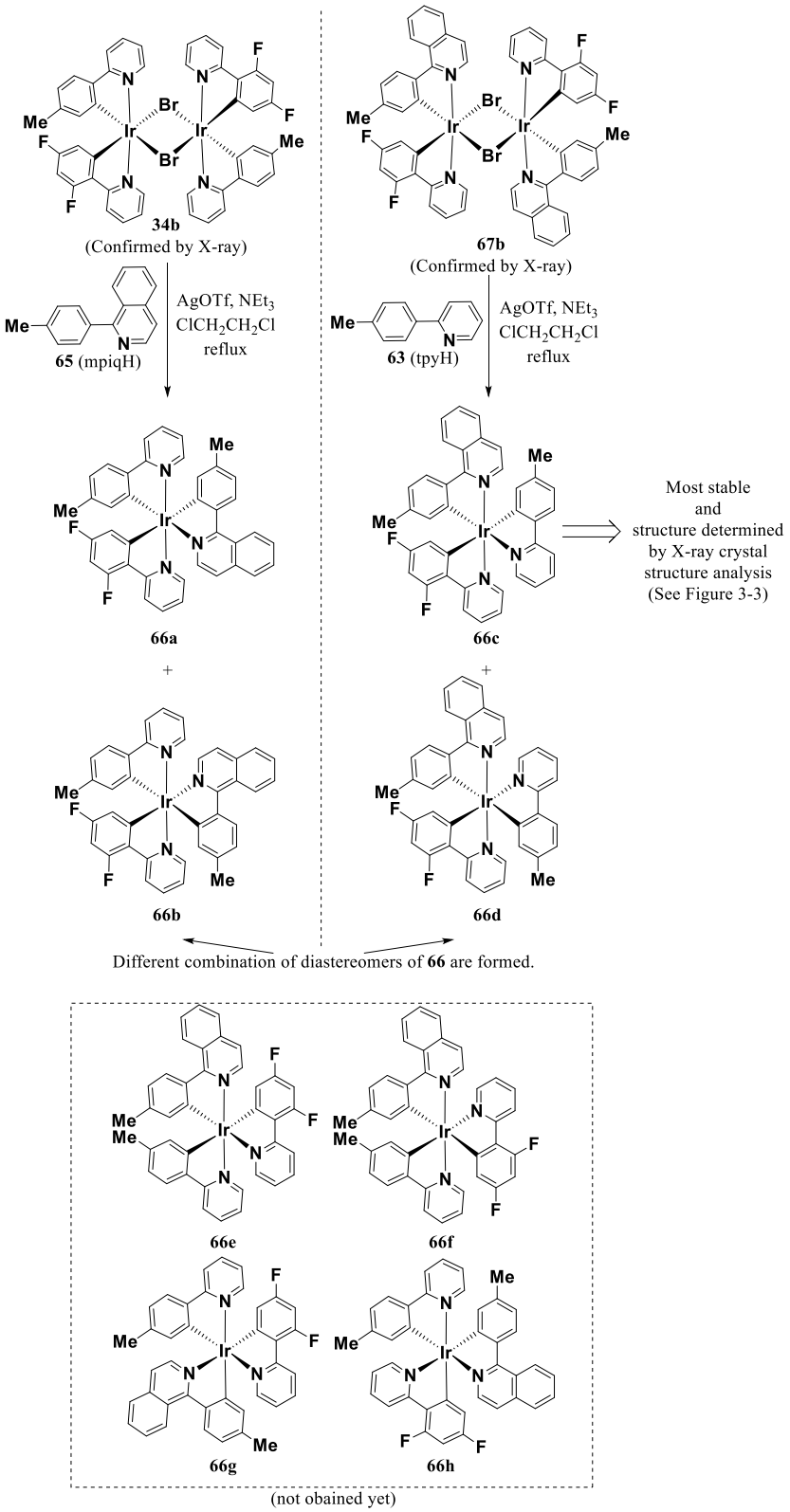
34b
(Confirmed by X-ray)
67b
(Confirmed by X-ray)
AgOTf, NEt3
ClCH2CH2Cl
reflux
65 (mpiqH)
63 (tpyH)
AgOTf, NEt3
ClCH2CH2Cl
reflux
66a
66c
Most stable
and
structure determined
by X-ray crystal
structure analysis
(See Figure 3-3)
66b
66d
Different combination of diastereomers of 66 are formed.
66e
66f
66g
66h
(not obained yet)

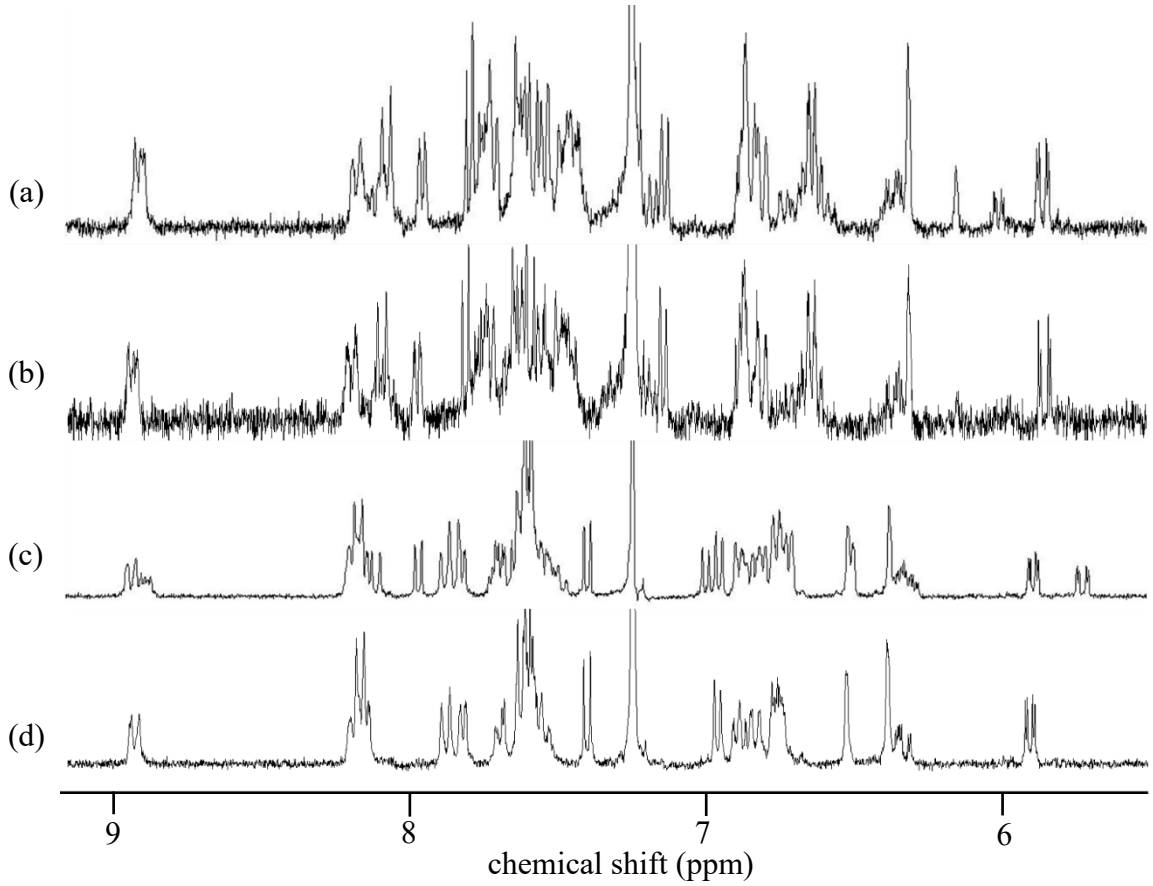

Figure 3-2 Aromatic regions of ^{1}H NMR spectra (300 MHz in $CDCl_3$) of (a) a mixture of **66a** and **66b**, (b) **66a** after purification, (c) a mixture of **66c** and **66d**, and (d) **66c** after isomerization.

On the contrary, the reaction of **67b** with **63** provided a mixture of two diastereomers of **66** (**66c** and **66d**), which are different from **66a** and **66b**, in a 1:0.7 ratio (right part of Chart 3-8). The comparison of aromatic regions of the ^{1}H NMR shown in Figure 3-2 suggests that these two diastereomer pair of **66a,b** and **66c,d** are completely different (Figure 3-2a and 3-2c). The diastereomer mixture of **66c** and **66d** could not be separated by purification using silica gel column chromatography, but the ratio of **66d** against **66c** was somewhat decreased after purification. Because we suspected these changes might be caused by silica gel, the isomerization of a mixture of **66a,b** and a mixture of **66c,d** in 1,2-dichloroethane was carried out in the presence of silica gel at 80 °C (Chart 3-9). The treatment of a mixture of **66a** and

66b with silica gel resulted in the decomposition and the product could not be isolated. On the other hand, the single isomer **66c** was obtained in 50% yield from a mixture of **66c** and **66d**. Note that negligible change was observed when two mixtures of **66a,b** and **66c,d** were warmed at reflux temperature in 1,2-dichloroethane without silica gel. Aromatic regions of the ^{1}H NMR spectrum of **66c** is shown in Figure 3-2d and its structure was determined by X-ray diffraction (Figure 3-3). These results strongly suggest that different stereoisomers of **66** (at least, **66a-h**) have different stability and that **66c** is the most stable isomer among **66a-d**, as calculated by DFT calculation (Chart 3-10).

Chart 3-9

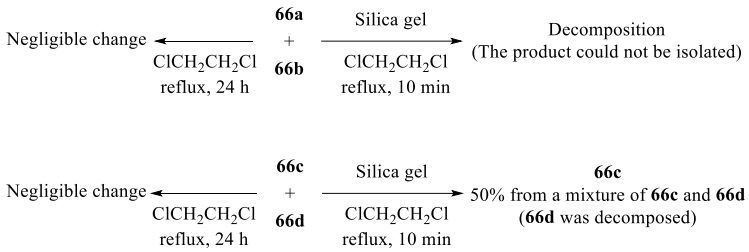

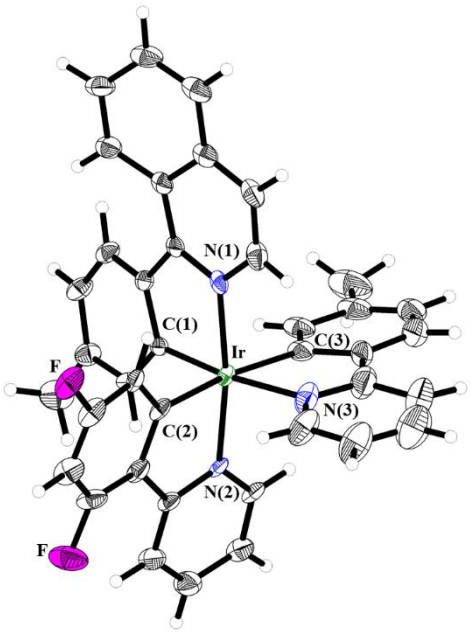

Figure 3-3. ORTEP drawing of single crystal structure of **66c** with 50% probability ellipsoids.

Chart 3-10

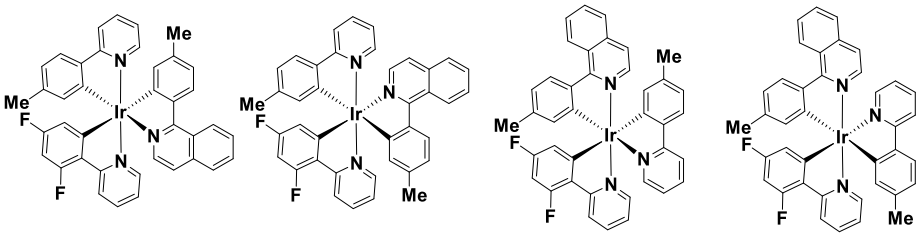

66a ΔG = + 18 J

66b ΔG = + 68 J

66c ΔG = 0 (defined as basis)

66d ΔG = + 272 J

For structural comparison with Ir(tpy)(F_2ppy)(mpiq) **66c**, X-ray crystal structure of Ir(F_2ppy)$_2$(mpiq) ***mer*-24**, prepared in our previous work, was determined in this paper, as shown in Figure 3-4. The Ir-C and Ir-N bond lengths for **66c** and ***mer*-24** are presented in Table 3-2. The difference of **66c** and ***mer*-24** is that contains one tpy ligand instead of one of two F_2ppy ligands in ***mer*-24**. The bond lengths of Ir-C(n) and Ir-N(n) (n = 1~3) in **66c** are quite similar to the corresponding pair of ***mer*-24**. It is interesting that the Ir-C and Ir-N bond lengths of mpiq ligand in **66c** (Ir-C(1) (mpiq): 1.99 Å, Ir-N(1) (mpiq): 2.04 Å) are *ca*. 0.1 Å shorter than those of ***mer*-24** (Ir-C(3) (mpiq): 2.08 Å, Ir-N(3) (mpiq): 2.14 Å), which might be resulted from weaker *trans* influences of N(3) atom in tpy and N(2) atom in F_2ppy than those of ***mer*-24**.[8] We assume that this point is important for the explanation of the different photophysical properties of **66c** and ***mer*-24**, as described below.

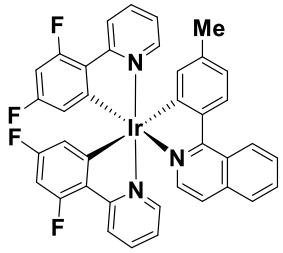

***mer*-24**

(*mer*-Ir(F_2ppy)$_2$(mpiq))

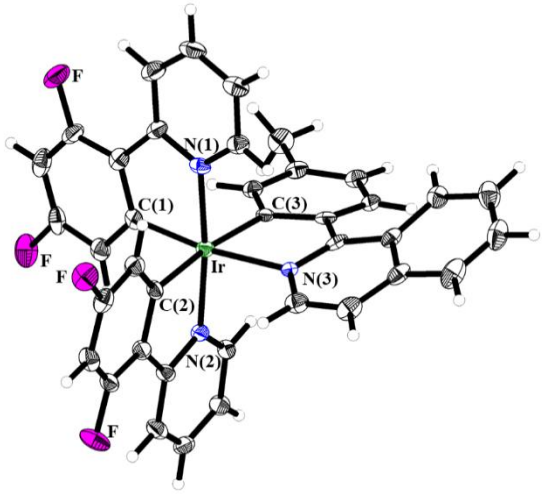

Figure 3-4. Stereochemical presentation and ORTEP drawing of single crystal structure of ***mer*-24** with 50% probability ellipsoids.

Table 3-2. Selected bond lengths (Å) in X-ray crystal structure of (a) **66c** and (b) ***mer*-24**.

(a)	X-ray structure bond lengths (Å)
Ir-C(1) (mpiq)	1.99
Ir-C(2) (F_2ppy)	2.05
Ir-C(3) (tpy)	2.07
Ir-N(1) (mpiq)	2.04
Ir-N(2) (F_2ppy)	2.04
Ir-N(3) (tpy)	2.15

(b)	X-ray structure bond lengths (Å)
Ir-C(3) (mpiq)	2.08
Ir-C(1) (F_2ppy)	1.99
Ir-C(2) (F_2ppy)	2.06
Ir-N(3) (mpiq)	2.14
Ir-N(1) (F_2ppy)	2.03
Ir-N(2) (F_2ppy)	2.04

3-2-2 Photophysical Properties of Tris-Heteroleptic Tris-Cyclometalated Ir Complexes

UV/Vis absorption spectra of **66a**, **66c**, and ***mer*-24** (10 μM in DMSO solutions at 298 K) are shown in Figure 3-5a and their photochemical properties are summarized in Table 3-3. These complexes also exhibited a weak absorption in the region of *ca*. 330-500 nm, which are due to spin-allowed and spin-forbidden metal-ligand charge transfer (MLCT) transitions and spin-forbidden π—π* transitions.

Emission spectra of **66a**, **66c**, and ***mer*-24** (10 μM in degassed DMSO) at 298 K (excitation at 366 nm) are shown in Figure 3-5b and their quantum yields were determined based on the Φ value of *fac*-Ir(mpiq)$_3$ in toluene (Φ = 0.26) used as a standard reference (See Table 3-3).[59] Most interestingly, **66a** emits a broad single emission (586 nm) and the spectrum of **66c** presents dual emission at *ca*. 509 nm and *ca*. 600 nm despite **66a** and **66c** have the same three ligands. It should be noted that **66a** and **66c** was recrystallized twice in order to minimize contamination and the exactly the same spectra were observed after recrystallization.

Table 3-3. Photophysical properties of **66a**, **66c**, and ***mer*-24** (in DMSO solutions) at 298 K (excitation at 366 nm) ([**66a**, **66c**, and ***mer*-24**] = 10 μM).

Compounds	λ_{abs} (nm)	λ_{em} (nm)	Quantum yield Φ^b	Emission liftime τ (μs)
66a (Ir(tpy)(F$_2$ppy)(mpiq))	313, 356, 410	586	0.25	2.4[c]
66c (Ir(tpy)(F$_2$ppy)(mpiq))	276, 342, 411	509, 600	0.30	1.5[d]
***mer*-24** (*mer*-Ir(F$_2$ppy)$_2$(mpiq))[a]	272, 354, 395	581	0.31	4.7[c]

[a] Data have been already reported in Ref 57 (Chapter 2). [b] Quantum yields were determined using *fac*-Ir(mpiq)$_3$ as a standard reference (Φ = 0.26 in toluene). [c] A 590 nm long wave pass filter was used. [d] A 475 nm long wave pass filter was used.

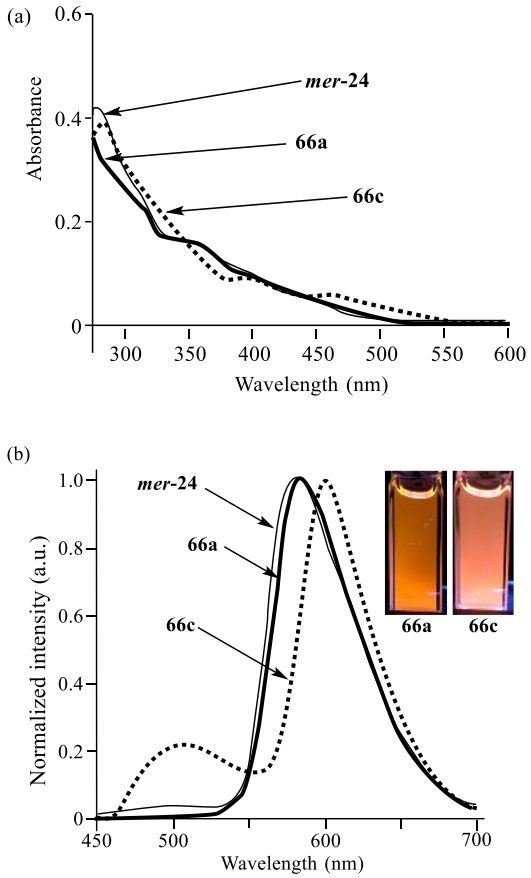

Figure 3-5. (a) UV/vis spectra of Ir complexes **66a** (bold curve), **66c** (dashed bold curve), and ***mer*-24** (plain curve) in DMSO at 298 K. (b) Normalized emission spectra of **66a** (bold curve), **66c** (dashed bold curve), and ***mer*-24** (plain curve) in degassed DMSO at 298 K ([Ir complex] = 10 μM and excitation at 366 nm). Inset: Photograph showing DMSO solution of **66a** and **66c** (10 μM) excited by UV light at 365 nm.

3-2-3 Mechanistic Study for Stereoselective Reaction from Heteroleptic Halogen-Bridged Ir Complexes to Tris-Heteroleptic Tris-Cyclometalated Ir Complexes

We asked ourselves why only two stereoisomers of tris-heteroleptic tris-cyclometalated Ir complexes are formed from two heteroleptic μ-complexes **34** and **67**, respectively? To answer this question, we tried the crystallization of **34a,b** and **67a,b** to determine their stereochemistry.

Based on the stereochemistry of **34b**, the reaction of **34** with **65** and **67** with **63** are shown in Chart 3-11, especially focused on the attack of **65** and **63** to **34** and **67**. Namely, we assume that the *cis*-*C*,*C*- or *trans*-*N*,*N*-configurations of **34** and **67** found in its X-ray single crystal structure (Figure 3-6a) are retained in **66a,b** and **66c,d**, and that **65** and **63** attack to Ir atom of **34** and **67** in two different directions (**68** and **69** in Chart 3-11). In support of our mechanism, it should be noted that the synthesis of meridional form of **2,** which was synthesized from **15a**[60] and its stereochemistry have been already discussed by Thompson and co-workers.[8] As shown in Chart 3-12, they referred that the *trans*-*N,N*-configurations of **15a** are retained when the cyclometallation by **63** was carried out even at 140-145 °C (glycerol was used as the solvent), which is *ca*. 60 °C higher than our synthetic method (direction of the attack of **63** is indicated in Chart 3-12).

Chart 3-11

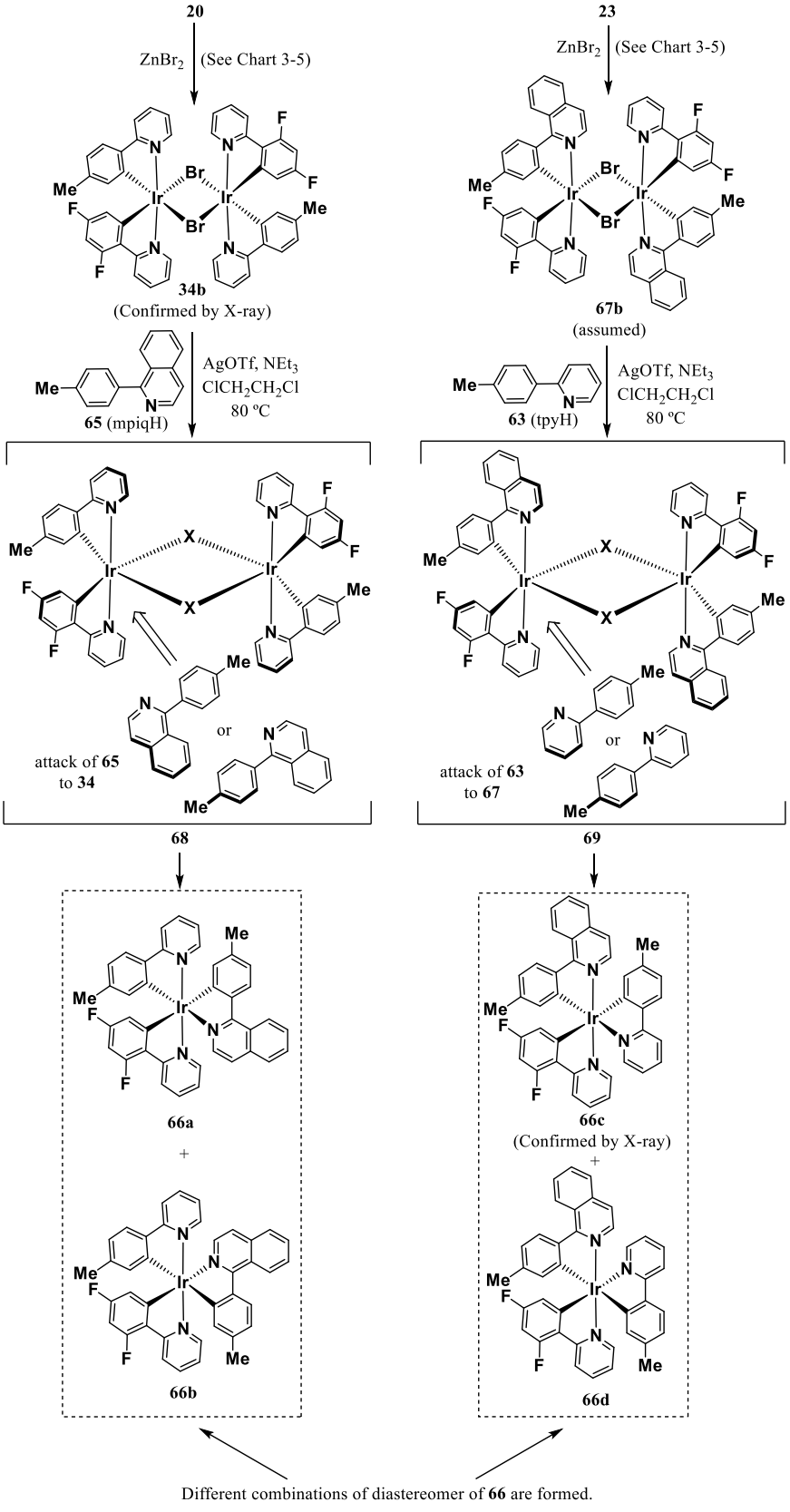
20
ZnBr2 (See Chart 3-5)
34b
(Confirmed by X-ray)
65 (mpiqH)
AgOTf, NEt3
ClCH2CH2Cl
80 °C
attack of 65
to 34
or
68
23
ZnBr2 (See Chart 3-5)
67b
(assumed)
63 (tpyH)
AgOTf, NEt3
ClCH2CH2Cl
80 °C
attack of 63
to 67
or
69
66a
+
66b
66c
(Confirmed by X-ray)
+
66d
Different combinations of diastereomer of 66 are formed.

Chart 3-12

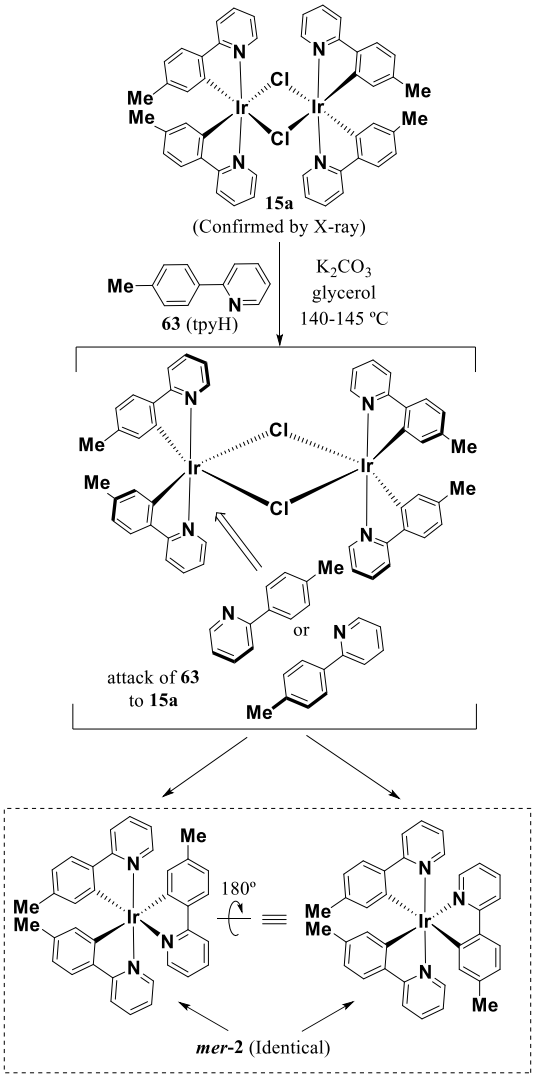
15a
(Confirmed by X-ray)
63 (tpyH)
K2CO3
glycerol
140-145 ºC
attack of 63
to 15a
or
180º
mer-2 (Identical)

3-2-4 DFT Calculation Study for Emission of Tris-Heteroleptic Tris-Cyclometalated Ir Complexes

TD-DFT calculations of **66a** and **66c** were performed by the Gaussian09 program.[54] The selected orbitals of **66a** and **66c** are shown in Table 3-4 and Figure 3-6. For **66a**, the calculated triplet energies T_1 is in good agreement with the experimentally determined values (T_1: 2.22 eV (559 nm)) (Table 3-4). The HOMO-1 and HOMO-2 of **66a** are mainly localized on the Ir center and mpiq ligands as shown in Figure 3-6a, respectively. The LUMO is localized on the mpiq. TD-DFT calculations show that $^3ML_{mpiq}CT$ (d(π)(Ir)→π*(mpiq)) and $^3L_{mpiq}C$ (π(mpiq)→π*(mpiq)) (Table 3-4) are included in the lowest-energy triplet excited state T_1. Because the emission of cyclometalated Ir complexes generally come from the gap of HOMO-LUMO,[61] this result shows the strong contribution of mpiq ligand to the emission of **66a**. Although HOMO-LUMO gap is presented in T_2 state, the experimental result is negligibly matched to the T_2 state.

The calculated triplet energies T_1 and T_2 of **66c** was 2.14 eV and 2.44, respectively. As shown in Figure 3-6b, the HOMO of **66c** are mainly localized on the Ir center and mpiq and its LUMO is mainly included in mpiq, respectively. The results of TD-DFT calculations suggest that the lowest-energy triplet excited state T_1 is a mixture of $^3ML_{mpiq}CT$ (d(π)(Ir)→π*(mpiq)) and $^3L_{mpiq}C$ (π(mpiq)→π*(mpiq)) (Table 3-4). In contrast with **66a**, the T_2 of **66c** is in good accordance with experimental state. Based on the TD-DFT calculations, T_2 of **66c** was mainly composed of $^3ML_{mpiq}CT$ (d(π)(Ir)→π*(mpiq)) and $^3L_{tpy}L_{mpiq}CT$ transitions (π(tpy)→π*(mpiq)), respectively. These results indicate the tpy in **66c** is strongly contributed to the experimental determined high energy band.

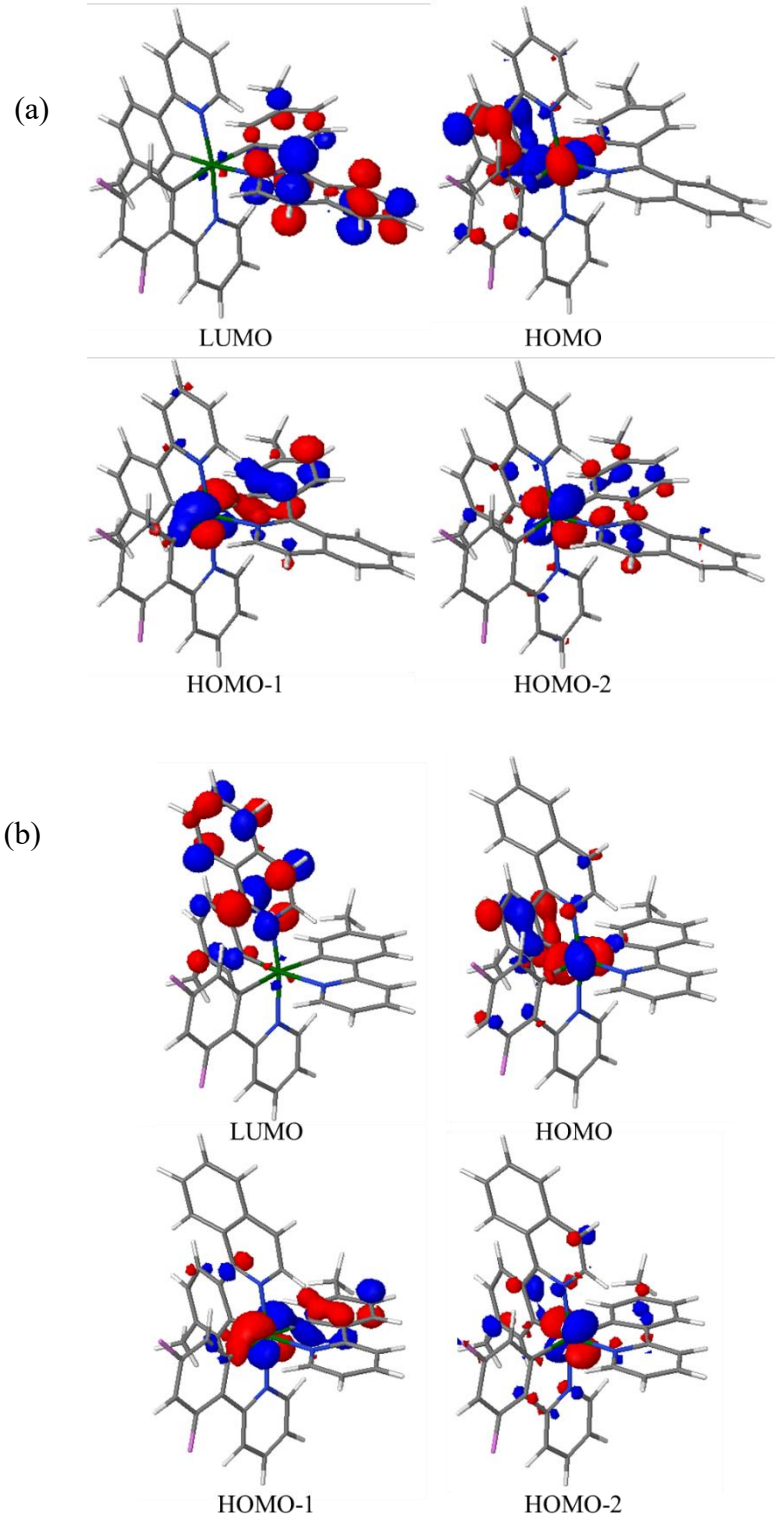

Figure 3-6. Selected molecular orbitals of (a) **66a** and (b) **66c** obtained from DFT calculations at B3LYP (the LANL2DZ/6-31G level). Color code: Ir = green, C = gray, H = white, N = blue, F = pink.

Table 3-4. Calculated triplet transition states and characteristics of the transitions of **66a** and **66c** using TD-DFT calculation at B3LYP (the LANL2DZ/6-31G level).

Compound	λ_{em} (nm) Exp.	E (eV) Exp.	E (eV) TD-DFT	State	Assignment	Main transition character[a]
66a	586	2.12	2.22	T_1	HOMO-1→LUMO (46%) HOMO-2→LUMO (22%)	$^3ML_{mpiq}CT+^3L_{mpiq}C+^3IL_{mpiq}CT$
	-	-	2.40	T_2	HOMO→LUMO (82%)	$^3ML_{mpiq}CT+^3L_{tpy}L_{mpiq}CT$
66c	600	2.06	2.14	T_1	HOMO→LUMO (63%)	$^3ML_{mpiq}CT+^3L_{mpiq}C+^3IL_{mpiq}CT$
	509	2.44	2.44	T_2	HOMO-1→LUMO (56%) HOMO→LUMO (26%)	$^3ML_{mpiq}CT+^3L_{tpy}L_{mpiq}CT$

[a] The metal-to-ligand charge transfer, interligand charge transfer, intraligand charge transfer, and ligand centered are represented by ML_xCT, L_xL_yCT, IL_xCT, and LC_x, respectively.

Localization of HOMO at the mpiq unit of **66c** was checked by the electrophilic substitution reaction. Previously, we found the ligand-selective and regioselective electrophilic reactions of heteroleptic Ir complexes.[14,24] For example, electrophilic reaction of **20** proceeds at the *p*-position of the phenyl group of a cyclometalating ligand that is *trans* to in Ir-N bond. Namely, the bromination of **20** was carried out with NBS to give Ir(tpy)(Br-tpy)(F_2ppy) ***mer*-50** in 64% yield (Chart 3-13). It was assumed that **66c** was also brominated to afford Ir(tpy)(F_2ppy)(Br-mpiq) in 87% yield, confirming the high reactivity of the HOMO speculated by DFT calculations.

Chart 3-13

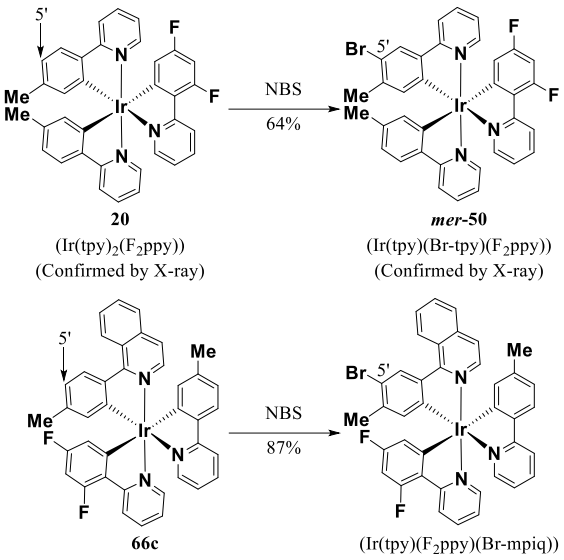

3-2-5 Photophysical Properties of Heteroleptic μ-Complexes

Finally, the unexpected finding on the strong emission from heteroleptic μ-complex is **67a** is described. The UV/Vis absorption spectra for **67a**, $[Ir(mpiq)_2(\mu\text{-}Cl)]_2$ 2**6a**, and $[Ir(F_2ppy)_2(\mu\text{-}Cl)]_2$ **30a** (5 μM in CH_2Cl_2 solutions at 298 K) were recorded in aerated DCM at 298 K and are shown in Figure 3-7a. The results of their photophysical properties are summarized in Table 3-5. All μ-complexes possess intense absorption bands below *ca*. 350 nm corresponding to spin-allowed singlet ligand-centered (^{1}LC) $^1\pi$—π^* transitions.[35a] These complexes also exhibited a weak absorption in the region of *ca*. 330-500 nm, which are due to spin-allowed and spin-forbidden metal-ligand charge transfer (MLCT) transitions and spin-forbidden π—π* transitions.

Emission spectra of **67a** and **26a** (5 μM in degassed CH_2Cl_2 solutions) at 298 K are shown in Figure 3-7b. We found that strong emission from **67a**, as shown in Figure 3-7b, whose color is almost the same as that of ***mer*-21**. The emission spectra of **67a** is broad including a low energy emission shoulder, possibly due to a mix of ^{3}MLCT/^{3}LC transition.[35a]

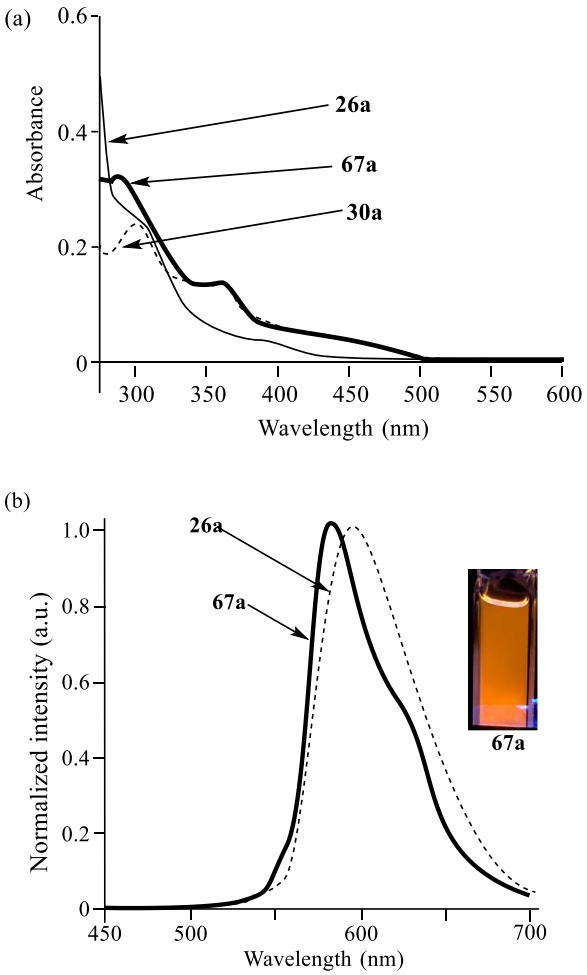

Figure 3-7. (a) UV/vis spectra of Ir complexes **67a** (bold curve), **26a** (plain curve), and **30a** (dashed curve) in CH_2Cl_2 at 298 K. (b) Normalized emission spectra of **67a** (bold curve) and **26a** (plain curve**)** in degassed CH_2Cl_2 at 298 K ([Ir complex] = 5 μM and excitation at 366 nm). Inset: Photograph showing CH_2Cl_2 solution of **67a** (5 μM) excited by UV light at 365 nm.

Table 3-5. Photophysical properties of **67a, 26a**, and **30a** (in CH_2Cl_2 solutions) at 298 K (excitation at 366 nm) ([**67a**, **26a**, and **30a**] = 5 μM).

Compounds		λ_{abs} (nm)	λ_{em} (nm)	Quantum yield Φ^b	Emission liftime τ (μs)
67a	$[Ir(mpiq)(F_2ppy)(\mu\text{-}Cl)]_2$	284, 356, 437	582	0.17	3.3[c]
26a	$[Ir(mpiq)_2(\mu\text{-}Cl)]_2$	296, 359, 453	594	0.04	0.9[c]
30a	$[Ir(F_2ppy)_2(\mu\text{-}Cl)]_2$[a]	303, 339, 386	too week	-	-

[a] Emission too weak to determine Φ or τ. [b] Quantum yields were determined using *fac*-$Ir(mpiq)_3$ as a standard reference (Φ = 0.26 in toluene). [c] A 590 nm long wave pass filter was used.

3-3 Conclusions

Herein, we report on the stereospecific synthesis of two single isomers of tris-heteroleptic tris-cyclometalated iridium(III) (Ir(III)) complexes consisting of three different nonsymmetric cyclometalating ligands via heteroleptic halogen-bridged Ir dimers $[Ir(tpy)(F_2ppy)(\mu\text{-}Br)]_2$ **34b** and $[Ir(mpiq)(F_2ppy)(\mu\text{-}Br)]_2$ **67b** (tpy: (2-(4'-tolyl)pyridine) and F_2ppy: (2-(4',6'-difluorophenyl)pyridine), and mpiq: (1-(4'-methylphenyl)isoquinoline)) prepared by Zn^{2+}-promoted degradation reactions of $Ir(tpy)_2(F_2ppy)$ **20** and $Ir(mpiq)_2(F_2ppy)$ **23**, as reported by us. Subsequently, **34b** and **67b** was converted to the tris-heteroleptic tris-cyclometalated Ir complexes Ir(tpy)(F_2ppy)(mpiq) **66** consisting of tpy, F_2ppy, and mpiq, as confirmed by spectroscopic and X-ray crystal structure analysis. The important findings of this work are that: i) the specific isomers of tris-heteroleptic tris-cyclometalated such as **66a,b** and **66c,d** can be prepared from the different halogen-bridged Ir dimers **34b** and **67b**, while all the stereoisomers are composed of the same ligands. The mechanism of the formation of only two diastereomers from the μ-complex is discussed based on the X-ray crystal structures of **34b** and the product **66c**. The mechanism of the formation of only two diastereomers from the μ-complex is discussed based on the X-ray crystal structures of **34b** and the product **66c**. ii) each **66** isomers have different stability (in the presence of silica gel, in this work). iii) different stereoisomers of **66** exhibit different emission spectra. Namely, one stereoisomer **66a** exhibits single broad emission from *ca*. 550 nm to *ca*. 650 nm (orange emission), while another stereoisomer **66c** emits dual emission at *ca*. 509 nm and *ca*. 600 nm (pale pink emission). To the best of our knowledge, this is the first report on the selective and efficient synthesis, different stability and different photophysical properties of tris-heteroleptic tis-cyclometalated Ir(III) complexes. These information of tris-heteroleptic tris-cyclometalated Ir complexes represents a potentially useful synthetic method for preparing not only Ir complexes but also other metal complexes.

Chapter 4

Synthesis and Anticancer Properties of Bis- and Mono(cationic peptide) Hybrids of Bis-Heteroleptic Cyclometalated Iridium(III) Complexes: Effect of the Number of Peptide Units on Anticancer Activity

4-1 Introduction

Aoki and co-workers previously reported Ir complex–peptide hybrids (IPHs) **70a–f** (with net charges from +9 to +12) containing a KKGG (K: lysine, G: glycine) cationic peptide a connected *via* a C6 or C8 alkyl chain linker between the peptide and the Ir(tpy)$_3$ core via regioselective substitution reactions of *fac*-Ir(tpy)$_3$ (**2**) and *fac*-Ir(ppy)$_3$ (**1**) at the 5'-position of the cyclometalated ligands (Chart 4-1).[27,30,31] These IPHs showed considerable levels of anticancer activity against Jurkat cancer cells with EC_{50} values of 7–16 μM.[27a,e,f,g] We also reported on the synthesis of the Ir(III) complex-peptide hybrid **71** containing three KKKGG peptide units at the 5'-position of the tpy ligand through C8 alkyl chain linkers, which showed a more potent cytotoxicity against Jurkat cancer cells with an EC_{50} value of 1.5 μM and which induced considerable morphological changes in Jurkat cells with a strong green emission.[27f] Mechanistic investigations suggested that **70** induces an intracellular Ca^{2+} overload, resulting in the induction of a paraptosis-like cell death associated with autophagy.

Chart 4-1. Structures of cationic amphiphilic Ir complexes derived from Ir(tpy)$_3$ **2** and their EC_{50} values against Jurkat cancer cells (net cationic charges in aqueous solution at natural pH are indicated in their structures).

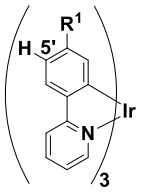

***fac*-1** (*fac*-Ir(ppy)$_3$)**:** R^1 = H
***fac*-2** (*fac*-Ir(tpy)$_3$)**:** R^1 = Me

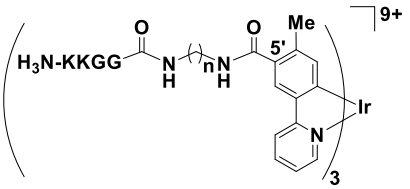

70a (n = 2): EC_{50} >50 μM against Jurkat cells
70b (n = 4): EC_{50} >50 μM
70c (n = 6): EC_{50} = 16 μM
70d (n = 8): EC_{50} = 7.3 μM
70e (n = 12): EC_{50} = 32 μM
70f (n = 16): EC_{50} >50 μM

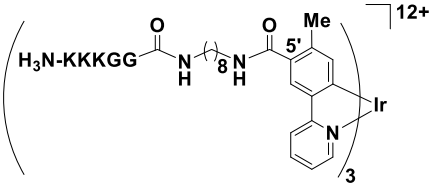

71: EC_{50} = 1.5 μM against Jurkat cells

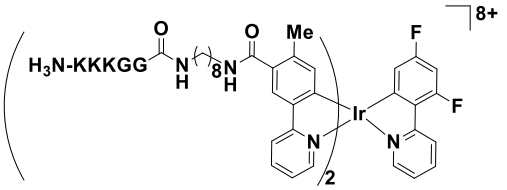

72

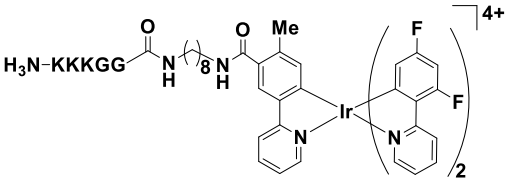

73

We report herein on the design and synthesis of Ir complexes, **72** and **73** containing two and one KKKGG sequences, respectively, for an evaluation of the effect of the number of the KKKGG peptide parts on their anticancer activities. The cytotoxicity of **72** (bispeptide) and **73** (monopeptide) against Jurkat, HeLa S3, and A549 cancer cells, and IMR90 normal cells was evaluated in comparison with the trispeptide complex **71**. The results of MTT assay indicated that complexes **71** and **72** exhibited more potent anticancer activity against Jurkat cells than **73**, indicating the existence of a positive correlation between the number of the KKKGG peptide units and their cytotoxicity, and a strong green emission was observed in dead cells. It was suggested that **71** and **72** induce the vacuolization of the cytoplasm in Jurkat cells, which are characteristic phenomena of paraptotic cell death, a relatively newly recognized type of programmed cell death, as confirmed by transmission electron microscopic (TEM) observations. It was also found that Ca^{2+} ions were transferred to mitochondria possibly from the endoplasmic reticulum (ER) and that this played a critical role in the induction of cell death. In addition, the localization of these complexes and intracellular morphology in the Jurkat cells were examined in co-staining experiments using specific probes for intracellular organelles and other microscopic methods.

4-2 Results and Discussions

4-2-1 Synthesis of Ir(III) Complexes Equipped with Bis or Mono Cationic Peptide Units

The synthesis of the bis-heteroleptic cyclometalated Ir(III) complex-bispeptide conjugate **72** and the monopeptide conjugate **73** is shown in Chart 4-2 and 4-3, respectively. The biscarboxylated Ir(III) complex (**75**) was prepared from *fac*-**20**[24] (in the form of a racemic mixture of Δ and Λ forms) via Vilsmeier-Haack formylation, followed by a Pinick oxidation, as described in our previous papers.[27a,g,30a] The structure (*facial* form) of the formylated intermediate **74** was determined by a X-ray crystal structure analysis, as shown in Figure 4-1 (typical parameters of the crystal structure of **74** are listed in Table 4-1). The condensation of **75** with a mono-Boc-protected diamine (C8 alkyl chain linker) gave **76** and its two Boc groups were removed by treatment with a mixture of TMSCl and NaI to give **77**. The coupling reaction of **77** with the protected KKKGG peptide, which was prepared by a Fmoc solid-phase peptide synthesis method, was conducted, followed by the deprotection with TMSCl and NaI in MeCN[27g] and purification by reverse phase high performance liquid chromatography (RP-HPLC) afforded a TFA salt of **72**.

Chart 4-2. Synthesis of bis-heteroleptic cyclometalated Ir(III) complex-peptide hybrid **72** containing two cationic peptide units.

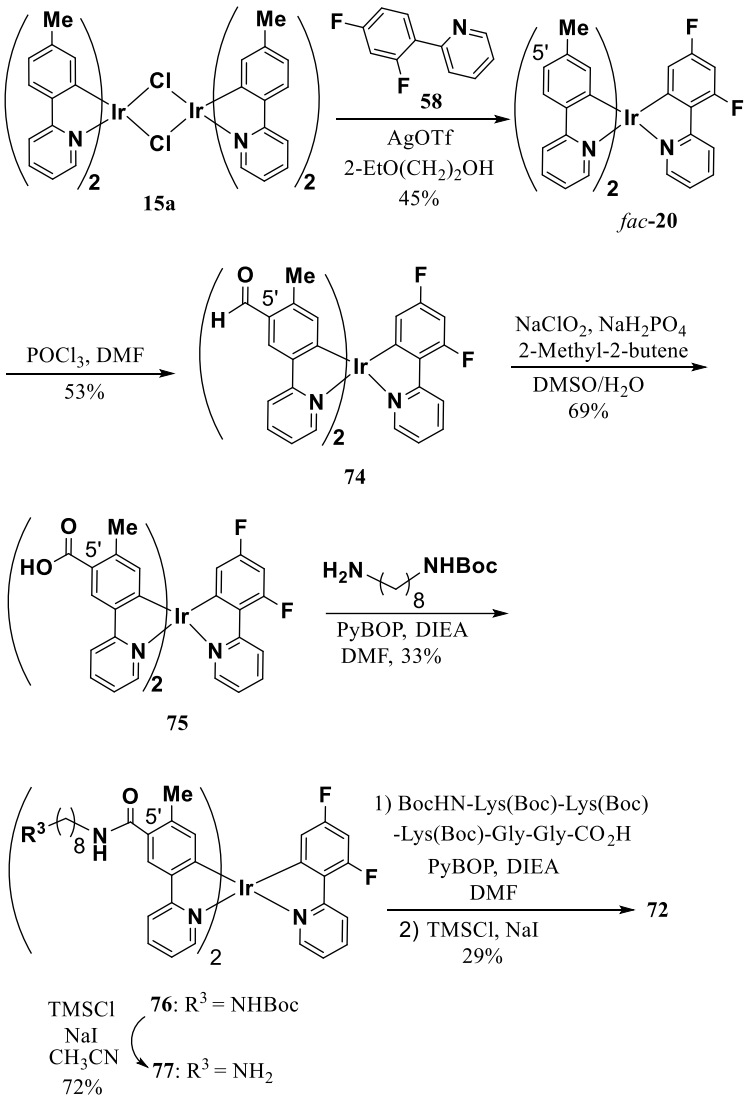

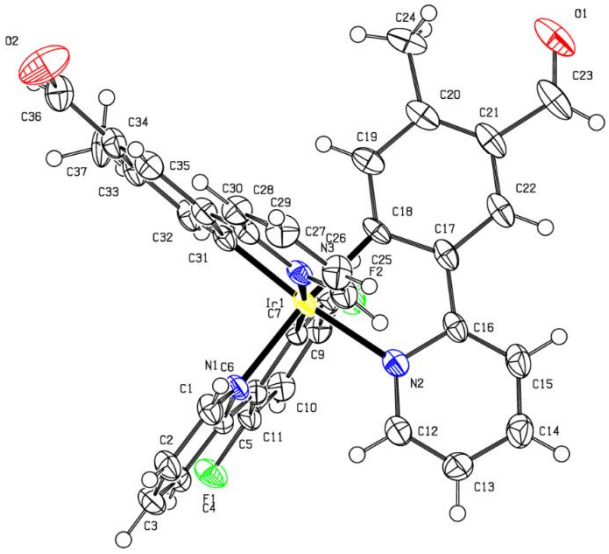

Figure 4-1. ORTEP drawing of single crystal structure of **74** with 50% probability ellipsoids.

Similarly, the cyclometalated Ir complex-monopeptide conjugate **73** was prepared from *fac*-**21** via **78-82** (Chart 4-3).[24] The structure of the intermediate **78** was previously reported by us[62] and that of **79** was also determined by a single crystal X-ray diffraction analysis, as shown in Figure 4-2 and Table 4-1. It should be noted that the diastereomers of **72** and **73** resulting from the racemic Ir centers (Δ and Λ forms) were not distinguished in the ^{1}H NMR spectra, and hence, were not separated.

Chart 4-3. Synthesis of bis-heteroleptic cyclometalated Ir(III) complex-peptide hybrid **73** that possess one cationic peptide unit.

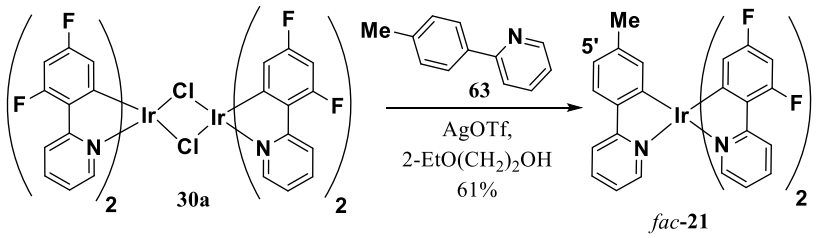

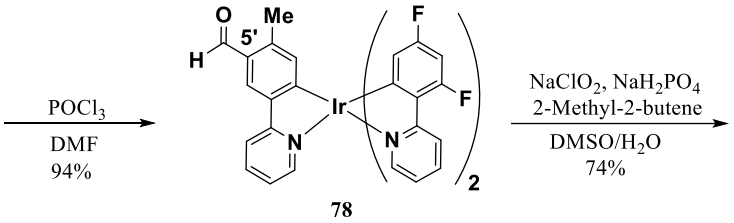

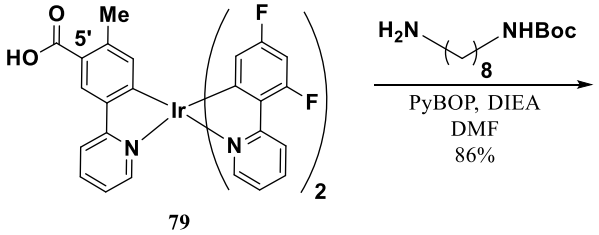

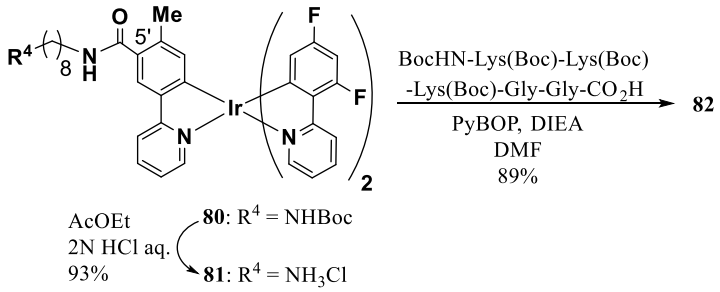

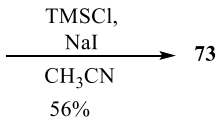

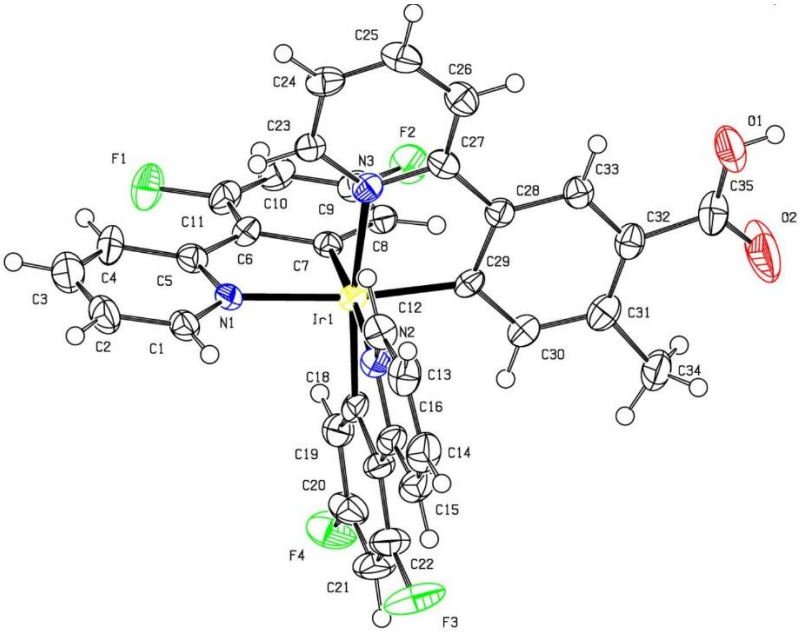

Figure 4-2. ORTEP drawing of molecular structure of **79** with 50% probability ellipsoids. The complex crystallizes with solvent which we could not identify unequivocally due to its partial occupancy and extended disorder. Eventually the solvent was SQUEEZE'd using PLATON.

Table 4-1. Crystal data and structure refinement for **74** and **79**.

	74	**79**
CCDC Deposition Number	2004202	2055929
Empirical formula	$C_{37}H_{26}F_2IrN_3O_2$	$C_{35}H_{22}F_4IrN_3O_2$
Formula weight	774.81	784.75
Temperature	293 K	123 K
Wavelength	0.71073 Å	0.71075 Å
Crystal system	Triclinic	Monoclinic
Space group	*P*-1	*C*2/*c*
Unit cell dimensions	a = 11.6449(2) Å	a = 44.975(7) Å
	b = 12.0042(1) Å	b = 9.0309(13) Å
	c = 15.4338(2) Å	c = 18.118(3) Å
	α = 81.793(1)°	α = 90°
	β = 84.931(1)°	β = 92.504(2)°
	γ = 74.780(1)°	γ = 90°
Volume	2057.54(5)Å^3	7352(2) Å^3
Z	2	4
Density (calcd.)	1.251 g cm^{-3}	0.709 g cm^{-3}
Absorption coefficient	3.282 mm^{-1}	1.841 mm^{-1}
F(000)	760	1528
Theta range for data collection	2.3 to 30.4°	3.2 to 27.5°
Index ranges	–16<=h<=16, –16<=k<=17, –22<=l<=22	–56<=h<=58, –11<=k<=11, –23<=l<=21
Reflections collected	50126	15279
Independent reflections	11234 [R(int) = 0.0330]	8397 [R(int) = 0.0437]
Completeness to theta = 27.496°	88.2 %	99.5 %
Absorption correction	Multi-scan	Multi-scan

Max. and min. transmission	0.789 and 1.000	0.778 and 1.000
Refinement method	Full-matrix least-square on F^2	Full-matrix least-square on F^2
Goodness-of-fit on F^2	0.585	0.791
Final R indices [I>2sigma(I)]	R_1 = 0.0327,	R_1 = 0.0383,
	wR_2 = 0.1186	wR_2 = 0.1051
R indices (all data)	R_1 = 0.0396,	R_1 = 0.0468,
	wR_2 = 0.1313	wR_2 = 0.1162

4-2-2 Photophysical Properties of IPHs 72 and 73

The UV/Vis absorption and fluorescence emission spectra of **72** and **73** (10 μM) in degassed 100 mM HEPES (4-(2-hydroxyethyl)-1-piperazineethanesulfonic acid) solution (pH 7.4) at 298 K are displayed in Figure 4-3 and relevant photophysical data are listed in Table 4-2. The UV-Vis spectra of the Ir complexes exhibited an absorption maxima at ca. 280 nm and ca. 355 nm, which correspond to a $^1\pi$–π^* transition of the cyclometalated ligands and spin-allowed singlet-to-singlet metal-to-ligand charge transfer (^{1}MLCT) transitions, spin-forbidden singlet-to-triplet (^{3}MLCT) transitions, and $^3\pi$–π^* transitions, as previously reported.[27a,g] Luminescence spectra of **72** and **73** exhibited an emission maxima at ca. 502 nm (Figure 4-3b) and the emission quantum yields (Φ) were determined to be 0.44 and 0.12, respectively, and their lifetimes were found to be 1.6 and 1.8 μs, respectively, as summarized in Table 4-2. The spectral results are consistent with those for previously reported cyclometalated Ir complexes.[27a,e,g,30a]

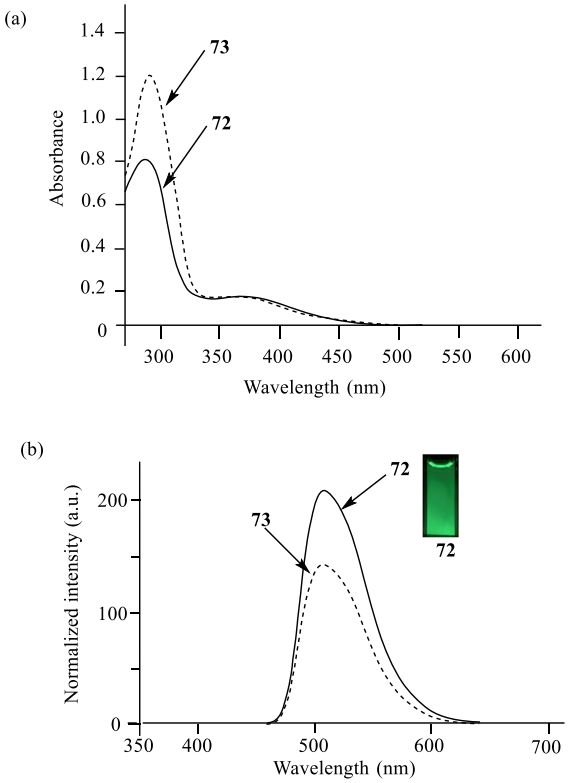

Figure 4-3. (a) UV/Vis absorption and (b) emission spectra of **72** (plain curve) and **73** (dashed curve) in degassed 100 mM HEPES (pH 7.4) at 25 ºC. [Ir complex] = 10 μM, excitation at λ = 366 nm. a.u. = arbitrary units. The photograph shows the emission image of **72** in 100 mM HEPES (pH 7.4) at 25 °C (excitation at λ = 366 nm).

Table 4-2. Photophysical properties of **2**, **71**, **72**, and **73** at [Ir complex] = 10 μM in degassed 100 mM HEPES (pH = 7.4) or CH_2Cl_2 at 25 ºC.

Compound	λ_{max} (absorption)	ε ($dm^3\ mol^{-1}\ cm^{-1}$)	λ_{max} (emission)	Φ	τ
2 (in CH_2Cl_2)[a]	287 nm, 373 nm	4.5×10^4, 1.2×10^4[b]	512 nm[c]	0.50	2.0 μs[b]
71[d]	280 nm, 360 nm	7.7×10^4, 1.4×10^4	507 nm[c]	0.41[e]	1.4 μs[f]
72	277 nm, 358 nm	8.2×10^4, 2.2×10^4	502 nm[c]	0.44[e]	1.6 μs[f]
73	278 nm, 352 nm	1.2×10^5, 2.0×10^4	498 nm[c]	0.12[e]	1.8 μs[f]

[a] Ref. 30a. [b] Ref. 8. [c] Excitation at 366 nm. [d] Ref. 27f. [e] Quinine sulfate in 0.1 M H_2SO_4 (Φ = 0.55) was used as a reference compound. [f] A 495 nm long wave pass filter was used.

4-2-3 Death of Cancer Cells Induced by 71–73.

The morphological features and fluorescence microscopic images of T-lymphocyte leukemia Jurkat cells treated with trispeptide- (**71**), bispeptide- (**72**), and monopeptide-hybrids (**73**) were observed by fluorescence microscopy. The Jurkat cancer cells were incubated with or without (as a control) **71–73** (25 μM) in Roswell Park Memorial Institute (RPMI) medium containing 10% fetal bovine serum (FBS) for 30 min or 1 h at 37 ºC under 5% CO_2, then collected by centrifugation, washed with PBS (phosphate buffer saline), and observed by fluorescence microscopy. The captured images suggest that **71** and **72** induce the death of Jurkat cancer cells and this is accompanied by considerable morphological changes and a strong green emission was detected in dead cells (Figure 4-4d-i for **71**, Figure 4-4j-o for **72**), while **73** weakly induced cell death (Figure 4-4p-u for **73**).

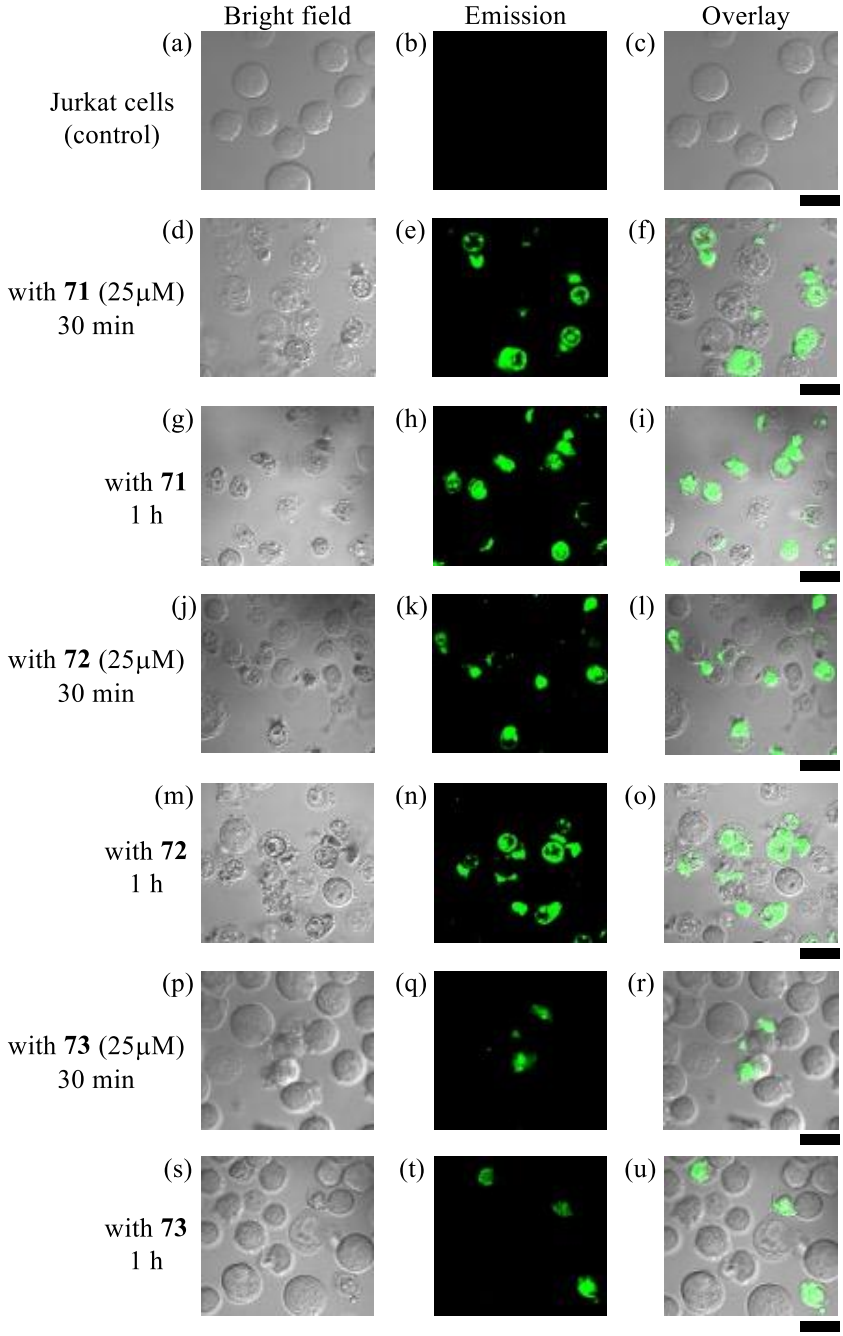

Figure 4-4. Representative luminescence microscopic images (Fluoview, FV-1000, Olympus) of Jurkat cells treated with **71**, **72,** and **73** (25 μM) complexes at 37 ºC for 30 min or 1 h, respectively. (a) Bright image of the control (in the absence of Ir complex), (b) emission image of the control, (c) overlay image of the control, (d) bright field image with **71** for 30 min, (e) emission image with **71** for 30 min, (f) overlay image with **71** for 30 min, (g) bright field image with **71** for 1 h, (h) emission image with **71** for 1 h, (i) overlay image with **71** for 1 h, (j) bright field image with **72** for 30 min, (k) emission image with **72** for 30 min, (l) overlay image with **72** for 30 min, (m) bright field image with **72** for 1 h, (n) emission image with **72** for 1 h, (o) overlay image with **72** for 1 h, (p) bright field image with **73** for 30 min, (q) emission image with **73** for 30 min, (r) overlay image with **73** for 30 min, (s) bright field image with **73** for 1 h, (t) emission image with **73** for 1 h, (u) overlay image with **73** for 1 h. Scale bar (black) denotes 10 μm.

4-2-4 Effect of the Number of Peptide Units in IPHs on cytotoxicity against Cancer (Jurkat, HeLa S3, and A549) and Normal (IMR90) Cell Lines

The cytotoxicities of Ir complexes **71–73** against Jurkat, HeLa S3 (human cervical), A549 (human lung) cancer, and IMR90 (human fetal lung) normal cell lines were evaluated by means of a 3-(4,5-dimethyl-2-thiazolyl)-2,5-diphenyl-2H-tetrazolium bromide (MTT) assay. Jurkat (2.0×10^4 cells/mL), HeLa S3 (1.5×10^4 cells/mL), A549 (1.5×10^4 cells/mL), and IMR90 (1.5×10^4 cells/mL) cells were incubated at 37 ºC for 24 h in 10% FBS/RPMI 1640 (Jurkat and IMR90), FBS/Eagle's Minimum Essential Medium (MEM) (HeLa S3), or FBS/Dulbecco's Modified Eagle Medium (DMEM) (A549) containing **71**, **72**, or **73** (0–25 μM or 0–50 μM). The plots of % of cell viability *versus* the concentration of the Ir complex are shown in Figure 4-5a–c, from which the half maximal effective concentration (EC_{50}) values of **71–73** against Jurkat cells were calculated to be 1.4 μM, 4.1 μM, and 16.3 μM, respectively. These results clearly indicate that a positive correlation exists between the number of H_2N–KKKGG peptide groups and the degree of cytotoxicity against Jurkat cells. In addition, the cytotoxicity of **71–73** is not so potent against HeLa S3 cells, A549 cells, and IMR90 cells (model of normal cells) (Figure 4-5b–d).

It was previously reported that celastrol, a naturally occurring triterpenoid, induces paraptosis with the swelling of the ER and/or mitochondria and an overload in the concentration of intracellular Ca^{2+}.[27e,f,63] The EC_{50} values of celastrol (Chart 4-4) against Jurkat, HeLa S3, and A549 cells were determined to be 0.5 μM (Jurkat), 26.9 μM (HeLa S3), and 40.5 μM (A459), respectively, as shown in Figure 4-5a–c and Table 4-3.

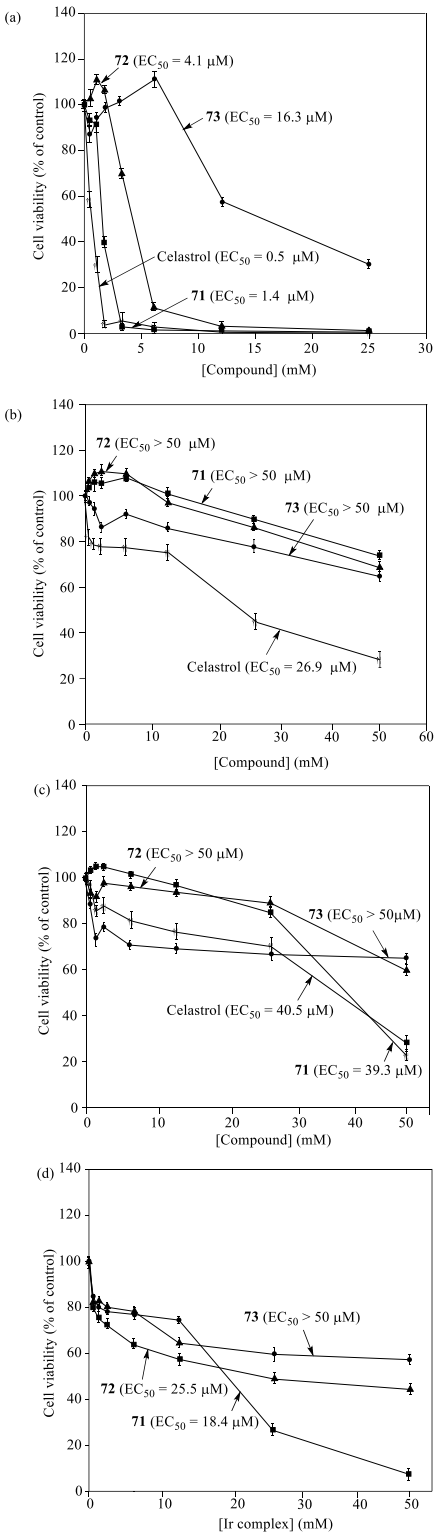

Figure 4-5. MTT assay results for (a) Jurkat cells, (b) HeLa S3 cells, (c) A459 cells, and (d) IMR90 normal cells treated with **71**, **72**, **73**, and celastrol in 10% FBS/RPMI (Jurkat and IMR-90 cells), 10% FBS/MEM (HeLa S3), or 10% FBS/DMEM (A459 cells) medium (incubation at 37 ºC for 24 h). The net charge of each Ir complex is assumed to be +12 (**71**), +8 (**72**), and +4 (**73**), respectively.

Chart 4-4. Chemical structure of celastrol.

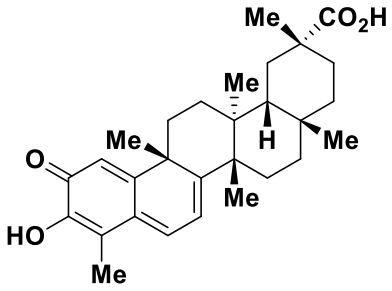

Celastrol

Table 4-3. The EC_{50} values of the Ir complexes **71**, **72**, **73**, and celastrol against Jurkat, HeLa S3, A549 cancer, and IMR90 normal cells.

Compound	Jurkat cells	HeLa S3 cells	A549 cells	IMR90 cells
71	1.4 μM	> 50 μM	39.2 μM	18.4 μM
72	4.1 μM	> 50 μM	> 50 μM	25.5 μM
73	16.3 μM	> 50 μM	> 50 μM	> 50 μM
Celastrol	0.5 μM	26.9 μM	40.5 μM	NT

NT = not tested

4-2-5 IPHs Induce Paraptotic Cell Death of Jurkat Cells

The programmed cell death (PCD) can be classified into several types, i.e., apoptosis (DNA fragmentation, chromatin condensation, blebbing, cell shrinkage, *etc*.,), autophagy (degradation of lysosomes), necroptosis (plasma membrane rupture or breakdown, swelling of organelles, *etc*.,), and paraptosis (cytoplasmic vacuolation involving the swelling of the ER and mitochondria, enhancement of intracellular Ca^{2+} concentration).[64-67] We previously reported that different types of IPHs induce different types of PCD in Jurkat cells.[27] More recently, we have reported that **71** and its analogs induce paraptosis-like cell death through cytoplasmic vacuolization by the damage of intracellular organelles (lysosomes, mitochondria, and the ER) and morphological changes in Jurkat cells, as confirmed by methylene blue staining and transmission electron microscopic (TEM) analyses,[27f] which are characteristic phenomena of paraptotic cell death.[68]

This background prompted us to determine whether vacuolization of cytoplasm and morphological changes of Jurkat cells treated with **71**, **72**, and celastrol had occurred. Jurkat cells were treated with **71**, **72** (25 μM, 1 h), or celastrol (1 μM, 24 h) and fixed with glutaraldehyde and osmium tetroxide (OsO_4), and then embedded in Poly 812 resin, which was sliced and stained for TEM analysis. The vacuolization of the cytoplasm in Jurkat cells shown in Figure 4-6 strongly suggest that these compounds induce similar PCD, which can be classified as paraptosis.[69]

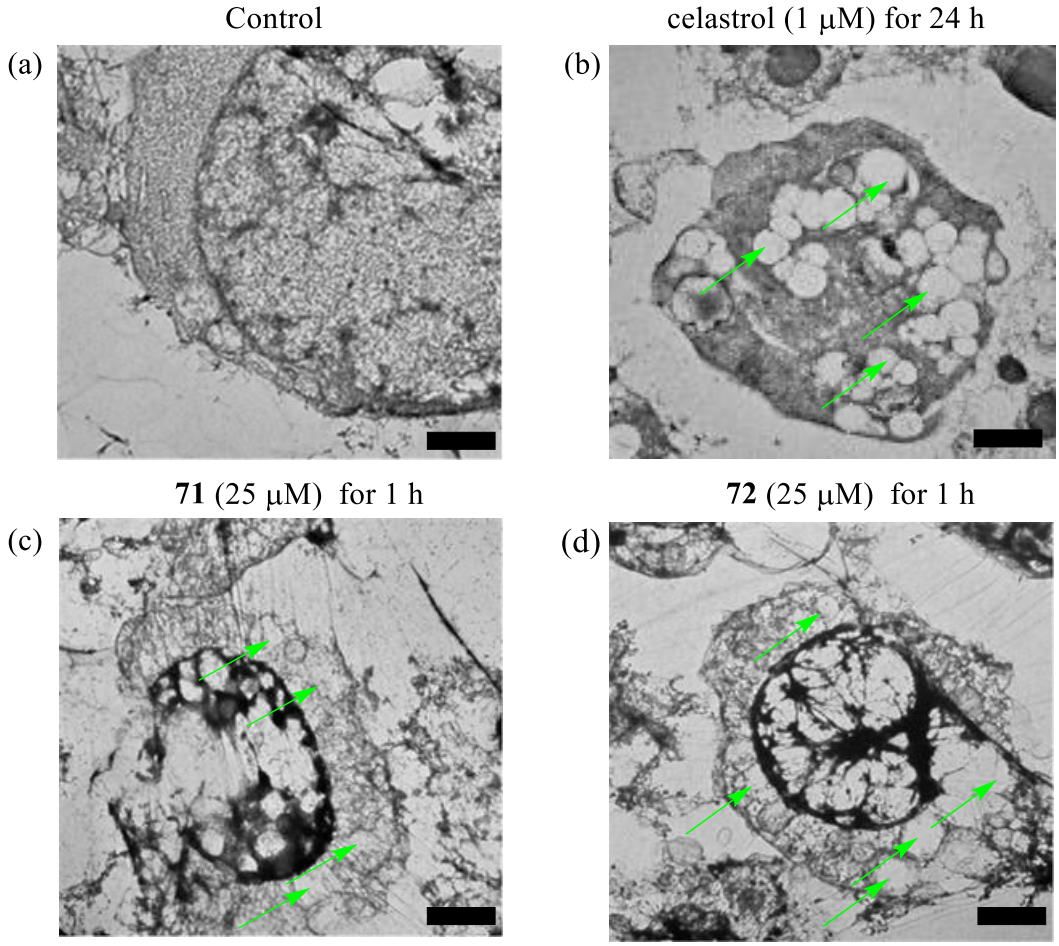

Figure 4-6. TEM images of Jurkat cells treated with (b) celastrol (1 μM, 24 h), (c) **71** (25 μM, 1 h) and (d) **72** (25 μM, 24 h) at 37 °C. Green arrows in (b), (c), and (d) show cytoplasmic vacuolization induced by **71** and **72**, respectively. Scale bar (black) = 2 μm.

4-2-6 Mitochondrial Ca^{2+} Overload Induced by 71 and 72

It is known that there is a relationship between intracellular Ca^{2+} signaling and paraptosis and other types of cell death.[63,70-74] The time-dependent enhancement in intracellular Ca^{2+} concentration was observed in fluorescence microscopic images when using Rhod-2/AM, which is a mitochondrial Ca^{2+} indicator, and Rhod-4/AM, a cytosolic Ca^{2+} indicator.[27a,f,g] The fluorescent intensity of Rhod-2 was enhanced in mitochondria compared to that of Rhod-4 in the cytosol (Figure 4-7a and 4-7b) within few minutes after the addition of **71** and **72 (**25 μM), and morphological changes were then observed in 30-60 minutes (see also Figure 4-8). In contrast, only a very weak emission was observed in the mitochondria (Figure 4-7a) and in the cytosol (Figure 4-7b) of the **73**–treated Jurkat cells.

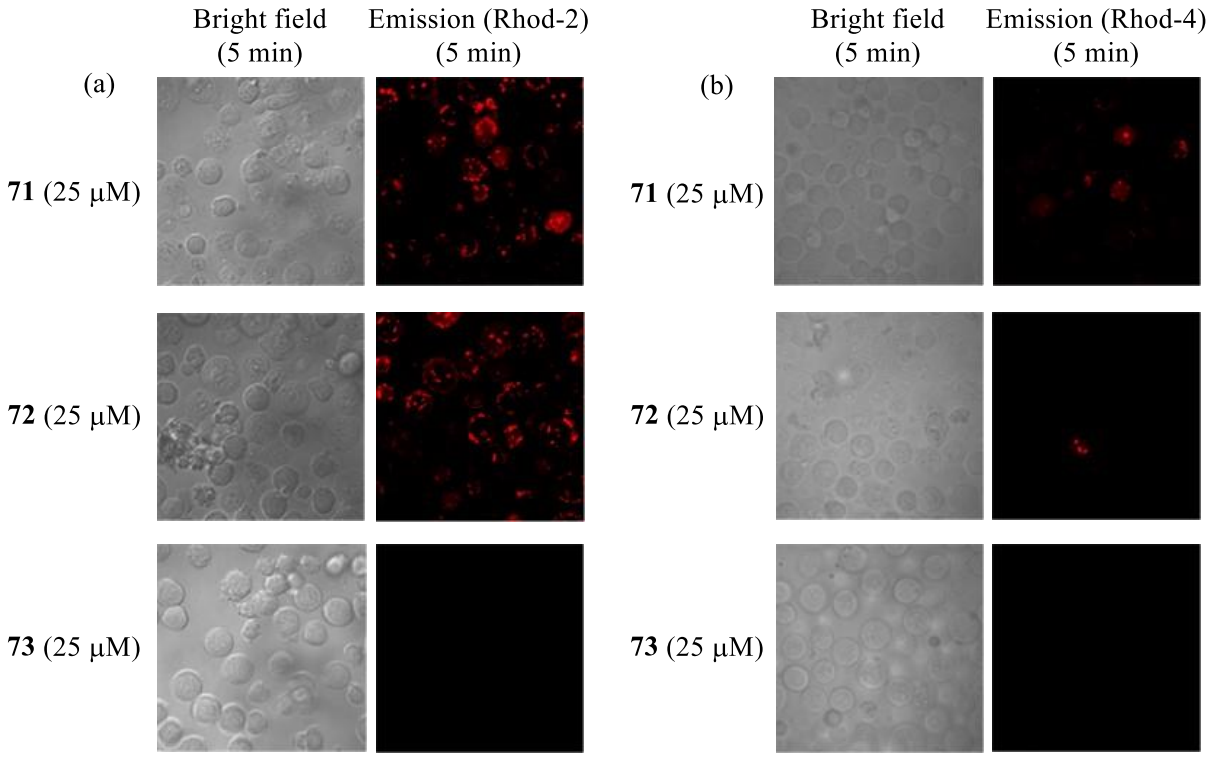

Figure 4-7. Representative luminescence confocal microscopic images of Jurkat cells treated with (a) Rhod-2 (red emission) and (b) Rhod-4 (red emission), followed by the treatment with **71–73** (25 μM for 5 min). Excitation at 540 nm for Rhod-2 and Rhod-4.

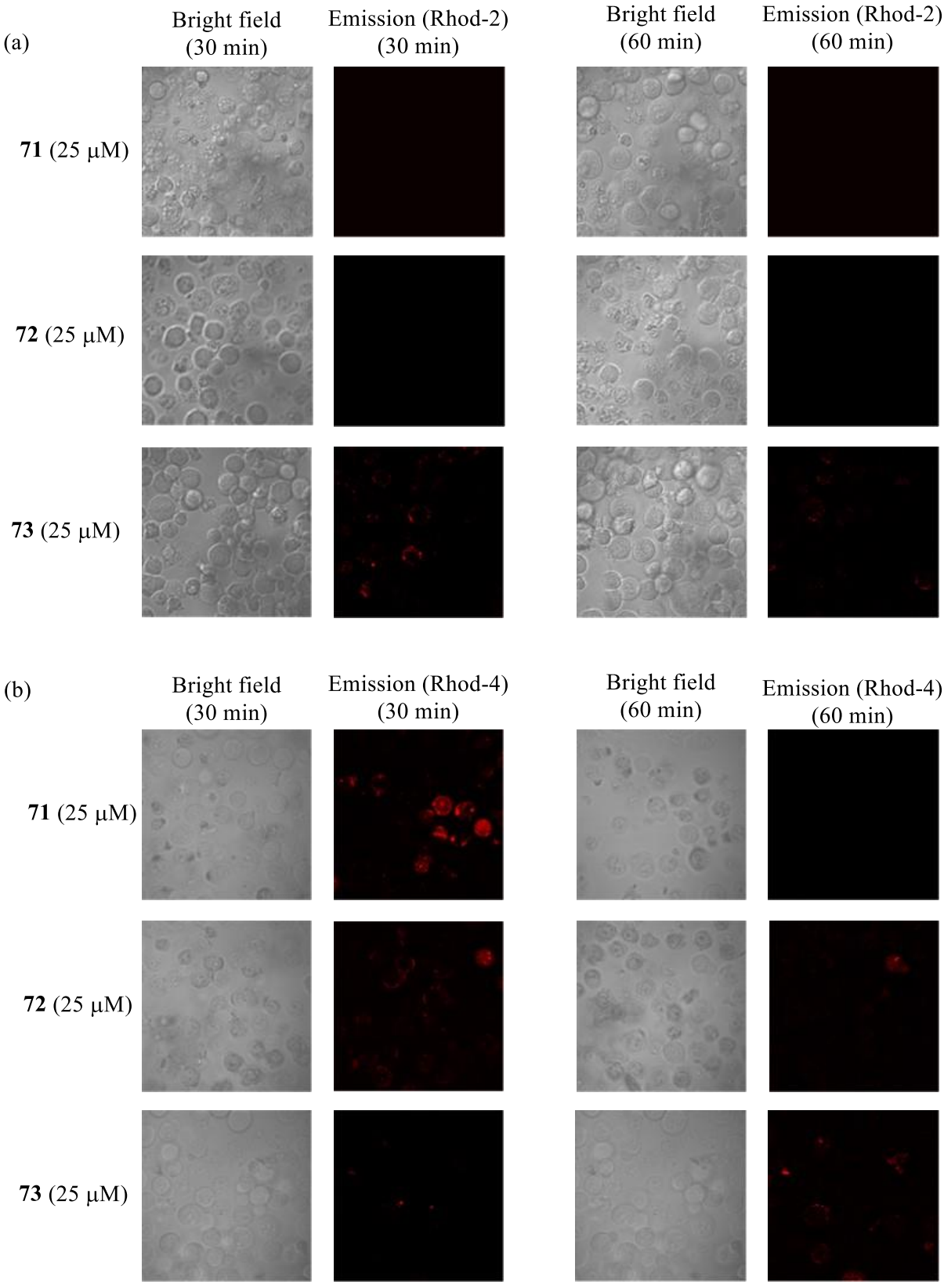

Figure 4-8. (a) Representative luminescence confocal microscopic images of Jurkat cells treated with Rhod-2 (red emission), followed by **71–73** (25 μM). (b) Representative luminescence confocal microscopic images of Jurkat cells treated with Rhod-4 (red emission), followed by **71–73** (25 μM). Excitation at 540 nm for Rhod-2 and Rhod-4.

Ca^{2+} concentrations in the cytosol and mitochondria were evaluated in more detail by means of flow cytometric analysis (Figure 4-9). Jurkat cells were pretreated with Rhod-4/AM or Rhod-2/AM for 30 minutes and then with **71**–**73** (25 μM) for specified amounts of time, after which the cells were immediately examined by flow cytometry. Figure 4-9a, 4-9c, and 4-9e present the emission intensity of Rhod-4 after the treatment with **71**–**73** for 0-60 min, and Figure 4-9b, 4-9d, and 4-9f display the emission changes in Rhod-2 after treatment with **71**–**73** for 0-60 min. Considerable enhancement in the red emission of Rhod-2 was induced by **71** and **72** (Figure 4-9b and 4-9d), respectively, while negligible enhancement was detected in the presence of **73** (Figure 4-9f). These results are nearly parallel to the anticancer activity of **71**–**73**, strongly suggesting the IPH–induced cell death is induced by an enhancement in Ca^{2+} concentration mainly in mitochondria. A weak correlation between the anticancer activity of **71–73** and the increase in Ca^{2+} concentrations in cytosol suggests the possible direct transfer of Ca^{2+} into mitochondria, possibly from the ER, which is a main Ca^{2+} reservoir in living cells. In contrast, celastrol induced a Ca^{2+} overload in the cytosol rather than in mitochondria, as shown in Figure 4-9g and4-9h. These data indicate that the paraptosis induced by **71–73** and celastrol proceeds *via* different mechanisms.

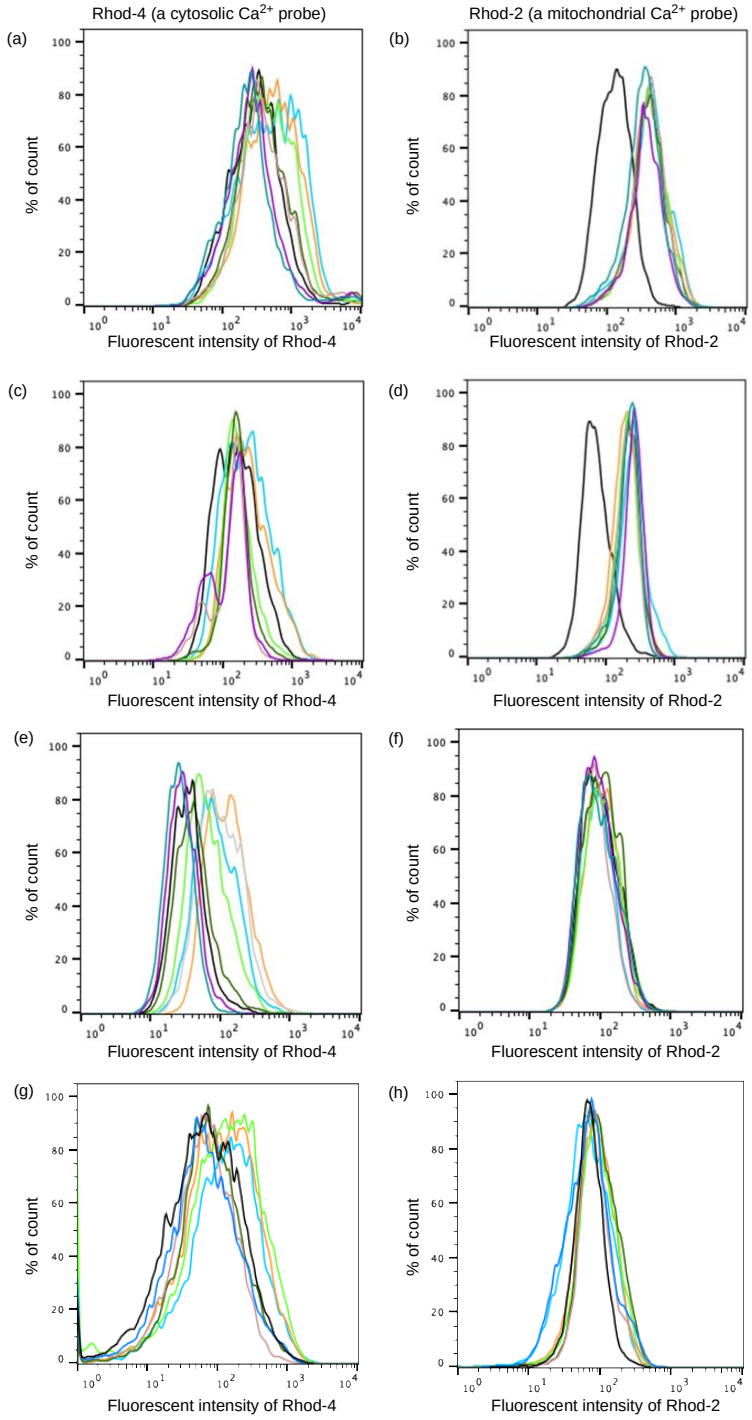

Figure 4-9. Flow cytometric analysis of Jurkat cells after the treatment with (a) Rhod-4 (5 μM) and **71** (25 μM), (b) Rhod-2 (5 μM) and **71** (25 μM), (c) Rhod-4 (5 μM) and **72** (25 μM), (d) Rhod-2 (5 μM) and **72** (25 μM), (e) Rhod-4 (5 μM) and **73** (25 μM), (f) Rhod-2 (5 μM) and **73** (25 μM), (g) Rhod-4 (5 μM) and celastrol (30 μM), and (h) Rhod-2 (5 μM) and celastrol (25 μM). Different colors correspond to the incubation time with **71–73** and celastrol: control (black), 5 min (light blue), 10 min (orange), 20 min (green), 30 min (dark green), 40 min (brown), 50 min (purple), 60 min (blue) in (a-f), respectively.

4-2-7 Co-staining of Jukat Cells with Ir(III) Complexes 71–73 and Fluorescence Probes for Intracellular Organelles

We next carried out co-staining experiments of Jurkat cancer cells with a mitochondria probe (MitoTracker Red), a lysosomal probe (LysoTracker Red), and an ER probe (ER-Tracker Red) in the presence or absence of **71–73** to examine their localization during the cell death process. In these experiments, Jurkat cells were treated with **71–73** (25 μM) for 30 min or 1 h, and then stained with MitoTracker Red (100 nM), LysoTracker Red (500 nM), or ER-Tracker Red (500 nM) at 37 ºC for 1 h.

Figure 4-10 shows confocal microscopic images (Fluoview, FV-1000, Olympus) of Jurkat cells treated with **71** and MitoTracker Red (Figure 4-10d-k), cells treated with **72** and MitoTracker Red **(**Figure 4-10l-s), and cells treated with **73** and MitoTracker Red (Figure 4-10t-aa), respectively (a green color emission from **71**–**73** indicates dead cells). Figure 4-11 shows confocal microscopic images of cells that had been treated with **71** and LysoTracker Red (Figure 4-11d-k), with **72** and LysoTracker Red **(**Figure 4-11l-s), and with **73** and LysoTracker Red (Figure 4-11t-aa), respectively. Figure 4-12 shows confocal microscopic images of cells treated with **71** and ER-Tracker Red (Figure 4-12d-k), with **72** and ER-Tracker Red **(**Figure 4-12l-s), and with **73** and ER-Tracker Red (Figure 4-12t-aa), respectively. Among these images, only Figures 4-10k and 4-10s show a yellow emission region resulting from overlay of the green emission of IPHs (**71** and **72)** and the red emission of MitoTracker, suggesting that **71** and **72** are localized mainly in mitochondria. In addition, a weak red emission of LysoTracker Red and ER-Tracker Red was observed in the presence of **71** and **72** (Figure 4-11j, 4-11k, 4-11r, and 4-11s for LysoTracker Red and Figure 4-12j, 4-12k, 4-12r, and 4-12s for ER-Tracker Red), suggesting the degradation (structural breakdown or disappearance) of lysosomes and the ER during the cell death process induced by these IPHs.

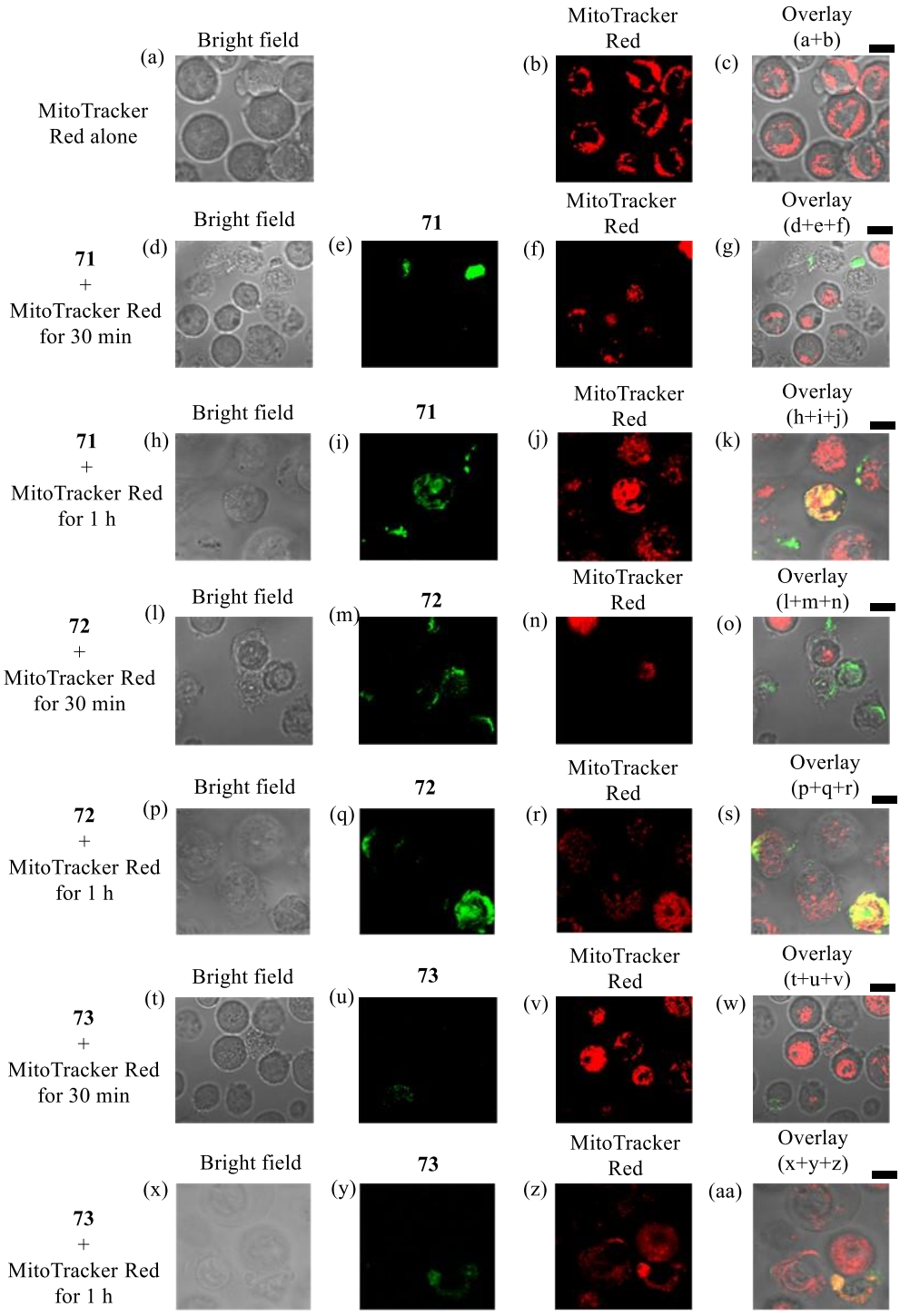

Figure 4-10. Representative luminescent confocal microscopic images (Fluoview, FV-1000, Olympus) of Jurkat cells incubated with **71**–**73** (25 μM) for 30 min or 1 h, followed by treatment with MitoTracker Red (100 nM, 1 h). (a), (d), (h), (l), (p), (t), and (x) Bright field images of Jurkat cells, (e) and (i) emission images with **71**, (m) and (q) emission images with **72**, and (u) and (y) emission images with **73**. (b), (f), (j), (n), (r), (v), and (z) Emission images with MitoTracker Red, (c) overlay image of (a) and (b), (g) overlay image of (d–f), (k) overlay image of (h–j), (o) overlay image of (l–n), (s) overlay image of (p–r), (w) overlay image of (t–v), and (aa) overlay image of (x–z). Excitation at 405 nm for (e), (i), (m), (q), (u), and (y) and 559 nm for (b), (f), (j), (n), (r), (v), and (z). Exposure time was 12.5 μs/pixel. Scale bar (black) = 10 μm.

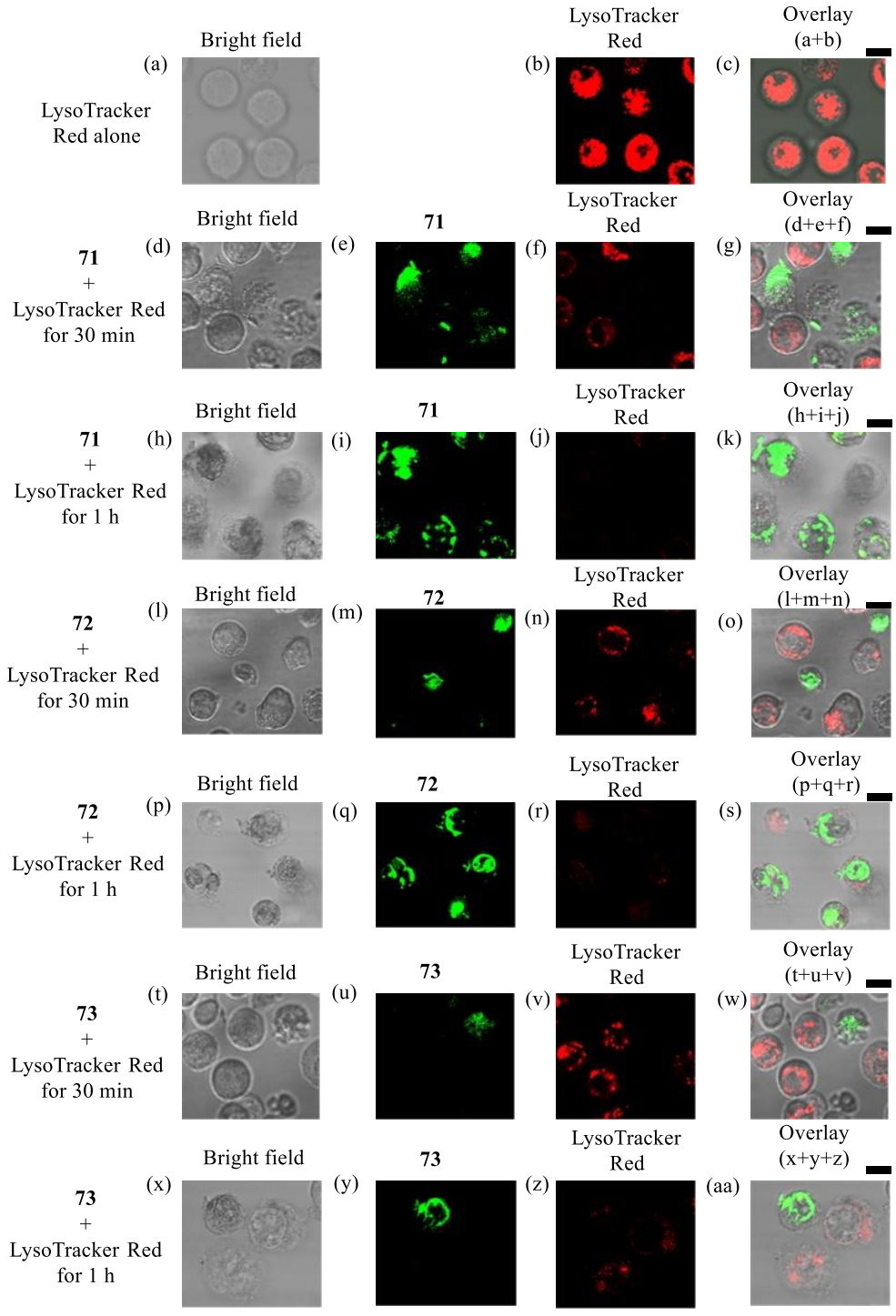

Figure 4-11. Representative luminescent confocal microscopic images (Fluoview, FV-1000, Olympus) of Jurkat cells incubated with **71**–**73** (25 μM) for 30 min or 1 h, followed by treatment with LysoTracker Red (500 nM, 1 h). (a), (d), (h), (l), (p), (t), and (x) Bright field images of Jurkat cells, (e) and (i) emission images with **71**, (m) and (q) emission images with **72** and (u) and (y) emission images with **73**. (b), (f), (j), (n), (r), (v), and (z) Emission images with LysoTracker Red, (c) overlay image of (a) and (b), (g) overlay image of (d–f), (k) overlay image of (h–j), (o) overlay image of (l–n), (s) overlay image of (p–r), (w) overlay image of (t–v), and (aa) overlay image of (x–z). Excitation at 405 nm for (e), (i), (m), (q), (u), and (y) and 559 nm for (b), (f), (j), (n), (r), (v), and (z). Exposure time was 12.5 μs/pixel. Scale bar (black) = 10 μm.

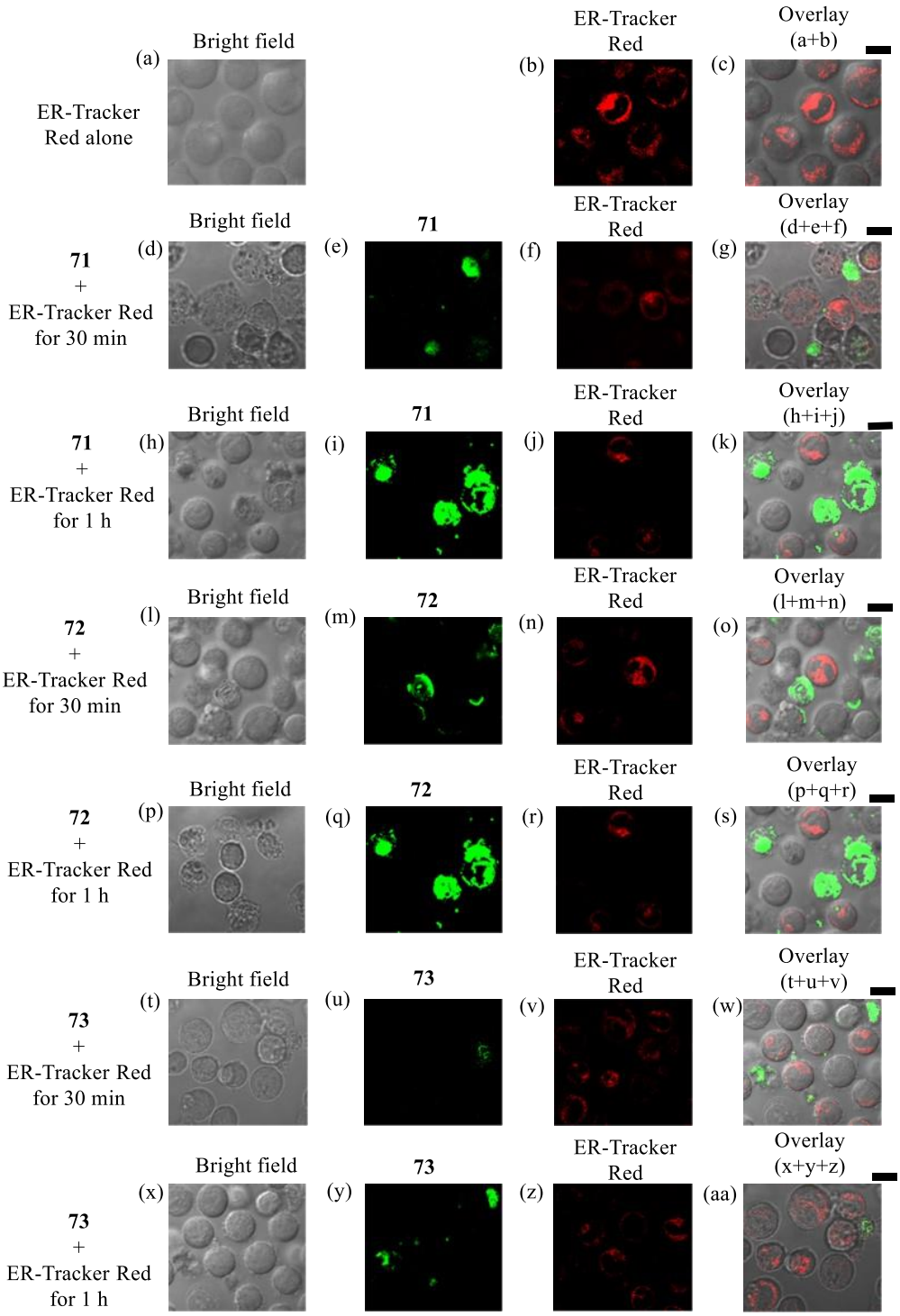

Figure 4-12. Representative luminescent confocal microscopic images (Fluoview, FV-1000, Olympus) of Jurkat cells incubated with **71–73** (25 μM) for 30 min or 1 h, followed by treatment with ER-Tracker Red (500 nM, 1 h). (a), (d), (h), (l), (p), (t), and (x) Bright field images of Jurkat cells, (e) and (i) emission images with **71**, (m) and (q) emission images with **72**, and (u) and (y) emission images with **73**. (b), (f), (j), (n), (r), (v), and (z) Emission images with ER-Tracker Red, (c) overlay image of (a) and (b), (g) overlay image of (d–f), (k) overlay image of (h–j), (o) overlay image of (l–n), (s) overlay image of (p–r), (w) overlay image of (t–v), and (aa) overlay image of (x–z). Excitation at 405 nm for (e), (i), (m), (q), (u), and (y) and 559 nm for (b), (f), (j), (n), (r), (v), and (z). Exposure time was 12.5 μs/pixel. Scale bar (black) = 10 μm.

4-2-8 Plausible Mechanism of Cell death Induced by IPHs

A plausible mechanism of the cell death of Jurkat cells induced by IPHs **71** and **72** is summarized in Figure 4-13 based on the aforementioned experimental results, as summarized below.

(1) IPHs containing three and two KKKGG peptide segments **71** and **72** induce the cell death of Jurkat cells stronger than the monopeptide conjugate **73**, as shown in Figures 4-5 and 4-6, indicating the existence of a positive relationship between the number of KKKGG chains and their cytotoxicity. In addition, a positive relationship between the cytotoxicity of **71**, **72**, and **73** against Jurkat cells and mitochondrial Ca^{2+} overload was observed (Figure 4-8 and 4-9).

(2) It is previously reported that cytotoxicity of IPHs having $Ir(tpy)_3$ core such as **70a-f** is dependent on the cationic charge and the peptide sequence as well as the linker length.[27a] In this work, however, the number of KKKGG sequence and the total cationic charge of **71**, **72**, and **73** are not separable. Therefore, we conclude that the cytotoxicity of **71**, **72**, and **73** is dependent on the number of KKKGG units and their net positive charge (+12 for **71**, +8 for **72**, and +4 for **73**).

(3) It is very likely that IPHs **71** and **72** induce paraptotic cell death in Jurkat cells, which is a newly recognized type of PCD,[66] as evidenced by cytoplasmic vacuolization (Figure 4-6) together with our previous results. Although metal complexes such as rhenium, copper, ruthenium, and titanium have been reported to induce paraptotic cell death in cancer cell lines,[75-81] our IPHs are the first example to induce the direct transfer of Ca^{2+} from the ER to mitochondria for the induction of paraptotic cell death in such a short incubation time (1 h). Very recently, the positive correlation between the increase in the intracellular uptake of IPHs and emission enhancement of IPHs in dead cells was discovered.[27f,j]

(4) IPHs **71** and **72** enhance the transfer of Ca^{2+} into mitochondria rather than to the cytosol possibly from the ER, which is an intracellular Ca^{2+}-storing organelle, at the early stage of cell death, as confirmed by confocal microscopic observations and flow cytometric analysis

using mitochondrial and cytosolic Ca^{2+} probes (Rhod-2 and Rhod-4, respectively) (Figures 4-8 and 4-9). In contrast, **73** induces only a negligible overload of mitochondrial Ca^{2+}. It was previously reported that the change in Ca^{2+} concentration in a culture medium negligibly changes the cell death induced by IPHs.[27a,g] These results suggest that the influx of Ca^{2+} into mitochondria possibly from the ER is one of the critical events for the induction of cell death in Jurkat cells.

(5) Celastrol, a naturally-occurring triterpenoid, also induces paraptosis (Figures 4-4 and 4-5). However, the paraptotic mechanism induced by celastrol is different from that by **71** and **72** (Figure 4-9). This difference may have some relationship with different cytotoxicity profiles of IPHs and celastrol against Jurkat, HeLa S3, A549, and IMR90 cells (Table 4-3).

(6) The findings of this study indicate that **71** and **72** are localized mainly in mitochondria (Figure 4-10) and induce the degradation (structural breakdown or disappearance) of the ER (Figure 4-11), as confirmed by co-staining experiments with MitoTracker Red and ER-Tracker Red, respectively. The relationship of mitochondria and ER with programmed cell death has been extensively discussed in the past.[82-86] We assume that **71** and **72** interact with biomolecules in/on mitochondria, the ER membrane or mitochondria-associated membranes (MAMs) to activate (or inactivate) some signaling pathways for the induction of mitochondria- and ER-related cell death.

(7) IPHs **71–73** induce the degradation of lysosomes during the cell death process (Figure 4-12). In our previous paper, we concluded that autophagy may not be a major pathway for the induction of paraptosis-like cell death, although lysosomal degradation and the upregulation of autophagy markers such as LC3, Beclin-1, and Atg-12 are induced by IPHs.[27f] Therefore, autophagy may not be a major cause for the induction of paraptosis-like cell death that is induced by IPHs **71** and **73**.

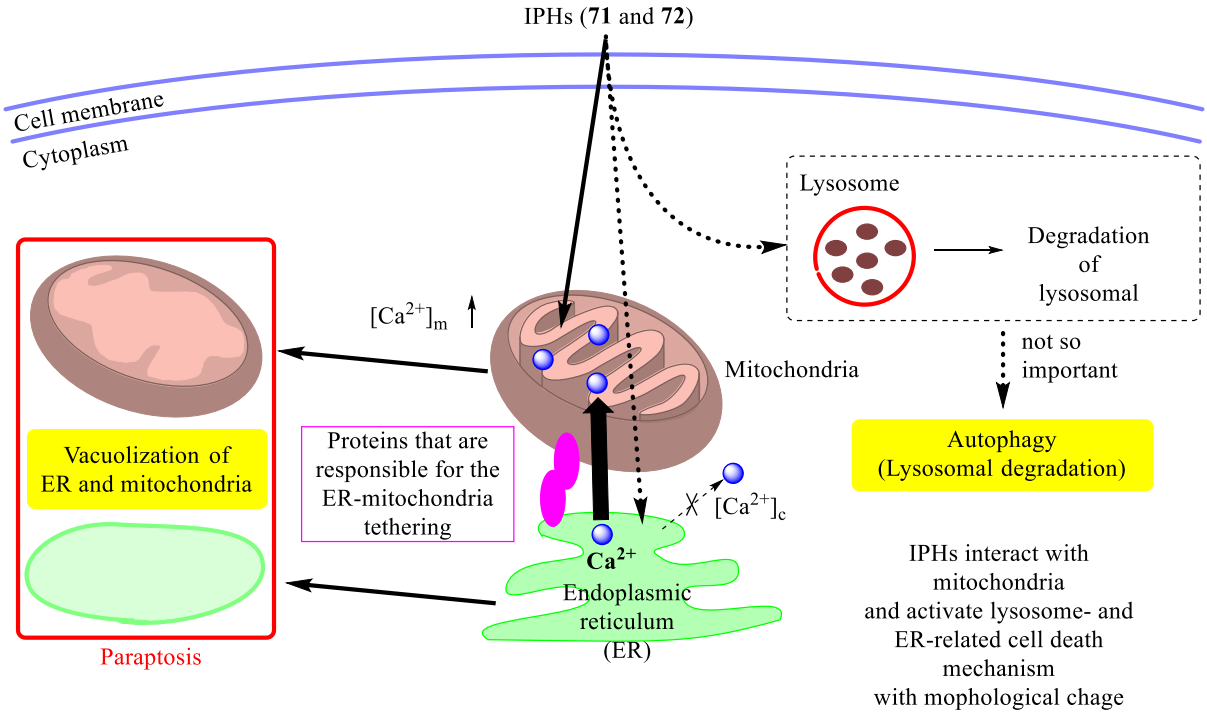

Figure 4-13. Proposed cell death mechanism for IPHs in Jurkat cancer cells.

4-3 Conclusions

In this study, bis(peptide) and mono(peptide) conjugates (**72** and **73**) of cyclometalted Ir(III) complexes were synthesized in addition to our previous tris(peptide) hybrid **71** and the effect of the number of H_2N-KKKGG chains in IPHs on their anticancer activity was examined. The new Ir complexes were extensively characterized by various spectroscopic and analytical methods including X-ray single crystal structure analysis of the synthetic intermediates. The prepared IPHs show a green emission with lifetimes are in the order of μs, which are due to phosphorescence from the excited triplet state.

The *in vitro* anticancer activity of IPHs, **71**, **72**, and **73**, against a panel of three cancer cell lines (Jurkat, HeLa S3, and A549) and one non-cancerous (IMR90) cell line was evaluated. The IPHs **71** and **72** exhibit potential anticancer activity against Jurkat cells and dead cells show a strong green emission. Complexes **71** and **72** show more potent activity towards Jurkat cancer cells, indicative of a positive relationship between the number of the KKKGG peptide chains and hence net cationic charges and their anticancer activity. Mechanistic studies of cell death suggest that **71**, **72**, and celastrol induce paraptotic cell death in Jurkat cells with the vacuolization of the cytoplasm, mitochondria, the ER, and lysosomes, as confirmed by TEM images of Jurkat cells, although the cell death mechanism between IPHs and celastol is different. The findings reported herein also strongly suggested that the direct transfer of Ca^{2+} from the ER to mitochondria is essential for the induction of cell death in Jurkat cells, as confirmed by fluorescent microscopic observations and flow cytometric analysis by using intracellular Ca^{2+} probes. The results of co-staining assays of **71**–**73** with probes that are specific for different intracellular organelles suggest that these IPHs are localized in mitochondria for the induction of paraptotic cell death in Jurkat cells. More detailed mechanistic studies regarding direct Ca^{2+} transfer from ER to mitochondria are currently underway.

These results provide useful information for the design and synthesis of metal complexes and other organic molecules containing a greater number of peptide units and their analogs as

potential anticancer agents in medicinal chemistry, bioinorganic chemistry, bioorganometallic chemistry, biomedical science, and other related research fields.

Chapter 5

Concluding Remarks

In this thesis, the efficient synthesis and photophysical properties of *tris-heteroleptic* Ir complexes represented by IrLL'A or IrLL'L'' and the biological applications of newly synthesized bis-heteroleptic Ir complexes IrL_2L' compared with homoleptic IrL_3 complexes are also reported.

In Chapter 2, the degradation reactions of tris-cyclometalated Ir complexes (IrL_3, L: cyclometalating ligand) promoted by Brønsted acids such as HCl/1,4-dioxane and Lewis acids such as ZnX_2 (X = Br or Cl), TMSCl, and $AlCl_3$ were reported. Among the various Lewis acids, $ZnBr_2$ exhibited a good reactivity for $Ir(ppy)_3$ **1**, $Ir(tpy)_3$ **2**, and $Ir(mppy)_3$ **12** to provide the corresponding halogen-bridged Ir dimers (μ-complexes). It was also found that the reactivity of tris-cyclometalated Ir complexes containing electron-withdrawing groups such as fluorine atoms, nitro or CF_3 groups on the ligands is quite low. This reaction was applied to the selective degradation of *mer*-tris-cyclometalated Ir complexes such as *mer*-$Ir(tpy)_2(F_2ppy)$ (***mer*-20**). The reaction of ***mer*-20** with $ZnBr_2$ gave a mixture of a halogen-bridged Ir dimer **15b** and **34b**, and the tris-heteroleptic Ir complex **25** (IrLL'A, A: ancillary ligand) was then obtained by treatment with acetylacetone. Furthermore, we successfully isolated a novel tris-heteroleptic Ir complex **42a** having a non-symmetric ancillary ligand after careful separation of its diastereomers. Mechanistic studies suggest that the formation of different products from some Ir complexes by H^+, TMSCl, and $AlCl_3$ and ZnX_2 is due to the hardness and softness of these Brønsted and Lewis acids used. The reactivity and selectivity in the ZnX_2-promoted degradation can be explained by the interaction of the HOMO of Ir complexes with the LUMO of ZnX_2 and by the difference of electronegativity of iridium and carbon in the ligand part. Further mechanistic study is now underway.

In Chapter 3, we report on the stereospecific synthesis of two single isomers of tris-heteroleptic tris-cyclometalated iridium(III) (Ir(III)) complexes consisting of three different nonsymmetric cyclometalating ligands via heteroleptic halogen-bridged Ir dimers $[Ir(tpy)(F_2ppy)(\mu\text{-}Br)]_2$ **34b** and $[Ir(mpiq)(F_2ppy)(\mu\text{-}Br)]_2$ **67b** (tpy: (2-(4'-tolyl)pyridine) and

F_2ppy: (2-(4',6'-difluorophenyl)pyridine), and mpiq: (1-(4'-methylphenyl)isoquinoline)) prepared by Zn^{2+}-promoted degradation reactions of Ir(tpy)$_2$(F_2ppy) **20** and Ir(mpiq)$_2$(F_2ppy) **23**, as reported by us. Subsequently, **34b** and **67b** was converted to the tris-heteroleptic tris-cyclometalated Ir complexes Ir(tpy)(F_2ppy)(mpiq) **66** consisting of tpy, F_2ppy, and mpiq, as confirmed by spectroscopic and X-ray crystal structure analysis. The important findings of this work are that: i) the specific isomers of tris-heteroleptic tris-cyclometalated such as **66a,b** and **66c,d** can be prepared from the different halogen-bridged Ir dimers **34b** and **67b**, while all the stereoisomers are composed of the same ligands. The mechanism of the formation of only two diastereomers from the μ-complex is discussed based on the X-ray crystal structures of **34b** and the product **66c**. The mechanism of the formation of only two diastereomers from the μ-complex is discussed based on the X-ray crystal structures of **34b** and the product **66c**. ii) each **66** isomers have different stability (in the presence of silica gel, in this work). iii) different stereoisomers of **66** exhibit different emission spectra. Namely, one stereoisomer **66a** exhibits single broad emission from *ca*. 550 nm to *ca*. 650 nm (orange emission), while another stereoisomer **66c** emits dual emission at *ca*. 509 nm and *ca*. 600 nm (pale pink emission). To the best of our knowledge, this is the first report on the selective and efficient synthesis, different stability and different photophysical properties of tris-heteroleptic tis-cyclometalated Ir(III) complexes.

In Chapter 4, bis(peptide) and mono(peptide) conjugates (**72** and **73**) of bis-heteroleptic cyclometalted Ir(III) complexes were synthesized in addition to our previous tris(peptide) hybrid **71** and the effect of the number of H_2N-KKKGG chains in IPHs on their anticancer activity was examined. The new Ir complexes were extensively characterized by various spectroscopic and analytical methods including X-ray single crystal structure analysis of the synthetic intermediates. The prepared IPHs show a green emission with lifetimes are in the order of μs, which are due to phosphorescence from the excited triplet state.

The *in vitro* anticancer activity of IPHs, **71**, **72**, and **73**, against a panel of three cancer cell lines (Jurkat, HeLa S3, and A549) and one non-cancerous (IMR90) cell line was evaluated. The IPHs **71** and **72** exhibit potential anticancer activity against Jurkat cells and dead cells show a strong green emission. Complexes **71** and **72** show more potent activity towards Jurkat cancer cells, indicative of a positive relationship between the number of the KKKGG peptide chains and hence net cationic charges and their anticancer activity. Mechanistic studies of cell death suggest that **71**, **72**, and celastrol induce paraptotic cell death in Jurkat cells with the vacuolization of the cytoplasm, mitochondria, the ER, and lysosomes, as confirmed by TEM images of Jurkat cells, although the cell death mechanism between IPHs and celastol is different. The findings reported herein also strongly suggested that the direct transfer of Ca^{2+} from the ER to mitochondria is essential for the induction of cell death in Jurkat cells, as confirmed by fluorescent microscopic observations and flow cytometric analysis by using intracellular Ca^{2+} probes. The results of co-staining assays of **71**–**73** with probes that are specific for different intracellular organelles suggest that these IPHs are localized in mitochondria for the induction of paraptotic cell death in Jurkat cells. More detailed mechanistic studies regarding direct Ca^{2+} transfer from ER to mitochondria are currently underway.

In conclusion, we have succeeded in the efficient synthesis and the measurements of photophysical properties of *tris-heteroleptic* Ir complexes represented by IrLL'A or IrLL'L'' and the biological applications of newly synthesized bis-heteroleptic Ir complexes IrL_2L' to compare with these properties with those of homoleptic IrL_3 complexes. These information of tris-heteroleptic tris-cyclometalated Ir complexes represents a potentially useful synthetic method for preparing not only Ir complexes but also other metal complexes. Moreover, the aforementioned results provide useful information for the design and synthesis of metal complexes and other organic molecules containing a greater number of peptide units and their analogs as potential anticancer agents in medicinal chemistry, bioinorganic chemistry, bioorganometallic chemistry, biomedical science, and other related research fields.

Experimental Section

General Information.

$IrCl_3 \cdot 3H_2O$ was purchased from KANTO CHEMICAL Co. Glycerol, AgOTf, and Trypsin was purchased from NACALAI TESQUE, INC. Anhydrous 1,2-dichloroethane was obtained by distillation from calcium hydride and 1,2-dichloroethane-d_4 was purchased from SIGMA-ALDRICH. Anhydrous *N*,*N*-dimethylformamide (DMF) was obtained by distillation from calcium hydride. All aqueous solutions were prepared using deionized and distilled water. MTT (3-(4,5-dimethyl-2-thiazolyl)-2,5-diphenyl-2*H*-tetrazolium bromide) was purchased from Dojindo. ^{1}H NMR spectra (300 MHz and 400 MHz) were recorded on a JEOL Always 300 spectrometer, a JEOL Lambda 400 spectrometer and IR spectra were recorded with a Perkin-Elmer FTIR Spectrum 100 (ATR). Luminescence imaging studies were performed using fluorescent microscopy (Biorevo, BZ-9000, Keyence). Electrospray ionization (ESI) mass spectra were recorded on a Varian 910-MS spectrometer. Mass of some tris-cyclometalated Ir complexes are observed as $[M]^+$ (rather than $[M+H]^+$) in ESI mode (Varian TQ-FT). Lyophilization was performed with freeze dryer FD-5N (EYELA). Thin-layer (TLC) and silica gel column chromatographies were performed using Merck 5554 (silica gel) TLC plates and Fuji Silysia Chemical FL-100D, respectively. Emission lifetimes were determined using a TSP-1000 spectrometer (Unisoku Co., Ltd.). Commercially available DMSO (spectrophotometric grade, WAKO CHEMICAL Co) was used for the measurement of photophysical data. Elemental analyses were performed on a Perkin-Elmer CHN 2400 series II CHNS/O analyzer. Elemental analyses of the Ir complexes, except for ***mer*-10** and **36** were not carried out because the metal and/or halogen contents of these compounds are >25%. GPC experiments were carried out using a system consisting of a POMP P-50 (Japan Analyrical Industry Co., Ltd.), a UV/VIS DETECTOR S-3740 (Soma, Japan), a Manual Sample Injector 7725i (Rheodyne, USA), a MDL-101 1 PEN RECORDER (Japan Analyrical Industry Co., Ltd.), equipped with two preparative GPC, JAIGEL-1H and JAIGEL-2 (Japan Analyrical Industry

Co., Ltd.) (20ϕ x 600 mm, No. A605201 and A605204) were used. HPLC experiments were carried out using a system consisting of two PU-980 intelligent HPLC pumps (JASCO, Japan), a UV-970 intelligent UV-visible detector (JASCO), a Rheodine injector (Model No. 7125) and a Chromatopak C-R6A (Shimadzu, Japan). For analytical HPLC, a SenshuPak Pegasil ODS column (Senshu Scientific Co., Ltd.) (4.6φ × 250 mm, No. 07051001) was used. For preparative HPLC, a SenshuPak Pegasil ODS SP100 column (Senshu Scientific Co., Ltd.) (20φ × 250 mm, No. 1302014G) was used. Density functional theory (DFT) calculations were also carried out using the Gaussian09 program[54] (B3LYP, the LanL2DZ basis set for a Ir and Br atoms and the 6-31G basis set for H, C, F, S, O, N atoms).[87] Time-dependent DFT (TD-DFT) calculations were carried out based on all the ground state geometries.[88] The chromaticity values obtained from emission spectra of Ir complexes were plotted on a color diagram using a ColorAC software.

Synthesis.

***fac*-1**,[8] ***mer*-1**,[8] ***fac*-2**,[8] ***mer*-2**,[8] ***fac*-3**,[8] ***mer*-3**,[8] ***fac*-12**,[27b] ***fac*-16**,[27a] ***fac*-17**,[28a] ***fac*-18**,[27a] ***fac*-19**,[28a] **6**,[55b] and **29b**[55b] were prepared in the form of a racemic mixture of Λ and Δ forms and their spectral data were in good agreement with reported data.

15b: A solution of ***fac*-2** (30 mg, 43 μmol) and $ZnBr_2$ (0.50 g, 2.2 mmol) in 1,2-dichloroethane (2.0 mL) was refluxed for 3 h. After cooling to room temperature, the insoluble materials were removed by filtration and the filtrate was concentrated under reduced pressure. The crude residue was purified by silica gel column chromatography using $CHCl_3$ as the eluent to give **15b** as a yellow powder (24 mg, 93% yield). mp > 300 ˚C. IR (ATR): ν = 1604, 1587, 1560, 1476, 1462, 1426, 1152, 1065, 769, 747, 664, 427 cm^{-1}. ^1H NMR (300 MHz, $CDCl_3/Si(CH_3)_4$) δ = 9.43 (d, *J* = 5.7 Hz, 4H), 7.82 (d, *J* = 6.9 Hz, 4H), 7.74 (td, *J* = 6.9, 1.2 Hz, 4H), 7.36 (d, *J* = 8.1 Hz, 4H), 6.81 (td, *J* = 6.3, 1.8 Hz, 4H), 6.55 (d, *J* = 7.2 Hz, 4H), 5.72 (s, 4H), 1.93 (s, 12H). ESI-MS (*m/z*). Calcd for $C_{48}H_{40}N_4{}^{81}Br_2{}^{191}Ir_2$ $[M]^+$: 1216.0782. Found: 1216.0841.

d_{12}-**15a:** A solution of **15a** (0.43 g, 0.38 mmol) in a mixture of 1,2-dichloroethane (8.0 mL) and DCl/D_2O (2.0 mL) was refluxed for 16 h. After cooling to room temperature, the solvent was removed imcompletely under reduced pressure and the insoluble materials was filtrated to give *d_{12}*-**15a** as a greenish yellow powder (0.30 g, 70% yield and deuteration rate is 92% determined by ^1H-NMR). mp > 300 ˚C. IR (ATR): ν = 3074, 2913, 2236, 2040, 1966, 1603, 1557,1471, 1440, 1397, 1372, 1336, 1304, 1264, 1237, 1160, 1035, 995, 967, 944, 887, 800, 764, 750, 717, 703, 667, 631, 565, 523, 505, 490, 456, 429, 416 cm^{-1}. ^1H NMR (300 MHz, $CDCl_3/Si(CH_3)_4$) δ = 9.16 (d, *J* = 5.7 Hz, 4H), 7.80 (d, *J* = 8.1 Hz, 4H), 7.70 (t, *J* = 7.2 Hz, 4H), 6.71 (t, *J* = 5.7 Hz, 4H), 1.93 (s, 12H).

***mer*-17:** A mixture of chloro-bridged Ir dimer [{Ir(mpiq)$_2$(μ-Cl)}$_2$] (**26a**) (prepared from 1-(4'-methylphenyl)isoquinoline (mpiq) and $IrCl_3 \cdot 3H_2O$ as shown in Chart 6) (0.20 g, 0.18 mmol), K_2CO_3 (0.56 g, 4.0 mmol) and mpiq (0.26 mg, 0.12 mmol) in glycerol (5.0 mL) was stirred at 150 °C for 8 h. After cooling to room temperature, water was added to the reaction mixture and extracted with $CHCl_3$. The combined organic layer was dried over Na_2SO_4 and filtered to obtain the filtrate, to which hexanes and CH_2Cl_2 were added to obtain ***mer*-17** as a red powder (0.13 g, 52% yield). mp 219-220 ˚C. IR (ATR): ν = 2917, 1580, 1499, 1438, 1347, 1311, 1269, 1206, 1146, 1120, 1040, 868, 811, 737, 672, 581, 418 cm^{-1}. ^{1}H NMR (300 MHz, $CDCl_3$/Si$(CH_3)_4$) δ = 8.99-8.87 (m, 3H), 8.20 (d, *J* = 8.4 Hz, 1H), 8.09 (t, *J* = 6.6 Hz, 3H), 7.70-7.56 (m, 10H), 7.52 (d, *J* = 6.3 Hz, 1H), 7.10 (d, *J* = 6.3 Hz, 1H), 6.97 (d, *J* = 6.9 Hz, 1H), 6.90 (d, *J* = 6.6 Hz, 1H), 6.85 (d, *J* = 8.1 Hz, 2H), 6.78 (d, *J* = 8.7 Hz, 1H), 6.74 (s, 1H), 6.47 (s, 1H), 6.32 (s, 1H), 2.13 (s, 3H), 2.11 (s, 3H), 2.09 (s, 3H). ESI-MS (*m/z*). Calcd for $C_{48}H_{36}N_3{}^{191}Ir$ $[M]^+$: 845.2510. Found: 845.2514. Anal. Calcd for $C_{48}H_{36}N_3Ir$: C, 68.06; H, 4.28; N, 4.96. Found: C, 67.70; H, 4.19; N, 4.89.

***fac*-20:** A solution of the F_2ppy ligand (0.15 g, 0.76 mmol), the chloro-bridged Ir dimer [{Ir(tpy)$_2$(μ-Cl)}$_2$] **15a** (0.20 g, 0.18 mmol), and AgOTf (90 mg, 0.35 mmol) in 2-ethoxyethanol (3.0 mL) was refluxed for 3 h. The yellow precipitate was filtrated on a filter and dried for 1 h. The combined bright yellow powder was purified by silica gel column chromatography using hexanes/CH_2Cl_2 (2/1) as the eluent to afford ***fac*-20** as a yellow powder (0.12 g, 46% yield). mp > 300 ˚C. IR (ATR): ν = 1597, 1554, 1470, 1397, 1264, 1237, 1159, 1098, 982, 829, 808, 769, 748, 725, 717, 567, 523, 429 cm^{-1}. ^{1}H NMR (300 MHz, $CDCl_3$/Si$(CH_3)_4$) δ = 8.26 (d, *J* = 8.4 Hz, 1H), 7.83 (dd, *J* = 7.8, 3.3 Hz, 2H), 7.62-7.50 (m, 6H), 7.44 (d, *J* = 5.4 Hz, 1H), 7.39 (d, *J* = 5.4 Hz, 1H), 6.88-6.79 (m, 3H), 6.73 (td, *J* = 7.2, 1.8 Hz, 2H), 6.64 (s, 1H), 6.61 (s, 1H), 6.39-

6.30 (m, 2H), 2.17 (s, 3H), 2.12 (s, 3H). ESI-MS (*m/z*). Calcd for $C_{35}H_{26}N_3F_2{}^{191}Ir$ $[M]^+$: 717.1695. Found: 717.1702.

***mer*-20:** A mixture of **20a** (0.20 g, 0.18 mmol), K_2CO_3 (0.25 g, 1.8 mmol) and the F_2ppy ligand (0.14 g, 0.72 mmol) in glycerol (5.0 mL) was stirred at 150 °C for 24 h. After cooling to room temperature, water was added to the reaction mixture and extracted with $CHCl_3$. The combined organic layer was dried over Na_2SO_4, filtered, and the resulting filtrate was concentrated under reduced pressure and then purified by silica gel column chromatography using hexanes/$CHCl_3$ (2/1) as the eluent to afford ***mer*-20** as a yellow powder (0.19 g, 74% yield). mp > 300 °C. IR (ATR): ν = 1588, 1552, 1466, 1420, 1392, 1281, 1262, 1231, 1158, 1095, 1054, 977, 872, 806, 769, 750, 717, 569, 522, 426 cm^{-1}. ^1H NMR (400 MHz, $CDCl_3/Si(CH_3)_4$) δ = 8.29 (d, *J* = 8.4 Hz, 1H), 8.00 (d, *J* = 6.0 Hz, 1H), 7.94 (d, *J* = 5.2 Hz, 1H), 7.75 (d, *J* = 8.0 Hz, 2H), 7.62-7.46 (m, 6H), 6.88 (t, *J* = 6.4 Hz, 1H), 6.78-6.68 (m, 4H), 6.39-6.33 (m, 3H), 6.18 (s, 1H), 2.14 (s, 3H), 2.12 (s, 3H). ESI-MS (*m/z*). Calcd for $C_{35}H_{26}N_3F_2{}^{191}Ir$ $[M]^+$: 717.1695. Found: 717.1696.

***fac*-21:** A solution of the tpy ligand (40 mg, 0.24 mmol), **30a** (0.10 g, 82 μmol), and AgOTf (78 mg, 0.30 mmol) in 2-ethoxyethanol (2.0 mL) was refluxed for 11 h. The yellow precipitate was dissolved in $CHCl_3$ and washed with water. The combined organic layer was dried over Na_2SO_4. After filtration, the solvent was concentrated under reduced pressure and the resulting residue was purified by silica gel chromatography using hexanes/$CHCl_3$ (10/1) as the eluent to give ***fac*-21** as a yellow powder (74 mg, 61% yield), IR (ATR): ν = 1596, 1565, 1555, 1471, 1396, 1282, 1236, 1158, 1098, 982, 823, 771, 746, 717, 566, 524, 419 cm^{-1}. ^1H NMR (300 MHz, $CDCl_3/Si(CH_3)_4$) δ = 8.29-8.27 (m, 2H), 7.85 (d, *J* = 8.7 Hz, 1H), 7.68-7.58 (m, 3H), 7.54 (d, *J* = 8.1 Hz, 1H), 7.50 (d, *J* = 5.7 Hz, 1H), 7.46 (d, *J* = 5.7 Hz, 1H), 7.34 (d, *J* = 6.6 Hz, 1H), 6.93-

6.83 (m, 3H), 6.74 (dd, *J* = 8.1, 1.2 Hz, 1H), 6.58 (s, 1H), 6.42-6.26 (m, 4H), 2.15 (s, 3H). ESI-MS (*m/z*). Calcd for $C_{34}H_{22}N_3F_4{}^{191}Ir$ $[M]^+$: 739.1350. Found: 739.1351.

***mer*-21:** A mixture of AgOTf (0.32 g, 1.2 mmol), chrolo-bridged Ir dimer [{Ir(F_2ppy)$_2$(μ-Cl)}$_2$] (0.30 g, 0.25 mmol), the tpy ligand (0.12 g, 0.75 mmol) and triethylamine (0.14 g, 0.75 mmol) in 1,2-dichloroethane (50 mL) was refluxed for 2 h. The mixture was then cooled to room temperature, and the precipitate was removed by filtration. The filtrate was evaporated under reduced pressure and purified by silica gel column chromatography using $CHCl_3$ as the eluent to afford ***mer*-21** as a yellow powder (0.26 g, 72% yield), mp > 300 ˚C. IR (ATR): ν = 1595, 1564, 1551, 1469, 1397, 1285, 1237, 1157, 1096, 981, 834, 807, 772, 749, 711, 566, 524 cm^{-1}. ^1H NMR (400 MHz, $CDCl_3$/Si(CH_3)$_4$) δ = 8.21-8.19 (m, 2H), 8.09 (d, *J* = 5.1 Hz, 1H), 7.89 (d, *J* = 8.1 Hz, 1H), 7.82 (d, *J* = 4.8 Hz, 1H), 7.65-7.50 (m, 5H), 6.89 (td, *J* = 6.0, 1.2Hz, 1H), 6.83 (dd, *J* = 7.5, 1.5 Hz, 1H), 6.75 (q, *J* = 7.5 Hz, 2H), 6.69 (s, 1H), 6.46-6.30 (m, 2H), 5.98 (dd, *J* = 6.9, 2.1 Hz, 1H), 5.81 (dd, *J* = 9.6, 2.1 Hz, 1H), 2.17 (s, 3H). ESI-MS (*m/z*). Calcd for $C_{34}H_{22}N_3F_4{}^{191}Ir$ $[M]^+$: 739.1350. Found: 739.1358.

***mer*-22: *mer*-22** was obtained as a yellow powder (67 mg, 17% yield) from [{Ir(mppy)$_2$(μ-Cl)}$_2$] (0.30 g, 0.25 mmol), K_2CO_3 (0.35 g, 2.5 mmol), glycerol (15 ml) and F_2ppy ligand (0.14 g, 0.76 mmol) using a precedure similar to that for ***mer*-20**. The product was purified by silica gel column chromatography with $CHCl_3$ as the eluent. mp > 300 ˚C. IR (ATR): ν = 1579, 1508, 1476, 1427, 1399, 1278, 1213, 1158, 1101, 1042, 984, 835, 768, 589, 567, 525, 420 cm^{-1}. ^1H NMR (300 MHz, $CDCl_3$/Si(CH_3)$_4$) δ = 8.30 (dd, *J* = 8.1, 2.1 Hz, 1H), 7.98-7.96 (m, 2H), 7.68-7.43 (m, 8H), 6.89 (t, *J* = 6.9 Hz, 1H), 6.71-6.63 (m, 2H), 6.56-6.34 (m, 4H), 6.10 (d, *J* = 2.7 Hz, 1H), 5.91 (d, *J* = 2.7 Hz, 1H), 3.62 (s, 3H), 3.58 (s, 3H). ESI-MS (*m/z*). Calcd for $C_{35}H_{26}N_3O_2F_2{}^{191}Ir$ $[M]^+$: 749.1593. Found: 749.1578.

***mer*-23: *mer*-23** was prepared as a red powder (0.20 g, 81% yield) from **25a** (0.20 g, 0.15 mmol), K_2CO_3 (0.42 g, 3.0 mmol), glycerol (5 mL) and F_2ppy ligand (0.22 g, 0.90 mmol) using a precedure similar to that for ***mer*-20**. The product was purified by silica gel column chromatography with hexanes/CH_2Cl_2 (2/1) as the eluent. mp 252-253 ˚C. IR (ATR): ν = 1583, 1554, 1500, 1470, 1440, 1391, 1348, 1264, 1231, 1159, 1148, 1122, 1096, 1043, 978, 867, 810, 751, 737, 717, 672, 579, 567, 522 cm^{-1}. ^1H NMR (300 MHz, $CDCl_3/Si(CH_3)_4$) δ = 8.98-8.89 (m, 2H), 8.31 (d, *J* = 8.1 Hz, 1H), 8.16 (d, *J* = 8.4 Hz, 1H), 8.11 (d, *J* = 8.1 Hz, 1H), 7.95 (d, *J* = 6.3 Hz, 1H), 7.78-7.73 (m, 3H), 7.66-7.57 (m, 5H) 7.43 (d, *J* = 6.3 Hz, 1H), 7.07-7.01 (m, 2H), 6.85-6.77 (m, 3H), 6.45-6.24 (m, 4H), 2.09 (s, 3H), 2.08 (s, 3H). ESI-MS (*m/z*). Calcd for $C_{43}H_{30}N_3F_2{}^{191}Ir$ $[M]^+$: 817.2008. Found: 817.2008.

***fac*-24:** A solution of the mpiq ligand (0.56 g, 2.6 mmol), **30a** (0.41 g, 0.34 mmol), and AgOTf (0.16 g, 0.63 mmol) in 2-ethoxyethanol (6.0 mL) was refluxed for 18 h. The orange precipitate was filtrated on a filter and dried for 1 h. The combined orange powder was purified by silica gel column chromatography using hexanes/$CHCl_3$ (1/1) as the eluent to afford ***fac*-30** as an orange powder (0.40 g, 75% yield). mp > 300 ˚C. IR (ATR): ν = 3081, 1972, 1599, 1567, 1556, 1504, 1472, 1445, 1431, 1397, 1351, 1283, 1265, 1238, 1160, 1100,981, 821, 807, 787, 750, 740, 717, 675, 578, 568, 525 cm^{-1}. ^1H NMR (300 MHz, $CDCl_3/Si(CH_3)_4$) δ = 8.95-8.92 (m, 1H), 8.29 (t, *J* = 9.3 Hz, 2H), 8.08 (d, *J* = 7.5 Hz, 1H), 7.78-7.75 (m, 1H), 7.69-7.58 (m, 4H), 7.47 (d, *J* = 5.4 Hz, 1H), 7.35 (d, *J* = 5.4 Hz, 1H), 7.29 (d, *J* = 6.0 Hz, 1H), 7.18 (d, *J* = 6.3 Hz, 1H), 6.92 (t, *J* = 6.0 Hz, 1H), 6.85-6.77 (m, 3H), 6.43-6.29 (m, 3H), 6.18 (dd, *J* = 9.6, 1.8 Hz, 1H), 2.21 (s, 3H). ESI-MS (*m/z*). Calcd for $C_{38}H_{24}N_3F_4{}^{191}Ir$ $[M]^+$: 789.1506. Found: 789.1511

***mer*-24:** The chloro-bridged Ir dimer [{Ir(F_2ppy)$_2$(μ-Cl)}$_2$] **30a** (0.10 g, 78 μmol), AgOTf (0.10 g, 0.39 mmol), triethylamine (23 mg, 0.24 mmol), the mpiq ligand (52 mg, 0.24 mmol) were reacted in 1,2-dichloroethane (15 mL) using a precedure similar to that for ***mer*-24**. The crude product was purified by silica gel column chromatography with hexanes/$CHCl_3$ (4/1) as the eluent to give ***mer*-24** as an orange powder (60 mg, 48% yield). mp > 300 °C. IR (ATR): ν = 1594, 1567, 1552, 1471, 1397, 1286, 1237, 1157, 1112, 1097, 1039, 981, 807, 783, 752, 740, 711, 676, 567, 524, 383 cm^{-1}. ^1H NMR (300 MHz, $CDCl_3$/$Si(CH_3)_4$) δ = 8.94-8.91 (m, 1H), 8.21-8.19 (m, 2H), 8.10 (d, *J* = 8.1 Hz, 1H), 8.06 (d, *J* = 5.7 Hz, 1H), 7.80-7.76 (m, 2H), 7.70-7.63 (m, 2H), 7.56-7.49 (m, 3H), 7.21 (d, *J* = 5.7 Hz, 1H), 6.90 (dd, *J* = 7.8, 1.5 Hz, 1H), 6.84 (s, 1H), 6.75-6.65 (m, 2H), 6.48-6.37 (m, 2H), 5.98 (dd, *J* = 8.1, 2.4 Hz, 1H), 5.81 (dd, *J* = 8.1, 2.4 Hz, 1H), 2.22 (s, 3H). ESI-MS (*m/z*). Calcd for $C_{38}H_{24}N_3F_4{}^{191}Ir$ $[M]^+$: 789.1507. Found: 789.1503.

d_6-**6**: a mixture of *d_{12}*-**15a** (10 mg, 8.6 μmol), tetrabutylammonium hydroxide (TBAH) (50 mg, 77 μmol) and acetylacetone (6.0 mg, 56 μmol) in CH_2Cl_2/MeOH (10/1, 1.1 mL) was refluxed for 1 h. After cooling to room temperature, water was added to the reaction mixture and the resulting solution was extracted with $CHCl_3$. The combined organic layer was dried over Na_2SO_4. After filtration, the solvent was concentrated under reduced pressure and the resulting residue was purified by silica gel chromatography using hexanes/CH_2Cl_2 (4/1) as the eluent to give *d_6*-**6** as a yellow powder (7.6 mg, 69%). IR (ATR): ν = 2918, 2161, 1723, 1606, 1574, 1517, 1473, 1423, 1395, 1358, 1308, 1259, 1223, 1202, 1156, 1068, 1042, 1017, 926, 871, 775, 750, 604, 586, 426 cm^{-1}. ^1H NMR (300 MHz, $CDCl_3$/$Si(CH_3)_4$) δ = 8.47 (d, *J* = 6.0 Hz, 2H), 7.79 (d, *J* = 7.8 Hz, 2H), 7.70 (td, *J* = 7.2, 1.5 Hz, 2H), 7.08 (td, *J* = 6.9, 1.5 Hz, 2H), 5.18 (s, 1H), 2.04 (s, 6H), 1.76 (s, 6H). ESI-MS (*m/z*). Calcd for $C_{29}{}^1H_{21}{}^2H_6N_2O_2F_2{}^{191}Ir$ $[M]^+$: 632.2049. Found: 632.2046.

25: A solution of ***mer*-20** (20 mg, 28 μmol) and $ZnBr_2$ (0.31 g, 1.4 mmol) in 1,2-dichloroethane (2.0 mL) was refluxed for 3 h. After cooling to room temperature, the insoluble materials were removed by filtration washing with $CHCl_3$ and the filtrate was concentrated under reduced pressure. The crude product was purified by silica gel column chromatography using $CHCl_3$ as the eluent to give the mixture of **15b** and **34b** (18 mg, quant. assuming that only **34b** was obtained) as a yellow powder.

As reported by Baranoff and co-workers,[36c] a mixture of **15b** and **34b** obtained above (18 mg, 14 μmol), tetrabutylammonium hydroxide (TBAH) (30 mg, 42 μmol) and acetylacetone (6.0 mg, 56 μmol) in CH_2Cl_2/MeOH (10/1, 1.1 mL) was refluxed for 1 h. After cooling to room temperature, water was added to the reaction mixture and the resulting solution was extracted with $CHCl_3$. The combined organic layer was dried over Na_2SO_4. After filtration, the solvent was concentrated under reduced pressure and the resulting residue was purified by silica gel chromatography using hexanes/CH_2Cl_2 (4/1) as the eluent to give **25** as a yellow powder (10 mg, 63% yield from ***mer*-20**). mp > 300 ˚C. IR (ATR): ν = 2923, 1579, 1508, 1477, 1399, 1101, 985, 836, 768, 587, 567, 422, 413 cm^{-1}. ^1H NMR (400 MHz, $CDCl_3$/$Si(CH_3)_4$) δ = 8.51 (dd, *J* = 6.4, 0.8 Hz, 1H), 8.40 (d, *J* = 5.6 Hz, 1H), 8.22 (d, *J* = 8.0 Hz, 1H), 7.80-7.68 (m, 3H), 7.43 (d, *J* = 7.6 Hz, 1H), 7.14 (td, *J* = 6.8, 1.2 Hz, 1H), 7.10 (td, *J* = 5.2, 1.2 Hz, 1H), 6.66 (dd, *J* = 8.0, 1.2 Hz, 1H), 6.28 (td, *J* = 10.8, 2.4 Hz, 1H), 6.00 (s, 1H), 5.71 (dd, *J* = 9.0, 2.4 Hz, 1H), 5.22 (s, 1H), 2.06 (s, 3H), 1.81 (s, 3H) , 1.79 (s, 3H). ESI-MS (*m/z*). Calcd for $C_{28}H_{23}N_2O_2F_2{}^{191}Ir$ $[M]^+$: 648.1328. Found: 648.1327.

26b: 26b was obtained as a red powder (25 mg, 98% yield) from ***fac*-17** (30 mg, 35 μmol) and $ZnBr_2$ (0.38 g, 1.7 mmol) using a precedure similar to that for **15b** (2.0 mL of 1,2-dichloroethane was used as the solvent). mp > 300 ˚C. IR (ATR): ν = 1585, 1501, 1444, 1378, 1348, 1271, 1148, 1124, 1045, 867, 812, 782, 738, 671, 579, 483, 414 cm^{-1}. ^1H NMR (300 MHz, $CDCl_3/Si(CH_3)_4$) δ = 9.22 (d, *J* = 6.3 Hz, 4H), 8.93 (d, *J* = 8.4 Hz, 4H), 8.00-7.93 (m, 8H), 7.82 (t, *J* = 7.2 Hz, 4H), 7.76 (t, *J* = 7.2 Hz, 4H), 6.70 (d, *J* = 6.0 Hz, 4H), 6.62 (d, *J* = 6.6 Hz, 4H), 5.85 (s, 4H), 1.86 (s, 12H). ESI-MS (*m/z*). Calcd for $C_{64}H_{48}N_4{}^{81}Br_2{}^{191}Ir_2$ $[M]^+$: 1416.1406. Found: 1416.1514.

***fac*-27:** A solution of ***fac*-2** (30 mg, 43 μmol) and $FeCl_3$ (58 mg, 2.2 mmol) in 1,2-dichloroethane (2.0 mL) was stirred at room temperature for 2 h. The solvent was removed by evaporation. The crude residue was purified by silica gel column chromatography using $CHCl_3$ as the eluent to give ***fac*-27** as a yellow powder (3.1 mg, 9% yield). mp > 300 ˚C. IR (ATR): ν = 1598, 1467, 1421, 1255, 1063, 1043, 882, 779, 741, 614 cm^{-1}. ^1H NMR (300 MHz, $CDCl_3/Si(CH_3)_4$) δ = 7.79 (d, *J* = 7.8 Hz, 3H), 7.59 (t, *J* = 9.0 Hz, 3H), 7.58 (s, 3H), 7.42 (d, *J* = 5.7 Hz, 3H), 6.86 (t, *J* = 5.7 Hz, 3H), 6.63 (s, 3H), 2.16 (s, 9H). ESI-MS (*m/z*). Calcd for $C_{36}H_{27}N_3{}^{35}Cl_3{}^{191}Ir$ $[M]^+$: 797.0871. Found: 797.0871.

30b: 30b was obtained as a yellow powder (12 mg, 55% yield) from ***mer*-3** (25 mg, 33 μmol) and $ZnBr_2$ (0.46 mg, 2.0 mmol) using a precedure similar to that for **15b** (2.0 mL of 1,2-dichloroethane was used as the solvent). mp > 300 ˚C. IR (ATR): ν = 1599, 1572, 1557, 1478, 1402, 1293, 1248, 11660, 1102, 988, 829, 782, 753, 715, 708, 568, 527 cm^{-1}. ^1H NMR (300 MHz, $CDCl_3/Si(CH_3)_4$) δ = 9.40 (d, *J* = 5.1 Hz, 4H), 8.33 (d, *J* = 8.4 Hz, 4H), 7.87 (td, *J* = 8.1, 1.8 Hz, 4H), 6.91 (td, *J* = 6.9, 0.9 Hz, 4H), 6.33 (td, *J* = 11.1, 2.1 Hz, 4H), 5.28 (dd, *J* = 9.3, 2.1 Hz, 4H). ESI-MS (*m/z*). Calcd for $C_{44}H_{24}N_4F_8{}^{81}Br_2{}^{191}Ir_2$ $[M]^+$: 1303.9406. Found: 1303.9467.

31b: 31b was obtained as a yellow powder (13 mg, 50% yield) from ***fac*-1** (30 mg, 46 μmol) and $ZnBr_2$ (0.51 g, 2.3 mmol) using a precedure similar to that for **15b** (2.0 mL of 1,2-dichloroethane was used as the solvent). mp > 300 ˚C. IR (ATR): ν = 1605, 1580, 1477, 1421, 1157, 1030, 754, 740, 732, 724, 670, 629, 420 cm^{-1}. ^1H NMR (300 MHz, $CDCl_3/Si(CH_3)_4$) δ = 9.51 (d, *J* = 5.4 Hz, 4H), 7.89 (d, *J* = 7.8 Hz, 4H), 7.78 (td, *J* = 7.2, 1.2 Hz, 4H), 7.48 (d, *J* = 7.8 Hz, 4H), 6.86 (td, *J* = 6.6, 1.5 Hz, 4H), 6.74 (td, *J* = 6.9, 1.2 Hz, 4H), 6.58 (td, *J* = 5.1, 1.5 Hz, 4H), 5.92 (d, *J* = 7.8 Hz, 4H). ESI-MS (*m/z*). Calcd for $C_{44}H_{32}N_4{}^{81}Br_2{}^{191}Ir_2$ $[M]^+$: 1160.0158. Found: 1160.0210.

d_4-**31a:** A solution of **31a** (37 mg, 34 μmol) in a mixture of 1,2-dichloroethane (2.0 mL) and DCl/D_2O (0.5 mL) was refluxed for 2 h. After cooling to room temperature, the solvent was removed incompletely under reduced pressure and the insoluble materials was filtrated to give *d_4*-**31a** as a greenish yellow powder (22 mg, 61% yield and deuteration rate is 99% determined by ^1H-NMR). mp > 300 ˚C. IR (ATR): ν = 3041, 2250, 1951, 1604, 1561, 1475, 1425, 1407, 1365, 1287, 1267, 1192, 1158, 1086, 1057, 1020, 969, 873, 804,752, 725, 662, 648, 624, 561 cm^{-1}. ^1H NMR (300 MHz, $CDCl_3/Si(CH_3)_4$) δ = 9.24 (d, *J* = 5.7 Hz, 4H), 7.86 (d, *J* = 7.2 Hz, 4H), 7.73 (t, *J* = 6.6 Hz, 4H), 6.79-6.73 (m, 8H), 6.56 (t, *J* = 7.5 Hz, 4H), 5.93 (t, *J* = 7.5 Hz, 4H).

32b: 32b was obtained as a yellow powder (20 mg, 80% yield) from ***fac*-12** (30 mg, 40 μmol) and $ZnBr_2$ (0.45 g, 2.0 mmol) using a precedure similar to that for **15b** (2.0 mL of 1,2-dichloroethane was used as the solvent). mp > 300 ˚C. IR (ATR): ν = 1581, 1547, 1459, 1425, 1277, 1209, 1158, 1033, 769, 748, 586 cm^{-1}. ^1H NMR (300 MHz, $CDCl_3/Si(CH_3)_4$) δ = 9.44 (d, *J* = 6.3 Hz, 4H), 7.76-7.68 (m, 8H), 7.41 (d, *J* = 8.7 Hz, 4H), 6.77 (td, *J* = 6.3, 1.8 Hz, 4H), 6.35

(dd, *J* = 8.4, 2.4 Hz, 4H), 5.43 (d, *J* = 2.7 Hz, 4H), 3.41 (s, 12H). ESI-MS (*m/z*). Calcd for $C_{48}H_{40}N_4O_4{}^{81}Br_2{}^{191}Ir_2$ $[M]^+$: 1280.0578. Found: 1280.0628.

d_{12}-**32a:** A solution of **32a** (36 mg, 25 μmol) in a mixture of 1,2-dichloroethane (2.0 mL) and DCl/D_2O (0.5 mL) was refluxed for 6 h. After cooling to room temperature, the solvent was removed incompletely under reduced pressure and the insoluble materials was filtrated to give *d_4*-**27a** as a greenish yellow powder (28 mg, 93% yield and deuteration rate is 99% determined by ^{1}H-NMR). mp > 300 ˚C. IR (ATR): ν = 2931, 2853, 2581, 2278, 2161, 2038, 1604, 1559, 1528, 1474, 1459, 1389, 1345, 1312, 1280, 1265, 1200, 1152, 1031, 977, 887, 848, 800, 772, 752, 690, 573 cm^{-1}. ^{1}H NMR (300 MHz, $CDCl_3/Si(CH_3)_4$) δ = 9.17 (d, *J* = 5.7 Hz, 4H), 7.74-7.60 (m, 8H), 6.68 (t, *J* = 7.5 Hz, 4H), 3.40 (s, 12H).

33: 33 was obtained as a yellow powder (20 mg, 83% yield) from ***fac*-16** (30 mg, 32 μmol) and $ZnBr_2$ (0.36 g, 1.6 mmol) using a precedure similar to that for **15b** (2.0 mL of 1,2-dichloroethane was used as the solvent). mp > 300 ˚C. IR (ATR): ν = 1606, 1574, 1558, 1471, 1422, 1358, 1267, 1221, 1156, 1068, 1039, 1016, 866, 776, 748, 604, 422 cm^{-1}. ^{1}H NMR (300 MHz, $CDCl_3/Si(CH_3)_4$) δ = 9.41 (d, *J* = 5.7 Hz, 4H), 7.82-7.77 (m, 8H), 7.62 (s, 4H), 6.89-6.85 (m, 4H), 5.69 (s, 4H), 1.98 (s, 12H). ESI-MS (*m/z*). Calcd for $C_{48}H_{36}N_4{}^{79}Br_4{}^{81}Br_2{}^{191}Ir_2$ $[M]^+$: 1527.7238. Found: 1527.7202.

34b: A solution of **20** (30 mg, 42 μmol) and $ZnBr_2$ (0.58 g, 2.6 mmol) in $ClCH_2CH_2Cl$ (2.0 mL) was refluxed for 3 h. After cooling to room temperature, the solvent was concentrated under reduced pressure. The acetone and water were added to the crude reside and sonicated for 10 min. The yellow precipitate was filtered on and dried, to which was added a mixture of hexanes and CH_2Cl_2 to give **34b** as a yellow crystaline powder (18 mg, 68% yield). mp > 300

°C. IR (ATR): ν = 1602, 1569, 1557, 1477, 1463, 1427, 1162, 1104, 986, 835, 751, 566, 527, 429 cm^{-1}. ^1H NMR (300 MHz, $CDCl_3/Si(CH_3)_4$) δ = 9.48 (m, 2H), 9.36 (m, 2H), 8.28 (d, *J* = 6.9 Hz, 4H), 7.87-7.75 (m, 6H), 7.40 (d, *J* = 3.9 Hz, 1H), 7.37 (d, *J* = 3.9 Hz, 1H), 6.90-6.84 (m, 4H), 6.63 (d, *J* = 3.9 Hz, 1H), 6.60 (d, *J* = 2.1 Hz, 1H), 6.27 (tt, *J* = 10.5, 2.7 Hz, 2H), 5.63 (s, 1H), 5.62 (s, 1H), 5.37 (dt, *J* = 9.3, 3.0 Hz, 2H), 1.96 (s, 3H), 1.95 (s, 3H). ESI-MS (*m/z*). Calcd for $C_{46}H_{32}N_4F_4{}^{81}Br_2{}^{191}Ir_2$ $[M]^+$: 1260.0094. Found: 1260.0149.

35 and **36**: **35** (yellow powder, 9.1 mg, 54% yield) and **36** (yellow powder, 2.0 mg, 13% yield) was obtained from ***mer*-22** (20 mg, 27 μmol), $ZnBr_2$ (0.30 g, 1.3 mmol), acetylacetone (6.0 mg, 54 μmol) and tetrabutylammonium hydroxide (TBAH) (25 mg, 40 μmol) using a procedure similar to that for **25**. The product was purified by silica gel column chromatography with hexanes/CH_2Cl_2 (4/1) as the eluent.

35: mp 261-263 °C. IR (ATR): ν = 2925, 1579, 1508, 1476, 1399, 1278, 1213, 1158, 1101, 1042, 984, 835, 768, 588, 567, 525, 420, 412 cm^{-1}. ^1H NMR (300 MHz, $CDCl_3/Si(CH_3)_4$) δ = 8.51 (dd, *J* = 5.4, 1.2 Hz, 1H), 8.36 (d, *J* = 5.7 Hz, 1H), 8.22 (d, *J* = 7.8 Hz, 1H), 7.75-7.69 (m, 3H), 7.50 (d, *J* = 8.7 Hz, 1H), 7.14 (td, *J* = 6.3, 1.2 Hz, 1H), 7.08 (td, *J* = 6.3, 2.1 Hz, 1H), 6.66 (dd, *J* = 8.0, 1.2 Hz, 1H), 6.28 (td, *J* = 10.8, 2.4 Hz, 1H), 5.72 (dd, *J* = 8.7, 2.7 Hz, 1H), 5.69 (d, *J* = 2.7 Hz, 1H), 5.20 (s, 1H), 3.55 (s, 3H), 1.80 (s, 3H), 1.79 (s, 3H). ESI-MS (*m/z*). Calcd for $C_{28}H_{23}N_2O_3F_2{}^{191}Ir$ $[M]^+$: 664.1277. Found: 664.1282.

36: mp > 300 °C. IR (ATR): ν = 2923, 1579, 1508, 1477, 1399, 1101, 985, 836, 768, 587, 567, 422, 413 cm^{-1}. ^1H NMR (300 MHz, $CDCl_3/Si(CH_3)_4$) δ = 8.43 (d, *J* = 5.4 Hz, 2H), 7.72-7.63 (m, 4H), 7.47 (d, *J* = 8.7 Hz, 2H), 7.04 (td, *J* = 6.3, 1.8 Hz, 2H), 6.40 (dd, *J* = 8.7, 2.4 Hz,

2H), 5.77 (d, *J* = 2.7 Hz, 2H), 5.20 (s, 1H), 3.53 (s, 6H), 1.78 (s, 6H). ESI-MS (*m/z*). Calcd for $C_{29}H_{27}N_2O_4{}^{191}Ir$ $[M]^+$: 658.1571. Found: 658.1578.

37: **37** was prepared as an orange powder (12 mg, 67% yield from ***mer*-23**) from ***mer*-23** (20 mg, 24 μmol), $ZnBr_2$ (0.27 g, 1.2 mmol), acetylacetone (6.0 mg, 54 μmol) and tetrabutylammonium hydroxide (TBAH) (25 mg, 40 μmol) using a precedure similar to that for **25**. The product was purified by silica gel column chromatography with hexanes/CH_2Cl_2 (2/1) as the eluent. mp > 300 °C. IR (ATR): ν = 1566, 1557, 1515, 1391, 1290, 1265, 1245, 1100, 985, 835, 813, 782, 753, 737, 714, 672, 588, 574, 567, 526 cm^{-1}. ^1H NMR (300 MHz, $CDCl_3$/$Si(CH_3)_4$) δ = 8.98-8.94 (m, 1H), 8.52 (d, *J* = 5.4 Hz, 1H), 8.33 (d, *J* = 6.3 Hz, 1H) 8.27 (d, *J* = 8.4 Hz, 1H), 8.10 (d, *J* = 8.1 Hz, 1H), 7.93-7.90 (m, 1H), 7.77 (t, *J* = 7.5 Hz, 1H), 7.72-7.69 (m, 2H), 7.44 (d, *J* = 6.0 Hz, 1H), 7.18 (td, *J* = 6.6, 1.2 Hz, 1H), 6.76 (dd, *J* = 7.8, 2.1 Hz, 1H), 6.28 (td, *J* = 10.2, 2.1 Hz, 1H), 6.15 (s, 1H), 5.70 (dd, *J* = 8.7, 2.4 Hz, 1H), 5.21 (s, 1H), 2.12 (s, 3H), 1.82 (s, 3H), 1.73 (s, 3H). ESI-MS (*m/z*). Calcd for $C_{32}H_{25}N_2O_2F_2{}^{191}Ir$ $[M]^+$: 698.1484. Found: 698.1476.

38: **38** was prepared for the characterization of the products of degradation reaction of ***mer*-23** (to prove that only **37** was produced, not **38**, from ***mer*-23**). A solution of **26b** (10 mg, 7.0 μmol), tetrabutylammonium hydroxide (TBAH) (13 mg, 21 μmol) and acetylacetone (5 mg, 50 μmol) in CH_2Cl_2/MeOH (10/1, 1.1 mL) was refluxed for 14 h. After cooling to room temperature, water was added to the reaction mixture and extracted with $CHCl_3$. The combined organic layer was dried over Na_2SO_4. After filtration, the filtrate was evaporated under reduced pressure and the resulting residue was purified by silica gel chromatography using hexanes/CH_2Cl_2 (5/1) as the eluent to give **38** as a red powder (8.9 mg, 89% yield). mp > 300 °C. IR (ATR): ν = 3021, 1576, 1513, 1502, 1437, 1395, 1373, 1350, 1271, 1252, 1148, 1123,

1049, 1014, 869, 813, 741, 733, 671, 584, 576, 415, 396 cm^{-1}. ^1H NMR (300 MHz, $CDCl_3/Si(CH_3)_4$) δ = 9.00-8.97 (m, 2H), 8.41 (d, *J* = 6.3 Hz, 2H), 8.10 (d, *J* = 8.4 Hz, 2H), 7.93-7.90 (m, 2H), 7.73-7.68 (m, 4H), 7.42 (d, *J* = 6.6 Hz, 2H), 6.71 (dd, *J* = 9.0, 1.8 Hz, 2H), 6.23 (s, 2H), 5.16 (s, 1H), 2.02 (s, 6H), 1.73 (s, 6H). ESI-MS (*m/z*). Calcd for $C_{37}H_{31}N_2O_2{}^{191}Ir$ $[M]^+$: 726.1986. Found: 726.1979.

42a: A solution of ***mer*-20** (10 mg, 14 μmol) and $ZnBr_2$ (0.20 g, 0.89 mmol) in 1,2-dichloroethane (1.0 mL) was refluxed for 4 h. After the precipitate was filtered off and the filtrate was concentrated under reduced pressure, the resulting residue was purified by silica gel column chromatography using $CHCl_3$ as the eluent to give the mixture of **15b** and **34b** as a yellow powder (6.4 mg, 72% yield assuming that only **34b** was obtained).

The next step was carried out according to our previous report.[13] The obtained mixture of **15b** and **34b** (6.4 mg, 5.2 μmol) was dissolved in a mixture of CH_2Cl_2/EtOH (4/1, 1.3 mL), and 8-benzenesulfonylamidoquinoline (5.0 mg, 18 μmol) and triethylamine (38 mg, 0.37 mmol) were then added. The reaction mixture was refluxed at 80 ºC for 1 h. The solvent was evaporated under reduced pressure and the residue purified by silica gel chromatography with $CHCl_3$ as the eluent to give the stereoisomer mixture of **37** as a brown powder (4.1 mg, 36% yield from ***mer*-20**). The stereoisomer mixture of **42** was subjected to further purification by silica gel column chromatography eluted with hexanes/$CHCl_3$/THF (4/1/1) to afford **42a** as a brown powder (1.0 mg, 10% yield from ***mer*-20**). mp > 300 ˚C. IR (ATR): ν = 2923, 1579, 1508, 1477, 1399, 1101, 985, 836, 768, 587, 567, 422, 413 cm^{-1}. ^1H NMR (300 MHz, $CDCl_3/Si(CH_3)_4$) δ = 9.20 (dd, *J* = 5.7, 0.6 Hz, 1H), 8.22-8.16 (m, 2H), 8.06 (dd, *J* = 8.7 1.5 Hz, 1H) 7.75-7.64 (m, 3H), 7.54-7.52 (m, 1H), 7.46 (t, *J* = 8.1 Hz, 1H), 7.36 (d, *J* = 8.1 Hz, 1H), 7.25-7.12 (m, 6H), 7.04-6.96 (m, 3H), 6.71-6.68 (m, 2H), 6.41 (td, *J* = 10.8, 2.4 Hz, 1H), 6.05 (s, 1H), 5.64 (dd, *J*

= 8.7, 2.1 Hz, 1H), 2.12 (s, 3H). ESI-MS (*m/z*). Calcd for $C_{38}H_{27}N_4O_2F_2S^{191}Ir$ $[M]^+$: 832.1423. Found: 832.1426.

43: The authentic sample of **43** was prepared as described in our previous report to characterize the products of the degradation reactions of ***mer*-20**.[13] A solution of the chloro-bridged Ir dimer [{Ir(tpy)$_2$(μ-Cl)}$_2$] **15a** (52 mg, 45 μmol), 8-benzenesulfonylamidoquinoline (28 mg, 97 μmol), and triethylamine (0.20 mg, 2.0 mmol)in CH_2Cl_2/EtOH (4/1, 2.5 mL) was stirred at room temperature for 10 min. The solvent was evaporated under reduced pressure and the residue was purified by silica gel chromatography with $CHCl_3$ as the eluent to give **43** as a brown powder (68 mg, 95% yield), mp > 300 ˚C. IR (ATR): ν = 1588, 1562, 1475, 1459, 1381, 1311, 1138, 1109, 1086, 942, 849, 822, 746, 689, 580, 566, 528, 427 cm^{-1}. ^{1}H NMR (300 MHz, $CDCl_3$/Si$(CH_3)_4$) δ = 9.12 (dd, *J* = 4.8, *J* = 0.9 Hz, 1H), 8.15 (dd, *J* = 7.8, 1.2 Hz, 1H), 8.00 (dd, *J* = 8.4, 1.2 Hz, 1H), 7.73-7.66 (m, 3H), 7.61-7.52 (m, 2H), 7.46-7.36 (m, 3H), 7.29 (d, *J* = 6.6 Hz, 1H), 7.19-7.09 (m, 5H), 7.00-6.91 (m, 3H), 6.74-6.64 (m, 3H), 6.13 (s, 1H), 5.97 (s, 1H), 2.10 (s, 3H), 2.08 (s, 3H). ESI-MS (*m/z*). Calcd for $C_{39}H_{31}N_4O_2S^{191}Ir$ $[M]^+$: 810.1768. Found: 810.1759. Anal. Calcd for $C_{39}H_{31}N_4O_2SIr \cdot 0.1CHCl_3$: C, 57.00; H, 3.80; N, 6.80. Found: C, 56.73; H, 3.78; N, 6.56.

***mer*-Ir(*d*$_3$-tpy)$_2$(ppy):** A mixture of *d*$_{12}$-**15a** (0.13 g, 0.12 mmol), K_2CO_3 (0.22 g, 1.6 mmol) and ppy (0.11 g, 0.70 mmol) in glycerol (1.0 mL) was stirred at 150 °C for 16 h. After cooling to room temperature, water was added to the reaction mixture and extracted with $CHCl_3$. The combined organic layer was dried over Na_2SO_4 and filtered to obtain the filtrate, to which hexanes and AcOEt were added to obtain *mer*-Ir(*d*$_3$-tpy)$_2$(ppy) as a yellow powder (0.13 g, 55% yield). IR (ATR): ν = 3322, 3061, 3039, 3018, 2918, 2859, 2255, 2217, 2030, 1973, 1863, 1733, 1596, 1574, 1556, 1465, 1431, 1409, 1391, 1297, 1256, 1237, 1221, 1159, 1115, 1054, 1034,

1025, 993, 932, 890, 880, 798, 786, 753, 733, 669, 649, 636, 629, 557, 522, 513, 410 cm^{-1}. ^1H NMR (300 MHz, $CDCl_3/Si(CH_3)_4$) δ = 8.06 (d, *J* = 6.0 Hz, 1H), 7.89-7.88 (m, 2H), 7.74-7.71 (m, 3H), 7.61-7.39 (m, 4H), 6.96-6.84 (m, 4H), 6.68-6.62 (m, 2H), 2.14 (s, 3H), 2.13 (s, 3H). ESI-MS (*m/z*). Calcd for $C_{48}H_{36}N_3{}^{191}Ir$ $[M]^+$: 845.2510. Found: 845.2514.

***mer*-50:** A solution of ***mer*-20** (11 mg, 15 μmol) and NBS (3.0 mg, 17 μmol) in CH_2Cl_2 (2 mL) was stirred at room temperature for 1 h. The solvent was removed under reduced pressure and the resulting residue was purified by silica gel chromatography using hexanes/$CHCl_3$ (4/1) as the eluent to give ***mer*-50** as a yellow powder (7.1 mg, 64% yield), mp > 300 ˚C. IR (ATR): ν = 1581, 1552, 1469, 1420, 1391, 1261, 1233, 1157, 1096, 980, 874, 771, 748, 603, 568, 522, 428 cm^{-1}. ^1H NMR (300 MHz, $CDCl_3/Si(CH_3)_4$) δ = 8.30 (d, *J* = 11 Hz, 1H), 7.98 (dd, *J* = 5.7, 0.9 Hz, 1H), 7.93 (dd, *J* = 5.7, 0.9 Hz, 1H), 7.75 (t, *J* = 5.7 Hz, 3H), 7.66-7.49 (m, 5H), 6.88 (td, *J* = 6.6, 1.2 Hz, 1H), 6.81-6.71 (m, 3H), 6.42-6.34 (m, 2H), 6.30 (s, 1H), 6.23 (s, 1H), 2.16 (s, 3H), 2.14 (s, 3H). ESI-MS (*m/z*). Calcd for $C_{35}H_{25}N_3F_2{}^{79}Br{}^{191}Ir$ $[M]^+$: 795.0800. Found: 795.0800.

67a: 67a was obtained as an orange crystaline powder (19 mg, 77% yield) from **23** (33 mg, 40 μmol), $ZnBr_2$ (0.33 g, 2.4 mmol) and $ClCH_2CH_2Cl$ (2.0 mL) using a precedure similar to that for **34b**. mp > 300 ˚C. IR (ATR): ν = 1709, 1602, 1571, 1557, 1478, 1403, 1292, 1270, 1245, 1220, 1163, 1147, 1104, 1053, 1042, 989, 869, 834, 815, 785, 753, 737, 713, 674, 567, 528, 418 cm^{-1}. ^1H NMR (300 MHz, $CDCl_3/Si(CH_3)_4$) δ = 9.30 (d, *J* = 4.8 Hz, 1H), 9.08 (d, *J* = 6.6 Hz, 1H), 9.00 (d, *J* = 5.4 Hz, 1H), 8.94 (t, *J* = 8.4 Hz, 2H), 8.77 (d, *J* = 6.3 Hz, 1H), 8.30-8.27 (m, 2H), 8.04 (d, *J* = 7.8 Hz, 1H), 8.00 (d, *J* = 8.1 Hz, 1H), 7.95 (d, *J* = 8.1 Hz, 1H), 7.85-7.70 (m, 6H), 7.05 (d, *J* = 6.6 Hz, 1H), 6.85 (t, *J* = 6.9 Hz, 1H), 6.73-6.66 (m, 2H), 6.36 (d, *J* = 6.3 Hz, 1H), 6.31-6.27 (m, 4H), 5.81 (s, 1H), 5.69 (s, 1H), 5.43 (dd, *J* = 6.3, 1.8 Hz, 1H), 5.35

(dd, *J* = 6.0, 1.8 Hz, 1H), 2.00 (s, 3H), 1.95 (s, 3H). ESI-MS (*m/z*). Calcd for $C_{54}H_{36}N_4F_4Cl_2Ir_2$ $[M]^+$: 1272.15061. Found: 1272.1489.

67b: 67b was obtained as an orange crystaline powder (24 mg, 93% yield) from **15** (31 mg, 38 μmol), $ZnBr_2$ (0.53 g, 2.3 mmol) and $ClCH_2CH_2Cl$ (2.0 mL) using a precedure similar to that for **34b**. mp > 300 ˚C. IR (ATR): ν = 1601, 1588, 1572, 1556, 1500, 1478, 1446, 1430, 1402, 1381, 1349, 1311, 1294, 1270, 1246, 1162, 1148, 1126, 1103, 986, 870, 843, 833, 814, 783, 754, 737, 710, 688, 672, 568, 527 cm^{-1}. ^1H NMR (300 MHz, $CDCl_3/Si(CH_3)_4$) δ = 9.57 (d, *J* = 5.4 Hz, 1H), 9.34 (d, *J* = 6.6 Hz, 1H), 9.29 (d, *J* = 4.8 Hz, 1H), 9.06 (d, *J* = 6.3 Hz, 1H), 8.92 (t, *J* = 9.0 Hz, 2H), 8.30 (d, *J* = 7.2 Hz, 2H), 8.03-7.99 (m, 3H), 7.90-7.74 (m, 7H), 7.13 (d, *J* = 7.2 Hz, 1H), 6.95-6.89 (m, 1H), 6.72-6.64 (m, 3H), 6.53 (t, *J* = 6.3 Hz, 1H), 6.31-6.23 (m, 2H), 5.79 (s, 1H), 5.68 (s, 1H), 5.42 (dd, *J* = 9.3, 1.5 Hz, 1H), 5.33 (dd, *J* = 9.3, 1.5 Hz, 1H), 2.00 (s, 3H), 1.95 (s, 3H). ESI-MS (*m/z*). Calcd for $C_{54}H_{37}N_4F_4Br_2Ir_2$ $[M + H]^+$: 1361.0574. Found: 1361.0543.

66a: A mixture of AgOTf (21 mg, 82 μmol), **34b** (14 mg, 12 μmol), the mpiq ligand (25 mg, 0.12 mmol) and triethylamine (15 mg, 0.15 mmol) in $ClCH_2CH_2Cl$ (1.0 mL) was refluxed for 1.5 h. The mixture was then cooled to room temperature, and the precipitate was removed by filtration. The filtrate was evaporated under reduced pressure and purified by silica gel column chromatography using hexanes/$CHCl_3$ as the eluent to afford single stereoisomer **66a** as an orange powder (2.5 mg, 13% yield). mp 206-207 ˚C. IR (ATR): ν = 1599, 1580, 1564, 1551, 1470, 1397, 1285, 1263, 1158, 1097, 981, 816, 772, 675, 666, 578, 567, 524, 419 cm^{-1}. ^1H NMR (300 MHz, $CDCl_3/Si(CH_3)_4$) δ = 8.94-8.91 (m, 1H), 8.19 (d, *J* = 7.2 Hz, 1H), 8.10-8.07 (m, 1H), 7.97 (dd, *J* = 5.1, 0.9 Hz, 1H), 7.82-7.12 (m, 3H), 7.65-7.61 (m, 2H), 7.58-7.54 (m, 1H), 7.51-7.44 (m, 3H), 7.15 (d, *J* = 6.0 Hz, 1H), 6.89-6.81 (m, 3H), 6.69-6.62 (m, 2H), 6.40-6.32 (m,

2H), 5.88 (dd, *J* = 9.6, 2.4 Hz, 1H), 2.22 (s, 3H), 2.17 (s, 3H). ESI-MS (*m/z*). Calcd for $C_{39}H_{28}N_3F_2{}^{191}Ir$ $[M]^+$: 767.1851. Found: 767.1847.

66c: A mixture of AgOTf (0.15 g, 0.58 mmol), **67b** (0.17 g, 0.13 mmol), the tpy ligand (0.16 g, 0.94 mmol) and triethylamine (89 mg, 0.88 mmol) in $ClCH_2CH_2Cl$ (10 mL) was refluxed for 30 min. The mixture was then cooled to room temperature, and the precipitate was removed by filtration. The filtrate was evaporated under reduced pressure and purified by silica gel column chromatography using hexanes/$CHCl_3$ as the eluent to afford the stereoisomer mixture of **66c** and **66d** as a red crystaline powder (0.16 g, 88% yield).

The obtained stereoisomer mixture of **66c** and **66d** (15 mg, 0.19 μmol) was dissolved in $ClCH_2CH_2Cl$ (1.0 mL) and silica gel (21 mg) was added. The reaction mixture was reflux for 10 min. The solvent was evaporated under reduced pressure and the residue was purified by silica gel column chromtography with hexanes/$CHCl_3$ as the eluent to afford single isomer **66c** as a red crystaline powder (7.6 mg, 50% yield from the stereoisomers mixture **66c** and **66d**). mp 263-264 °C. IR (ATR): ν = 2915, 1583, 1565, 1552, 1500, 1468, 1421, 1441, 1395, 1348, 1310, 1285, 1261, 1236, 1208, 1158, 1097, 1038, 979, 808, 772, 749, 739, 713, 671, 569, 523 cm^{-1}. ^1H NMR (300 MHz, $CDCl_3/Si(CH_3)_4$) δ = 8.94 (d, *J* = 7.2 Hz, 1H), 8.21-8.15 (m, 3H), 7.89 (d, *J* = 8.7 Hz, 1H), 7.83 (d, *J* = 5.4 Hz, 1H), 7.70-7.65 (m, 1H), 7.62-7.54 (m, 5H), 7.41 (d, *J* = 6.0 H, 1H), 6.97 (d, *J* = 6.3 H, 1H), 6.89 (t, *J* = 5.7 Hz, 2H), 6.84 (d, *J* = 5.1 H, 1H), 6.78-6.76 (m, 2H), 6.53 (s, 1H), 6.39-6.31 (m, 2H), 5.90 (dd, *J* = 7.5, 2.1 Hz, 1H), 2.22 (s, 3H), 2.09 (s, 3H). ESI-MS (*m/z*). Calcd for $C_{39}H_{28}N_3F_2{}^{191}Ir$ $[M]^+$: 767.1851. Found: 767.1860.

Ir(tpy)(F_2ppy)(Br-mpiq): The obtained stereoisomer mixture of **66c** (44 mg, 57 μmol) was dissolved in CH_2Cl_2 (12 mL) and NBS (11 mg, 63 μmol) was added. The reaction mixture was stirred at room temperature for 10 min. The solvent was evaporated under reduced pressure

and the residue was purified by silica gel column chromtography with hexanes/$CHCl_3$ as the eluent to afford **70** as a red powder (43 mg, 87% yield). mp 248-249 ˚C. IR (ATR): ν = 2920. 1595, 1469, 1396, 1286, 1262, 1237, 1159, 1098, 1059, 980, 809, 773, 749, 732, 569, 523, 415 cm^{-1}. ^1H NMR (300 MHz, $CDCl_3/Si(CH_3)_4$) δ = 8.88 (d, *J* = 8.1 Hz, 1H), 8.44 (s, 1H), 8.21 (d, *J* = 8.1 Hz, 1H), 8.13 (d, *J* = 6.0 Hz, 1H), 7.89 (d, *J* = 7.8 Hz, 1H), 7.82 (d, *J* = 5.7 Hz, 1H), 7.71 (t, *J* = 9.0 Hz, 2H), 7.65-7.55 (m, 4H), 7.43 (d, *J* = 6.3 Hz, 1H), 7.01 (d, *J* = 6.3 Hz, 1H), 6.90 (t, *J* = 7.2 Hz, 1H), 6.80-6.75 (m, 2H), 6.57 (s, 1H), 6.42-6.34 (m, 2H), 5.89 (ddd, *J* = 7.5, 2.1, 1.2 Hz, 1H), 2.25(s, 3H), 2.11 (s, 3H). ESI-MS (*m/z*). Calcd for $C_{39}H_{27}N_3F_2{}^{79}Br^{191}Ir$ $[M]^+$: 845.0956. Found: 845.0961.

74: Phosphorus oxychloride (0.5 mL) was added dropwise to DMF (4.8 mL), and the resulting mixture was stirred at room temperature for 30 min, after which *fac*-**20** (140 mg, 0.16 mmol) was added to produce a yellow solution. After stirring overnight at 80 ºC, the deep-red colored reaction mixture was allowed to cool at 0 ºC, and 3 M aqueous NaOH (10 mL) was then added. After stirring at room temperature for 1 h, the yellow solid was isolated by filtration and washed with water to afford **74** as a bright yellow powder (60 mg, 53%). IR (ATR): ν = 1671, 1577, 1559, 1524, 1472, 1421, 1398, 1286, 1240, 1205, 1162, 1099, 1066, 1033, 1021, 983, 929, 887, 859, 829, 783, 746, 718, 665, 566, 523 cm^{-1}. ^1H NMR (400 MHz, $CDCl_3$/TMS): δ = 10.20 (s, 1H), 10.17 (s, 1H), 8.30 (d, *J* = 8.8 Hz, 1H), 8.07 (d, *J* = 7.6 Hz, 2H), 8.01 (d, *J* = 8.4 Hz, 2H), 7.71-7.67 (m, 3H), 7.46-7.41 (m, 3H), 7.09-6.92 (m, 3H), 6.78 (s, 1H), 6.65 (s, 1H), 6.43-6.38 (m, 1H), 6.23 (dd, *J* = 9.0, 2.1 Hz, 1H), 2.48 (s, 3H), 2.41 (s, 3H). ^{13}C NMR (100 MHz, $CDCl_3$/TMS): δ = 173.6, 166.0, 165.8, 163.7, 147.5, 143.5, 142.6, 140.6, 137.8, 129.0, 128.8, 126.5, 123.8, 123.3, 123.3, 122.8, 120.0, 118.7, 97.28, 19.6, 19.5. ESI-MS (*m/z*). Calcd for $C_{37}H_{26}N_3O_2F_2{}^{191}Ir$ $[M]^+$: 775.1622; found: 775.1680.

75: A mixture of $NaClO_2$ (430 mg, 4.7 mmol) and $NaH_2PO_4 \cdot 2H_2O$ (465 mg, 2.9 mmol) in water (12 mL) was added dropwise to a solution of **74** (82 mg, 106 μmol) and 2-methyl-2-butene (500 μL, 4.7 mmol) in DMSO (3 mL) at room temperature. After stirring at room temperature for 5 h, the mixture was concentrated under reduced pressure, and 1 M aqueous HCl was then added until pH 1. The resulting solid was filtered off and washed with water and $CHCl_3$ to afford **75** as a yellow powder (58 mg, 69% yield). IR (ATR): ν = 2916, 1671, 1597, 1583, 1559, 1524, 1472, 1421, 1400, 1284, 1240, 1160, 1098, 1069, 1032, 1017, 984, 910, 883, 861, 827, 778, 750, 718, 626, 567, 524 cm^{-1}. ^1H NMR (400 MHz, d_6-DMSO/TMS): δ = 12.31 (brs, 2H), 8.31-8.17 (m, 5H), 7.95-7.85 (m, 3H), 7.53 (d, *J* = 6.3 Hz, 2H), 7.44 (d, *J* = 5.7 Hz, 1H), 7.25-7.17 (m, 3H), 6.66 (t, *J* = 9.3 Hz, 1H), 6.54 (s, 1H), 6.52 (s, 1H), 6.13 (dd, *J* = 9.3, 2.1 Hz, 1H), 2.28 (s, 3H), 2.23 (s, 3H). ^{13}C NMR (100 MHz, d_6-DMSO/TMS): δ = 169.6, 167.8, 167.4, 164.7, 164.5, 161.8, 147.8, 147.4, 142.8, 140.5, 139.5, 138.6, 128.0, 126.5, 123.9, 123.4, 122.9, 122.7, 120.0, 117.6, 96.6, 22.8, 22.7. ESI-MS (*m/z*). Calcd for $C_{37}H_{26}N_3O_4F_2{}^{191}Ir$ $[M]^+$: 807.1521; found: 807.1513.

76: DIEA (0.10 g, 0.74 mmol), PyBOP (0.29 g, 0.56 mmol), and mono-Boc-protected octamethylenediamine (0.11 g, 0.42 mmol) were added to a solution of **75** (76 mg, 95 μmol) in freshly distilled DMF (1 mL). The reaction mixture was stirred overnight at room temperature, and then concentrated under reduced pressure. The remaining residue was purified by silica gel column chromatography ($CHCl_3$) and gel permeation chromatography ($CHCl_3$) to afford the Boc protected **76** (40 mg, 33%) as a yellow powder. R_f value of TLC ($CHCl_3$): 0.58. IR (ATR): ν = 2926, 2855, 1693, 1634, 1598, 1556, 1512, 1471, 1424, 1398, 1364, 1248, 1161, 1109,1097, 1068, 1029, 1012, 982, 887, 863, 828, 809, 780, 749, 718, 694, 672, 566, 524 cm^{-1}. ^1H NMR (400 MHz, $CDCl_3$/TMS): δ = 8.25 (d, *J* = 9.0 Hz, 1H), 7.87 (t, *J* =5.4 Hz, 2H), 7.69-7.62 (m, 5H), 7.45 (d, *J* = 5.1 Hz, 1H), 7.41 (d, *J* = 5.1 Hz, 1H), 7.38 (d, *J* = 5.1 Hz, 1H), 6.92-6.88 (m, 3H), 6.64 (s, 1H), 6.63 (s, 1H), 6.36-6.32 (m, 2H), 4.52 (brs, 2H), 3.49-3.40 (m,

4H), 3.10-3.08 (m, 4H), 2.26 (s, 3H), 2.22 (s, 3H), 1.46 (s, 18H), 1.31-1.20 (m, 24H). ^{13}C NMR (100 MHz, $CDCl_3$/TMS): δ = 172.1, 166.5, 164.1, 156.8, 147.7, 142.2, 139.9, 137.5, 137.1, 129.6, 128.1, 123.4, 122.6, 96.6, 79.4, 40.7, 40.0, 30.1, 29.8, 29.3, 28.5, 27.1, 26.8, 20.6, 20.4. ESI-MS (*m/z*). Calcd for $C_{63}H_{79}N_7O_6F_2{}^{191}Ir$ $[M + H]^+$: 1260.5689; found: 1260.5696.

77: A mixture of TMSCl (130 µL, 1.03 mmol) and NaI (154 mg, 1.03 mmol) in CH_3CN (2.0 mL) was added to a suspension of Boc protected **76** (65 mg, 0.05 mmol) in CH_3CN (3.0 mL). After stirring the mixture at room temperature for 20 min, it was sonicated for 2 min. The insoluble compound was isolated by centrifugation and washed with CH_3CN to give **77** as the HI salt (49 mg, 72%). IR (ATR): ν = 2927, 2856, 1598, 1555, 1529, 1471, 1424, 1398, 1285, 1264, 1240, 1160, 1097, 1068, 983, 863, 830, 784, 750, 720, 567, 517 cm^{-1}. ^{1}H NMR (400 MHz, CD_3OD/TMS): δ = 8.30 (dd, *J* = 12.6, 5.2 Hz, 1H), 8.09-8.01 (m, 2H), 7.83-7.72 (m, 5H), 7.58-45 (m, 3H) 7.08-6.95 (m, 3H), 6.68 (s, 1H), 6.61 (s, 1H), 6.45-6.38 (m, 1H), 6.35-6.29 (m, 1H), 2.91 (t, *J* = 4.0 Hz, 4H), 2.18 (s, 3H), 2.12 (s, 3H), 1.69-1.61 (m, 10H), 1.47-1.43 (m, 18H). ESI-MS (*m/z*). Calcd for $C_{53}H_{63}N_7O_2F_2{}^{191}Ir$ $[M + H]^+$: 1060.4641; found: 1060.4630. Anal. Calcd for $C_{85}H_{114}F_4IrN_{13}O_{14}$: C, 60.08; H, 6.24; N, 7.78%; found: C, 60.23; H, 6.42; N, 7.97%.

72: DIEA (44 µL, 0.25 mmol), PyBop (113 mg, 0.21 mmol), and the protected KKKGG peptide (54 mg, 59 µmol) were added to a solution of **77** (26 mg, 20 µmol) in dist. DMF (1 mL). The reaction mixture was stirred overnight at room temperature and then concentrated under reduced pressure and purified by silica gel column chromatography ($CHCl_3$/MeOH = 1/0 to 10/1) to afford the protected Ir complex R_f value of TLC ($CHCl_3$/MeOH (10/1)): 0.70. To the protected Ir complex in CH_3CN (2.0 mL) was added a mixture of TMSCl (62 µL, 0.49 mmol) and NaI (73 mg, 0.49 mmol) in CH_3CN (3.0 mL). The reaction mixture was stirred at room temperature for 20 min and then sonicated for 2 min. The insoluble compound was isolated by

centrifugation and washed with CH_3CN to give **69** as the HI salt. The product was purified by preparative RP-HPLC [H_2O (0.1% TFA)/CH_3CN (0.1% TFA) = 80/20 to 40/60 (30 min), t_r = 17 min, 8.0 mL/min], lyophilized to give **72** as a yellow powder (6.2 mg, 29% as 8TFA salt). IR (ATR): ν = 3061, 2929, 1662, 1599, 1565, 1553, 1470, 1420, 1397, 1282, 1267, 1236, 1196, 1183, 1132, 1095, 1067, 1035, 980, 863, 837, 826, 798, 785, 750, 723, 568, 523, 419, 405 cm^{-1}. ^1H NMR (400 MHz, CD_3OD/TMS): δ = 8.19 (d, J = 8.4 Hz, 2H), 8.03-7.88 (m, 3H), 7.71-7.63 (m, 3H), 7.47-7.36 (m, 3H), 6.97-6.88 (m, 3H), 6.59 (s, 1H), 6.52 (s, 1H), 6.32-6.26 (m, 1H), 6.16-6.13 (m, 1H), 4.28-4.20 (m, 2H), 4.18-4.16 (m, 2H), 3.87-3.80 (m, 14H), 3.77-3.20 (m, 12H), 2.08 (s, 3H), 2.02 (s, 3H), 1.80-1.25 (m, 64H). ESI-MS (*m/z*). Calcd for $C_{97}H_{148}N_{23}O_{12}F_2{}^{191}Ir$ $[M + 2H]^{2+}$: 1029.0637; found: 1029.0638.

78: Phosphorus oxychloride (0.25 mL) was added dropwise to dimethylformamide (2 mL) solution and the resulting reaction mixture was stirred at room temperature for 30 min, after which *fac*-**21** (55 mg, 74 μmol) was added to yield a yellow color solution. After stirring the reaction mixture at 80 °C for 14 h, the deep-red colored reaction mixture was allowed to cool to 0 °C, and 2 M aqueous NaOH (6.0 mL) was then added whereupon the product was precipitated as a yellow precipitate. The yellow colored Ir complex was isolated by filtration and washed with water to afford **78** as a yellow powder (54 mg, 94%). IR (ATR): ν = 1679, 1595, 1566, 1556, 1472, 1396, 1283, 1239, 1208, 1161, 1098, 1067, 984, 857, 823, 784, 747, 716, 567, 523, 500, 432 cm^{-1}. ^1H NMR (400 MHz, $CDCl_3$/TMS): δ = 10.18 (s, 1H), 8.31 (d, J = 8.4 Hz, 2H), 8.07 (s, 1H), 8.02 (d, J = 8.1 Hz, 1H), 7.74-7.65 (m, 3H), 7.48-7.43 (m, 3H), 6.99-6.88 (m, 3H), 6.73 (s, 1H), 6.42-6.28 (m, 3H), 6.18 (dd, J = 8.4, 2.4 Hz, 1H), 2.47 (s, 3H) ppm. ESI-MS (*m/z*). Calcd for $C_{35}H_{22}N_3OF_4{}^{191}Ir$ $[M]^+$: 769.1328; found: 769.1322.

79: A mixture of $NaClO_2$ (190 mg, 2.1 mmol) and $NaH_2PO_4 \cdot 2H_2O$ (328 mg, 2.1 mmol) in water (10 mL) was added dropwise to a solution of **78** (65 mg, 85 μmol) and 2-methyl-2-butene (230 μL, 2.3 mmol) in DMSO (8 mL) at room temperature. After stirring for 5 h at room temperature, the mixture was concentrated under reduced pressure followed by the addtion of 1 M aqueous HCl to pH 1 to precipitate the yellow solid product. The solid was isolated by filtration and washed with water to obtain **79** as a yellow powder (49 mg, 74%). IR (ATR): ν = 1718, 1678, 1596, 1557, 1472, 1421, 1398, 1283, 1238, 1160, 1098, 983, 860, 822, 777, 750, 718, 567, 524, 427 cm^{-1}. ^1H NMR (400 MHz, DMSO-d_6/TMS): δ = 12.34 (brs, 1H), 8.28-8.24 (m, 3H), 8.20 (d, J = 9.6 Hz, 1H), 7.96-7.86 (m, 3H), 7.54 (d, J = 5.1 Hz, 2H), 7.45 (d, J = 5.7 Hz, 1H), 7.27-7.21 (m, 3H), 6.72-6.66 (m, 2H), 6.49 (s, 1H), 6.11-6.05 (m, 2H), 2.27 (s, 3H). ESI-MS (*m/z*). Calcd for $C_{35}H_{22}N_3O_2F_4{}^{191}Ir$ $[M]^+$: 785.1277; found: 785.1272.

80: DIEA (30 mg, 0.23 mmol), PyBOP (0.10 g, 0.19 mmol), and mono-Boc-protected octamethylenediamine (22 mg, 81 μmol) were added to a solution of **79** (32 mg, 41 μmol) in freshly distilled DMF (1 mL). The reaction mixture was stirred overnight at room temperature, and then concentrated under reduced pressure. The resulting residue was purified by silica gel column chromatography ($CHCl_3$) and gel permeation chromatography ($CHCl_3$) to afford the Boc protected **80** (36 mg, 86%) as a yellow powder. R_f value of TLC ($CHCl_3$): 0.91. IR (ATR): ν = 3279, 2927, 2856, 1704, 1637, 1598, 1567, 1557, 1473, 1424, 1398, 1365, 1284, 1266, 1240, 1163, 1099, 984, 860, 824, 787, 752, 718, 567, 525 cm^{-1}. ^1H NMR (400 MHz, $CDCl_3$/TMS): δ = 8.27 (t, J = 8.1 Hz, 2H), 7.85 (d, J = 5.4 Hz, 1H), 7.68-7.61 (m, 4H), 7.47 (d, J = 5.1 Hz, 1H), 7.43 (d, J = 5.7 Hz, 1H), 7.40 (d, J = 5.7 Hz, 1H), 6.93-6.85 (m, 3H), 6.59 (s, 1H), 6.46-6.32 (m, 2H), 6.30 (dt, J = 9.3, 3.0 Hz, 2H), 4.56 (brs, 1H), 3.50-3.40 (m, 2H), 3.10-3.07 (m, 2H), 2.23 (s, 3H), 1.43 (s, 9H), 1.34-1.20 (m, 12H). ^{13}C NMR (100 MHz, $CDCl_3$/TMS): δ = 171.2, 165.7, 163.5, 163.2, 156.0, 146.9, 141.5, 139.2, 136.7, 136.4, 129.3, 128.9, 127.4, 122.7, 122.0, 118.9, 118.2, 96.0, 79.0, 40.5, 39.8, 30.0, 29.2, 29.0, 28.4, 26.9,

26.7, 20.5, 20.3 ppm. ESI-MS (*m/z*). Calcd for $C_{48}H_{49}N_5O_3F_4{}^{191}Ir$ $[M + H]^+$: 1012.3323; found: 1012.3391.

81: **80** (19 mg, 19 μmol) was dissolved in 2.0 mL of ethyl acetate and treated with 1.0 mL of 2 M aqueous HCl. After stirring at 60 ºC for 4 h, the mixture was concentrated under reduced pressure and the residue was purified by silica gel column chromatography ($CHCl_3$/MeOH = 10/1) to afford **81** as a yellow powder (16 mg, 93% yield as HCl salt). R_f value of TLC ($CHCl_3$/MeOH (10/1)): 0.87. IR (ATR): ν = 2926, 2855, 1596, 1566, 1556, 1471, 1422, 1397, 1283, 1264, 1238, 1161, 1098, 1067, 982, 860, 823, 785, 750, 717, 566, 524 cm^{-1}. ^1H NMR (400 MHz, CD_3OD/TMS): δ = 8.32-8.26 (m, 2H), 8.07 (d, *J* = 7.8 Hz, 1H), 7.81-7.77 (m, 3H), 7.73 (s, 1H), 7.61 (d, *J* = 4.5 Hz, 1H), 7.55 (d, *J* = 6.9 Hz, 1H), 7.51 (d, *J* = 4.5 Hz, 1H), 7.10-7.00 (m, 3H), 6.59 (s, 1H), 6.50-6.41 (m, 2H), 6.21 (dd, *J* = 9.3, 2.4 Hz, 1H), 6.15 (dd, *J* = 9.3, 2.4 Hz, 1H), 2.90 (t, *J* = 7.5 Hz, 2H), 2.17 (s, 3H), 1.66-1.58 (m, 4H), 1.41-1.26 (m, 11H). ^{13}C NMR (100 MHz, $CDCl_3$/TMS): δ = 173.9, 166.2, 163.4, 148.1, 147.9, 147.8, 142.6, 139.1, 138.1, 137.9, 137.2, 130.3, 128.3, 123.1, 122.9, 119.6, 118.0, 96.1, 39.6, 39.5, 29.1, 28.8, 27.3, 26.6, 26.1, 18.8 ppm. ESI-MS (*m/z*). Calcd for $C_{43}H_{41}N_5OF_4{}^{191}Ir$ $[M + H]^+$: 912.2876; found: 912.2855.

82: DIEA (11 mg, 86 μmol), PyBop (31 mg, 55 μmol), and protected KKKGG peptide (31 mg, 33 μmol) were added to a solution of **81** (11 mg, 11 μmol) in dist. DMF (1 mL). The reaction mixture was stirred at room temperature for 23 h. The reaction mixture was concentrated under reduced pressure and resulting residue was purified by silica gel column chromatography ($CHCl_3$/MeOH = 1/0 to 10/1) and gel permeation chromatography ($CHCl_3$) to afford **82** as a yellow powder (18 mg, 89%). R_f value of TLC ($CHCl_3$/MeOH (10/1)): 0.62. IR (ATR): ν = 3289, 3072, 2931, 2861, 1692, 1628, 1599, 1555, 1513, 1473, 1399, 1365, 1283, 1245, 1164, 1099, 1067, 984, 862, 834, 824, 782, 752, 718, 567, 524 cm^{-1}. ^1H NMR (400 MHz,

$CDCl_3$/TMS): δ = 8.29 (t, J = 8.1 Hz, 2H), 7.90 (d, J = 7.2 Hz, 1H), 7.68-7.65 (m, 3H), 7.47 (d, J = 6.0 Hz, 1H), 7.44 (d, J = 5.4 Hz, 1H), 7.40 (d, J = 6.9 Hz, 1H), 6.95-6.89 (m, 3H), 6.60 (s, 1H), 6.38-6.30 (m, 2H), 6.29 (d, J = 9.0 Hz, 3H), 4.90-4.74 (m, 3H), 4.08-3.99 (m, 15H), 3.16-3.03 (m, 12H), 2.24 (s, 3H), 1.66-1.27 (m, 62H). ESI-MS (*m/z*). Calcd for $C_{85}H_{115}N_{13}F_4O_{14}{}^{191}Ir$ $[M + H]^+$: 1832.8252; found: 1810.8264. Anal. Calcd for $C_{85}H_{114}F_4IrN_{13}O_{14}\cdot 2.8CHCl_3$: C, 49.18; H, 5.49; N, 8.49%; found: C, 49.01; H, 5.43; N, 8.66%.

73: A mixture of TMSCl (0.34 g, 3.2 mmol) and NaI (0.40 g, 2.7 mmol) in CH_3CN (2.0 mL) was added to a mixture of **82** (18 mg, 10 μmol) in CH_3CN (3.0 mL). The mixture was stirred at room temperature for 10 min and sonicated for 2 min. The insoluble compound was centrifuged and washed with CH_3CN to give **73** as the HI salt. The product was purified by preparative RP-HPLC [H_2O (0.1% TFA)/CH_3CN (0.1% TFA) = 80/20 to 30/70 (30 min), t_r = 26 min, 8.0 mL/min], and lyophilized to give **73** as a yellow powder (10 mg, 56% as 4TFA salt). IR (ATR): ν = 1599, 1580, 1564, 1551, 1470, 1397, 1285, 1263, 1158, 1097, 981, 816, 772, 675, 666, 578, 567, 524, 419 cm^{-1}. ^1H NMR (400 MHz, CD_3OD/TMS): δ = 8.30 (t, J = 8.7 Hz, 2H), 8.07 (d, J = 8.4 Hz, 1H), 7.84-7.77 (m, 3H), 7.73 (s, 1H), 7.61 (d, J = 4.2 Hz, 1H), 7.55 (d, J = 4.8 Hz, 1H), 7.51 (d, J = 4.8 Hz, 1H), 7.08-7.00 (m, 3H), 6.59 (s, 1H), 6.48-6.37 (m, 2H), 6.21 (dd, J = 9.0, 2.7 Hz, 1H), 6.16 (dd, J = 9.0, 2.4 Hz, 1H), 4.38-4.32 (m, 1H), 4.29-4.25 (m, 1H), 3.96-3.83 (m, 5H), 3.21-3.15 (m, 2H), 2.96-2.91 (m, 6H), 2.17 (s, 3H), 1.87-1.82 (m, 4H), 1.71-1.64 (m, 8H), 1.59-1.51 (m, 10H), 1.45-1.35 (m, 10H). ESI-MS (*m/z*). Calcd for $C_{65}H_{83}N_{13}F_4O_6{}^{191}Ir$ $[M + H]^+$: 1410.6155; found: 1410.6160.

X-ray Data Collection and Refinement

All crystalline samples of the Ir complexes were recrystallized from hexanes/CH_2Cl_2 (for **15b**, ***fac*-20**, ***mer*-20**, ***mer*-23**, ***mer*-24**, **29b**, and **42a**), hexanes/$CHCl_3$ (for ***mer*-50**), methanol/CH_2Cl_2 (for **66c**) or CHCl3/DMSO (for **74** and **79**) to give crystals suitable for single-crystal X-ray analysis. Single-crystal X-ray studies were performed on a Bruker APEX CCD

diffractometer equipped with a Bruker Instruments low-temperature attachment. Data were collected at 103 K (for **34b**, **42a**, and **66c**), 123 K (for **74**), 173 K (for ***fac*-20**, ***mer*-20**, ***mer*-23**, ***mer*-24**, and ***mer*-50**), or 296K (for **15b** and **74**) using graphite-monochromated Mo−K α radiation (λ = 0.71073 Å). The frames were indexed, integrated, and scaled using the SMART and SAINT software packages.[89] An empirical absorption correction was applied to the collected reflections with SADABS[90] using XPREP.[91] All of the structures were solved by the direct method using the program SHELXS-97 and were refined on F^2 by the full-matrix leastsquares technique using the SHELXL-97 program package.[92] All non-hydrogen atoms were refined anisotropically in the structure. Hydrogen atoms of **34b** were placed in calculated positions by means of the 'riding' model. Disorder problems were found during the refinement of **34b** and solved using the split model. All crystal data in this manuscript can be obtained free of charge from the Cambridge Crystallographic Data Centre via www.summary.ccdc.cam.ac.uk/structure-summary-form.

Crystal Data for 15b. $C_{48}H_{40}Br_2Ir_2N_4$, *Mr* = 1217.06, monoclinic, $P2_1/n$, a = 11.6206(6) b = 14.8110(7), c = 25.0132(13) Å, β = 96.241(2), V = 4279.6(4) $Å^3$, Z = 4, ρ_{calc} = 1.889 $g.cm^{-3}$, R = 0.0650 (for 5375 reflection with $I > 2\sigma(I)$), Rw = 0.1570 (for 7525 reflections), GOF = 1.139. CCDC 1501488 contains the supplementary crystallographic data for the paper.

Crystal Data for *fac*-20. $C_{35}H_{26}F_2IrN_3$, *Mr* = 718.79, monoclinic, $C2/c$, a = 34.105(16) b = 9.227(4), c = 17.928(8) Å, β = 99.7100(2), V = 5561(5) $Å^3$, Z = 8, ρ_{calc} = 1.717 $g.cm^{-3}$, R = 0.0484 (for 5437 reflection with $I > 2\sigma(I)$), Rw = 0.1094 (for 6249 reflections), GOF = 1.137. CCDC 1501443 contains the supplementary crystallographic data for the paper.

Crystal Data for *mer*-20. $C_{35}H_{26}F_2IrN_3 \cdot CH_2Cl_2$, Mr = 803.71, monoclinic, $P2/c$, a = 19.6105(16) b = 8.6627(7), c = 17.9826(15) Å, β = 96.5980(1), V = 3024.6(4) Å^3, Z = 4, ρ_{calc} = 1.759 g.cm^{-3}, R = 0.0366 (for 5970 reflection with $I > 2\sigma(I)$), Rw = 0.0972 (for 6870 reflections), GOF = 1.042. CCDC 1502134 contains the supplementary crystallographic data for the paper.

Crystal Data for *mer*-23. $C_{43}H_{30}F_2IrN_3 \cdot CH_2Cl_2$, Mr = 903.83, triclinic, $P\bar{1}$, a = 10.878(3) b = 12.483(4), c = 13.740(4) Å, α = 76.509(5), β = 73.212(5), γ = 89.340(6) °, V = 1733.9(9) Å^3, Z = 2, ρ_{calc} = 1.731 g.cm^{-3}, R = 0.0582 (for 5600 reflection with $I > 2\sigma(I)$), Rw = 0.1103 (for 6426 reflections), GOF = 1.140. CCDC 1501444 contains the supplementary crystallographic data for the paper.

Crystal Data for *mer*-24. $C_{38}H_{24}F_4IrN_3$, Mr = 790.08, monoclinic, $P2_1/c$, a = 13.336(2) b = 10.9986(18), c = 20.398(3) Å, β = 101.168(3), V = 2934.0(8) Å^3, Z = 4, ρ_{calc} = 1.790 g.cm^{-3}, R = 0.0399 (for 4794 reflections with $I > 2\sigma(I)$), Rw = 0.0770 (for 5331 reflections), GOF = 1.099. CCDC 1817976 contains the supplementary crystallographic data for the paper.

Crystal Data for 34b. $C_{47}H_{32}Br_2Cl_{1.79}F_4Ir_2N_4O_2$, Mr =1370.48, tetragonal, $I4_1cd$, a = 16.8132(19) b = 16.8132(19), c = 31.087(3) Å, V = 8788(2) Å^3, Z = 8, ρ_{calc} = 2.072 g.cm^{-3}, R = 0.0360 (for 4623 reflections with $I > 2\sigma(I)$), Rw = 0.0799 (for 5158 reflections), GOF = 1.094. CCDC 1817974 contains the supplementary crystallographic data for the paper.

Crystal Data for 42a. $C_{38}H_{27}F_2IrN_4O_2S$, Mr = 833.90, triclinic, $P\bar{1}$, a = 10.215(5) b = 10.959(5), c = 16.413(5) Å, α = 80.353(5), β = 86.921(5), γ = 71.791(5) °, V = 1720.7(13) Å^3, Z = 2, ρ_{calc} = 1.610 g.cm^{-3}, R = 0.0623 (for 5131 reflection with $I > 2\sigma(I)$), Rw = 0.1380 (for 6240

reflections), GOF = 1.050. CCDC 1501455 contains the supplementary crystallographic data for the paper.

Crystal Data for *mer*-50. $C_{35}H_{25}BrF_2IrN_3 \cdot 1.5H_2O$, Mr = 821.69, triclinic, $P\bar{1}$, a = 9.5171(7) b = 12.9204(9), c = 13.0846(10) Å, α = 70.745(1), β = 86.152(1), γ = 84.710(1) °, V = 1511.32(19) Å^3, Z = 2, ρ_{calc} = 1.806 g.cm^{-3}, R = 0.0311 (for 5767 reflection with $I > 2\sigma(I)$), Rw = 0.0893 (for 5992 reflections), GOF = 1.066. CCDC 1504245 contains the supplementary crystallographic data for the paper.

Crystal Data for 66c. $C_{39}H_{28}F_2IrN_3$, Mr = 786.84, monoclinic, $P2_1/c$, a = 13.0751(19) b = 14.971(2), c = 15.705(2) Å, β = 95.642(2), V = 3059.3(7) Å^3, Z = 4, ρ_{calc} = 1.669 g.cm^{-3}, R = 0.0424 (for 4298 reflections with $I > 2\sigma(I)$), Rw = 0.1120 (for 5390 reflections), GOF = 1.059. CCDC 1817970 contains the supplementary crystallographic data for the paper.

Crystal Data for 74. $C_{37}H_{26}F_2IrN_3O_2$; FW = 774.81, triclinic, space group P-1, a = 11.6449(2) Å, b = 12.0042(1) Å, c = 15.4338(2) Å, α = 81.793(1)°, β = 84.931(1)°, γ = 74.780(1)°, V = 2057.54(5) Å^3, Z = 2, D_{calcd} = 1.251 g cm^{-3}; R_1 = 0.0327 (for 11234 reflections with $I > 2\,s\,(I)$), wR_2 = 0.1313 (for 50126 reflections), GOF = 0.585. CCDC 2004202 contains the supplementary crystallographic data for the paper.

Crystal Data for 79. $C_{35}H_{22}F_4IrN_3O_2$; FW = 784.75, monoclinic, space group $C2/c$, a = 44.975(7) Å, b = 9.0309(13) Å, c = 18.118(3) Å, $\alpha = \gamma$ = 90°, β = 92.504(2)°, V = 7352(2) Å^3, Z = 4, D_{calcd} = 0.709 g cm^{-3}; R_1 = 0.0383 (for 8397 reflections with $I > 2\,s\,(I)$), wR_2 = 0.1162 (for 27902 reflections), GOF = 0.791. CCDC 2055929 contains the supplementary crystallographic data for the paper.

Measurements of UV/vis Absorption and Luminescence Spectra.

UV/vis spectra were recorded on a JASCO V-550 UV/vis spectrophotometer and emission spectra were recorded at 25 ºC on a JASCO FP-6200 and FP-6500 spectrofluorometer, respectively. All samples for spectroscopic measurements were carefully purified by recrystalization twice prior to use in order to minimize contamination and the same spectra were observed after recrystallization. Sample solutions in quartz cuvettes equipped with teflon septum screw caps were degassed by bubbling Ar through the solution for 10 min prior to conducting the luminescence measurements. Phosphorescence quantum yields (Φ) were determined using quinine sulfate (Φ = 0.55 in 0.1 M H_2SO_4)[93] or *fac*-Ir(mpiq)$_3$ (***fac*-17**) (Φ = 0.26 in toluene).[59] Equation (1) was used to calculate the emission quantum yields, in which Φ_s and Φ_r denote the quantum yields of the sample and the reference compound, respectively. The η_s and η_r terms are the refractive indexes of the solvents used for the measurements of the sample and the reference (η: 1.477 for DMSO, 1.333 for H_2O, 1.422 for CH_2Cl_2, and 1.497 for toluene). The A_s and A_r terms are the absorbance of the sample and the reference, and the I_s and I_r terms stand for the integrated areas under the emission spectra of the sample and reference, respectively (all of the Ir compounds were excited at 366 nm for luminescence measurements in this study).

$$\Phi_s = \Phi_r(\eta_s^2 A_r I_s)/(\eta_r^2 A_s I_r) \qquad (1)$$

The luminescence lifetimes of sample solutions of Ir(III) complexes in degassed DMSO at 298 K were measured on a TSP1000-M-PL (Unisoku, Osaka, Japan) instrument by using THG (355 nm) of Nd: YAG laser, Minilite I (Continuum, CA, USA) as excitation source. The signals were monitored with an R2949 photomultiplier. Data were analyzed using a single exponential decay equation (for ***mer*-20-24**, ***fac*-20**, **6**, **25**, **29b**, **35-38, 66a,c**, **66a**, and **67**) or a biexponential decay equation (for **41**, **42a**, and **43**). Sample solutions in quartz cuvettes equipped with teflon

septum screw caps were degassed by bubbling Ar through the solution for 20 minutes prior to measuring the lifetime.

Cell Culture

Cancer (Jurkat, HeLa S3, and A549) and normal IMR90 cells were cultured in RPMI 1640 (Jurkat and IMR-90), MEM (HeLa S3), or DMEM (A549) medium supplemented with 10% fetal bovine serum (FBS), L-glutamine, HEPES (2-[4-(2-hydroxyethyl)-1-piperazinyl]ethanesulfonic acid, pH = 7.5), penicillin/streptomycin, and monothioglycerol (MTG) in a humidified 5% CO_2 incubator at 37 ºC.

MTT assay

Jurkat (2.0×10^5 cells/mL), HeLa S3, A549 cancer cells, and IMR90 normal cells (1.5×10^5 cells/mL) cells were incubated in 10% FBS RPMI 1640 medium, MEM, or DMEM medium (100 μL) containing the Ir complexes (**71–73**) under 5% CO_2 at 37 ºC for 24 h in 96 well plates (BD Falcon), and then 0.5% MTT reagent in PBS (10 μL) was then added to the cells. After incubation at 37 ºC for 4 h, a formazan lysis solution (10% SDS in 0.01N HCl, 100 μL) was added and the resulting solution was incubated overnight under the same conditions, followed by measurement of the absorbance at 570 nm using a microplate reader (BIO-RAD).

Fluorescent Microscopic Studies of Jurkat Cells with Ir Complexes.

Jurkat cells (1.0×10^5 cells) were incubated without or with Ir complexes **71–73** (25 μM) in RPMI 1640 medium containing 10% FBS for 30 min (100 μL) and 1 h under 5% CO_2 at 37 ºC. After the incubation, the cells were washed twice with ice-cold PBS containing 0.1 % NaN_3

and 0.5% FBS, and observed on fluorescent microscopy (Fluoview, FV-1000, Olympus) by using Greiner CELLview^{TM} petri dish (35 × 10 mm). Excitation was 405 nm for Ir complexes.

Microscopic Observations of Jurkat Cells Stained with Rhod-4 or Rhod-2

Jurkat cells (2.0×10^5 cells) were incubated with Rhod-2/AM (5 μM) or Rhod-4/AM (5 μM) in RPMI 1640 medium containing 10% FBS (100 μL) at 37 °C for 30 min, respectively. The cells were collected by centrifuge (2000rpm at 4 °C, 3 min), wash with PBS, and then incubated in RPMI 1640 medium containing 10% FBS (100 μL) in the presence of **71–73** (25 μM) at 37 °C for 5, 30, or 60 min. The cells were plated on Greiner CELLview^{TM} petri dish (35 × 10 mm) and the fluorescent intensity of Rhod-2 or Rhod-4 was observed by confocal fluorescent microscopy (Fluoview, FV-1000, Olympus). Excitation was 559 nm for Rhod-2 and Rhod-4.

Flow Cytometric Analysis of Jurkat Cells Stained with Rhod-2 or Rhod-4

Jurkat cells (2.0×10^5 cells) were preincubaed with Rhod-2/AM (5 μM) or Rhod-4/AM (5 μM) in RPMI 1640 medium containing 10% FBS (100 μL) under 5% CO_2 at 37 ºC for 30 min, centrifuged (2000rpm at 4 °C for 3 min) and wash with PBS. The collected cells were incubated in RPMI 1640 (10% FBS) in the presence of **71–73** (25 μM) for a given incubation time (0, 5, 10, 20, 30, 40, 50, and 60 min), instantly after which the cells were suspended in 300 μL RPMI 1640 medium and then analyzed on flow cytometer (FACSCalibur cytometer, Becton), and the data were analyzed on FlowJo software (FlowJo, LCC).

Fluorescent Confocal Microscopic Studies of Jurkat Cells Treated with LysoTracker Red, MitoTracker Red, and ER-Tracker Red in the Presence of Ir Complexes 71–73

Jurkat cells (2.0×10^5 cells) were incubated with **71–73** (25 μM) in RPMI 1640 medium containing 10% FBS (100 μL) at 37 ºC under 5% CO_2 for 30 min or 1 h, and then stained with LysoTracker Red (500 nM, 100 μL), MitoTracker Red (100 nM, 100 μL), or ER-Tracker Red (500 nM, 100 μL) in PBS for 1 h. After the incubation, the cells were washed with ice-cold PBS containing 0.1 % NaN_3 and 0.5% FBS and observed by confocal fluorescent microscopy (Fluoview, FV-1000, Olympus) using a Greiner CELLview^{TM} petri dish (35 × 10 mm). Excitation was 405 nm for Ir complexes, 559 nm for LysoTracker Red, MitoTracker Red and ER-Tracker Red. Emission from 470–530 nm for **71–73**, 580–660 nm for LysoTracker Red, MitoTracker Red, and ER-Tracker Red was used.

Methylene Blue Staining and Transmission Electron Microscopy (TEM) of Jurkat cells Treated with 71 and 72

Jurkat cells (3×10^6 cells) were treated with **71** or **72** (25 μM) in RPMI 1640 medium with 10% FBS (100 μL) and incubated at 37 ºC under 5% CO_2 for 1 h. The cells were fixed with 2.5% glutaraldehyde at 4 °C for 40 min and washed twice with ice-cold PBS. Post-fixation was conducted with 1% osmium tetroxide and the cells were then included in an agarose gel, which was dehydrated by treatment with 50-100% anhydrous EtOH. The cells were embedded in epoxy resin (Poly 812, Nisshin EM Co. Ltd.) at 60 °C for 3 days. The resin was sliced with a glass knife (150 nm thickness) and stained with methylene blue for microscopic observation on a microscope (BX51, Olympus). For TEM observation, the sliced samples (100 nm thickness) were stained with EM stainer (Nisshin EM Co. Ltd.) and observed by TEM instrument (H-7650, HITACHI) with electron irradiation at 100 kV.

References

(1) (a) Balzani, V.; Scandola, F. *Supramolecular Photochemistry*; Ellis Horwood: Chichester, U.K., 1991. (b) Balzani, V.; Credi, A.; Scandola, F. In *Transition Metals in Supramolecular Chemistry*; Fabbrizzi, L., Poggi, A., Eds.; Kluwer: Dordrecht, The Netherlands, 1994; p 1. (c) Lehn, J.-M. *Supramolecular Chemistry-Concepts and Properties*; VCH: Weinheim, Germany, 1995. (d) Bignozzi, C. A.; Schoonover, J. R.; Scandola, F. *Prog. Inorg. Chem.* **1997**, *44*, 11.

(2) (a) Kalyanasundaran, K. Photophysics, photochemistry and solar energy conversion with tris(bipyridyl)ruthenium(II) and its analogue. *Coord. Chem. Rev.* **1982**, *46*, 159–244. (b) Chin, K.-F.; Cheung, K.-K.; Yip, H.-K.; Mak, T. C. W.; Che, C. M. Luminescent nitridometal complexes. Photophysical and photochemical properties of the $^3[(d_{xy})^1(d_{\pi^*})^1]$ excited state of nitridoosmium(VI) complexes with polypyridine ligands. *J. Chem. Soc., Dalton Trans.* **1995**, *4*, 657–663. (c) Sonoyama, N.; Karasawa, O.; Kaizu, Y. Solvent effect on the photoinduced electron-transfer reactions between dicyanobis(polypyridine)ruthenium(II) complexes and tris(*β*-diketonato)ruthenium(III) complexes *J. Chem. Soc., Faraday Trans.* **1995**, *91*, 437–443. (d) Tan-Sien-Hee, L.; Mesmaeker, A. K.-D. Spectroelectrochemical and flash photochemical reduction of 1,4,5,8-tetraazaphenanthrene and 1,4,5,8,9,12-hexaaza-triphenylene mono- and bi-metallic ruthenium(II) complexes *J. Chem. Soc., Dalton Trans.* **1994**, *24*, 3651–3658. (e) Kalyanasundaram, K.; Gratzel, M. Applications of functionalized transition metal complexes in photonic and optoelectronic devices *Coord. Chem. Rev.* **1998**, *177*, 347–414.

(3) (a) Anderson, P. A.; Anderson, R. F.; Furue, M.; Junk, P. C.; Keene, F. R.; Patterson, B. T.; Yeomans, B. D. Protonation Studies of Reduced Ruthenium(II) Complexes with Polypyridyl Ligands *Inorg. Chem.* **2000**, *39*, 2721–2728. (b) Li, C.; Hoffman, M. Z.

Electron Localization or Delocalization in the MLCT Excited States of $Ru(bpy)_3^{2+}$ and $Ru(phen)_3^{2+}$. Consequences to Their Photochemistry and Photophysics in Fluid Solution *Inorg. Chem.* **1998**, *37*, 830–832. (c) Berg-Brennan, C.; Subramanian, P.; Absi, M.; Stern, C.; Hupp, J. T. Luminescent Ruthenium Polypyridyl Complexes Containing Pendant Pyridinium Acceptors *Inorg. Chem.* **1996**, *35*, 3719–3722. (d) Kawanishi, Y.; Kitamura, N.; Tazuke, S. Dependence of spectroscopic, electrochemical, and excited-state properties of tris chelate ruthenium(II) complexes on ligand structure *Inorg. Chem.* **1989**, *28*, 2968–2975.

(4) (a) Balzani, V.; Juris, A.; Venturi, M.; Campagna, S.; Serroni, S. Luminescent and Redox-Active Polynuclear Transition Metal Complexes. *Chem. Rev.* **1996**, *96*, 759–834. (b) Shaw, J. R.; Sadler, G. S.; Wacholtz, W. F.; Ryu, C. K.; Schmehl, R. H. Toward the development of supramolecular metal complex light harvesting arrays: factors affecting photoinduced energy transfer in bimetallic complexes *New J. Chem.* **1996**, *20*, 749–758.

(5) (a) Sprouse, S.; King, K. A.; Spellane, P. J.; Watts, R. J. Photophysical effects of metal-carbon σ bonds in ortho-metalated complexes of iridium(III) and rhodium(III) *J. Am. Chem. Soc.* **1984**, *106*, 6647–6653. (b) King, K, A.; Spellane, P. J.; Watts, R. J. Gas-phase photofragmentation of chromium hexacarbonyl: time-resolved infrared spectrum and decay kinetics of "naked" chromium pentacarbonyl *J. Am. Chem. Soc.* **1985**, *107*, 1432–1433. (c) Ohsawa, Y.; Sprouse, S.; King, K. A.; DeArmond, M. K.; Hanck, K. W.; Watts, R. J. Electrochemistry and spectroscopy of ortho-metalated complexes of iridium(III) and rhodium(III) *J. Phys. Chem.* **1987**, *91*, 1047–1054. (d) Ichimura, K.; Kobayashi, T.; King, K. A.; Watts, R. J. Excited-state absorption spectroscopy of ortho-metalated iridium(III) complexes *J. Phys. Chem.* **1987**, *91*, 6104–6106. (e) Garces, F. O.; King, K. A.; Watts, R. J. Synthesis, structure, electrochemistry, and photophysics of methyl-substituted phenylpyridine ortho-metalated iridium(III) complexes *Inorg. Chem.*

1988, *27*, 3464–3471. (f) Garces, F. O.; Watts, R. J. A new ortho-metalated dichloro-bridged complex of iridium(III) with 2,2'-bipyridine: [{Ir(bpy-C3,N')(bpy-N,N')Cl}2][Cl]2 *Inorg. Chem.* **1990**, *29*, 582–584. (g) Wilde, A. P.; King, K. A.; Watts, R. J. Resolution and analysis of the components in dual emission of mixed-chelate/ortho-metalate complexes of iridium(III) *J. Phys. Chem.* **1991**, *95*, 629–634. (h) Dedeian, K.; Djurovich, P. I.; Garces, F. O.; Carlson, G.; Watts, R. J. A new synthetic route to the preparation of a series of strong photoreducing agents: fac-tris-ortho-metalated complexes of iridium(III) with substituted 2-phenylpyridines *Inorg. Chem.* **1991**, *30*, 1685–1687. (i) Garces, F. O.; Watts, R. J. ^{1}H and ^{13}C NMR Assignments with Coordination-Induced Shift Calculations of Carbon σ-Bondedorthometalated Rhodium(III) and Iridium(III) Complexes. *Magn. Reason. Chem.* **1993**, *31*, 529–536.

(6) (a) Colombo, M. G.; Hauser, A.; Gudel, H. U. Evidence for strong mixing between the LC and MLCT excited states in bis(2-phenylpyridinato-C2,N')(2,2'-bipyridine)iridium(III) *Inorg. Chem.* **1993**, *32*, 3088–3092. (b) Colombo, M. G.; Brunold, T. C.; Riedener, T.; Gudel, H. U. Facial tris cyclometalated rhodium(3+) and iridium(3+) complexes: their synthesis, structure, and optical spectroscopic properties *Inorg. Chem.* **1994**, *33*, 545–550.

(7) (a) Sprouse, S.; King, K. A.; Spellane, P. J.; Watts, R. J. Photophysical effects of metal-carbon .sigma. bonds in ortho-metalated complexes of iridium(III) and rhodium(III) *J. Am. Chem. Soc.* **1984**, *106*, 6647–6653. (b) Crosby, G. A. Optical excitation of transition-metal ions via intramolecular energy transfer *J. Chim. Phys.* **1967**, *64*, 160–164.

(8) Tamayo, A. B.; Alleyne, B. D.; Djurovich, P. I.; Lamansky, S.; Tsyba, I.; Ho, N. N.; Bau, R.; Thompson, M. E. Synthesis and Characterization of Facial and Meridional Tris-Cyclometalated Iridium(III) Complexes. *J. Am. Chem. Soc.* **2003**, *125*, 7377–7387.

(9) Tsuboyama, A.; Iwawaki, H.; Furugori, M.; Mukaide, T.; Kamatani, J.; Igawa, S.; Moriyama, T.; Miura, S.; Takiguchi, T.; Okada, S.; Hoshino, M.; Ueno, K. *J. Am. Chem. Soc.* **2003**, *125*, 12971–12979.

(10) Douglas, B.; McDaniel, D.; Alexander, J. **1994** Concepts and models in inorganic chemistry, 3rd edn. Wiley, New York.

(11) Nonoyama, M. [Benzo[h]quinolin-10-yl-N]iridium(III) Complexes. *Bull. Chem. Soc. Jpn.* **1974**, *47*, 767–768.

(12) Lamansky, S.; Djurovich, P.; Murphy, D.; Abdel-Razzaq, F.; Kwong, R.; Tsyba I.; Borts, M.; Mui, B.; Bau, R.; Thompson, M. E. *Inorg Chem.* **2001**, *40*, 1704–1711.

(13) Kumar, S.; Hisamatsu, Y.; Tamaki, Y.; Ishitani, O.; Aoki, S. Design and Synthesis of Heteroleptic Cyclometalated Iridium(III) Complexes Containing Quinoline-Type Ligands that Exhibit Dual Phosphorescence. *Inorg. Chem.* **2016**, *55*, 3829–3843.

(14) Hisamatsu, Y.; Kumar, S.; Aoki, S. Design and Synthesis of Tris-Heteroleptic Cyclometalated Iridium(III) Complexes Consisting of Three Different Nonsymmetric Ligands Based on Ligand-Selective Electrophilic Reactions via Interligand HOMO Hopping Phenomena *Inorg. Chem.* **2017**, *56*, 886–899.

(15) Amano, Y.; Ishikawa, Y.; Okura I. *Anal Chim Acta* **2001**, *445*, 177-182.

(16) (a) Maity, A.; Anderson, B. L.; Deligonul, N.; Gray, T. G. Room-Temperature Synthesis of Cyclometalated Iridium(III) Complexes: Kinetic Isomers and Reactive Functionalities. *Chem. Sci*. **2013**, *4*, 1175–1181. (b) Fernández-Hernández, J. M.; Yang, C. H.; Beltran, J. I.; Lemaur, V.; Polo, F.; Frohlich, R.; Cornil, J.; De Cola, L. Control of the Mutual Arrangement of Cyclometalated Ligands in Cationic Iridium(III) Complexes. Synthesis, Spectroscopy, and Electroluminescence of the Different Isomers. *J. Am. Chem. Soc*. **2011**, *133*, 10543–10558. (c) Aubert, V.; Ordronneau, L.; Escadeillas, M.; Williams, J. A. G.; Boucekkine, A.; Coulaud, E.; Dragonetti, C.; Righetto, S.; Roberto, D.; Ugo, R.; Valore,

A.; Singh, A.; Zyss, J.; Ledoux-Rak, I.; Le Bozec, H.; Guerchais, V. Linear and Nonlinear Optical Properties of Cationic Bipyridyl Iridium(III) Complexes: Tunable and Photoswitchable? *Inorg. Chem*. **2011**, *50*, 5027–5038. (d) Valore, A.; Colombo, A.; Dragonetti, C.; Righetto, S.; Roberto, D.; Ugo, R.; De Angelis, F.; Fantacci, S. Luminescent Cyclometallated Ir(III) and Pt(II) Complexes with β-Diketonate Ligands as Highly Active Second-Order NLO Chromophores. *Chem. Commun*. **2010**, *46*, 2414–2416. (e) Dragonetti, C.; Falciola, L.; Mussini, P.; Righetto, S.; Roberto, D.; Ugo, R.; Valore, A.; De Angelis, F.; Fantacci, S.; Sgamellotti, A.; Ramon, M.; Muccini, M. The Role of Substituents on Functionalized 1,10-Phenanthroline in Controlling the Emission Properties of Cationic Iridium(III) Complexes of Interest for Electroluminescent Devices. *Inorg. Chem*. **2007**, *46*, 8533–8547. (f) Dragonetti, C.; Righetto, S.; Roberto, D.; Ugo, R.; Valore, A.; Fantacci, S.; Sgamellotti, A.; De Angelis, F. Cyclometallated Iridium(III) Complexes with Substituted 1,10-Phenanthrolines: A New Class of Highly Active Organometallic Second Order NLO-Phores with Excellent Transparency with Respect to Second Harmonic Emission. *Chem. Commun*. **2007**, 4116–4118. (g) Huo, S.; Deaton, J. C.; Rajeswaran, M.; Lenhart, W. C. Highly Efficient, Selective, and General Method for the Preparation of Meridional Homo- and Heteroleptic Tris-Cyclometalated Iridium Complexes. *Inorg. Chem*. **2006**, *45*, 3155–3157. (h) Tamayo, A. B.; Alleyne, B. D.; Djurovich, P. I.; Lamansky, S.; Tsyba, I.; Ho, N. N.; Bau, R.; Thompson, M. E. Synthesis and Characterization of Facial and Meridional Tris-Cyclometalated Iridium(III) Complexes. *J. Am. Chem. Soc.* **2003**, *125*, 7377–7387. (i) Obara, S.; Itabashi, M.; Okuda, F.; Tamaki, S.; Tanabe, Y.; Ishii, Y.; Nozaki, K.; Haga, M. Highly Phosphorescent Iridium Complexes Containing Both Tridentate Bis(Benzimidazolyl)-Benzene or -Pyridine and Bidentate Phenylpyridine: Synthesis, Photophysical Properties, and Theoretical Study of Ir-Bis(Benzimidazolyl)Benzene Complex. *Inorg. Chem*. **2006**, *45*,

8907–8921. (j) Boudreault, P.-T.; Esteruelas, M. A.; Mora, E.; Onate, E.; Tsai, J.-Y. Bromination and C-C Cross-Coupling Reactions for the C-H Functionalization of Iridium(Ⅲ) Emitters. *Organometallics in press*.

(17) (a) Zhuang, J.; Li, W.; Wu, W.; Song, M.; Su, W.; Zhou, M.; Cui, Z. Homoleptic Tris-Cyclometalated Iridium(III) Complexes with Phenylimidazole Ligands for Highly Efficient Sky-Blue OLEDs. *New J. Chem.* **2015**, *39*, 246–253. (b) Ladouceur, S.; Fortin, D.; Zysman-Colman E. Enhanced Luminescent Iridium(III) Complexes Bearing Aryltriazole Cyclometalated Ligands. *Inorg. Chem.* **2011**, *50*, 11514–11526. (c) Bolink, H. J.; De Angelis, F.; Baranoff, E.; Kline, C.; Fantacci, S.; Coronado, E.; Sessolo, M.; Kalyanasundaram, K.; Gratzel, M.; Nazeeruddin, Md. K. White-Light Phosphorescence Emission from a Single Molecule: Application to OLED. *Chem. Commun*. **2009**, 4672–4674. (d) Endo, A.; Suzuki, K.; Yoshihara, T.; Tobita, S.; Yahiro, M.; Adachi, C. Measurement of Photoluminescence Efficienty of Ir(III) Phenylpyridine Derivatives in Solution and Solid-State Films. *Chem. Phys. Lett.* **2008**, 460, 155-157. (e) Lowry, M. S.; Bernhard, S. Synthetically Tailored Excited States: Phosphorescent, Cyclometalated Iridium(III) Complexes and Their Applications. *Chem. Eur. J.* **2006**, *12*, 7970–7977. (f) Baldo, M. A.; Thompson, M. E.; Forrest, S. R. High-Efficiency Fluorescent Organic Light-Emitting Devices Using a Phosphorescent Sensitizer. *Nature* **2000**, *403*, 750–753. (g) Friend, R. H.; Gymer, R. W.; Holmes, A. B.; Burroughes, J. H.; Marks, R. N.; Taliani, C.; Bradley, D. D. C.; Dos Santos, D. A.; Bredas, J. L.; Logdlund, M.; Salaneck, W. R. Electroluminescence in Conjugated Polymers. *Nature* **1999**, *397*, 121–128.

(18) (a) Patra, M.; Gasser, G. Organometallic Compounds: an Opportunity for Chemical Biology? *ChemBioChem* **2012**, *13*, 1232–1252. (b) Baggaley, E.; Weinstein, J. A.; Williams, J. A. G. Lighting the Way to See Inside the Live Cell with Luminescent Transition Metal Complexes. *Coord. Chem. Rev*. **2012**, *256*, 1762–1785. (d) Lo, K. K.-

W.; Louie, M.-W.; Zhang, K. Y. Design of Luminescent Iridium(III) and Rhenium(I) Polypyridine Complexes as in Vitro and in Vivo Ion, Molecular and Biological Probes. *Coord. Chem. Rev*. **2010**, *254*, 2603–2622. (d) Zhan, S.-J.; Hosaka, M.; Yoshihara, T.; Negishi, K.; Iida, Y.; Tobita, S.; Takeuchi, T. Phosphorescent Light-Emitting Iridium Complexes Serve as a Hypoxia-Sensing Probe for Tumor Imaging in Living Animals. *Cancer Res.* **2010**, *70*, 4490–4498. (e) Yoshihara, T.; Karasawa, Y.; Zhang, S.; Hosaka, M.; Takeuchi, T.; Iida, Y.; Endo, K.; Imamura, T.; Tobita, S. In-Vivo Phosphorescence Imaging of Cancer Using Iridium Complexes. *Proc. of SPIC*, **2009**, *7190*, 71900X-1. (f) Zhao, Q.; Huang, C.; Li, F. Phosphorescent Heavy-Metal Complexes for Bioimaging. *Chem. Soc. Rev*. **2011**, *40*, 2508–2524. (g) Lo, K. K.-W.; Chung, C.-K.; Lee, T. K.-M.; Lui, L.-K.; Tsang, K. H.-K. Zhu, N. New Luminescent Cyclometalated Iridium(III) Diimine Complexes as Biological Labeling Reagents. *Inorg. Chem*. **2003**, *42*, 6886–6897.

(19) (a) Yoshihara, T.; Yamaguchi, Y.; Hosaka, M.; Takeuchi, T.; Tobita, S. Ratiometric Molecular Sensor for Monitoring Oxygen Levels in Living Cells. *Angew. Chem., Int. Ed.* **2012**, *51*, 4148–4151. (b) Gao, R.; Ho, D. G.; Hernandez, B.; Selke, M.; Murphy, D.; Djurivich, P. I.; Thompson, M. E. Bis-Cyclometalated Ir(III) Complexes as Efficient Singlet Oxygen Sensitizers. *J. Am. Chem. Soc.* **2002**, *124*, 14828–14829.

(20) a) Liu, Z.; Sadler, P. J. Organoiridium Complexes: Anticancer Agents and Catalysts. *Acc. Chem. Res*. **2014**, *47*, 1174–1185. (b) Geldmacher, Y.; Oleszak, M.; Sheldrick, W. S. Rhodium(III) and Iridium(III) Complexes as Anticancer Agents. *Inorg. Chim. Acta.* **2012**, *393*, 84–102.

(21) (a) Huo, H.; Shen, X.; Wang, C.; Zhang, L.; Röse, P.; Chen, L.-A.; Harms, K.; Marsch, M.; Hilt, G.; Meggers, E. Asymmetric Photoredox Transition-Metal Catalysis Activated by Visible Light. *Nature* **2014**, *515*, 100–103. (b) Lalevée, J.; Tehfe, M.-A; Dumur, F.;

Gigmes, D.; Blanchard, N.; Morlet-Savary, F.; Fouassier, J. P. Iridium Photocatalysts in Free Radical Photopolymerization under Visible Lights. *ACS Macro Lett*. **2012**, *1*, 286–290. (c) Goldsmith, J. I.; Hudson, W. R.; Lowry, M. S.; Anderson, T. H.; Bernhard, S. Discovery and High-throughput Screening of Heteroleptic Iridium Complexes for Photoinduced Hydrogen Production. *J. Am. Chem. Soc*. **2005**, *127*, 7502–7510.

(22) (a) Arm, K. J.; Leslie, W.; Williams, J. A. G. Synthesis and pH-Sensitive Luminescence of Bis-Terpyridyl Iridium(III) Complexes Incorporating Pendent Pyridyl Groups. *Inorg. Chim. Acta.* **2006**, *359*, 1222–1232. (b) Licini, M.; Williams, J, A. G. Iridium(III) Bis-Terpyridine Complexes Displaying Long-Lived pH Sensitive Luminescence. *Chem. Commun*. **1999**, 1943–1944.

(23) For review, see: (a) Omae, I. Application of Five-membered Ring Products of Cyclometalation Reactions as Sensing Materials in Sensing Devices. *J. Organomet. Chem*. **2016**, 823, 50–75. (b) You, Y.; Nam, W. Photofunctional Triplet Excited States of Cyclometalated Ir(III) Complexes: Beyond Electroluminescence. *Chem. Soc. Rev*. **2012**, *41*, 7061–7084. (c) Flamigni, L.; Barbieri, A.; Sabatini, C.; Ventura, B.; Barigelletti, F. Photochemistry and Photophysics of Coordination Compounds: Iridium. *Top. Curr. Chem.* **2007**, *281*, 143–203. (d) You, Y.; Park, S. Y. Phosphorescent Iridium(III) Complexes: toward High Phosphorescence Quantum Efficiency through Ligand Control. *Dalton Trans.* **2009**, 1267–1282. (e) Ulbricht, C.; Beyer, B.; Friebe, C.; Winter, A.; Schubert, U. S. Recent Developments in the Application of Phosphorescent Iridium(III) Complex Systems. *Adv. Mater*. **2009**, *21*, 4418–4441. (f) Wong, W.-Y.; Ho, C.-L. Heavy Metal Organometallic Electrophosphors Derived from Multi-Component Chromophores. *Coord. Chem. Rev*. **2009**, *253*, 1709–1758. (g) Chi, Y.; Chou, P.-T. Transition-Metal Phosphors with Cyclometalating Ligands: Fundamentals and Applications. *Chem. Soc. Rev.* **2010**, *39*, 638–655.

(24) Tamura, Y.; Hisamatsu, Y.; Kumar, S.; Itoh, T.; Sato, K.; Kuroda, R.; Aoki, S. Efficient Synthesis of Tris-Heteroleptic Iridium(III) Complexes Based on the Zn^{2+}-Promoted Degradation of Tris-Cyclometalated Iridium(III) Complexes and Their Photophysical Properties *Inorg. Chem.* **2017**, *56*, 812–833.

(25) (a) Tamura, Y.; Hisamatsu, Y.;Kazama, A.; Yoza, K.; Sato, K.; Kuroda, R.; Aoki, S. Stereospecific Synthesis of Tris-heteroleptic Tris-cyclometalated Iridium(III) Complexes via Different Heteroleptic Halogen-Bridged Iridium(III) Dimers and Their Photophysical Properties *Inorg. Chem.* **2018**, *57*, 8124571-4589.

(26) (a) Mishra, A. P.; Salehi, B.; Sharifi-Rad, M.; Pezzani, R.; Kobarfard, F.; Sharifi-Rad, J.; Nigam, M.; Programmed cell death, from a cancer perspective: an overview. *Mol. Diagn. Ther.* **2018**, *22*, 281–295. (b) Lee, D.; Kim, I. Y.; Saha, S.; Choi, K. S. Paraptosis in the anti-cancer arsenal of natural products. *Pharmacol. Ther.* **2016**, *162*, 120–133. (c) Wang, Y.; Wen, Z.; Zhang, N.; Wang, L.; Hao, D.; Jiang, Z.; He, G. Small- molecule compounds target paraptosis to improve cancer tharapy. *Biomed. Pharmacol.* **2019**, *118*, 109–203.

(27) (a) Y. Hisamatsu, N. Suzuki, A. -A. Masum, A. Shibuya, A. Abe, A. Sato, S. Tanuma, S. Aoki, *Bioconjugate Chem.* **2017**, *28*, 507−523. (b) A.-A. Masum, Y. Hisamatsu, K. Yokoi, S. Aoki, *Bioinorg. Chem. Appl.* **2018**, Article ID: 758965. (c) A.-A. Masum, K. Yokoi, Y. Hisamatsu, K. Naito, B. Shashni, S. Aoki, *Bioinorg. Med. Chem.* **2018**, *26*, 4804–4816. (d) K. Yokoi, Y. Hisamatsu, K. Naito, S. Aoki, *Eur. J. Inorg. Chem*. **2017**, 5295−5309. (e) K. Naito, K. Yokoi, C. Balachandrana, Y. Hisamatsua, S. Aoki, *J. Inorg. Biochem.* **2019**, *199*, 110785. (f) K. Yokoi, C. Balachandran, M. Umezawa, K. Tsuchiya, A. Mitrić, S. Aoki, *ACS Omega* **2020**, 5, 6983–7001. (g) Y. Hisamatsu, A. Shibuya, N. Suzuki, T. Suzuki, R. Abe, S. Aoki, *Bioconjugate Chem.* **2015**, *26*, 857−879. (h) Aoki, S.; Yokoi, K.; Balachandran, C.; Hisamatsu, Y. Synthesi and Functionalization of

Cyclometalated Iridium(III) Complexes by Post-Complexation Functionalization for Biomedical and Material Sciences – Development of Intelligent molecules Using Metal Complex Building Block- (review in Japanese) *Journal of Synthetic Organic Chemistry*, *Japan*, **2021**, *79*, 1113-1124. (i) Balachandran, C.; Yokoi, K.; Naito, K.; Haribabu, J.; Tamura, Y.; Umezawa, M.; Tsuchiya, K.; Yoshihar, T.; Tobita, S.; Aoki, S. Cyclometalated Iridium(III) Complex-Cationic Peptide Hybrids Trigger Paraptosis in Cancer Cells via Intracellular Ca^{2+} Overload from Endoplasmic Reticulum and a Decrease in a Mitochondrial Membrane Potential *Molecules* **2021,** *26*, 7028 (32 pages). (j) Yokoi, K.; Yamaguchi, K.; Umezawa, M.; Tsuchiya, K.; Aoki, S. Induction of Paraptosis by Cyclometalated Iridium Complex-Peptide Hybrids and CGP37157 via a Mitochondrial Ca^{2+} Overload Triggered by Membrane Fusion between Mitochondria and the Endoplasmic Reticulum *Biochemistry*, **2022,** *61*, 639−655. (k) Yamaguchi, K.; Yokoi, K.; Umezawa, M.; Tsuchiya, K.; Yamada, Y.; Aoki, S. Design, Synthesis, and Anticancer Activity of Triptycene-Peptide Hybrids that Induce Paraptotic Cell Death in Cancer Cells *Bioconjugate Chemistry*, **2022,** *33*, 691−717. (l) Aoki, S.; Yokoi, K.; Hisamatsu, Y.; Balachandran, C.; Tamura, Y.; Tanaka, T.; Post-Complexation Functionalization of Cyclometalated Iridium(III) Complexes and Applications to Biomedical and Material Sciences *Top. Curr. Chem.* **2022**, in press.

(28) Haribabu, J.; Tamura, Y.; Yokoi, K.; Balachandran, C.; Umezawa, M.; Tsuchiya, K.; Yamada, Y.; Karvembu, R.; Aoki, S. Synthesis and Anticancer Properties of Bis- and Mono(cationic peptide) Hybrids of Cyclometalated Iridium(III) Complexes: Effect of the Number of Peptide Units on Anticancer Activity. *Eur. J. Inorg. Chem.* **2021**, *18*, 1796–1814.

(29) (a) Felici, M.; Contreras-Carballada, P.; Smits, J. M. M.; Nolte, R. J. M.; Williams, R. M.; De Cola, L.; Feiters, M. C. Cationic Heteroleptic Cyclometalated Iridium(III)

Complexes Containing Phenyl-Triazole and Triazole-Pyridine Clicked Ligands. *Molecules* **2010**, *15*, 2039–2059. (b) Edkins, R. M.; Wriglesworth, A.; Fucke, K.; Bettington, S. L.; Beeby, A. The Synthesis and Photophysics of Tris-Heteroleptic Cyclometalated Iridium Complexes. *Dalton Trans.* **2011**, *40*, 9672–9678. (c) Baranoff, E.; Curchod, B. F. E.; Frey, J.; Scopelliti, R.; Kessler, F.; Tavernelli, I.; Rothlisberger, U.; Grätzel, M.; Nazeeruddin, M. K. Acid-Induced Degradation of Phosphorescent Dopants for OLEDs and its Application to the Synthesis of Tris-Heteroleptic Iridium(III) Bis-Cyclometalated Complexes. *Inorg. Chem.* **2012**, *51*, 215–224. (d) Tordera, D.; Delgado, M.; Ortí E.; Bolink, H. J.; Frey, J.; Nazeeruddin, M. K.; Baranoff, E. Stable Green Electroluminescence from an Iridium Tris-Heteroleptic Ionic Complex. *Chem. Mater.* **2012**, *24*, 1896–1903. (e) Xu, X.; Yang, X.; Wu, Y.; Zhou, G.; Wu, C.; Wong, W.-Y. Tris-Heteroleptic Cyclometalated Iridium(III) Complexes with Ambipolar or Electron Injection/Transport Features for Highly Efficient Electrophosphorescent Devices. *Chem. Asian J.* **2015**, *10*, 252–262.

(30) (a) Aoki, S.; Matsuo, Y.; Ogura, S.; Ohwada, H.; Hisamatsu, Y.; Moromizato, S.; Shiro, M.; Kitamura, M. Regioselective Aromatic Substitution Reactions of Cyclometalated Ir(III) Complexes: Synthesis and Photochemical Properties of Substituted Ir(III) Complexes that Exhibit Blue, Green, and Red Color Luminescence Emission. *Inorg. Chem.* **2011**, *50*, 806–818. (b) Hisamatsu, Y.; Aoki, S. Design and Synthesis of Blue-Emitting Cyclometalated Iridium(III) Complexes Based on Regioselective Functionalization. *Eur. J. Inorg. Chem*. **2011**, 5360–5369.

(31) (a) Kando, A.; Hisamatsu, Y.; Ohwada, H.; Itoh, T.; Moromizato, S.; Kohno, M.; Aoki, S. Photochemical Properties of Red-Emitting Tris(Cyclometalated) Iridium(III) Complexes Having Basic and Nitro Groups and Application to pH Sensing and Photoinduced Cell Death. *Inorg. Chem*, **2015**, *54*, 5342–5357. (b) Hisamatsu, Y.;

Shibuya, A.; Suzuki, N.; Suzuki, T.; Abe, R.; Aoki, S. Design and Synthesis of Amphiphilic and Luminescent Tris-Cyclometalated Iridium(III) Complexes Containing Cationic Peptides as Inducers and Detectors of Cell Death via a Calcium-Dependent Pathway. *Bioconjugate Chem.* **2015**, *26*, 857−879. (c) Nakagawa, A.; Hisamatsu, Y.; Moromizato, S.; Kohno, M.; Aoki, S. Synthesis and Photochemical Properties of pH Responsive Tris-Cyclometalated Iridium(III) Complexes that Contain a Pyridine Ring on the 2-Phenylpyridine Ligand. *Inorg. Chem*. **2014**, *53*, 409–422. (d) Moromizato, S.; Hisamatsu, Y.; Suzuki, T.; Matsuo, Y.; Abe, R.; Aoki, S. Design and Synthesis of a Luminescent Cyclometalated Iridium(III) Complex Having *N*,*N*-Diethylamino Group that Stains Acidic Intracellular Organelles and Induces Cell Death by Photoirradiation. *Inorg. Chem.* **2012**, *51*, 12697–12706.

(32) To help the readers refer to the structures of each Ir complex, the structures of all the complexes in this chapter are listed in Chart 2-6.

(33) Nonoyama, M. [Benzo[h]quinolin-10-yl-N]iridium(III) Complexes. *Bull. Chem. Soc. Jpn*. **1974**, *47*, 767–768.

(34) Preparation of *fac*-heteroleptic Ir complexes by photochemical isomerization of the corresponding *mer*-isomers was reported by van Koten and co-workers. See: McDonald, A. R.; Lutz, M.; von Chzanowski, L. S.; van Klink, G. P. M.; Spek, A. L.; van Koten, G. Probing the *mer*- to *fac*-Isomerization of Tris-Cyclometallated Homo- and Heteroleptic $(C,N)_3$ Iridium(III) Complexes. *Inorg. Chem.* **2008**, *47*, 6681–6691.

(35) (a) Deaton, J. C.; Young, R. H.; Lenhard, J. R.; Rajeswaran, M.; Huo, S. Photophysical Properties of the Series *fac*- and *mer*-(1-Phenylisoquinolinato-$N^{\wedge}C^{2'}$)$_x$(2-Phenylpyridinato-$N^{\wedge}C^{2'}$)$_{3-x}$iridium(III) (x = 1–3). *Inorg. Chem.* **2010**, *49*, 9151–9161. (b) DeRosa, M.C.; Hodgson, D. J.; Enright G. D.; Dawson, B.; Evans, C. E. B.; Crutchley,

R. J. Iridium Luminophore Complexes for Unimolecular Oxygen Sensors. *J. Am. Chem. Soc*. **2004**, *126*, 7619–7626.

(36) Li, J. L. PCT. Patent. WO 2015/131158 A1.

(37) (a) Johnson, C. K. *ORTEP : A FORTRAN Thermal-Ellipsoid Plot Program for Crystal Structure Illustrations*. Report ORNL-5138, Oak Ridge National Laboratory, Oak Ridge, Tenn., 1971. (b) Pennington, W. T. *DIAMOND* - Visual Crystal Structure Information System. *J. Appl. Crystallogr.* **1999**, *32*, 1028–1029. (c) Cordier, G. A Versatile Tool for Displaying Crystal Structures. *Nachr. Chem. Tech. Lab.* **1999**, *47*, 1437–1438.

(38) The similar structures were reported previously. See: (a) Wong, M. Y.; Xie, G.; Tourbillon, C.; Sandroni, M.; Cordes, D. B.; Slawin, A. M. Z.; Samuel. I. D. W.; Zysman-Colman, E. Formylated Chloro-Bridged Iridium(III) Dimers as OLED Materials: Opening up New Possibilities. *Dalton Trans*. **2015**, *44*, 8419–8432. (b) Davies, D. L.; Lowe, M. P.; Ryder, K. S.; Singh, K.; Singh, S. Tuning Emission Wavelength and Redox Properties through Position of the Substituent in Iridium(III) Cyclometallated Complexes. *Dalton Trans*. **2011**, *40*, 1028–1030. (c) McGee, K. A.; Mann, K. R. Selective Low-Temperature Syntheses of Facial and Meridional Tris-Cyclometalated Iridium(III) Complexes. *Inorg. Chem*. **2007**, *46*, 7800–7809.

(39) The reaction of crude product of Entry 11 in Table 2 with acacH afforded **6** in 30% yield for 2 steps.

(40) (a) Hisamatsu, Y.; Miyazawa, Y.; Yoneda, K.; Miyauchi, M.; Zulkefeli, M.; Aoki, S. Supramolecular Complexes Formed by the Self-Assembly of Hydrophobic Bis(Zn^{2+}-Cyclen) Complexes, Copper, and Di- or Triimide Units for the Hydrolysis of Phosphate Mono- and Diesters in Two-Phase Solvent Systems (Cyclen=1,4,7,10-Tetraazacyclododecane). *Chem. Pharm. Bull*. **2016**, *64*, 451–464. (b) Zulkefeli. M.; Hisamatsu, Y.; Suzuki, A.; Miyazawa, Y.; Shiro, M.; Aoki, S. Supramolecular

Phosphatases Formed by the Self-Assembly of the Bis(Zn^{2+}-Cyclen) Complex, Copper(II), and Barbital Derivatives in Water. *Chem. Asian J.* **2014**, *9*, 2831–2841. (c) Itoh, S.; Sonoike, S.; Kitamura, M.; Aoki, S. Design and Synthesis of Chiral Zn^{2+} Complexes Mimicking Natural Aldolases for Catalytic C-C Bond Forming Reactions in Aqueous Solution. *Int. J. Mol. Sci*. **2014**, *15*, 2087–2118. (d) Itoh, S.; Tokunaga, T.; Sonoike, S.; Kitamura, M.; Yamano, A.; Aoki, S. Asymmetric Aldol Reactions Between Acetone and Benzaldehydes Catalyzed by Chiral Zn^{2+} Complexes of Aminoacyl 1,4,7,10-Tetraazacyclododecane: Fine-Tuning of the Amino-Acid Side Chains and a Revised Reaction Mechanism. *Chem. Asian J.* **2013**, *8*, 2125–2135. (e) Aoki, S.; Suzuki, S.; Kitamura, M.; Haino, T.; Shiro, M.; Zulkefeli, M.; Kimura, E. Molecular Recognition of Hydrocarbon Guests by a Aupramolecular Capsule Formed by the 4:4 Self-Assembly of Tris(Zn^{2+}-Cyclen) and Trithiocyanurate in Aqueous Solution. *Chem. Asian J.* **2012**, *7*, 944–956. (f) Zulkefeli, M.; Suzuki, A.; Shiro, M.; Hisamatsu, Y.; Kimura E.; Aoki, S. Selective Hydrolysis of Phosphate Monoester by a Supramolecular Phosphatase Formed by the Self-Assembly of a Bis(Zn^{2+}-Cyclen) Complex, Cyanuric Acid, and Copper in an Aqueous Solution (Cyclen = 1,4,7,10-Tetraazacyclododecane). *Inorg. Chem.* **2011**, *50*, 10113–10123. (g) Kitamura, M.; Suzuki, T.; Abe, R.; Ueno, T.; Aoki, S. ^{11}B NMR Sensing of d-Block Metal Ions in Vitro and in Cells Based on the Carbon-Boron Bond Cleavage of Phenylboronic Acid-Endant Cyclen (Cyclen = 1,4,7,10-Tetraazacyclododecane). *Inorg. Chem.* **2011**, *50*, 11568–11580. (h) Ohshima, R.; O.; Kitamura, M.; Morita, A.; Yamada, Y.; Ikekita, M.; Kimura, E.; Aoki, S. Design and Synthesis of a Fluorescent Probe for Zn^{2+}, 5,7-Bis(*N*,*N*-Dimethylaminosulfonyl)-8-Hydroxyquinoline-Pendant 1,4,7,10-Tetraazacyclododecane and Zn^{2+}-Dependent Hydrolytic and Zn^{2+}-Independent Photochemical Reactivation of Its Benzenesulfonyl-Caged Derivative. *Inorg. Chem.* **2010**, *49*, 888–899.

(41) For review, see: (a) Kimura, E.; Koike, T.; Aoki S. in *Macrocyclic and Supramolecular Chemistry: How Izatt-Christensen Award Winners Shaped the Field*; Izatt, R. M., Ed.; John Wiley & Sons, Ltd.: New Jersey, 2016, pp 417–445. (b) Aoki, S.; Ariyasu, S.; Hanaya, K.; Hisamatsu, Y.; Sugai, T. Chemical Reactions of 8-Quinolinol Derivatives and Their Applications to Biochemical Tools and Enzyme Inhibitors. *J. Synth. Org. Chem., Jpn*., **2016**, *74*, 482–493. (c) Aoki, S.; Zulkefeli, M.; Kitamura, M.; Hisamatsu Y. in *Synergy in Supramolecular Chemistry*; Nabeshima, T., Ed.; CRC: Boca Raton, FL., 2015, pp 35–56. (d) Kimura, E. Evolution of Macrocyclic Polyamines from Molecular Science to Supramolecular Science. *Bull. Jpn. Soc. Coord. Chem.* **2012**, *59*, 26–47. (e) Aoki, S.; Kimura, E. Zinc-Nucleic Acid Interaction. *Chem. Rev.* **2004**, *104*, 769–787.

(42) The crude product of the BF_3-promoted decomposition reaction (Entry 20 of Table 2-2) was directly reacted with acacH to give **4** in 19% (2 steps), suggesting that the $BF_3{\cdot}Et_2O$-promoted decomposition of ***fac*-2** affords the uncharacterized intermediate, not **15a**, which reacts with acacH to give **6** in a low yield.

(43) The ^{1}H NMR signals of **34a** and **34b** in the lowest magnetic field were assigned to be hydrogen atoms on carbon next to the nitrogen (Figure 2-4). The left peaks of **34b** (at δ = *ca*. 9.5) exhibits downfield shift than **34a** (at δ = *ca*. 9.2), inidicating that the shielding effect of bromine atom is weaker than that of chlorine atom.

(44) It should be mentioned that the decomposition of ***fac*-20** requires longer reaction time than that of ***mer*-20** (Entry 1 vs. Entry 2 in Table 2-6), possibly because ***fac*-20** is more stable by *ca*. 26 kJ/mol than ***mer*-20**, as calculated by DFT calculation (Difference in total energies of ***fac*-20** and ***mer*-20** is 0.01 a.u., which corresponds to *ca*. 26 kJ/mol, as indicated in Table 2-7).

(45) Dual emitting Ir complexes have been reported as useful phosphorescent materials and bioimaging probes. See: (a) Zhang, K. Y.; Liu, H.-W.; Tang, M.-C.; Choi, A. W.-T.;

Zhu, N.; Wei, X.-G.; Lau, K.-C.; Lo, K. K.-W. Dual-Emissive Cyclometalated Iridium(III) Polypyridine Complexes as Ratiometric Biological Probes and Organelle-Selective Bioimaging Reagents. *Inorg. Chem.* **2015**, *54*, 6582–6593. (b) Ladouceur, S.; Danato, L.; Romain, M.; Mudraboyina, B. P.; Johansen, M. B.; Wisner, J. A.; Zysman-Colman, E. A Rare Case of Dual Emission in a Neutral Heteroleptic Iridium(III) Complex. *Dalton Trans.* **2013**, *42*, 8838–8847. (c) You, Y.; Han. Y.; Lee, Y.-M.; Park, S. Y.; Nam, W.; Lippard, S. J. Phosphorescent Sensor for Robust Quantification of Copper(II) Ion. *J. Am. Chem. Soc.* **2011**, *133*, 11488–11491. (d) You, Y.; Lee, S.; Kim, T.; Ohkubo, K.; Chae, W.-S.; Fukuzumi, S.; Nam, W.; Lippard, S. J. Phosphorescent Sensor for Biological Mobile Zinc. *J. Am. Chem. Soc.* **2011**, *133*, 18328–18342. (e) Lo, K. K.-W.; Zhang, K.Y.; Leung, S.-K.; Tang, M.-C. Exploitation of the Dual-Emissive Properties of Cyclometalated Iridium(III)-polypyridine Complexes in the Development of Luminescent Biological Probes. *Angew. Chem., Int. Ed.* **2008**, *47*, 2213–2216. (f) Lee, Y. H.; Park, G. Y.; Kim, Y. S. White Light Emission Using Heteroleptic Tris-Cyclometalated Iridium(III) Complexes. *J. Korean Phys. Soc.* **2007**, *50*, 1722–1728. (g) Yeh, Y.-S.; Cheng, Y.-M.; Chou, P.-T.; Lee, G.; Yang, C.-H.; Chi, Y.; Shu, C.-F.; Wang, C.-H. A New Family of Homoleptic Ir(III) Complexes: Tris-Pyridyl Azolate Derivatives with Dual Phosphorescence. *ChemPhysChem* **2006**, *7*, 2294–2297.

(46) Baranoff and co-workers reported the X-ray structure analysis of Ir(ppy)(F_2ppy)(acac) having two pyridines of its ppy and F_2ppy ligands in *trans* positions to each other (Ref. 26c), which is similar to the structure of **42a**.

(47) (a) Atkins, P.; Overton, T.; Rourke, J.; Weller, M.; Armstrong, F. *Inorganic Chemistry, 4th Ed.*; Oxford University Press: Oxford, U. K., 2006. (b) Pearson, R. G. Hard and Soft Acids and Bases. *J. Am. Chem. Soc.* **1963**, *85*, 3533–3539.

(48) Zhou, B.; Hu, Y.; Wang, C. Manganase-Catalyzed Direct Nucleophilic C(sp^2)-H Addition to Aldehydes and Nitriles. *Angew. Chem., Int. Ed.* **2015**, *54*, 13659–13663.

(49) It is described that ligands functionalized with NO_2 and Br groups stabilize metal complexes. See: Lima, C. F. R. A. C.; Teveira, R. J. S.; Costa, J. C. S.; Fernandes, A. M.; Melo, A.; Silva, A. M.; Santos, L. M. N. B. F. Understanding M–Ligand Bonding and *mer*-/*fac*-Isomerism in Tris(8-Hydroxyquinolinate) Metallic Complexes. *Phys. Chem. Chem. Phys.* **2016**, *18*, 16555–16565.

(50) Housecroft, C. E.; Sharp, A. G. *Inorganic Chemistry, 4th Ed.*; Pearson Education Ltd.: London, 2012.

(51) Uneyama, K.; Katagiri, T.; Amii, H. α–Trifluoromethylated Carbanion Synthons. *Acc. Chem. Res.* **2008**, *41*, 817–829.

(52) The Ir-C and Ir-N bond lengths obtained by our DFT calculations of the *fac*- and *mer*-forms of **1**, **2**, **3**, and **20** are nearly identical to the values reported by Thompson and co-workers (Ref. 8) (See Table 2-7).

(53) As shown in Figure 2-16, the emission maxima of ***fac*-20**(516 nm) is 12 nm shorter than that of the ***mer*-20** and the luminescent quantum yield of ***fac*-20** ($\Phi = 0.57$) is nearly ten times higher than that ***mer*-20** ($\Phi = 4.7 \times 10^{-2}$). It should be noted that Thompson and co-workers reported that *fac*-form of tris-cyclometalated homoleptic Ir complexes exhibit higher emission quantum yield than the corresponding *mer*-complexes (*e.g.*; ***fac*-2** and ***mer*-2**) (Ref. 1h). The emission lifetime of ***fac*-20** ($\tau = 1.9$ μs) is longer than that for ***mer*-20** ($\tau = 0.3$ μs). The slightly shorter emission wavelength of ***mer*-21** (504 nm) compared to ***mer*-20** can be attributed to the electron-withdrawing effect of the fluorine atom. The quantum yield and emission lifetimes of ***mer*-22** are both small ($\Phi = 8.3 \times 10^{-2}$, $\tau = 0.25$ μs) and the emission maxima is 512 nm. Interestingly, the emission maxima of ***mer*-24** (581 nm) is somewhat shorter than that of ***mer*-23** (603 nm) and its

Φ value and emission lifetime (Φ = 0.31, τ = 4.7 μs) are greater than those of ***mer*-23** (Φ = 0.22, τ = 1.1 μs).

(54) Frisch, M. J.; Trucks, G. W.; Schlegel, H. B.; Scuseria, G. E.; Robb, M. A.; Cheeseman, J. R.; Scalmani, G.; Barone, V.; Mennucci, B.; Petersson, G. A.; Nakatsuji, H.; Caricato, M.; Li, X.; Hratchian, H. P.; Izmaylov, A. F.; Bloino, J.; Zheng, G.; Sonnenberg, J. L.; Hada, M.; Ehara, M.; Toyota, K.; Fukuda, R.; Hasegawa, J.; Ishida, M.; Nakajima, T.; Honda, Y.; Kitao, O.; Nakai, H.; Vreven, T.; Montgomery, J. A., Jr.; Peralta, J. E.; Ogliaro, F.; Bearpark, M.; Heyd, J. J.; Brothers, E.; Kudin, K. N.; Staroverov, V. N.; Kobayashi, R.; Normand, J.; Raghavachari, K.; Rendell, A.; Burant, J. C.; Iyengar, S. S.; Tomasi, J.; Cossi, M.; Rega, N.; Millam, M. J.; Klene, M.; Knox, J. E.; Cross, J. B.; Bakken, V.; Adamo, C.; Jaramillo, J.; Gomperts, R.; Stratmann, R. E.; Yazyev, O.; Austin, A. J.; Cammi, R.; Pomelli, C.; Ochterski, J. W.; Martin, R. L.; Morokuma, K.; Zakrzewski, V. G.; Voth, G. A.; Salvador, P.; Dannenberg, J. J.; Dapprich, S.; Daniels, A. D.; Farkas, Ö.; Foresman, J. B.; Ortiz, J. V.; Cioslowski, J.; Fox, D. J. *Gaussian 09*, Revision D.01, Gaussian, Inc., Wallingford CT, **2009.**

(55) Lepeltier, M.; Graff, B.; Lalevée, J.; Wantz, G.; Ibrahim-Ouali, M.; Gigmes, D.; Dumur, F. Heteroleptic Iridium (III) Complexes with Three Different Ligands: Unusual Triplet Emitters for Light-Emitting Electrochemical Cells. *Org. Electr.* **2016**, *37*, 24–34.

(56) Cudré, Y.; de Carvalho, F. F.; Burgess, G. R.; Male, L.; Pope, S. J. A.; Tavernelli, I.; Baranoff, E. Tris-heteroleptic Iridium Complexes Based on Cyclometalated Ligands with Different Cores. *Inorg. Chem.* **2017**, *56*, 11565–11576.

(57) (a) Thompson, D. W.; Wishart, J. F.; Brunschwig, B. S.; Sutin, N. Efficient Generation of the Ligand Field Excited State of Tris-(2,2'-bipyridine)-ruthenium(II) through Sequential Two-Photon Capture by $[Ru(bpy)_3]^{2+}$ or Electron Capture by $[Ru(bpy)_3]^{3+}$. *J. Phys. Chem. A* **2001**, *105*, 8117–8122. (b) Alay, F. Heully, J. L.; Bijeire, L.; Vicendo, P.

Is the 3MLCT the Only Photoreactive State of Polypyridyl Complexes? *Inorg. Chem.* **2007**, *46*, 3154–3165. (c) Sivasubramaniam, V.; Brodkorb, F.; Hanning, S.; Loebl, H. P.; van Elsbergen, V.; Scherf, U; Kreyenschmidt, M. Fluorine Cleavage of the Light Blue Heteroleptic Triplet Emitter FIrpic. *J. Fluor. Chem.* **2009**, *130*, 640–649. (d) Dumur, F.; Bertin, D.; Mayer, C. R.; Guerlin, A.; Wantz, G.; Nasr, G.; Dumas, E.; Miomandre, F.; Clavier, G.; Gigmes, D. Design of Blue or Yellow Emitting Devices Controlled by the Deposition Process of a Cationic Iridium(III) Complex. *Synth, Met.* **2011**, *161*, 1934–1939.

(58) (a) Park, G. Y.; Kim, Y.; Ha, Y. Iridium Complexes Containing Three Different Ligands as White OLED Dopants. *Mol. Cryst. Liq. Crsyt.* **2007**, *462*, 179–188. (b) Lepeltier, M.; Dumur, F.; Graff, B.; Xiao, P.; Gigmes, D.; Lalevée, J.; Mayer, C. R. Tris-Cyclometalated Iridium(III) Complexes with Three Different Ligands: a New Example with 2-(2,4-Difluorophenyl)pyridine-Based Complex. *Helv. Chim. Acta.* **2014**, *97*, 939–956.

(59) Okada, S.; Okinaka, K.; Iwawaki, H.; Furugori, M.; Hashimoto, M.; Mukaide, T.; Kamatani, J.; Igawa, S.; Tsuboyama, A.; Takiguchi, T.; Ueno, K. Substituent Effects of Iridium Complexes for Highly Efficient Red OLEDs. *Dalton Trans.* **2005**, *9*, 1583–1590.

(60) Garces, F. O., Dedeian, K., Keder, N. L., and Watts, R. J. Structures of Ortho-Metalated [2-(p-tolyl)pyridine]iridium(III) Complexes. *Acta Crystallogr.* **1993**, *C49*, 1117–1120.

(61) Kwon, T.-H.; Cho, H. S.; Kim, M. K.; Kim, J.-W.; Kim, J.-J.; Lee, K. H.; Park, S. J.; Shin, I.-S.; Kim, H.; Shin, D. M.; Chung, Y. K.; Hong, J.-I. Color Tuning of Cyclometalated Iridium Complexes through Modification of Phenylpyrazole Derivatives and Ancillary Ligand Based on ab Initio Calculations. *Organometallics* **2005**, *24*, 1578–1585.

(62) Kazama, A.; Imai, K.; Okayasu, Y.; Yamada, Y.; Yuasa, J.; Aoki, S. Design and Synthesis of Cyclometalated Iridium(III) Complexes-Chromophore Hybids that Exhibit Long-Emission Lifetimes Based on Reversible Electronic Energy Trnsfer Mechanism. *Inorganic Chemistry* **2020**, *59*, 6905-6922.

(63) (a) Yoon, M. J.; Lee, A. R.; Jeong S. S.; Kim, Y. -S.; Kim, J. Y.; Kwon, Y. -J.; Choi, K. S. *Oncotarget* **2014**, *5*, 6816-6831. (b) Kim, E.; Lee, D. M.; Seo, M. J.; Lee, H. J.; Choi, K. S. *Front. Cell Dev. Biol.* **2021**, *8*, 1-15.

(64) Ly, L. D.; Brubb, D. R.; Lawen, A. *Apoptosis* **2003**, *8*, 115-128.

(65) Galluzzi, L.; Vitale, I. *Cell Death Differ* **2018**, *25*, 486-541.

(66) Lee, D.; Kim, I. Y.; Saha, S.; Choi, K. S. *Pharmacol. Ther*. **2016**, *162*, 120-133.

(67) Liu, X.; Yang, W.; Guan, Z.; Yu, W.; Fan, B.; Xu, N.; Liao, D. J. *Cell Biosci* **2018**, *8*, 6-18.

(68) It is known that the photoirridation of iridium(III) complexes generate ROS, which may give a damage to cancer cells. Indeed, some of our previous Ir complexes induced necrosis (not PCD) of HeLa S3 cells upon photoirridation, as reported in ref. 24a,c,d. Previously, the possibility of photoinduced cell death in the presence of **68** was excluded due to the following facts. i) The observation of Jurkat cells treated with IPHs by microscopy was carried out quickly and very carefully to avoid the effect of the photoirridation (refs. 66a-c). ii) The EC_{50} values of different IPHs are dependent on the peptide sequences and the length of linkers between Ir core and peptide parts, implying that IPHs have specific interactions with their intracellular target molecules and induce PCD. iii) However, we don't deny the generation of ROS *via* the activation of intracellular signaling pathways stimulated by IPHs, because ROS might be generated in intracellular signaling systems even by the compounds that negligibly absorb UV/vis light (ROS generation not *via* photoirridation of photosensitizers).

(69) Jurkat cells were fixed using glutaraldehyde and osmium tetroxide (OsO_4) after the treatment with **68** and **69** (25 μM for 1 h) and observed on microscopy. Vacuolization of cytoplasm and morphological alternations in the cell membrane were observed, which show good agreement with Figure 4-6 in the text.

(70) Varghese, E.; Samuel, S. M.; Sadiq, Z.; Kubataka, P.; Liskova, A.; Benacka, J.; Pazinka, P.; Kruzliak, P.; Busselberg, D. *Int J. Mol. Sci*. **2019**, *20*, 3017-3039.

(71) La Rovere, R. M. J.; Roest, G.; Bultynck, G.; Parys, J. B. *Cell Calcium* **2016**, *60*, 74-87.

(72) Monteith, G. R.; Mcandrew, D.; Faddy, H. M. *Nat .Rev. Cancer.* **2007**, *7*, 519-530.

(73) Orrenius, S.; Gogvadze, V.; Zhivotovsky, B. *Biochem. Biophys. Res. Commun.* **2015**, *460*, 72-81.

(74) Smaili, S. S.; Hsu, Y.-T.; Carvalho, A. C. P.; Rosenstock, T. R.; Sharpe, J. C. Youle, R. J. *Braz. J. Med. Biol. Res.* **2003**, *36*, 183-190.

(75) Ye, R.-R.; Tan, C.-P.; Chen, M.-H.; Hao, L.; Ji, L.-N.; Mao, Z.-W. *Chem. Eur. J.* **2016**, *22*, 7800-7809.

(76) Gandin, V.; Tisato, F.; Dolmella, A.; Pellei, M.; Santini, C.; Giorgetti, M.; Marzano, C.; Porchia, M. *J. Med. Chem.* **2014**, *57*, 4745-4760.

(77) Tardito, S.; Bassanetti, I.; Bignardi, C.; Elviri, L.; Tegoni, M.; Mucchino, C.; Bussolati, O.; Franchi-Gazzola, R.; Marchio, L. *J. AM. Chem. Soc.* **2011**, *133*, 6235-6242.

(78) Marzano, C.; Gandin, V.; Pellei, M.; Colavito, D.; Papini, G.; Lobbia, G. G.; Del Giudice, E.; Porchia, M.; Tisato, F. Santini, C. *J. Med. Chem.* **2008**, *133*, 798-808.

(79) Li, C.; Ip, K. W.; Man, L.; Song, D.; He, M. L.; You, S. M.; Lau, T. C.; Zhu, G. *Chem. Sci.* **2017**, *8*, 6865-6870.

(80) Pierroz, V; Rubbiani, R.; Gentili, D.; Patra, M.; Mari, C.; Gasser, G.; Ferrari, S. *Chem. Sci.* **2016**, *7*, 6115-6124.

(81) Cini, M.; Williams, H.; Fay, M. W.; Searle, M. S.; Woodward, S.; Bradshaw, T. D.

Metallomics. **2016**, *8*, 286-297.

(82) Bras, M.; Quwwnan, B.; Susin, S. A. *Biochem*. **2005**, *70*, 284-293.

(83) Kashatus, D. F. *Biochem. Biophys. Res. Commun*. **2018**, *500*, 9-16.

(84) Xie, L.-L.; Shi, F.; Tan, Z.; Li, Y.; Bode, A. M. Cao, Y. *Cancer Sci*. **2018**, *109*, 3686-3694.

(85) Danese, A.; Patergnani, S.; Bonora, M.; Wieckwski, M. R.; Previati, M.; Giorgi, C.; Pinton, P. *Biochem. Biophys. Acta.* **2017**, *185*8, 615-627.

(86) Missiroli, S.; Patergnani, DS.; Caroccia, N.; Pedriali, G.; Perrone, M.; Previati, M. Wieckwski, M. R. Giorgi, C. *Cell Death Dis.* **2018**, *9*, 329.

(87) (a) Jacquemin, D.; Perpète, E. A., Scuseria, G. E., Ciofini, I., Adamo, C. TD-DFT Performance for the Visible Absorption Spectra of Organic Dyes: Conventional Versus Long-Range Hybrids. *J. Chem. Theory Comput.* **2008**, *4*, 123−125. (b) Volpi, G.; Garino, C.; Salassa, L., Fiedler, J.; Hardcastle, K. I.; Gobetto, R.; Nervi, C. Cationic Heteroleptic Cyclometalated Iridium Complexes with 1-Pyridylimidazo[1,5-α]pyridine Ligands: Exploitation of an Efficient Intersystem Crossing. *Chem. Eur. J.* **2009**, *15*, 6415−6427. (c) Srivastava, R.; Rao Joshi, L. The Effect of Substituted 1,2,4-Triazole Moiety on the Emission, Phosphorescent Properties of the Blue eEmitting Heteroleptic Iridium(III) Complexes and the OLED Performance: a Theoretical Study. *Phys. Chem. Chem. Phys.* **2014**, *16*, 17284−17294.

(88) (a) Ladouceur, S.; Donato, L.; Romain, M.; Mudraboyina, B. P.; Johansen, M. B.; Wisner, J. A.; Zysman-Colman, E. A Rare Case of Dual Emission in a Neutral Heteroleptic Iridium(III) Complex. *Dalton Trans.* **2013**, *42*, 8838−8847. (b) Zhang, K. Y.; Liu, H.-W.; Tang, M.-C.; Choi, A. W.-T.; Zhu, N.; Wei, X.-G.; Lau, K.-C.; Lo, K. K.-W. Dual-Emissive Cyclometalated Iridium(III) Polypyridine Complexes as Ratiometric

Biological Probes and Organelle-Selective Bioimaging Reagents. *Inorg. Chem.* **2015**, *54*, 6582−6593.

(89) Smart & SAINT Software Reference Manuals, Version 6.45, Bruker Analytical X-ray Systems, Inc., Madison, WI, **2003**.

(90) Sheldrick, G. M., SADABS, Software for Empirical Absorption Correction, Ver.2.05, University of Göttingen, Göttingen, Germany, **2002**.

(91) XPREP, 5.1 ed. Siemens Industrial Automation Inc., Madison, WI, **1995**.

(92) Sheldrick, G. M., SHELXL97, Program for Crystal Structure Refinement, University of Göttingen, Göttingen, Germany, **2008.**

(93) (a) Murov, S. L.; Carmichael, I.; Hug, G. L. *Handbook of Photochemistry*, *2nd Ed*.; Marcel Dekker, Inc.: New York, 1993. (b) DeBernardo, S.; Weigele, M.; Toome, V.; Manhart, K.; Leimgruber, W.; Böhlen, P.; Stein, S.; Udenfriend, S. Studies on the Reaction of Fluorescamine with Primary Amines. *Arch. Biochem. Biophys*. **1974**, *163*, 390−399.

ACKNOWLEDGEMENT

This research performed under supervision of Prof. Shin Aoki. I was much assisted with appropriate suggestions and sincere encouragement by Dr. Yutaka Saga (Assistant professor (2017-)), Dr. Yousuke Hisamatsu (Assistant professor (2014-2016)), Dr. Sarvendra Kumar (Postdoctoral fellow (2014-2016)), Dr. Shinya Ariyasu (Postdoctoral fellow (2014)), Dr. Tomohiro Tanaka (Postdoctoral fellow (2014-2016)), and Dr. Babita Shashni (Postdoctoral fellow (2015-)). I gratefully appreciate Prof. Shin Aoki. I appreciate Mrs. Fukiko Hasegawa (Faculty of Pharmaceutical Sciences, Tokyo University of Science) for collecting and interpreting the mass spectral data, Mrs. Noriko Sawabe (Faculty of Pharmaceutical Sciences, Tokyo University of Science) for the measurement of NMR. I wish to acknowledge Dr. Kenji Yoza (Bruker AXS), Dr. Kyouhei Sato (Research Institute for Science and Technology, Tokyo University of Science), Prof. Reiko Kuroda (Research Institute for Science and Technology, Tokyo University of Science). I appreciate the aid of Dr. Miho Hatanaka (Institute for Research Initiatives, Division for Research Strategy, Graduate School of Materials Sciences, Nara Institute for Science and Technology) for the helpful discussion of mechanistic study of selective degradation reaction.

In close, I would like to express sincere gratitude to my parents for great financial support and keeping me in good health spiritually.